Frequency Comb Driven Raman Transitions in the THz Range: High Precision Isotope Shift Measurements in Ca^+

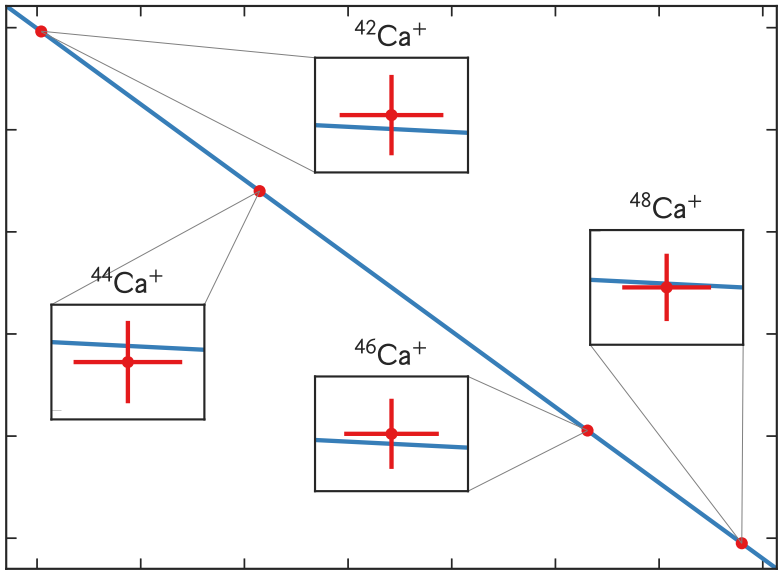

PhD thesis

Steffen Meyer

September 30, 2017
(Revised: June 27, 2018)

Department of Physics and Astronomy
Aarhus University

This thesis is submitted to the Faculty of Science and Technology at Aarhus University, Denmark, in order to fulfill the requirements for obtaining the PhD degree in Physics. The studies have been carried out under the supervision of Prof. Michael Drewsen in the Ion Trap Group at the Department of Physics and Astronomy at Aarhus University from July 2014 to September 2017.

Abstract in English

This thesis presents for the first time the experimental implementation of coherent Raman oscillations with a femtosecond frequency comb for transition frequencies in the THz range. The technique has been successfully demonstrated before to drive Raman transitions between hyperfine structure states in $^{171}Yb^+$ ions, with a transition frequency of 12.6 GHz. To extent this idea to the THz regime, the frequency comb light must have a spectral bandwidth equal or larger compared to the addressed transition frequency, requiring short laser pulses on the order of tens of femtoseconds, compared to picoseconds in the previous experiments. For the broad spectrum, the additional effect of group delay dispersion (GDD) has to be taken into account, since the Raman process relies on the coherent interaction of all frequency components of the spectrum, with GDD influencing the relative phase which leads to destructive interference. Therefore, GDD is compensated using a prism compressor and it is shown quantitatively that the measured GDD matches the theoretically predicted effect on the total Raman Rabi frequency. For the measurements and compensation of GDD, the techniques of interferometric autocorrelation and frequency resolved optical gating (FROG) are used, and the two frequency comb systems used for the experiments are thoroughly characterized, a Coherent Mira Ti:sapph oscillator and a MenloSystems fiber based frequency comb system.

The potential of *frequency comb driven Raman transitions* is shown by measuring the D-finestructure frequency in a single $^{40}Ca^+$ ion confined in a linear Paul trap, determining the transition frequency to 1 819 599 021 524(32) Hz. Moreover, the D-finestructure frequency of all even, naturally abundant Ca^+ isotopes is measured with the same technique, and the spectroscopic isotope shifts are extracted. To complement these measurements, the isotopes shifts of the 729 nm $|S_{1/2}\rangle \rightarrow |D_{5/2}\rangle$ transition for the same series of isotopes are also determined with a relative accuracy of 5×10^{-12}, using a different technique. To the best of my knowledge, these measurements represent the most accurate spectroscopic isotope shifts reported in literature so far.

The spectroscopic isotope shift relies partly on the interaction of the electron with the nuclear charge distribution, and deviations from the predictions of the standard model can be used to test theories predicting forces beyond the standard model. Hence, the measured isotope shifts of the two transitions are used in a so-called King plot analysis to set bounds on these hypothetical „new“ forces.

Frequency comb driven Raman transitions in the THz range will be a driving force in future spectroscopic studies on molecular ions, where the rotational transition frequencies typically are on the order of a few THz. High precision measurements on these ions have many intriguing applications, for example the test of time-variations of fundamental constants, ultracold chemistry on the quantum level, and quantum information and computing, to name just a few. In the Ion Trap Group in Aarhus, we plan to use the developed technique for spectroscopy and state manipulation of single MgH^+ ions.

Résumé på Dansk

I denne afhandling præsenteres den første eksperimentelle realisering af kohærente Raman-oscillationer med en femtosekunds frekvens-kam for overgangsfrekvenser i THz-området. Teknikken er tidligere blevet brugt til at drive Raman-overgange imellem hyperfine tilstande i $^{171}Yb^+$ ioner med en overgangsfrekvens på 12.6 GHz. For at udvide denne idé til THz-regimet, kræves det at lyset fra frekvens-kammen skal have en spektral båndbredde, der er lig med eller større end den addresserede overgangsfrekvens. Dette kræver laserpulser i størrelsesordenen 10 femtosekunders varighed, i forhold til picosekunders varighed i tidligere eksperimenter. For det brede spektrum er det nødvendigt at tage hensyn til såkaldt gruppe forsinkelsesdispersion (group delay dispersion, GDD), da Raman-processen er afhængig af kohærent interaktion af alle frekvenskomponenter. GDD fører derfor til ændringer i den relative fase og således til destruktiv interferens. Der kompenseres for GDD med en prisme kompressor, og det vises kvantitativt, at den målte GDD passer med den teoretisk forventede effekt på den fulde Raman-Rabi frekvens. Teknikkerne interferometrisk autokorrelation og frekvensafhængig optisk gating bruges til at karakterisere og kompensere for GDD. To frekvens-kamme benyttes til eksperimenterne, en Coherent Mira Ti:sapph oscillator og en MenloSystems fiberbaseret frekvens-kam, og de karakteriseres grundigt.

Mulighederne som *frekvens-kam drevne Raman overgange* åbner op for, vises ved at måle D-finstrukturen af en enkel $^{40}Ca^+$ ion indfanget i en lineær Paul fælde. Herved måles overgangsfrekvensen til 1 819 599 021 524(32) Hz. Derudover måles alle D-finstruktur frekvenser for alle naturlige Ca^+ isotoper ved hjælp af samme teknik, og de spektroskopiske isotop-skift bestemmes. Isotop-skiftene for 729 nm $|S_{1/2}\rangle \rightarrow |D_{5/2}\rangle$ overgangen for den samme serie isotoper måles også med en relativ præcision på 5×10^{-12} ved en anden metode. Disse målinger repræsenterer de mest præcise spektroskopiske isotop-skift der er målt til dags dato.

Det spektroskopiske isotop-skift er delvist afhængig af interaktionen mellem elektronen og fordelingen af ladningen i kernen. Standardmodellen laver forudsigelser om dette, og derfor vil forskelle fra forudsigelserne føre til at kunne teste teorier om kræfter udover standardmodellen. De målte isotop-skift af de to overgange er brugt i en såkaldt King plot-analyse til at sætte grænser i disse hypotetiske *nye* kræfter.

Frekvens-kam drevne Raman overgange i THz området vil blive en vigtig teknik i fremtidige spektroskopiske studier på molekulære ioner, hvor den rotationelle overgangsfrekvens typisk er i størrelsesordenen af et par THz. Højpræcisionsmålinger på disse ioner har mange interessante anvendelser. For eksempel tidsvariationen af fundamentale konstanter, ultrakold kemi på kvanteniveau, kvanteinformation og *quantum computing*, for at nævne nogle få. I Ionfælde Gruppen i Aarhus planlægger vi at udvikle teknikken til spektroskopi og tilstands-manipulation af enkle MgH^+ ioner.

Acknowledgements

First and foremost, I want to thank my supervisor Michael Drewsen for giving me the opportunity to work on this exciting PhD project, and for continuously criticizing my work. And a big thank you to all the members of the Ion Trap Group and the Optomechanics Lab. Thanks to Mike DePalatis and Thomas Lauprêtre, two former postdocs, for many inspiring discussions about physics and the world, especially on Friday evenings. Special thanks goes to Karin Fisher and Cyrille Solaro, with whom I am currently working on the same setup, for making the work in the basement fun, and also for proofreading this thesis. Without you this PhD project would not have been so successful. Thanks to Andreas Næsby, for helping me with the Danish translation of the abstract. Thank you Julian, for many entertaining coffee breaks and questions about physics.
And thanks to all other colleagues and friends in the group, current and former, Aurelien, Bhagya, Hans, Jacob, Katérina, Olivier, and Sepideh.
Also, I am grateful for having the chance of being part of the COMIQ network, a Marie Curie initial training network[1] funded by the European Commission, which did not only provide the funding for my PhD but also the opportunity to share knowledge with the other nodes, and to meet 14 other curious young researchers. Thank you Celia, for organizing COMIQ and always coming up with a solution for administrative challenges.
I also very much valued the support from our Electronics Department, especially Frank Korfix Mikkelsen.

Thank you all!

[1] FP7-PEOPLE-2013-ITN, grant agreement no 607491 - COMIQ (COld Molecular Ions at the Quantum limit). `http://itn-comiq.eu/`

The Ion Trap Group on September 21, 2017.

The Ion Trap Group in 2015.

Contents

List of Figures

List of Tables

Introduction

The field of research in ion traps is still a vivid one, full of new and astonishing physics, with a history going back more than 60 years, since the invention of the RF trap by Wolfgang Paul in 1953 [**paul_notizen_1953**, A1], and the Penning trap by Dehmelt in 1959 [A2], for which both were rewarded the Nobel prize in 1989 [O1].

Since these early developments, ion trapping was so successful, that in 2012 the Nobel prize was awarded partly to David Wineland "for ground-breaking experimental methods that enable measuring and manipulation of individual quantum systems" [O2]. A trapped and laser cooled ion basically represents the experimental quantum physicists dream. Trapped via the long ranging Coulomb interaction, the internal atomic structure is mostly undisturbed, close to a particle in free space. Ions can be stored on timescales of hours and longer, providing long interrogation and coherence times, and the development of the linear Paul trap [A3] enabled good optical access for lasers to the ion.

The idea of working with single quantum particles and directly observing the abrupt transition between two states of a quantum system as a *quantum jump* [A4], was unthinkable for the founders of quantum mechanics. Even Erwin Schrödinger asked, as late as 1952, still the question: "Are there quantum jumps" [A5], and ridicules the idea of ever experimenting with single quantum systems. Quantum mechanics with all its surprising effects, quite often opposite of daily life experience in the macroscopic world, has a profound impact on philosophical questions, such as long-range entanglement and other non-local phenomena [B1, B2].

However, in 1980, a single Ba^+ ion was trapped and imaged [A6] in a Paul trap, and it took only six years when in 1986 the first quantum jumps in a single quantum system were observed almost simultaneously in three different experiments [A7, A8, A9]. More than ten years before that, Dehmelt and Wineland had already suggested detecting quantum jumps via the shelving technique [A10], converting the excitation of a single quantum into millions of fluorescence photons, a standard technique in nowadays ion trap experiments.

To be able to observe single trapped ions, they need to be localized by slowing them down from their initial room temperature velocities of typically hundreds of m/s to several cm/s, corresponding to mK temperatures. This can be achieved via laser cooling [R1], first suggested in 1974 by Hänsch and Schawlow [A11].

A trapped, laser cooled ion is ideal for spectroscopy, which is the art of exploring the internal structure of a quantum system by measuring the frequency of a light field in resonance with a quantum transition in this system. Moreover, a frequency measurement corresponds to counting the number of oscillations in a well defined timespan, so that spectroscopy of a *known* transition can also be

used to measure time instead, not fundamentally different from a simple pendulum clock. In fact, time itself has been defined[2] since 1967 by radio frequency spectroscopy in ^{133}Cs, only about a decade after the first demonstration of a Cs clock [A13]. Even though current Cs clocks reach fractional stabilities below 10^{-15} [A14, A15], the question of "When should we change the definition of the second?" [A16] is becoming more pressing.

The first clock operating in the optical regime [R3] was demonstrated in 2001 with a single trapped $^{199}Hg^{+}$ ion, already reaching a stability of 7×10^{-15} in 1 s [A17]. State of the art optical clocks reach stabilities of 3×10^{-18} [A18, A19, A20, A21], surpassing the Cs stability by more than two orders of magnitude. Time is the quantity that can be measured most precisely, and the strategy nowadays is often to relate a given quantity to a measurement of time, for instance, the meter[3] is defined via time [A22]. Arthur Schawlow highlights this by recommending his students: "Never measure anything but frequency!" [A23]

Driven by the huge success of atomic ion physics, the study of molecular ions is currently gaining more and more attention [R4]. It is of fundamental interest to understand molecular structure, where not even the simplest 3-body systems can be solved analytically. The combination of atoms to a molecule gives rise to motion on very different timescales, due to the different masses of nuclei and electrons, leading to a much richer structure compared to atoms.

Additionally, some molecular transitions are highly insensitive to external perturbations, and are used in high resolution spectroscopy experiments for the search of time variation of fundamental constants [R5], the possible dipole moment of the electron [A24], and the search for a "fifth force" [A25]. "Atomic" clocks based on molecular transitions in the infrared are also considered [A26].

The field of quantum information, sensing, simulation and computing is currently on the verge of making the jump to the consumer market, supported by the European quantum technologies flagship program [A27, A28], and actual implementations of a large scale quantum computer are discussed [A29]. The idea of a universal quantum computer [R6] already began to grow in the 1980s [A30, A31, A32], and the use of molecular ions [A33] could surpass atomic ion implementations [R7, R8].

The techniques developed for trapping and manipulating single atomic ions are so advanced today, apparent from the incredible accuracy of optical clocks (1 s off in 10 billion years, that is close to the age of the universe!), that it seems natural to move forward, to these larger, more complex quantum systems, exploiting their described potential for future applications. But, all the discussed features of molecular ions come at a cost in the form of experimental challenges. For instance, molecules generally lack closed transitions due to the rich internal structure, and thus cannot be directly laser cooled. However, more sophisticated methods such as quantum logic spectroscopy [A34], where the state of a trapped molecular ion is detected via its shared motion with a co-trapped atomic ion, are well developed today and allow one to bypass these problems.

[2] "The second is the duration of 9 192 631 770 periods of the radiation corresponding to the transition between the two hyperfine levels of the ground state of the caesium-133 atom." [R2, A12]

[3] Since 1983, "The metre is the length of the path travelled by light in vacuum during a time interval of 1/(299792458) of a second." [A22]

The transition frequencies in molecular ions are typically in the mid-infrared for vibrational transitions, and the THz regime for rotational transitions. Mid-infrared transitions can be addressed with quantum cascade lasers [A35, B3, R9], discussed in the outlook of this thesis, but even though the development of the laser is already over 50 years ago, there still exist no powerful coherent sources in the THz regime [B4, R10]. One option to circumvent this challenge is to drive these THz transitions via a two photon Raman process. This was demonstrated using two CW lasers in an atomic system to measure the D-finestructure in $^{40}Ca^{+}$ by Yamazaki et al. in 2008, with a transition frequency of 1.8 THz [A36]. However, spanning the large THz frequency gap in this way is difficult and not very flexible, since the two separate laser systems need to be phase-locked. Conventional light modulators such as acousto- or electro-optic modulators are limited to about 10 GHz, which is why Yamazaki et al. had to use an optical comb generator for this purpose [A37].

A different approach to drive Raman transitions is to exploit the natural phase coherence of the individual frequency components of a frequency comb [R11, B5, A38, A39, A40]. The frequency comb spectrum consists of many well-defined frequency components, with a fixed and measurable spacing between them. This spectrum is conveniently generated by a pulsed laser, when the repetition rate of the emitted laser pulses is stabilized. The spectral spacing is then given by the repetition rate, and the spectral bandwidth is inversely proportional to the pulse length. One popular type of laser is the Ti:sapphire oscillator, such as the Mira laser I use in the experiments detailed in this thesis, where the passive mode-locking technique guarantees the phase coherence over the generated comb spectrum. In fact, already Theodor Hänsch worked in the 1990s on a Mira laser in his laboratory in Garching [R12, A41]. He later, in 2005, shared half the Nobel prize with John L. Hall "for their contributions to the development of laser-based precision spectroscopy, including the optical frequency comb technique" [O3, R12]. Before the optical frequency comb, direct measurements of optical frequencies were extremely challenging. For example, one experiment bridged the gap to the Cs clock with a frequency chain, distributed over several laboratories in separate buildings [A42]. Today, the frequency comb is a mature and reliable tool and is, for instance, used as a calibration source for spectroscopy in astronomy [A43], for the generation of attosecond pulses [A44], and a frequency comb has even been brought to space on board of a sounding rocket for spectroscopic measurements [A45].

The experimental implementation of the idea to drive coherent Raman transitions with a frequency comb was shown by Hayes et al. in 2010 [A46, T1], demonstrating coherent population transfer between hyperfine transitions in $^{171}Yb^{+}$. The $|F = 1, m_F = 0\rangle \rightarrow |F = 0, m_F = 0\rangle$ hyperfine states of the $^2S_{1/2}$ level in $^{171}Yb^{+}$ are split by 12.6428 GHz. Thus, transitions can be driven with a relatively long laser pulse time of about 1 ps, corresponding to a bandwidth limited frequency comb spectral width of only about 400 GHz.

In this thesis, I demonstrate the extension of this scheme to the THz range, by coherently driving the D-finestructure transition in Ca^{+} with a frequency comb. This technique, *frequency comb driven Raman transitions*, is extremely versatile, since the resonance condition can be met with any combination of comb teeth over the total spectral bandwidth of the comb, spanning several

THz for frequency combs emitting laser pulses in the fs regime. The effective laser linewidth for the Raman process is given by the stability of the difference frequency between the spectral components driving the transition. This frequency spacing in the comb spectrum, given by the repetition rate of the laser generating the comb, can easily be controlled and stabilized. I demonstrate the potential of the technique by determining the D-finestructure transition frequency in $^{40}Ca^+$ to 1 819 599 021 524(32) Hz, where the uncertainty of 32 Hz is limited by external perturbations, and not the laser itself. A team at NIST in Boulder is currently implementing the same technique for the spectroscopy of CaH^+. Molecular spectroscopy in general might be strongly influenced by this new technique, and I will discuss planned experiments on MgH^+ in the Ion Trap Group in the outlook of this thesis.

In addition to the absolute $^{40}Ca^+$ transition measurement, I measured the spectroscopic isotope shifts of all naturally abundant even isotopes of Ca^+ using the same technique. The energy of a spectral line is a characteristic property of an element, that means a characteristic of the number of protons in the nucleus. However, precision spectroscopy reveals a slight dependence of the transition energy on the number of neutrons in the core, so different isotopes of an element have slightly different transition energies between the same electronic levels. This effect is called the spectroscopic isotope shift [R13, B6].

The isotope shift in Ca^+ has been studied before [A47, A48, A49, A50], and has the potential to give insight into some exciting "new physics." That our current physical understanding in terms of the standard model is not complete, is obvious for instance from the existence of dark matter, apparently only interacting gravitationally with our "normal" matter [R14]. The isotope shift in an atom stems partly from the forces the electron experiences while penetrating the nucleus. Thereby, relativistic and QED effects become important [A51, A52], and even physics beyond the standard model can be tested. For example, new forces between nuclei and the electron [A53, A54] can be identified by nonlinearities in the so-called King plot [A55, A56], which relates the isotope shift of two separate transition measurements to eliminate dependencies expected from the standard model.

The spectroscopic isotope shifts presented in this thesis are, to the best of my knowledge, the most accurate reported in literature so far. An active discussion with researchers at the Weizmann Institute of Science about the impact of these measurements on the mentioned theoretical predictions on "new physics," is currently still ongoing.

Thesis outline

This thesis is divided into four main parts. In part I, **Ion Trapping and the Interaction with Light Fields**, I discusses the linear Paul trap in chapter 1, and focus in chapter 2 on the interaction of a trapped ion with light fields.

Part II, **The Optical Frequency Comb and its Characterization**, describes the frequency comb, both theoretically and its implementation. The concept of generating a broad, comb-like spectrum with a repetition rate stabilized pulsed laser is mathematically introduced in chapter 3. Chapter 4 then describes in detail the two frequency comb laser systems used in the experiments, the Mira laser and the Menlo comb, pointing out the ways in which they differ. Since the accuracy of spectroscopy measurements using the frequency comb relies on the accuracy of the frequency standard used as a reference, chapter 5 gives a thorough characterization of our newly implemented GPS disciplined rubidium standard. Similarly important for the dynamics of *frequency comb driven Raman transitions* is the stability of the repetition rate of the laser, and chapter 6 is dedicated to the comparison of the two laser systems in this respect. The last chapter in this part covers the two experimental techniques used for fs pulse characterization in this work, interferometric autocorrelation and frequency resolved optical gating (FROG), in chapter 7.

Finally, the main experiments of this thesis are presented in part III, **Experiments with Ca^+: High Precision Spectroscopy and Isotope Shifts**. First, chapter 8 describes the quantification of systematic frequency shifts influencing spectroscopic measurements in our trap. An overview of the experimental setup is given in chapter 9, including a description of the trap chamber, lasers, as well as the control software and hardware. The experimental realization and implementation of the most important techniques used in the experiments is summarized in chapter 10, including laser cooling and internal state preparation of the ion. A measurement of the $|S_{1/2}\rangle \rightarrow |D_{5/2}\rangle$ transition frequency in $^{40}Ca^+$ with an absolute accuracy of 2 kHz, only limited by our reference clock, is presented in chapter 11. In chapter 12, I present the main technique developed during this thesis work, *frequency comb driven Raman transitions* in the THz-range, by coherently driving Rabi oscillations between the D-finestructure levels in $^{40}Ca^+$. In chapter 13, the technique is then used to obtain an absolute transition measurement of the $|D_{5/2}\rangle \rightarrow |D_{3/2}\rangle$ transitions in $^{40}Ca^+$, thereby spanning 1.8 THz with the frequency comb light, and reaching an absolute accuracy of 32 Hz. The measurements presented in the two previous chapters are extended to all naturally abundant even isotopes of Ca^+ in chapter 14. By measuring the most precise spectroscopic isotope shifts in literature so far, I provide the data to discuss theoretical models predicting "new physics" beyond the standard model.

Lastly, in part IV, **Outlook and Conclusion**, I outline future experiments we intend to conduct in the Ion Trap Group in chapter 15, and conclude this thesis in chapter 16.

Part I

Ion Trapping and the Interaction with Light Fields

I sometimes fall into the trap of doing what I think I should be doing rather than what I want to be doing.

Björk

1 Ion Trapping

Traps for neutral particles rely on the interaction of external magnetic or optical fields with the internal structure of the trapped atom, and are limited to trap depths of about 1 mK for dipole traps to about 1 K for magneto-optical traps [A57, A58]. Compared to neutral particles, it is possible to construct very deep traps for ions by exploiting their net electric charge via the long range Coulomb interaction in an electric field. Since these trapping fields are small compared to the intra-atomic fields, the internal structure of an ion trapped in this way is almost unaffected, so that its structure can be studied almost without perturbations. However, the Laplace equation in free space

$$\nabla^2\phi(x,y,z) = \frac{\partial^2\phi(x,y,z)}{\partial x^2} + \frac{\partial^2\phi(x,y,z)}{\partial y^2} + \frac{\partial^2\phi(x,y,z)}{\partial z^2} = 0\,, \tag{1.1}$$

does not allow a global potential minimum in all three dimensions (Earnshaw's Theorem), which would require all second derivatives to be positive.

There exist two solutions to circumvent this problem. The first is to use a magnetic field in addition to the electric field which confines the motion of a trapped particle into a stable orbit in a so-called Penning trap [R15, A59], invented by H.G. Dehmelt. The other approach uses a radio frequency field in addition to a static electric field to generate three dimensional confinement. This RF trap [A1] was invented by Wolfgang Paul who later shared half the Nobel Prize in Physics with Dehmelt "for the development of the ion trap technique" [A60, A61].

1.1 The linear Paul trap

For the experiments presented in this thesis, I use a variation of the original RF-trap, a so-called linear Paul trap [A3], depicted in figure 1.1, which allows good optical access to the trapping region.

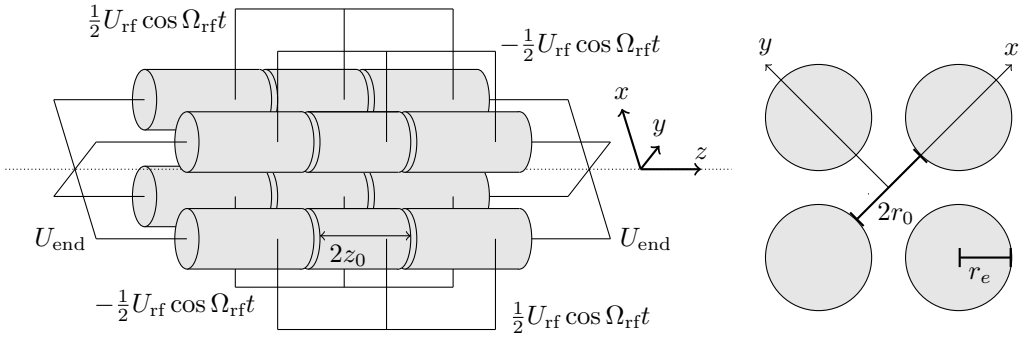

Figure 1.1: Geometry of the linear Paul trap and applied voltages. The 8 outer electrodes are called "end-cap" electrodes and are supplied with a DC voltage relative to the 4 central electrodes. RF voltages are applied on each rod, consisting of 3 electrodes each.

The trap consists of 4 parallel rods, which are segmented in three separate electrodes each. A positive dc voltage U_{end} is applied to the 8 end-cap electrodes relative to the 4 central electrodes with a length of $2z_0$. This creates a confining harmonic potential in the axial direction of the trap given by

$$\phi_{\mathrm{dc}}(x,y,z) = \kappa U_{\mathrm{end}}\frac{z^2}{z_0^2} - \frac{1}{2}\kappa U_{\mathrm{end}}\frac{x^2+y^2}{z_0^2}\ , \tag{1.2}$$

but a repulsive potential in the radial direction due to the Laplace equation (1.1). The factor κ is determined by the geometry of the trap. Radial confinement is achieved by adding an rf voltage $\pm\frac{1}{2}U_{\mathrm{rf}}\cos(\Omega_{\mathrm{rf}}t)$ to the four rods of the trap. Opposite rods are separated by $2r_0$ and the rf voltage is in-phase, while adjacent rods are 180° out-of-phase. In total, this results in an rf quadrupole potential in the radial directions

$$\phi_{\mathrm{rf}}(x,y,t) = -\frac{1}{2}U_{\mathrm{rf}}\cos(\Omega_{\mathrm{rf}}t)\,\frac{x^2-y^2}{r_0}\,. \tag{1.3}$$

1.2 Equations of motion

The equations of motion for a trapped particle of mass m and charge Q can be separated in all three dimensions. Axially, the potential (1.2) resembles the harmonic oscillator with eigenfrequency

$$\omega_z = \sqrt{\frac{2\kappa U_{\mathrm{end}}}{z_0^2}\frac{Q}{m}}\,. \tag{1.4}$$

The equation of motion in the radial direction can be transformed into a well-studied mathematical form called the Mathieu equation

$$\frac{d^2u}{d\tau^2} + \big(a_r - 2q_u\cos(2\tau)\big)\,u = 0; \quad u = x,\,y\,, \tag{1.5}$$

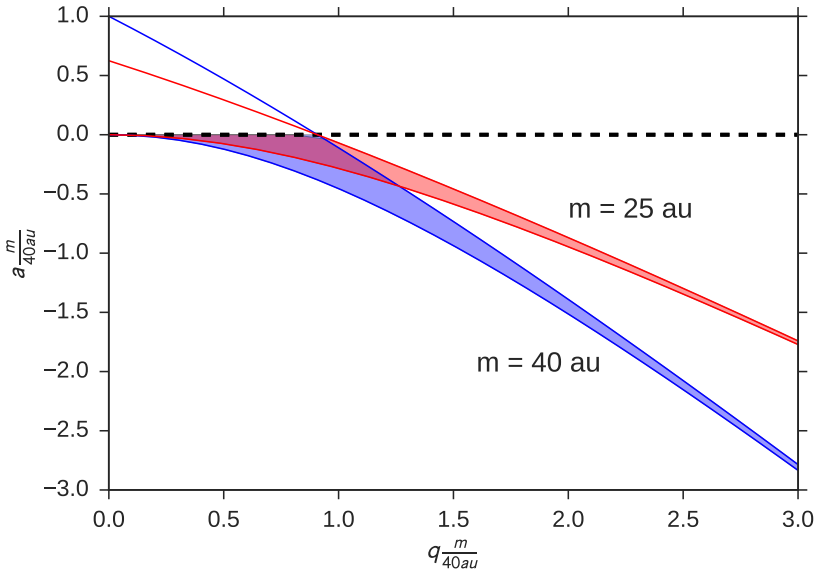

Figure 1.2: Trap stability diagram for Ca^+ and MgH^+ .

with the dimensionless parameters

$$\tau = \frac{\Omega_{\mathrm{rf}} t}{2} \tag{1.6}$$

$$a_r = -\frac{4Q\kappa U_{\mathrm{end}}}{m\, z_0^2 \Omega_{\mathrm{rf}}^2} \tag{1.7}$$

$$q_x = -q_y = 2\,\frac{QU_{\mathrm{rf}}}{m\, r_0^2 \Omega_{\mathrm{rf}}^2}\,. \tag{1.8}$$

Stable, non diverging solutions of the Mathieu equation do not exist for arbitrary parameters a_r and q_x. In particular, confinement for a positively charged ion requires positive end-cap voltages and thereby $a_r < 0$. The stable and confining solutions are plotted in a so-called stability diagram [A62] in figure 1.2 for Ca^+ and MgH^+ together. In future experiments, we plan to trap a single MgH^+ ion together with a single $^{40}Ca^+$ ion, so that the parameters a_r and q_x have to be chosen such that trapping of both species is stable.

For $|a_r| \ll 1$ and $|q_x| \ll 1$, the solution can be approximated to

$$u(t) = u_0 \left(1 - \frac{q_u}{2}\cos\left(\Omega_{\mathrm{rf}} t\right)\right)\cos\left(\omega_r t\right)\,, \tag{1.9}$$

with the radial trap frequency

$$\omega_r = \sqrt{\frac{U_{\mathrm{rf}}^2}{2r_0^4\Omega_{\mathrm{rf}}^2}\frac{Q^2}{m^2} - \frac{1}{2}\omega_z^2}\,. \tag{1.10}$$

This solution corresponds to a harmonic motion with frequency ω_r with an additional driven motion at the rf frequency Ω_{rf} superimposed on it. The motion

at the rf frequency is called micromotion since its amplitude will be small compared to the secular motion at frequency ω_r for suitably chosen trap parameters in eq. (1.9). The trap axis $x = y = 0$ is a line of zero micromotion, so that micromotion is minimized for experiments with a single ion or a string of ions on this axis. The radial potential can then be approximated as

$$\phi_r = \frac{1}{2} m \omega_r^2 r^2 \,, \tag{1.11}$$

with $r = \sqrt{x^2 + y^2}$.

1.3 Multiple ions in the trap

For future experiments using quantum logic spectroscopy discussed in section 2.4, we will trap two ions of different species, $^{40}Ca^+$ and MgH^+ together. If multiple ions are trapped together in the same trap they will repel each other due to the Coulomb repulsion, and the effective potential on the trap axis becomes

$$\phi_z = \frac{1}{2} u_0 \left(z_1^2 + z_2^2 \right) + \frac{Q^2}{4\pi\epsilon_0 \left| z_2 - z_1 \right|}; \quad u_0 = \frac{2Q\kappa}{z_0^2} U_{\text{end}} \,, \tag{1.12}$$

when the trap parameters are chosen such that the confinement is stronger in the radial than in the axial direction. The motion of the two ions is not independent, but coupled by the Coulomb interaction.

The equations of motion for the two ions can be separated into normal modes, such that for two ions with masses m and M, with $M \geq m$, the frequencies of the two modes are [A63]

$$\omega_\pm^2 = \omega_z^2 \left(1 + \frac{m}{M} \mp \sqrt{1 + \frac{m^2}{M^2} - \frac{m}{M}} \right) . \tag{1.13}$$

The frequency ω_- corresponds to the center-of-mass mode where the two ions move together in phase while the frequency ω_+ belongs to the breathing mode where the two ions move 180° out of phase. In the case of two equal species $M = m$ we find the two frequencies to be related to the single ion trap frequency ω_z by

$$\omega_- = \omega_z \tag{1.14}$$

$$\omega_+ = \sqrt{3}\omega_z \,. \tag{1.15}$$

The coupled motion of a molecular ion with a co-trapped atomic ion can be exploited to transfer internal state information from one ion to the other. This is the idea quantum logic spectroscopy, discussed in chapter 2.4.

Treat me right and you will see the light...
Treat me wrong and you will be gone!!

C. V. Raman

2

Atom-Light Interaction and Laser Cooling

In this chapter, I will describe the iteration of a trapped ion with a light field in section 2.1 beginning with the simple two-level system in free space, and discussing the coupling to the motion in the case of a trapped ion. The theory is then extended to the three-level atom interacting with two light fields in a Raman process. Section 2.2 describes different approaches to model the coherent oscillations between the internal states of the atom induced by the interaction with the light field. From there, laser cooling is discussed in section 2.3, and quantum logic spectroscopy, a scheme to transfer information between two ions trapped together by exploiting their coupled motion, in section 2.4.

2.1 The trapped ion in one or more light fields

In many relevant cases for our experiment we can consider each laser or light field to be resonant with one specific internal transition of the ion of interest but far detuned from any other transitions ot the ion. In this case, the internal structure of the ion can be modeled as a 2-level system with ground state $|0\rangle$ and excited state $|1\rangle$, split by the energy difference $\hbar\omega_a$.

The atomic Hamiltonian can be written as

$$\mathrm{H}^{\mathrm{a}} = \hbar\omega_a \left(|1\rangle\langle 1| - |0\rangle\langle 0|\right) = \hbar\frac{\omega_a}{2}\sigma_z \tag{2.1}$$

where is the z-component of the Pauli spin vector.

2.1.1 Electric field interaction

The electric field of a laser with frequency ω_L at the ion can be approximated as a plane wave

$$\vec{E}(x,\,t) = \frac{E_0}{2}\hat{\epsilon}\left[e^{-i(kx-\omega_L t+\phi)} + e^{+i(kx-\omega_L t+\phi)}\right], \tag{2.2}$$

where $k = \omega_L/c$ is the wavenumber, $\hat{\epsilon}$ is the polarization, and ϕ is the phase of the field. In terms of intensity, the electric field amplitude squared is given by

$$|E_0|^2 = \frac{2I}{\epsilon_0 c}\,. \tag{2.3}$$

For a dipole allowed transition, the interaction can be modeled by

$$\mathrm{H^i} = -e\hat{x}\cdot\vec{E}(x,\,t)\,, \tag{2.4}$$

where e is the electron charge, and can be written in in terms of the Pauli operators σ_+, σ_- as

$$\mathrm{H^i} = \frac{\hbar}{2}\Omega_0\left(\sigma_+ + \sigma_-\right)\left[e^{-i(kx-\omega_L t+\phi)} + e^{+i(kx-\omega_L t+\phi)}\right] \tag{2.5}$$

where Ω_0 is the so-called Rabi frequency [R16]

$$\Omega_0 = \frac{eE_0}{\hbar}\left\langle 0\right|\hat{\epsilon}\cdot\hat{x}\left|1\right\rangle\,. \tag{2.6}$$

This description assumed the dipole approximation, where the amplitude of the electric field E_0 can be considered constant over the extend of the atom. Similarly, the Rabi frequency for a quadrupole transition is given by [T2]

$$\Omega_0^{\mathrm{quad}} = \frac{eE_0}{2\hbar}\left\langle 0\right|(\hat{\epsilon}\cdot\hat{x})(\vec{k}\cdot\hat{x})\left|1\right\rangle\,. \tag{2.7}$$

The total Hamiltonian for the atom interacting with the electric field is then

$$\mathrm{H} = \mathrm{H^a} + \mathrm{H^i}\,. \tag{2.8}$$

For the atom at rest, the term kx in eq. (2.7) can be considered constant and absorbed as a complex phase, so that transformed in the interaction picture the Hamiltonian reads

$$\mathrm{H_I} = \frac{\hbar}{2}\Omega_0\left(\sigma_+ e^{i\omega_a t} + \sigma_- e^{-i\omega_a t}\right)\left[e^{-i(\omega_L t+\phi)} + e^{+i(\omega_L t+\phi)}\right]\,. \tag{2.9}$$

The fast rotating terms at the frequency $\omega_L + \omega_a$ can be neglected, if the laser is close to resonance, that means if the detuning $\delta = \omega_L - \omega_a$ is small compared to the sum frequency. This is called the rotating wave approximation, and we find

$$\mathrm{H_I} = \frac{\hbar}{2}\Omega_0\left(\sigma_+ e^{-i(\delta t+\phi)} + \sigma_- e^{+i(\delta t+\phi)}\right)\,. \tag{2.10}$$

A unitary transformation into the frame rotating at laser detuning δ finally gives the simple Hamiltonian

$$\mathrm{H} = \frac{\hbar}{2}\begin{pmatrix}\delta & \Omega\\ \Omega^* & -\delta\end{pmatrix}\,, \tag{2.11}$$

with the complex Rabi frequency, absorbing the phase ϕ

$$\Omega = \Omega_0\, e^{i\phi}\,. \tag{2.12}$$

From here, we can solve the Schrödinger equation to calculate the ground and excited state population P_0, P_1 as function of time. Starting with $P_0 = 0$, we find

$$P_1(t) = \frac{\Omega_0^2}{\Omega_0^2 + \delta^2} \sin^2\left(\sqrt{\Omega_0^2 + \delta^2}\,\frac{t}{2}\right); \quad P_0 = 1 - P_1\,. \tag{2.13}$$

The population will undergo coherent oscillations between the two states of the system at the generalized Rabi frequency

$$\Omega_G = \sqrt{\Omega_0^2 + \delta^2}\,, \tag{2.14}$$

and the slowest oscillation frequency $\Omega_G = \Omega_0$ arises when the laser is directly on transition with no detuning $\delta = 0$. Additionally, the amplitude of the oscillation is maximal for zero detuning, resulting in perfect population transfer between the two states. For a laser pulse timed such that it results in a pulse area $\Omega_0 t = \pi$, the population is inverted. More details on the dynamics of this so-called Rabi-flopping are given in section 2.2.

2.1.2 Rabi frequency for dipole transitions

The complex resonant Rabi frequency, equation (2.12), for a dipole transition interacting with a known light field with complex amplitude E can be calculated directly from experimentally determined decay rates, in form of the Einstein A coefficients, to [A64]

$$\Omega = \frac{eE_0}{\hbar\sqrt{c\alpha}}\sqrt{\frac{A}{k^3}}\sigma\,. \tag{2.15}$$

Here, σ is defined as

$$\sigma = \sqrt{\frac{3(2j'+1)}{4}}\left|\sum_{q=-1}^{1}\begin{pmatrix} j & 1 & j' \\ -m_j & q & m'_j\end{pmatrix}\boldsymbol{c}^{(q)}\cdot\boldsymbol{\epsilon}\right|, \tag{2.16}$$

with the term in parenthesis being the Wigner 3-j symbols, and $\boldsymbol{c}^{(q)}$ are the normalized spherical basis vectors [A64, Appendix]

$$\boldsymbol{c}^{(1)} = -\frac{1}{\sqrt{2}}(1, -i, 0) \tag{2.17}$$

$$\boldsymbol{c}^{(0)} = (0, 0, 1) \tag{2.18}$$

$$\boldsymbol{c}^{(-1)} = \frac{1}{\sqrt{2}}(1, i, 0)\,. \tag{2.19}$$

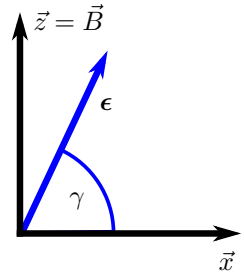

Figure 2.1: Polarization scheme

For a magnetic field $\boldsymbol{B} = B_0\ (0, 0, 1)$ along the vertical z direction, the polarization of the field $\boldsymbol{\epsilon}$ is defined as [T2, p. 30]

$$\boldsymbol{\epsilon} = (\cos\gamma\cos\phi,\ \sin\gamma,\ -\cos\gamma sin\phi)\,, \tag{2.20}$$

where γ is the angle between the polarization and the magnetic field, and ϕ is the angle between the wave-vector $\boldsymbol{k}$ and the magnetic field, as depicted in figure 2.1, where $\vec{k} \perp \vec{B}$, $\hat{x}$, and $\phi = \pi/2$, as in our trap setup, detailed in chapter 9). I will use equation (2.15) in chapter 12 for the calculation of the Rabi frequencies in Ca^+ interacting with the frequency comb light.

2.1.3 Interaction with the ion motion

For a trapped ion interacting with a light field, we have to consider its motion in the trap additional to the atoms internal structure, given by the two levels $|0\rangle$ and $|1\rangle$. The motion can be modeled in a given direction x as a one-dimensional harmonic oscillator with the trap frequency ω_x as described in chapter 1, so that the motional Hamiltonian is

$$\mathrm{H}^{\mathrm{m}} = \hbar\omega_x \left(\hat{a}^\dagger \hat{a} + \frac{1}{2}\right) , \tag{2.21}$$

with the ladder operators $\hat{a}^\dagger$, $\hat{a}$. The system has to be described in the product space of motional Fock states $|n\rangle$ and atomic levels $|0\rangle$, $|1\rangle$, with the total Hamiltonian, consisting of atomic, motional, and light interaction part, is then given by

$$\mathrm{H} = \mathrm{H}^{\mathrm{a}} + \mathrm{H}^{\mathrm{i}} + \mathrm{H}^{\mathrm{m}} , \tag{2.22}$$

with H^{i} from equation (2.5) describing the atom interacting with the light field, and the atomic Hamiltonian H^{a} from equation (2.1).

Now, we cannot assume $k\hat{x}$ as constant anymore in H^{i} , since the light can couple to the motion of the ion via

$$\hat{x} = \sqrt{\frac{\hbar}{2m\omega_x}} \left(a + a^\dagger\right) . \tag{2.23}$$

In the interaction picture, the total Hamiltonian becomes

$$\mathrm{H}_{\mathrm{int}} = \frac{\hbar}{2}\Omega\sigma_+ \exp\left[i\,\eta\left(\hat{a}e^{-i\omega_z t} + \hat{a}^\dagger e^{i\omega_z t}\right)\right] e^{i(\phi-\delta t)} + \mathrm{H.c.} , \tag{2.24}$$

with the Lamb-Dicke parameter

$$\eta = k\hat{x}\sqrt{\frac{\hbar}{2m\omega_z}} = kx_0 , \tag{2.25}$$

where x_0 is the one-dimensional extension of the ion's ground state wave function in the harmonic trapping potential. If the ion is confined in a way that the extension of its wave function is small compared to the wavelength of the light, we can expand equation (2.24) in lowest order of η. This limit is called the Lamb-Dicke Regime where we find

$$\mathrm{H}_{\mathrm{int}} = \frac{\hbar}{2}\Omega\sigma_+ \left[1 + i\,\eta\left(\hat{a}e^{-i\omega_z t} + \hat{a}^\dagger e^{i\omega_z t}\right)\right] e^{i(\phi-\delta t)} + \mathrm{H.c.} . \tag{2.26}$$

For laser detunings $\delta = 0, \pm\omega_z$ the light is resonant with the following transitions

1. *Carrier transition*: $\delta = 0$
   If the light field is resonant with the atomic transition frequency it drives transitions $|g, n\rangle \rightarrow |e, n\rangle$ with Rabi frequency Ω.

2. *First red sideband transition*: $\delta = -\omega_z$
   The light drives transitions $|0, n\rangle \rightarrow |1, n-1\rangle$ with Rabi frequency

$$\Omega_{n,n-1} = \eta\sqrt{n}\,\Omega \tag{2.27}$$

3. *First blue sideband transition*: $\delta = +\omega_z$
   The light drives transitions $|0, n\rangle \rightarrow |1, n+1\rangle$ with Rabi frequency

$$\Omega_{n,n+1} = \eta\sqrt{n+1}\,\Omega \tag{2.28}$$

Red sideband transitions are used for resolved sideband cooling discussed in section 2.3.2, and probing on the red and blue sideband one after the other can be used to determine the temperature of a trapped ion [A65, T3]. Sideband transitions also introduce entanglement of the internal and motional states of two co-trapped ions which is the main idea of quantum logic spectroscopy (QLS) discussed in section 2.4.

2.1.4 Light shifts

So far we only considered light with frequencies close to the atomic resonance. A light field which is far detuned from an atomic resonance will not lead to significant population transfer, but instead shifts the atomic energy levels. This shift, called the *light shift* or AC-Stark shift, is illustrated in figure 2.2. For a laser blue detuned by $\Delta = \omega_L - \omega_a > 0$ to the atomic resonance, the ground state $|0\rangle$ is shifted up in energy by

$$\Delta_{0,\,AC} = \frac{|\Omega|^2}{4\Delta}\,, \tag{2.29}$$

whereas the excited state is shifted down by the same amount. Thereby, the transition frequency, when probed by another light field, changes by

$$\Delta_{0\rightarrow 1,\mathrm{AC}} = -\frac{|\Omega|^2}{2\Delta}\,. \tag{2.30}$$

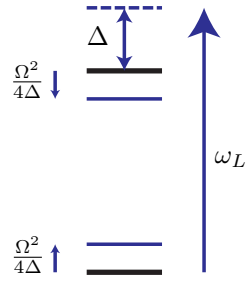

Figure 2.2: A laser beam detuned by Δ from an atomic resonance shifts both levels by $\frac{\Omega^2}{4\Delta}$ in opposite directions.

In other words, if the laser frequency is larger than the transition frequency, the shifted transition frequency is reduced by lifting the lower state and lowering the upper state by the same amount. This will be relevant when discussing Raman transitions in a three-level atom in the following section.

2.1.5 Raman transitions

Now we consider a three-level atom interacting with two lasers. A Raman transition is a two photon process where population is moved between two states $|0\rangle$ and $|1\rangle$ via off resonant coupling to a third auxiliary level $|e\rangle$, as sketched in figure 2.3. The two states are split in energy by $\hbar\omega_a$ and the level $|e\rangle$ is $\hbar\omega_e$ above the ground state $|0\rangle$. Two light fields with single photon detuning Δ_0, Δ_1 and resonant Rabi frequencies Ω_0, Ω_1 are interacting with the atomic three level system. The

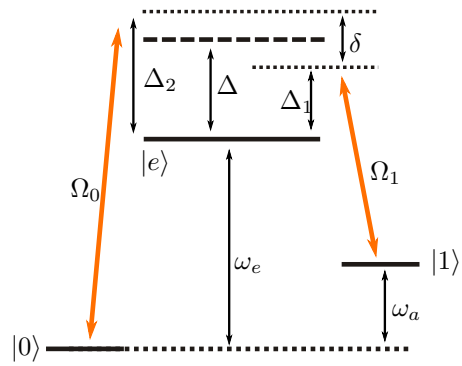

Figure 2.3: Schematic drawing of a Raman transition.

average single photon detuning is $\Delta = \frac{\Delta_0+\Delta_1}{2}$ and the two photon detuning is defined as $\delta = \Delta_0 - \Delta_1$.

The interaction picture Hamiltonian can then be written as [A66]

$$\mathrm{H_I} = \frac{\hbar}{2}\begin{pmatrix} -\delta & 0 & \Omega_0 \\ 0 & \delta & \Omega_1 \\ \Omega_0^* & \Omega_1^* & 2\Delta \end{pmatrix} . \tag{2.31}$$

If the single photon detunings are large compared to linewidth of the transition $\Delta \gg \Gamma_e$, the auxiliary state $|e\rangle$ does not get populated, and its population $\left|c_e(t)\right|$ does not change ($\frac{\partial}{\partial t}c_e(t) = 0$). Solving the Schrödinger equation with this assumption is called "adiabatic elimination", reducing the problem to a two level system with the effective Hamiltonian

$$\mathrm{H_{eff}} = -\hbar\begin{bmatrix} \frac{\delta}{2} + \frac{|\Omega_0|^2}{4\Delta} & \frac{\Omega_R^*}{2} \\ \frac{\Omega_R}{2} & -\frac{\delta}{2} + \frac{|\Omega_1|^2}{4\Delta} \end{bmatrix} . \tag{2.32}$$

This leads to the solution for the population

$$P_1(t) = \frac{|\Omega_0|^2\,|\Omega_1|^2}{4\Delta^2\Omega_R^2}\sin^2\left(\Omega_R\, t/2\right) ; \quad P_0(t) = 1 - P_1(t)\,, \tag{2.33}$$

where the effective Raman Rabi frequency is given by

$$\Omega_R^2 = \frac{1}{(4\Delta)^2}\left(|\Omega_0|^2 + |\Omega_1|^2\right)^2 + \frac{\delta}{2\Delta}\left(|\Omega_0|^2 - |\Omega_1|^2\right) + \delta^2\,. \tag{2.34}$$

For the special two photon detuning

$$\delta = \delta_0 = \frac{|\Omega_1|^2 - |\Omega_0|^2}{4\Delta}\,, \tag{2.35}$$

the Raman Rabi frequency simplifies to

$$\tilde{\Omega}_R = \Omega_R\left(\delta = \delta_0\right) = \frac{\Omega_0\Omega_1^*}{2\Delta} = |\Omega_R|\, e^{i\phi}\,, \tag{2.36}$$

where the phase ϕ is given by the phase difference of the two light fields. We can rewrite equation (2.34) in terms of the resonant Raman Rabi frequency $\Omega_R\left(\delta_0\right)$

$$\Omega_R^2 = \frac{\left(\Omega_0^2\Omega_1^2\right)^2}{(2\Delta)^2} + \left(\frac{\Omega_1^2}{4\Delta} - \frac{\Omega_0^2}{4\Delta} + \delta^2\right) \tag{2.37}$$

$$= \tilde{\Omega}_R^2 + \left(\delta - \delta_0\right)^2\,, \tag{2.38}$$

and the population dynamics, equation (2.33) becomes

$$P_1(t) = \frac{\tilde{\Omega}_R^2}{\tilde{\Omega}_R^2 + \left(\delta - \delta_0\right)^2}\,\sin^2\left(\Omega_R\, t/2\right)\,, \tag{2.39}$$

which is identical to the solution for a 2-level system interacting with a single light field, if we identify $\delta - \delta_0$ as the *effective* detuning.

This result can be easily interpreted when we compare it to the light shift introduced in section 2.1.4, so that condition (2.35) can be understood as the selected detuning

$$\delta_0 = \Delta_{1,\,AC} - \Delta_{0,\,AC}\,, \tag{2.40}$$

exactly canceling the induced light shifts, and thereby being in resonance with the light shifted transition. The prefactor in equation (2.33) becomes $\frac{1}{2}$ for $\delta = \delta_0$, resulting in perfect population oscillation between the two states $|0\rangle$ and $|1\rangle$, just as in the two-level case discussed earlier.

2.1.6 Multiple light fields and auxiliary levels

For the study of *frequency comb driven Raman transitions*, we are interested in the interaction of *many* light fields with the atomic system. Additionally, the real systems we work with, Ca^+ and MgH^+ in future experiments, are not three level systems, but many auxiliary levels $|e\rangle$ have to be taken into account.

Light shift

For multiple light fields interacting with the system, the total light shift of a state $|i\rangle$ is just given as the sum over all the light shifts introduced by the different light fields n [A66]

$$\Delta_{\text{tot, AC}} = \sum_n \Delta_{i,n,\text{AC}} = \sum_n \frac{\Omega_{i,n}^2}{4\Delta_n}\,, \tag{2.41}$$

according to (2.29), where the index n labels the different light fields with Rabi frequency $\Omega_{i,n}$ on the transition $|i\rangle \to |e\rangle$.

In a real system, more than one auxiliary state $|e\rangle$ can contribute to the total light shift, so that we also have to sum over the different auxiliary levels $|e\,(k)\rangle$ the light fields couple to

$$\Delta_{\text{tot, AC}} = \sum_{n,k} \Delta_{i\to e(k),n,\text{AC}} = \sum_{n,k} \frac{\Omega_{i\to e(k),n}^2}{4\Delta_{n,k}}\,. \tag{2.42}$$

This formula is used in chapter 12.3 to calculate the light shift induced by the frequency comb light.

Raman Rabi frequency

The total Raman Rabi frequency when coupling to multiple light fields n, n' and multiple auxiliary levels $|e\,(k)\rangle$, needs to be summed coherently taking the phase of the light (2.36) into account

$$\Omega_{R,\text{tot}} = \sum_{n,n',k} \frac{\Omega_{n,i\to e(k)}\Omega^*_{n',i\to e(k)}}{2\Delta_{n,n',i\to e(k)}}\,. \tag{2.43}$$

The phase dependence will be important when we investigate the effect of dispersion in chapter 3.2, and also lead to destructive interference when driving Raman transitions between the D-finestructure levels in Ca^+ with the frequency comb, due to coupling to multiple Zeeman sub-states with different Clebsch-Gordon coefficients with opposite signs, as shown in chapter 12.3.

2.2 Modeling Rabi flopping

In the Raman Rabi flopping experiments with the frequency comb, described in chapter 12, I observe dynamics which cannot be explained by the "simple" model in equation (2.39). Therefore, I introduce the Optical Bloch equations to take decoherence into account, and also describe a simple model to describe the dynamics for a laser with a given linewidth, compared to the single frequency fields discussed above. In the experiments on the Ca^+ D-finestructure presented later, the population is first initialized in the "excited" state $|D_{5/2}\rangle$ and is transferred to the $|D_{3/2}\rangle$ state. Therefore, the plots shown in this section and in the data-plots in the rest of this thesis are inverted compared to the usual definition.

2.2.1 Bloch model

Complementary to the description earlier in this chapter, the dynamics of a two-level atom, interacting with a single frequency light can also be described by the optical Bloch equations (OBEs)[1] [A68]

$$\dot{u} = -\gamma_t u + \Delta v \tag{2.44}$$

$$\dot{v} = -\gamma_t v - \Delta u + \frac{\Omega}{2} w \tag{2.45}$$

$$\dot{w} = -\gamma w - 2\Omega v + \gamma\,. \tag{2.46}$$

In our experiments, we usually measure the population of the excited state given by

$$P_1 = \frac{1-w}{2}\,. \tag{2.47}$$

which only depends on w, while u and v determine the coherences. The Rabi frequency Ω and detuning Δ are defined as before, but the model also includes spontaneous decay and decoherence. The decay rate from the excited state is given by γ, but is not very relevant for the D-levels in Ca^+ with lifetimes of about one second. The decay of the coherences $\gamma_t = \gamma/2 + \gamma_c$ is usually determined by the spontaneous emission rate γ, but for our long lived states with $\gamma \approx 0$ on experimental timescales, the decoherence is dominated by additional decoherence $\gamma_c \geq 0$, for instance due to magnetic field fluctuations shifting the Zeeman levels.

The solution of the OBEs in terms of equation (2.47), are plotted in figure 2.4 for various detunings without decoherence, in figure 2.5 for different coherence times γ_c without detuning, and in figures 2.6 and 2.7 for non-zero detuning and decoherence simultaneously. These plots will be helpful when interpreting the experimental Raman Rabi flopping traces in chapter 12.

The OBEs can be solved in different parameter ranges analytically [A68], which I implemented to fit the experimental Raman Rabi flopping traces, discussed in chapter 12.2. The python implementation has been verified by plotting it against numerically integrated solutions of the OBEs.

The resulting spectrum, when driving the ion with a laser pulse with exposure time t and scanning the laser detuning Δ is plotted in figure 2.8 for various pulse times.

[1] The OBEs are similar to nuclear resonance as described by F. Bloch [A67], hence the name.

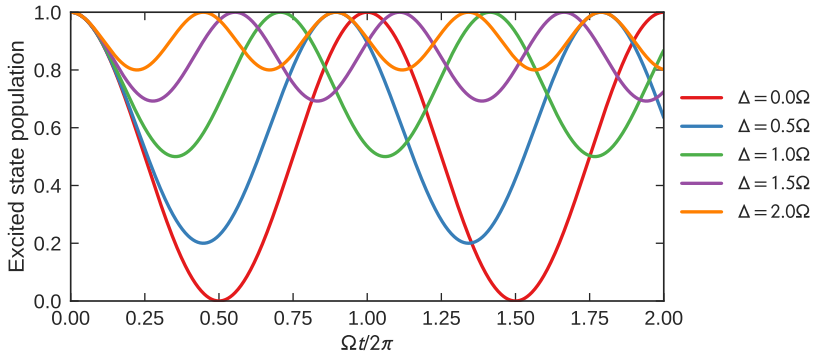

Figure 2.4: Solution to the OBEs (2.47) scaled by the Rabi frequency Ω for variable detuning Δ and no decoherence $\gamma_t = 0$.

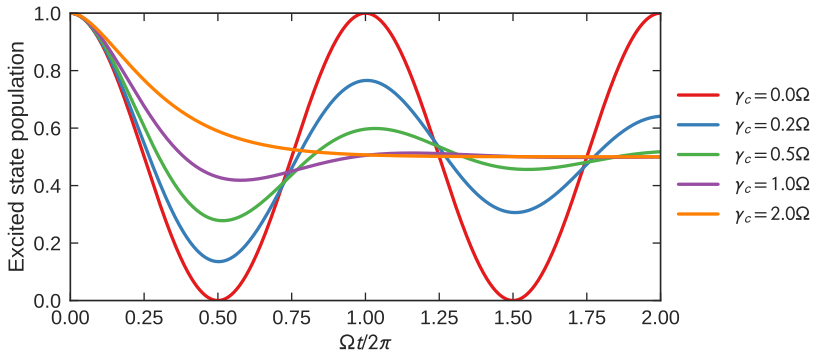

Figure 2.5: Solution to the OBEs (2.47) scaled by the Rabi frequency Ω for no detuning $\Delta = 0$ and variable decoherence $\gamma_t = \gamma_c$).

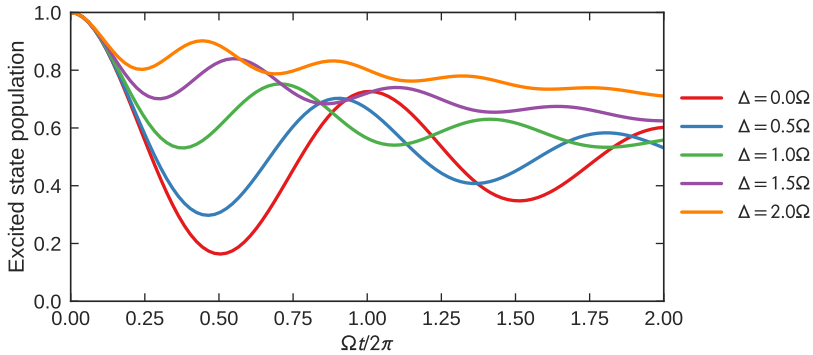

Figure 2.6: Solution to the OBEs (2.47) scaled by the Rabi frequency Ω for variable detuning Δ and fixed decoherence $\gamma_t = \gamma_c = \Omega/4$.

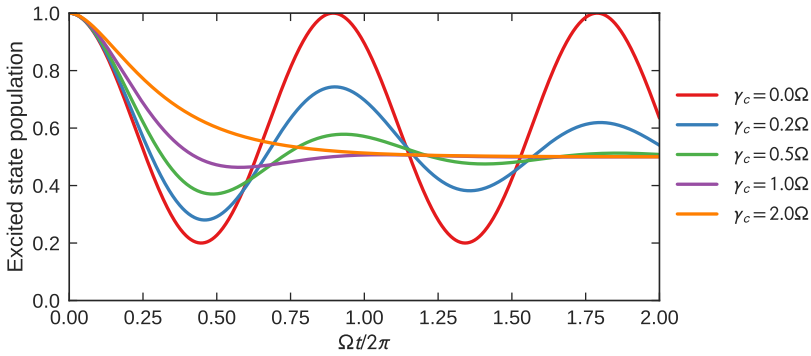

Figure 2.7: Solution to the OBEs (2.47) scaled by the Rabi frequency Ω for fixed detuning Δ and variable decoherence $\gamma_t = \gamma_c$.

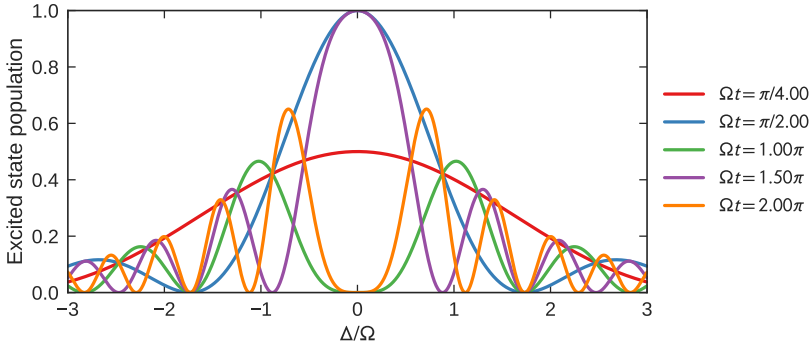

Figure 2.8: Spectroscopy signal for different pulse times according to the Bloch model (2.47), i.e. excited state population as function of laser detuning.

2.2.2 Simple model

The OBEs, as discussed in the previous chapter, have a simple analytical solution for negligible decoherence, i.e. $\gamma_t \ll \Omega, \Delta$, resulting in the "simple Rabi model" we derived in equation (2.39)

$$P_1 = \frac{\Omega^2}{\Omega^2 + \Delta^2} \left[1 - \cos\left(\sqrt{\Omega^2 + \Delta^2} \cdot t \right) \right] / 2 \,. \tag{2.48}$$

Phenomenologically, some authors include decoherence by introducing an exponential decay term

$$P_1 = \frac{\Omega^2}{\Omega^2 + \Delta^2} \left[1 - e^{-t/\tau} \cos\left(\sqrt{\Omega^2 + \Delta^2} \cdot t \right) \right] / 2 \tag{2.49}$$

with coherence time

$$\tau = \frac{2}{\gamma_c} \,. \tag{2.50}$$

However, this formula is only correct in the resonant case ($\Delta = 0$). For $|\Delta| > 0$, the steady state solution of the (correct) Bloch model description converges to 50 % excited state population, independent of the detuning, while the simplified model has a steady state solution with more than 50 % excited state population[2]. This behavior is plotted in figure 2.9. However, in the experiments with the Mira frequency comb, discussed in chapter 12.2.1, we observe Rabi flopping converging to more than 50 % excited state population, which led me to the model discussed in the next section.

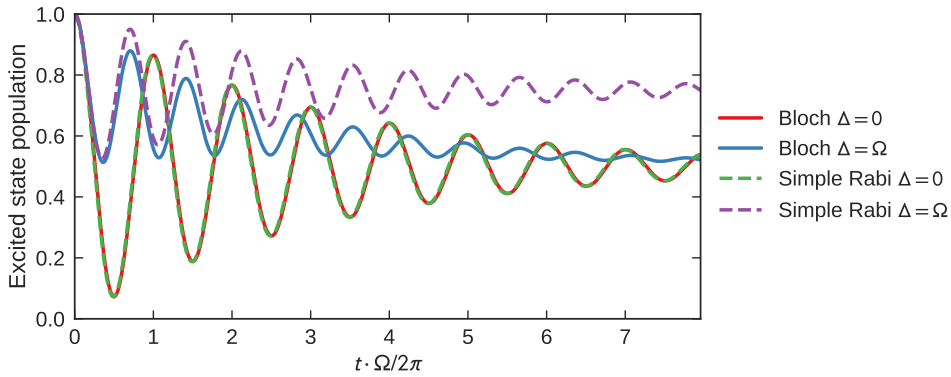

Figure 2.9: Comparison of the simple Rabi model with and without detuning, to the (correct) solution of the OBEs with dephasing $\gamma_c = \Omega/10$.

2.2.3 Linewidth model

The standard formula for Rabi flopping in a two level system, equation (2.48), describes the interaction with a single frequency light field, and does not take the linewidth of the laser into account. If this linewidth is not small compared to the Rabi frequency broadening the transition, we cannot ignore it any longer. In a single ion experiment, statistics needs to be gathered by repeating the measurement. For the special case of a laser detuning Δ slowly varying on the order of the time between two measurements, the statistical average for the whole experiment can be modeled as a sum Rabi flopping traces with different detunings, distributed according to the laser line-shape $g(\Delta)$, such that

$$P_1(t) = \int_{-\infty}^{+\infty} d\Delta\, g(\Delta)\, \frac{\Omega}{\Omega^2 + \Delta^2} \left[1 - \cos\left(\sqrt{\Omega^2 + \Delta^2}\, t\right)\right] /2\,. \tag{2.51}$$

In general, $g(\Delta)$ can be an arbitrary function describing the laser line-shape. For an infinitely narrow linewidth, represented by a Dirac-δ function, equation (2.51) becomes identical with the simple Rabi model (2.48). In chapter 12.2.1, I will use a Gaussian convolution core g to model Rabi flopping with the relatively unstable Mira frequency comb. The model (2.51) is plotted in figure 2.10 for different full width at half maximum (FWHM) Gaussian linewidths.

[2]Remember, that the initial state is the excited state in our definition.

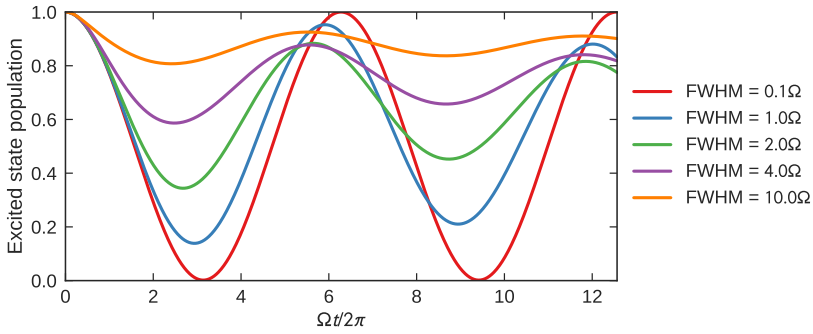

Figure 2.10: Rabi flopping according to the laser linewidth model (2.51) with a Gaussian laser linewidth different full width at half maximum (FWHM).

2.3 Laser cooling

Laser cooling was first proposed by Theodor Hänsch and David Wineland in 1975 [A11, A10] with the first experimental realization in 1978 [A69, A70]. About 20 years later, the Nobel Prize in Physics was awarded in 1997 jointly to Steven Chu, Claude Cohen-Tannoudji and William D. Phillips "for development of methods to cool and trap atoms with laser light" [A71].

2.3.1 Doppler cooling

Doppler cooling can be described in classical terms and is based on the idea that an ion will "see" an effective light field with a frequency ω_{eff} that depends on the velocity v of the ion compared to the wave vector of that field, similar to the classical Doppler effect for sound waves. The effective frequency is given by the relativistic Doppler effect

$$\frac{\omega_{\text{eff}}}{\omega_L} = \sqrt{\frac{1 \mp \beta}{1 \pm \beta}}; \quad \beta = \frac{v}{c} \tag{2.52}$$

where ω_L is the frequency of the light field in the laboratory frame. Typically, atomic transitions used for Doppler cooling have a broad linewidth corresponding to a fast spontaneous emission rate compared to the timescale of the motion of the ion in the trap $\left(\frac{2\pi}{\omega_z} \approx 1\,\mu\text{s}\right)$. The Doppler cooling $|S_{1/2}\rangle \rightarrow |P_{1/2}\rangle$ transition in Ca^+ has a linewidth of 21.6 MHz, leading to fast cooling rates and allows to treat the atom in the trap as in the free space case.

The ion will scatter photons with a rate Γ_{scatter}, and each photon will transfer the momentum $\hbar k$, so that the average force can be written as

$$F = \hbar k \Gamma_{\text{scatter}}\,, \tag{2.53}$$

The scattering rate of a two-level atom in steady state is given by the spontaneous decay rate Γ multiplied by the population in the excited state P_1 which can be expressed in terms of the saturation parameter s

$$\Gamma_{\text{scatter}} = \Gamma P_1 = \Gamma \frac{1}{2} \frac{s}{1+s}\,, \tag{2.54}$$

where the saturation parameter s is defined as

$$s = \frac{2\,|\Omega|^2}{\left(\frac{\Gamma}{2}\right)^2 + \Delta^2} \tag{2.55}$$

with Ω and Δ being the Rabi frequency and the detuning in the laboratory frame . Expanding the effective frequency defined by equation (2.52) to first order around $v = 0$ we find the effective detuning

$$\Delta_{\text{eff}} = \omega_{\text{eff}} - \omega_0 \approx \Delta \mp kv\,. \tag{2.56}$$

Combining the equations above, the average force (2.53) takes the form of a constant force plus a friction force proportional to the velocity

$$F = F_0 + \frac{\mu_{\text{fr}}}{2} v\,. \tag{2.57}$$

The coefficient of friction μ_{fr} is a function of the detuning so that $\mu_{\text{fr}} < 0$ for a red-detuned laser ($\Delta < 0$), effectively slowing the ion down, resembling Doppler cooling. The constant force F_0 as part of the radiation pressure will push the ion slightly away from the center of the trap. Each time a photon is absorbed slowing down the ion, another photon will be spontaneously emitted in a random direction after an average time $1/\Gamma$. The momentum kicks $\hbar k$ associated with each photon emission lead to a random walk of the ion in momentum space similar to Brownian motion. This random process sets a lower energy or temperature limit T_D, reachable with Doppler cooling to

$$k_B T_D = \frac{1}{2}\hbar\Gamma \tag{2.58}$$

for a detuning $\Delta = -\Gamma/2$. Typical Doppler temperatures are for instance $T_D = 0.5\,\text{mK}$ for Ca^+ cooled on the $|S_{1/2}\rangle \rightarrow |P_{1/2}\rangle$ transition. The Doppler limit has been experimentally verified in one [A72] and three dimensions [A73] for neutral two-level atoms.

2.3.2 Resolved sideband cooling

Resolved sideband cooling exploits the quantized motion of the ion in the trap, as discussed in chapter 1. The idea is to apply a laser red-detuned to the red sideband ($\Delta = -\omega_z$) of the trapped ion. The natural linewidth of the addressed transition needs to be small compared to the trap frequency ($\Gamma \ll \omega_z$) in order to address an individual sideband. For the same reason, the laser linewidth and Rabi frequency also need to be small ($\delta_\omega, \Omega \ll \omega_z$).

A sketch of the process is shown in figure 2.11. The red sideband transition $|g, n\rangle \rightarrow |e, n-1\rangle$ removes one motional quantum and brings the ion to the excited state, as discussed in chapter 2.1.3. Spontaneous emission thereafter will predominantly occur on the carrier transition $|e, n-1\rangle \rightarrow |g, n-1\rangle$ without changing the motional state so that in total one motional quantum of energy is removed in each cycle. After a certain number of cycles the ion reaches the motional ground state and cannot couple to the light field any longer since the red sideband Rabi frequency $\Omega_{n,n-1} = \eta\sqrt{n}\,\Omega$ vanishes for $n = 0$.

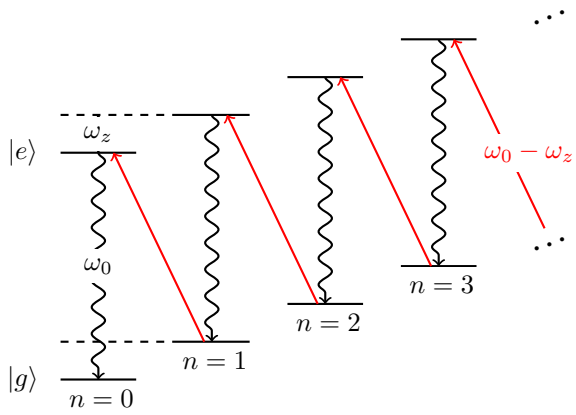

Figure 2.11: Principle of resolved sideband cooling. A narrow linewidth laser transfers population on the red sideband transition $|g, n\rangle \rightarrow |e, n-1\rangle$. Spontaneous decay happens predominantly on the carrier transition so that one motional quantum is removed in each cycle.

For a two-level atom, the requirement of narrow natural linewidth equivalent to a long lifetime of the excited state limits the cooling rate. This can be circumvented using a three level system and a pulsed sideband cooling scheme, as implemented in the experiments with Ca^+.

The Ca^+ ion is excited with a shuttered laser at 729 nm on the red sideband $|S_{1/2}\rangle \rightarrow |D_{5/2}\rangle$ quadrupole transition to the long lived D-state. A second laser at 854 nm then couples the $|D_{5/2}\rangle$ state with the $|P_{3/2}\rangle$ state from which the ion will spontaneously decay rapidly ($\tau = 7$ ns) back to the ground state. This sequence is repeated many times, each time removing one quantum of energy.

Sideband cooling to the motional ground state was experimentally first reported in 1989 using a quadrupole transition in $^{198}Hg^+$ [A74] and later using resolved-sideband stimulated Raman cooling in $^9Be^+$ [A75]. In my experiments, sideband cooling of Ca^+ to 99(1) % ground state population is achieved routinely [T3, T4, A76].

2.4 Quantum logic spectroscopy

For atomic ions such as Ca^+ it is easy to determine the internal state by fluorescence detection methods. When the ion is "shelved" to the long lived D-states, the Doppler cooling light cannot couple on the $|S_{1/2}\rangle \rightarrow |P_{1/2}\rangle$ transition anymore, so that no photons are scattered and the ion appears "dark" on a CCD camera collecting the fluorescence, as described in chapter 9.1.4.

For spectroscopy of other species lacking transitions for easy fluorescence readout, *quantum logic spectroscopy* [A34] is a more sophisticated method to determine the internal state of this "spectroscopy ion" by exploiting the motional coupling with a co-trapped "logic ion". The idea is to transfer the internal state information from the spectroscopy ion, which will be the molecular ion MgH^+ in future experiments, onto the Ca^+ logic ion, so that fluorescence detection on Ca^+ reveals the internal state of MgH^+ .

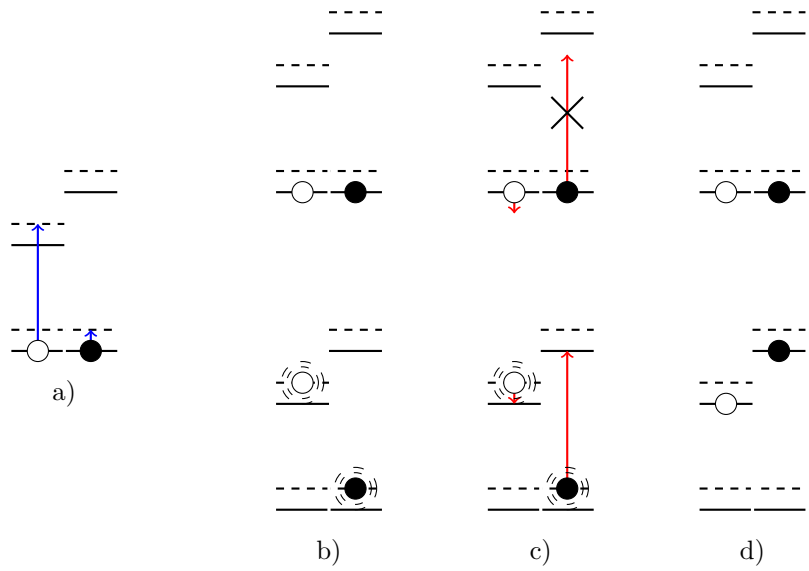

Figure 2.12: Scheme of quantum logic spectroscopy. The internal state of a spectroscopy ion (white) is mapped onto a co-trapped logic ion (black) via a series of sideband transitions on the two ions, exploiting the common motional modes of the two ions in the trap as explained in the main text. The excited and ground states of the two ions are indicated by the solid lines, with the first motional states above as dashed lines.

This information transfer is sketched in figure 2.12. The common motional mode of the two ion crystal can be excited by driving sideband transitions on either of the two ions. The scheme is initialized by cooling the motion to the absolute ground state $|n = 0\rangle$ via sideband cooling on the logic ion, and then applying a spectroscopy pulse on the spectroscopy ion (figure 2.12(a)). From here, two scenarios can be distinguished. In figure 2.12(b, top), the spectroscopy pulse did not excite the spectroscopy ion, and the two ions remain in their motional ground state $|n = 0\rangle$. The other case of exciting the spectroscopy ion on the blue sideband is shown in figure 2.12(b, bottom), exciting the common motion to $|n = 1\rangle$. A red sideband π pulse on the logic ion (figure 2.12c) only acts on the system if it was excited before, since the coupling on the red sideband vanishes if the system is still in the motional ground state $|0\rangle$. This maps the internal state of the spectroscopy ion (figure 2.12b) on the internal state of the logic ion (figure 2.12d). A simple fluorescence readout on the logic ion now reveals the state of the spectroscopy ion.

Quantum logic spectroscopy was proposed and implemented in 2005 by Schmidt et al. using $^{9}Be^{+}$ as the logic ion and $^{27}Al^{+}$ as the spectroscopy ion [A34]. In the Ion Trap Group, we are working towards quantum logic spectroscopy on MgH^{+} driving sideband transitions with the frequency comb technique presented in this thesis, as detailed in the outlook in chapter 15.

Part II

The Optical Frequency Comb and its Characterization

3 Ultrashort Pulses

To understand the light generated by a pulsed laser I will first introduce the relation between the electric field in the time-domain and in the frequency-domain, connected via the Fourier transform. The description and characterization of the light will be much easier in one or the other representation, depending on the situation. The effect on the light of propagating through a dispersive material will be straight forward in the frequency domain, leading to a broadening of the pulse in the time domain, and a time dependent instantaneous frequency in the frequency domain. A continuous train of short pulses with equidistant spacing in time leads to a broad spectrum, consisting of well defined frequency components in the frequency domain, resembling the frequency comb. The interaction of an ion with such a pulse train can be understood as an interaction with a large number of phase locked cw lasers. The frequency of each comb tooth is given by the two parameters describing the frequency comb, the repetition rate of the laser and the so-called carrier envelope offset frequency. A broader discussion can be found in the book by Jun Ye [B7].

3.1 Time and frequency domain

The time dependent electric field amplitude can be written as a complex quantity

$$\vec{E}_{\text{real}}(t,\vec{r}) = E(t) + c.c\,, \tag{3.1}$$

with the complex electric field $E(t)$ and it's complex conjugate. The corresponding spectral field amplitude $\tilde{E}(\omega)$ is related to $E(t)$ via the Fourier transform

$$\tilde{E}(\omega) = \int_{-\infty}^{+\infty} E(t)e^{-i\omega t}\,dt \tag{3.2}$$

$$E(t) = \frac{1}{2\pi}\int_{-\infty}^{+\infty} \tilde{E}(\omega)e^{i\omega t}\,d\omega\,. \tag{3.3}$$

The light of a pulsed laser typically has a spectrum centered around a given carrier frequency ω_c, and will only have a significant amplitude in an interval $\Delta\omega \ll \omega_c$ around the carrier frequency. In this case, it is convenient to write the complex electric field as the product of a carrier wave and a complex envelope function

$$E(t) = \mathcal{E}(t)\, e^{i\omega_c t}\,. \tag{3.4}$$

The complex envelope function itself can be written as

$$\mathcal{E}(t) = \left|\mathcal{E}(t)\right|\, e^{i(\phi_{\mathrm{CEO}}+\phi(t))}\,, \tag{3.5}$$

where the time independent phase ϕ_{CEO} is the carrier envelope offset (CEO) phase (see figure 3.3). Note that $\phi(t)$ depends on the mathematical choice of the carrier frequency ω_c, which should be chosen to minimize the time dependence of $\phi(t)$. The instantaneous frequency $\omega(t)$ of the field is defined as the time derivative of the total phase of $E(t)$

$$\omega(t) = \omega_c + \frac{d}{dt}\phi(t)\,. \tag{3.6}$$

If the instantaneous frequency is actually time dependent ($\frac{d}{dt}\phi(t) \neq 0$), the pulse is said to have a frequency "chirp". In the simple case of a quadratic time dependence of $\phi(t)$, the instantaneous frequency changes linearly in time. A decreasing frequency ($\frac{d^2}{dt^2}\phi(t) < 0$) is called down-chirp while an increasing frequency is called up-chirp.

Let us now consider a simple but realistic example of a pulse, namely an electric field according to (3.4) with a Gaussian envelope function

$$\mathcal{E}(t) = E_0\, \frac{1}{\sqrt{2\pi}\sigma}\, e^{-\frac{t^2}{2\tau_G^2}}\,. \tag{3.7}$$

Equation (3.2) gives the spectral field amplitude

$$\tilde{E}(\omega) = E_0 e^{-\frac{\omega^2}{2\delta\omega_G^2}}\,, \tag{3.8}$$

with $\delta\omega_G = 1/\tau_G$ and we find the time-bandwidth product

$$\delta\omega_G \tau_G = 1\,. \tag{3.9}$$

In general, for an arbitrary envelope function, it can be shown that the product of the FWHM in the time-domain Δt, and frequency-domain $\Delta\omega$ obeys an inequality

$$\Delta t \Delta\omega \leq C\,, \tag{3.10}$$

where the constant C depends on the specific envelope function, and equality in (3.10) holds if and only if the phase $\phi(t)$ is time independent. In this case, the pulse is called bandwidth-limited or Fourier-limited. For a Gaussian envelope with the spectral FWHM in Hertz Δf and temporal pulse FWHM Δt in seconds, the constant C is

$$\Delta f\, \Delta t = \frac{1}{2\pi}\, 2\sqrt{2\log 2}\, \delta\omega_G \cdot 2\sqrt{2\log 2}\, \tau_G = 0.883\,. \tag{3.11}$$

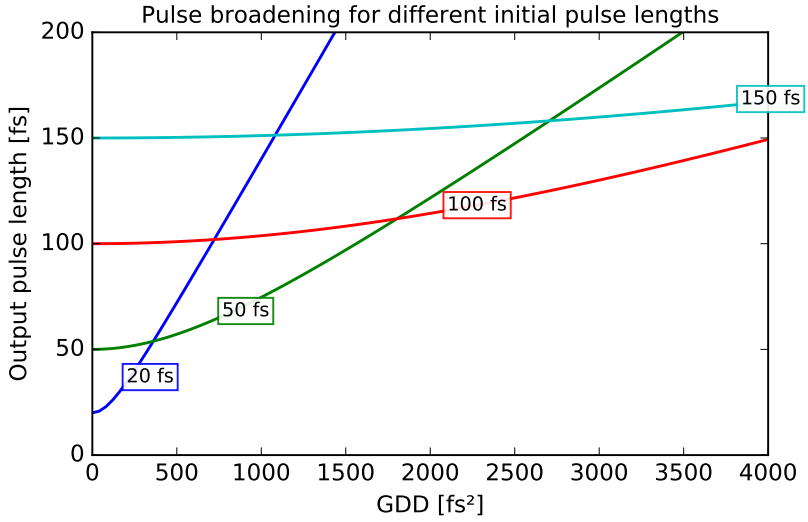

Figure 3.1: Pulse broadening as function of GDD. Shorter bandwidth-limited pulses are more heavily affected due to the broader spectrum. A GDD of 1000 fs^2 corresponds to 28 mm of BK7 glass or 6.4 mm of SF10 glass at 800 nm.

3.2 Pulse propagation in dispersive material

We investigate the effect on a pulse with center frequency ω_c traveling through a dispersive medium of length L. The spectral phase of the electric field changes by

$$\phi(\omega) = k(\omega)L\,, \tag{3.12}$$

where the wave number k is in general frequency dependent. This is equivalent to a frequency-dependent refractive index $n(\omega)$ or phase velocity $v_p(\omega)$

$$v_p(\omega) = \frac{\omega}{k(\omega)} = \frac{c}{n(\omega)}\,. \tag{3.13}$$

It is common in this context to expand the phase in a Taylor series [A77]

$$\phi(\omega) = \phi\left(\omega_c\right) + \frac{\partial\phi}{\partial\omega}\Big|_{\omega=\omega_c} \cdot (\omega-\omega_c) + \frac{1}{2}\frac{\partial^2\phi}{\partial\omega^2}\Big|_{\omega=\omega_c} \cdot (\omega-\omega_c)^2 + \mathcal{O}(\omega^3)\,. \tag{3.14}$$

The first term is a constant phase equal for all frequencies. The second linear term defines the *group velocity* v_g or the *group delay* τ_g at the frequency ω_c

$$\tau_g = \frac{\partial\phi}{\partial\omega} = \frac{L}{v_g}; \quad v_g = \left(\tfrac{\partial k}{\partial\omega}\right)^{-1}. \tag{3.15}$$

The group velocity determines the time delay of the pulse through the medium but does not influence the shape of the pulse. The third and most important term is the *group delay dispersion* (GDD)

$$D_2 = \frac{\partial\tau_g}{\partial\omega} = \frac{\partial^2\phi}{\partial\omega^2} = \frac{\partial}{\partial\omega}\frac{1}{v_g}\,, \tag{3.16}$$

and is usually given in units of fs^2. Higher order terms, including the third order term simply called *third order dispersion* (TOD), can be neglected for the relatively long fs pulses and optical materials considered in this thesis.

Thus, a pulse which has traveled through a medium with a refractive index with vanishing third and higher order dispersion accumulated the spectral phase

$$\phi = \phi_0 + \tau_g \cdot (\omega - \omega_c) + \frac{D_2}{2} \cdot (\omega - \omega_c)^2 \ . \tag{3.17}$$

The temporal phase ϕ_t is calculated by Fourier transform of $e^{-i\phi}$ and we find

$$\phi_t = -\frac{(t-\tau_g)^2}{2D_2} - \omega_c t + \phi_0 \tag{3.18}$$

which represents a linearly changing instantaneous frequency over time

$$\omega(t) = \frac{\partial \phi_t}{\partial t} = -\omega_c - \frac{t-\tau_g}{D_2}. \tag{3.19}$$

For D_2 less (larger) than zero, the medium is said to have positive (negative) dispersion. Positive (negative) dispersion leads to an increasing (decreasing) instantaneous frequency of the pulse over time, also called positive (negative) or up-chirp (down-chirp).

In the time domain, the length of a bandwidth-limited pulse while traveling through the dispersive material increases from τ_0 to

$$\tau = \tau_0 \sqrt{1 + \left(4ln(2)\frac{D_2}{2}\right)^2} \tag{3.20}$$

and shorter bandwidth-limited pulses are more heavily affected, as illustrated in figure 3.1 and 3.2.

3.3 The optical frequency comb

After investigating a single pulse in the time- and frequency-domain in the previous sections, we characterize the spectrum of a laser emitting a continuous pulse train in the following. We start with an infinite train of δ-functions in the time domain, separated by a time T_r,

$$E(t) = \sum_{n=-\infty}^{+\infty} \delta(t - nT_\mathrm{r}) \tag{3.21}$$

where $f_\mathrm{r} = 1/T_\mathrm{r}$ is the repetition rate of the laser. The right hand side of equation (3.21) is mathematically termed *Dirac comb distribution* and can also be written as

$$\sum_{n=-\infty}^{+\infty} \delta(t - nT_\mathrm{r}) \equiv \frac{1}{T_\mathrm{r}} \sum_{n=-\infty}^{+\infty} e^{i2\pi \frac{2\pi n}{T_\mathrm{r}} t} \, . \tag{3.22}$$

This can be interpreted as a sum of an infinite number of plane waves, all interfering to generate the pulse train. Consequently, the Fourier transform gives

$$\tilde{E}(\omega) = \frac{1}{T_\mathrm{r}} \sum_{n=-\infty}^{+\infty} \delta(\omega - n/T_\mathrm{r}) \, , \tag{3.23}$$

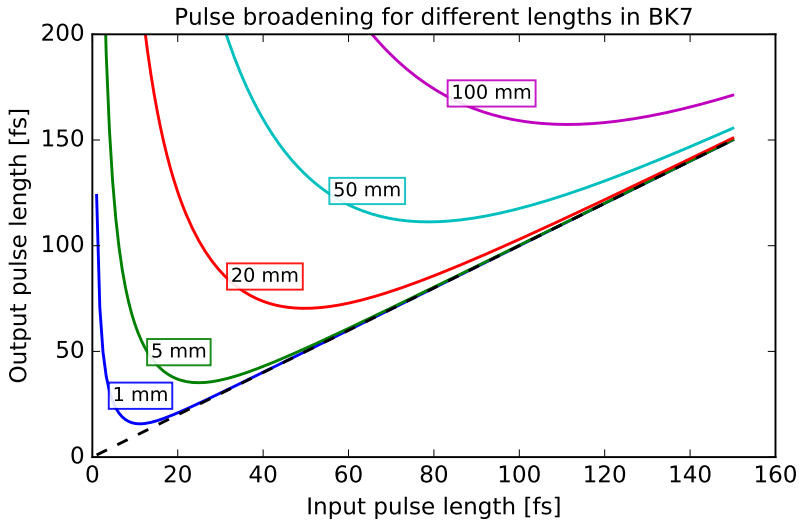

Figure 3.2: Pulse broadening as function of input pulse length for different path length in dispersive material

which is a Dirac comb distribution itself with frequency spacing $1/T_\mathrm{r} = f_\mathrm{r}$. Using basic Fourier relations we can construct the spectrum of a more realistic electric field emitted by a pulsed laser. First of all, the pulses are not δ-distributions but instead composed of a carrier term $e^{i\omega_c t}$ and a pulse envelope function $\mathcal{E}(t)$ (see eq. (3.4)), so that we can write

$$E(t) = \sum_{n=-\infty}^{+\infty} \delta(t - nT_\mathrm{r}) \ast \mathcal{E}(t)\, e^{i\omega_c t}\,, \tag{3.24}$$

where $\ast$ is the convolution operator. In the Fourier domain, convolution becomes simple multiplication, and modulation ($e^{i\omega_c t}$) becomes a displacement and vice versa. Thus, the spectral amplitude is

$$\tilde{E}(\omega) = \frac{1}{T_\mathrm{r}}\, \mathcal{E}(\omega - \omega_c) \sum_{n=-\infty}^{+\infty} \delta(\omega - n2\pi f_\mathrm{r})\,. \tag{3.25}$$

To take into account that the pulse train will only exist for a limited amount of time, experimentally e.g. given by a shutter with opening time T_s , we multiply in the time domain by

$$\Pi_{T\mathrm{s}}(t) = \begin{cases} 1 & \text{for } |t| \le T_\mathrm{s}/2 \\ 0 & \text{otherwise}\,, \end{cases} \tag{3.26}$$

or convolute in the frequency domain the Fourier transform of the rectangular function $\Pi_{T\mathrm{s}}$

$$T_\mathrm{s}\,\mathrm{sinc}(\omega T_\mathrm{s}/2)\,. \tag{3.27}$$

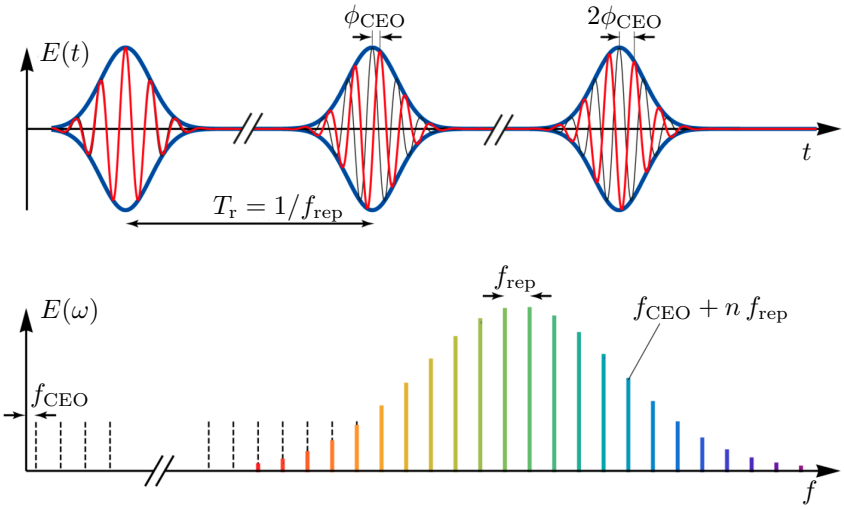

Figure 3.3: Frequency comb in the time- and frequency domain. The spacing of the comb teeth is given by the repetition rate f_{rep} of the pulsed laser generating the comb. The laser carrier frequency defines the center of the envelope with a width inversely proportional to the pulse length. The whole spectrum is offset by the carrier envelope offset frequency f_{CEO} originating from the carrier envelope offset phase ϕ_{CEO}. Figure adapted from ref. [A78]

In the description above, we neglected the carrier envelope offset (CEO) phase from equation (3.5), which leads to an offset ω_{CEO} in the frequency domain.

In total, we can write equation (3.25) as,

$$\tilde{E}(\omega) = \frac{T_{\mathrm{s}}}{T_{\mathrm{r}}}\, \mathcal{E}(\omega - \omega_c) \sum_{n=-\infty}^{+\infty} \mathrm{sinc}(\omega - n\, 2\pi f_{\mathrm{r}} - \omega_{\mathrm{CEO}})\,. \tag{3.28}$$

This result is sketched in figure 3.3 for a Gaussian envelope function and can be interpreted as follows:

1. The carrier frequency determines the center of the spectrum.
2. The envelope of the spectrum is given by the Fourier transform of the pulse envelope. The bandwidth is determined by the time-bandwidth product (3.10).
3. The spectrum is not continuous but built up by many *comb teeth*, with significant intensity only at frequencies spaced by the repetition rate of the laser.
4. The spectrum is offset from zero by the CEO frequency.
5. The actual shape of each comb tooth is given by the Fourier transform of the total envelope (shutter) in time.

In simpler terms, the frequency components of the comb have frequencies

$$f = f_{\mathrm{CEO}} + n\, f_{\mathrm{rep}}\,, \tag{3.29}$$

where n is an integer identifying a specific tooth. Typically, the repetition rate of mode-locked lasers is on the order of 100 MHz, and the spectral width on the order of THz for fs pulses, such that the spectrum consists of tens of thousands of comb teeth.

4

Frequency Comb Laser Systems

For the Raman experiments presented in this thesis, I used two separate, completely independent frequency comb systems. The first laser is a commercial Menlo frequency comb system FC1500, described in section 4.1. It is a "real" frequency comb, with locked repetition rate *and* carrier envelope offset frequency, making it a versatile, high precision, frequency measurement tool. For the Raman experiments, the Menlo system provides higher repetition rate stability over the second frequency comb system, and is used to obtain the high accuracy optical isotope shift measurements in Ca^+ , discussed in chapter 14. Since we use the frequency doubled and amplified output of the fiber based Menlo system, its spectrum is, however, strongly affected by nonlinear effects and group velocity dispersion (GVD).

On the contrary, the second frequency comb is a passively mode-locked Coherent Mira Ti:sapph laser, described in section 4.2. Even though we do not lock the carrier envelope offset frequency of this laser, it is perfectly suited for the Raman experiments, where the atomic dynamics are completely determined by the repetition rate, as well as the spectral intensity and shape of the light. Using the Mira laser, having a broader spectral bandwidth and little intrinsic dispersion compared to the Menlo system, I will experimentally confirm the theoretically predicted effects of GVD on the dynamics of *frequency comb driven Raman transitions*.

In the end of this chapter, I describe the prism compressor in section 4.3, used to compensate the GVD in the beam-path of the Mira laser, and comapre the spectra of the two frequency combs in section 4.4.

4.1 Menlo comb

The heart of our Menlo frequency comb system (M-Comb), which we installed in 2015, is a passively mode-locked Er-doped fiber ring laser with a carrier wave-

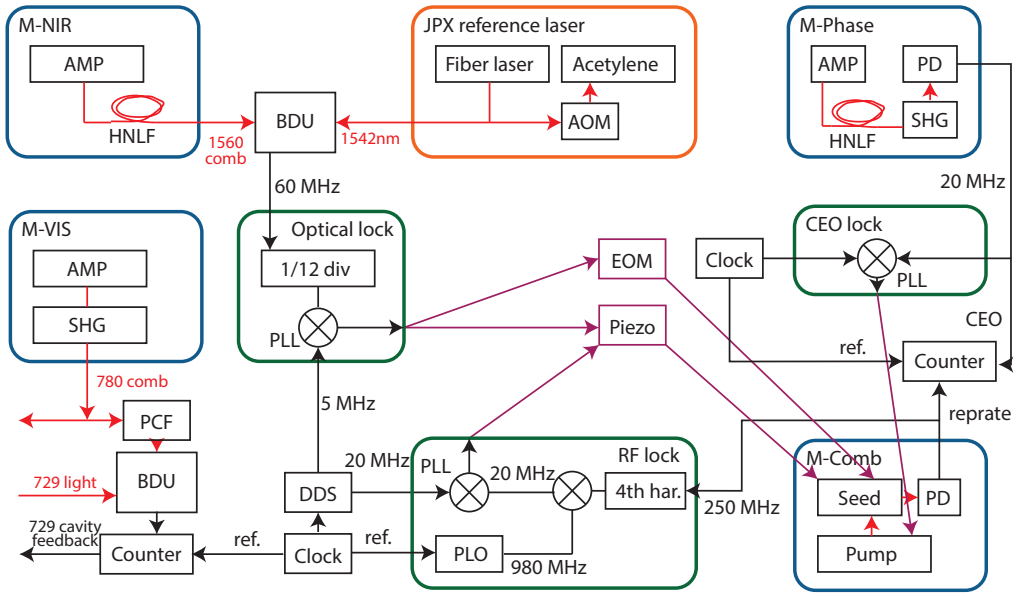

Figure 4.1: Schematic drawing of the Menlo frequency comb system. Light is colored in red, electronic signals in black, and feedback in purple. The laser modules M-NIR, M-VIS, and M-Phase are connected to the seed laser module M-Comb via direct fiber connections. Counter and clock are shown in two places for clarity, but are in fact only one physical device each. The optical and RF locking schemes for the repetition rate, and the carrier envelope offset frequency stabilization, are discussed in the text.

length of 1560 nm. A schematic drawing of the complete setup is shown in figure 4.1. The M-comb seed laser incorporates a piezo and motorized translation stage, as well as an electro optical modulator (EOM), to control the repetition rate, while the carrier envelope offset frequency (CEO) is stabilized via current modulation of the pump laser. The light of the seed laser (M-Comb) is split into three separate fibers, connecting the other modules.

One goes to M-Phase, an Erbium doped fiber amplifier (EDFA) with a highly non-linear fiber (HNLF). This results in an output with an octave spanning spectrum from 1050 nm to 2100 nm, used in an f-2f interferometer to measure the CEO frequency.

A second output of the seed connects a similar EDFA (M-NIR), with a free-space output of about 200 mW total optical power. This light can be used in a beat detection unit (BDU) to lock the repetition rate to an ultra stable optical reference (JPX), as explained in section 4.1.4.

The third output is connected to yet another EDFA (M-VIS) followed by a second harmonic generation (SHG) stage, generating the light used in the Raman experiments, and for beatnote measurements with CW lasers, as described in the following section.

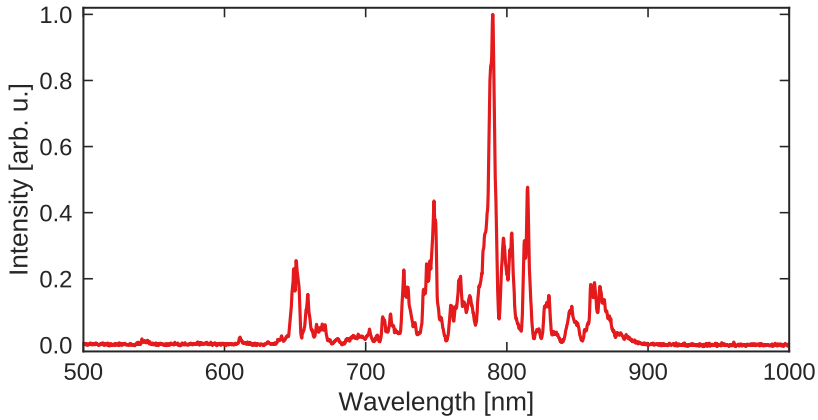

Figure 4.2: Spectrum of the red PCF. Note the third harmonic around 540 nm, and the low power around 729 nm.

4.1.1 External Spectral broadening

Instead of sending the light from M-VIS with a rather narrow spectrum, centered around 790 nm (see figure 4.11a), to the ion trap, we can alternatively send it through one of two available photonic crystal fibers (PCF). Nonlinear processes such as four-wave mixing generate new frequencies [R17, R18], obeying the frequency comb condition

$$f = f_{ceo} + n\, f_{rep}\,. \tag{4.1}$$

The "green" PCF generates a spectrum roughly between 520 nm and 950 nm, while the "red" PCF gives a spectrum between 650 nm and 880 nm, as shown in figure 4.2. The broad spectra after the PCF together with the output from M-NIR allow us to measure beatnotes with any CW laser between 520 nm and 2.1 μm. A permanent beatnote setup between the red PCF and the 729 nm laser compensates drifts of the cavity this laser is locked to, as described in chapter 9.2.6.

4.1.2 Carrier envelope offset frequency lock

Compared to the second frequency comb system we are using, the Mira laser described in section 4.2, we have control over the CEO in the Menlo system. The CEO is measured in a f-2f interferometer by detecting a beatnote between the low wavelength end of the spectrum with the frequency doubled spectrum [A79, R11]. Stabilizing this beatnote by feeding back to the pump current of the seed laser effectively locks the CEO frequency, in our system to -20 MHz[1]. The bandwidth of this lock is reflected in the CEO jitter of about 100 kHz, limiting the linewidth of each *individual* comb tooth when the repetition rate is directly stabilized with the RF lock, as explained in the following section. The stability

[1] The frequency doubled output (M-VIS) has twice the CEO frequency of -40 MHz. Indeed, the CEO frequency is negative in our setup.

of the CEO frequency is shown in a later chapter in terms of the Allan deviation in figure 6.3.

4.1.3 Repetition rate RF lock

The seed laser's repetition rate of nominally 250 MHz is internally detected by a fast photodiode (PD). This signal is monitored on a frequency counter, and can be directly used to phase-lock the repetition rate to a radio frequency (RF) reference signal, generated by our local frequency standard, described in section 5.

In detail, the 4th harmonic of the repetition rate at nominally 1 GHz is mixed with a 980 MHz signal, generated by a phase-locked oscillator (PLO). The difference signal of nominally 20 MHz is then phase-locked to a reference signal derived from a DDS. Feedback on the repetition rate is facilitated by adjusting the seed laser's cavity length with a piezo actuator, and a motorized translation stage for larger, slow adjustments up to ± 1.2 MHz. All the electronics, except for the DDS, are contained in a single 19 inch, rack mounted, module (Menlo SYNCRO).

When the repetition rate lock to the DDS is engaged, the repetition rate can be controlled and scanned simply by controlling the DDS output frequency. Using only the piezo, we can tune the repetition rate by a maximum of about 2.5 kHz within about 1 s. Adjusting the repetition rate using the motor takes significantly more time. In contrast to the optical lock, described in the following section, the EOM is not used for the RF lock, due to the limited short term stability of the reference clock.

The repetition rate and the CEO are locked independently in the RF locking scheme, so that the linewidth of one individual comb tooth is given by the sum of the CEO jitter, plus the repetition rate noise multiplied with the comb tooth number, according to equation (4.1). The linewidth was measured to be 270 kHz on a 10 ms timescale [A80]. As explained in the next section, the optical lock results in narrower comb teeth around the optical locking laser frequency, beneficial for beatnote measurements of CW lasers, but at the expense of a more noisy repetition rate.

However, only the repetition rate stability determines the effective laser linewidth for the Raman experiments presented in chapter 12, where the CEO is not even locked. A thorough investigation of the RF locked repetition rate stability is presented in section 6.

4.1.4 Optical lock to the JPX reference laser

Instead of locking the repetition rate directly to an RF reference, as described in the previous section, we can lock one specific comb tooth to an optical reference laser, by stabilizing the beatnote of this laser with the comb. We use the light from M-NIR to beat a central comb tooth close to 1542 nm with the JPX, an acetylene-stabilized[2] fiber laser developed by NKT photonics, and the

[2]The Acetylene absorption line is 194 369 569 384 kHz with a relative standard uncertainty of 2.6×10^{-11} [O4]. The JPX laser output is shifted from this frequency by -40 MHz, due to the AOM, to 194 369 529 384 kHz. The AOM is not externally referenced to a stable frequency reference, and its drivers accuracy is specified to 1 ppm or 40 Hz. This might be relevant for future, high accuracy measurements.

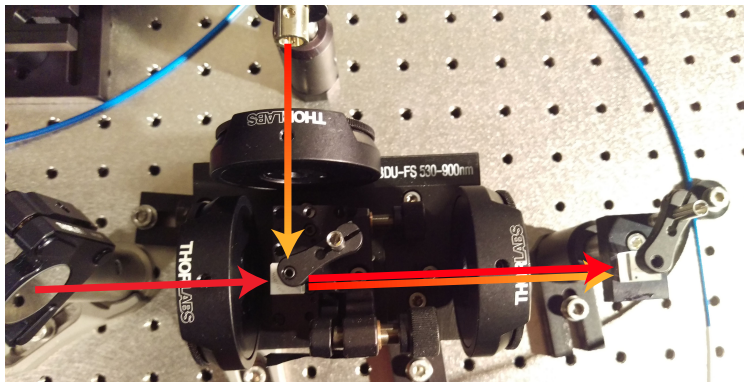

Figure 4.3: Photo of a beat detection unit (BDU). Two beams, comb and CW laser, are sent through a $\lambda/2$ waveplate each, allowing power adjustments. One beam comes from the top and one from the left, combined in a polarizing beam splitter cube (PBS). Another $\lambda/2$ waveplate rotates both combined beams by 45°, so that their vertically polarized components pass mode-matched through a second PBS. The beam is sent on a reflection grating, separating the broad comb spectrum from the comb teeth close to the CW laser (not shown). Finally, the beatnote frequency of the CW laser and the closest comb tooth is measured on a fast photo-diode.

Danish Fundamental Metrology institute (DFM) [A81]. Its sub-kHz short-term linewidth and relative frequency uncertainty of 2×10^{-12} was partly characterized using our Menlo frequency comb in 2016 [A80].

A photo of a beat detection unit (BDU) is shown in figure 4.3, and its design is explained in the figure caption. For the optical lock (compare with the schematic drawing in figure 4.1), the beat signal with the JPX of nominally 60 MHz is band-pass filtered and amplified, before it is divided by a factor of 12 to nominally 5 MHz. This signal is compared to a 5 MHz signal, generated by a DDS, in a phase-locked loop. Feedback is given to the cavity length via the piezo actuator. Additionally, an EOM allows feedback at an increased bandwidth compared to the RF lock.

The result of this locking scheme are extremely stable comb teeth around the reference laser frequency, with a measured linewidth of 900 Hz for a sampling time of 100 ms [A80]. This stability is transferred to the doubled frequency around 790 nm, which can be used to stabilize the 729 nm laser, as described in chapter 9.2.6. However, the CEO is still locked as described above with comparably low bandwidth. This means that noise in the CEO will be converted to noise on the repetition rate in order to keep the one comb tooth, which we lock to, stable (compare equation 4.1). The stability of the repetition rate for the two locking schemes is discussed in section 6, and for all frequency comb Raman experiments, the repetition rate was locked with the RF lock, and free running CEO.

Table 4.1: Parameters of the Mira laser. Listed is a summary of typical values I measured or set in the Raman experiments.

Quantity	Typical value
central wavelength	800 nm
spectral width	18 nm, 8 THz
tuning range (BFR)	30 nm
cavity length	2 m
tuning range (tr. stage)	1.5 mm
round trip time	13.2 ns
repetition rate	76 MHz
tuning range (piezo)	3 kHz
pump power (532 nm)	4.5 W
output power (mode-locked)	550 mW
power fluctuations	1 %
pulse length	60 fs
pulse length	18 µm
carrier envelope offset	not locked

4.1.5 Frequency counter

The Menlo frequency comb system comes with a frequency counter[3]. It continuously measures the absolute phase of up to 4 input signals and returns a frequency value based on the absolute acquired phase at one second intervals without dead time.

Three counter channels are used to continuously monitor the proper operation of the frequency comb system, one measuring the CEO frequency, one the direct repetition rate on the internal photo-diode, and one the optical beatnote for the optical locking scheme. The fourth channel is used, alternatively, to measure the beatnote frequency of the 729 nm CW laser with the comb, or to measure the repetition rate of the Mira femtosecond laser for the repetition rate characterization experiments, discussed in section 6.

4.2 Coherent Mira

The Coherent Mira 900 laser is a passively mode-locked Ti:sapph laser system. Compared to the Menlo system, it provides a much higher optical bandwidth of about 8 THz, as shown in the spectra in section 4.4. I start explaining the laser design in section 4.2.1, followed by a description of the repetition rate lock, and a characterization of the stability of the free running CEO frequency. Measurements of the individual laser pulse power behavior over time, affecting the repetition rate stability, are detailed in section 4.2.4. A summary of the Mira's characteristic features is given in table 4.1.

[3] Model FXM50, 5 MHz to 50 MHz, 50 Ω

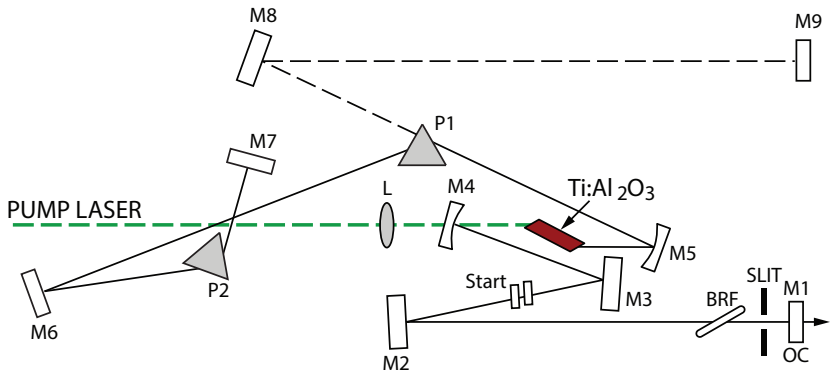

Figure 4.4: Schematic drawing of the Mira laser with mirrors (M), group velocity dispersion compensation prisms (P), output coupler (OC), pump focusing lens (L), rough wavelength tuning birefringent filter (BRF), and starter mechanism (Start). The mirrors M8 and M9 can be used for initial, rough cavity alignment, if the prism P1 is removed.

4.2.1 Laser design

A schematic drawing of the cavity is shown in figure 4.4. The titanium sapphire crystal - the laser's gain medium - is placed in the focus of a telescope between the two mirrors M4 and M5. The crystal is optically pumped with 532 nm light to create the population inversion for laser operation. The pump source is a Coherent Verdi V5, a diode pumped and internally frequency doubled Nd:Vanadate ($Nd:YVO_4$) single frequency laser with 5 W maximum output power.

The laser cavity is terminated by mirror M7 on the one side, and the output coupler (OC, M1) on the other side. On the output coupler side, a birefringent filter (BFR) allows selection and continuous tuning of the center wavelength. On the other side, a double passed tunable prism compressor, formed by the two prisms P1 and P2, allows to compensate the group delay dispersion introduced by normal dispersion of the intra-cavity optical elements, and by self-phase modulation inside the Ti:sapph crystal. The prism P2 is mounted on a translation stage for continuous tuning of the intra-cavity GVD, influencing the final laser pulse length.

Passive mode-locking is achieved via the Kerr lens effect in the Ti:sapph crystal [A82, R19]. The Kerr effect describes the intensity dependent refractive index of an optical material. For low intensities, when the laser operates in continuous wave (CW) mode, the beam is not influenced by the Kerr effect. However, for high intensities, occurring in pulsed operation, the Gaussian spatial beam profile results in a focusing effect, also called self-focusing. The cavity is designed such that the overlap of the pump beam and the cavity mode is maximal in the case of pulsed operation, due to the self-focusing in the Ti:sapph crystal. Additionally, an adjustable slit introduces losses for the CW mode, whereas the mode in pulsed operation fits lossless through the slit.

Even though pulsed operation is preferred by the cavity due to the lower losses, the laser will usually operate CW if it is not forced to pulsed operation at

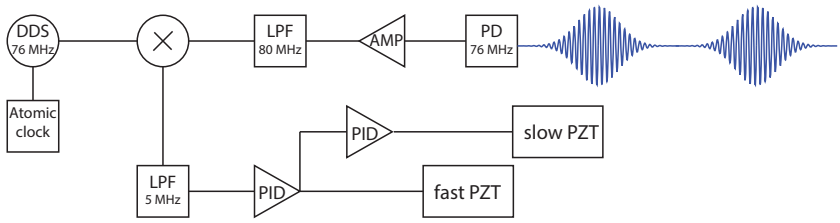

Figure 4.5: Schematic drawing of the Mira repetition rate phase lock. The repetition rate is measured on a fast photo-diode (PD), amplified (AMP) and low pass filtered (LPF), before it is mixed with the output of a direct digital synthesizer (DDS), which is referenced to our GPS disciplined frequency standard. The difference signal from the mixer is low pass filtered, and used for fast and slow feed back on the cavity length via PID controlled piezo actuators (PZT).

a given time. The "switch" formed by the Kerr lens effect and the slit remains "closed" unless an initial pulse reaches high enough intensity to open this switch. This initial event is triggered by a starter mechanism, a pair of parallel mirrors, rotatable around their symmetry axis. This small rotation displaces the beam in the cavity and leads to a rapid change of the cavity length, forming an initial pulse with high enough intensity to introduce self-focusing in the crystal. The initial pulse will bounce back and forth in the cavity, gaining in intensity each time it travels through the Ti:sapph crystal, and each time it hits the output coupler, a pulse is emitted from the laser. The cavity length of about 2 m results in a pulse round trip time of 13.2 ns, and thereby a repetition rate of 76 MHz.

The cavity length can be controlled by adjusting the position of mirror M2, mounted on a translation stage[4] with 1.5 mm travel range. This allows to adjust the cavity length, and thereby the repetition rate by about 60 kHz. Small manual adjustments can be done while the laser is mode-locked, so that we can monitor the repetition rate in real time during these adjustments. For precise control of the repetition rate, the translation stage incorporates a 25 µm tunable piezo for slow feedback, corresponding to a change of 1 kHz in repetition rate, and the mirror itself is mounted on a second, smaller piezo with less range for faster feedback. The details of the repetition rate lock are described in section 4.2.2. The carrier envelope frequency can not be locked, but a qualitative measurement of its stability is discussed in section 4.2.3.

4.2.2 Repetition rate lock

Since the repetition rate is directly given by the cavity length, we can use the repetition rate as error signal to feed back to the cavity length via the piezo mounted mirror. This is done using a simple phase lock loop, comparable to the Menlo RF lock, and sketched in figure 4.5. After the output coupler, a small amount of light from a pick off mirror is send to a fast photodiode[5]. The weak signal is amplified by 43 dB and low pass filtered at 80 MHz to remove higher harmonics of the repetition rate, before it is mixed with a local oscillator signal

[4] Thorlabs NF15AP25
[5] Thorlabs DET10A, 1 ns typical rise time with 50 Ω termination

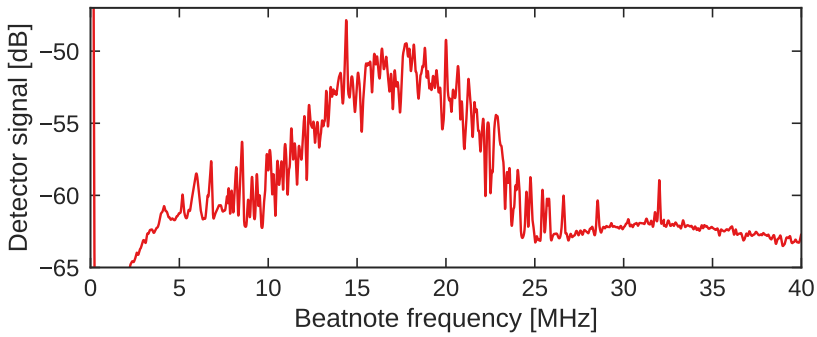

Figure 4.6: Beatnote on a spectrum analyzer of the repetition rate locked Mira laser with a CW laser at 794 nm, and 1 minute averaging time. The width of the distribution gives an idea of the long term, free running CEO stability.

provided by a home built DDS. The output signal of the mixer contains the difference and sum frequencies of the two inputs, and the sum signal is removed by a 5 MHz low pass filter. Finally, the remaining difference signal is amplified and directly applied to the fast piezo. A servo amplifier is used to integrate the difference signal and feed back to the slow piezo. This is on the one hand used to compensate long term drifts e.g. due to temperature fluctuations, and on the other hand to allow continuous tuning of the repetition rate. When the DDS frequency is changed, the repetition rate will follow this change up to about $1\,\mathrm{kHz\,s^{-1}}$ within the tuning range of the slow piezo.

4.2.3 Carrier envelope offset frequency

As mentioned above, we do not lock the Mira's carrier envelope offset frequency (CEO). To get a rough idea of its free running stability, I measured a beatnote between the Mira comb, and a CW laser at 794 nm[6] locked to a cavity. Before the beatnote measurement, the stability of the CW laser cavity lock is verified via a separate beatnote measurement of this CW laser with the Menlo comb.

Figure 4.6 shows the beatnote frequency between the repetition rate locked Mira comb with the 794 nm CW laser. Since the repetition rate is fixed, and the CW laser is stabilized well below 1 MHz, the width of the beatnote is given by CEO fluctuations. The shown frequency distribution was measured with a sweeping spectrum analyzer[7], and one minute averaging time. Since the single sweep time is about 10 s, the fast dynamics of the CEO fluctuations cannot be resolved, but the plotted one minute average gives an idea of CEO noise on a longer time scale. The CEO frequency stays within about ±10 MHz, and does not randomly fluctuate within its maximum range of half the repetition rate[8].

[6]The 794 nm laser's frequency doubled light is usually used in another trap setup in our lab for Doppler cooling. It is a Toptica TA Pro.

[7]Rohde & Schwarz HMS-X

[8]The lowest frequency beatnote will always be at frequency $\leq f_{rep}/2$, since the beating happens with the comb tooth at higher frequency than the CW laser, *and* the comb tooth at lower frequency, so that the maximum frequency difference is $f_{rep}/2$.

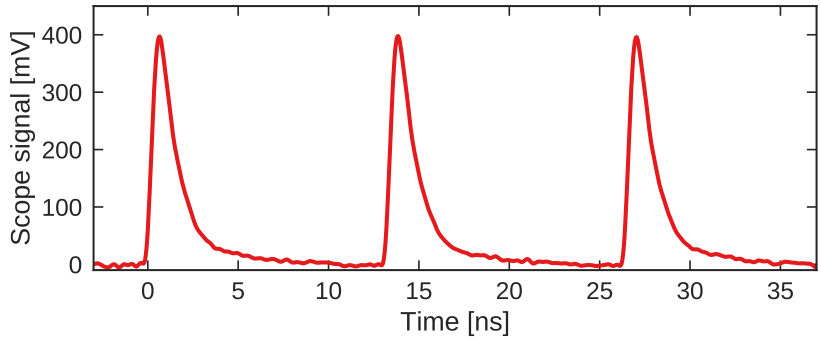

Figure 4.7: Mira laser pulses measured on an oscilloscope.The length of each pulse is given by the detector rise time of about 1 ns, and the spacing between pulses of 13.2 ns corresponds to the laser's repetition rate of 76 MHz.

As already mentioned, the CEO behavior does not influence the Raman experiments, and is not locked, even in the experiments with the Menlo comb.

4.2.4 Power fluctuations

The Raman Rabi frequency is directly proportional to the intensity of the driving light field and thereby depends on the laser output power, so that power fluctuations will lead to decreased coherence. Power fluctuation can also translate into an effective detuning via changing light shifts. Here, I investigate the power stability of the Mira laser with single pulse resolution, and analyze the measured, per pulse energy, statistically.

The measurement uses the signal from the repetition rate photo-detector, split off before it is mixed with the DDS reference, and recorded using a 2 GHz analog bandwidth, 50 ps digital resolution sampling oscilloscope[9]. Figure 4.7 shows three example pulses from such a scope trace. The pulses are separated by 13.2 ns, corresponding to the repetition rate of the laser. The rise time is given by the specified 1 ns for the photo-detector[10], and the total pulse shape and width is obviously given by the electronics involved, rather than the 60 fs pulse length (compare chapter 7). Based on a trace of a total length of 5 ms, corresponding to about 380 000 individual pulses, the height of each pulse is extracted and plotted in figure 4.8 against time (red dots). Additionally, the moving average (blue) with a window of 100 pulses, corresponding to 1.3 µs is shown. It is clearly visible that the output power drops randomly by about 1 % on a timescale of 100 µs. These power drops are most likely related to pump power fluctuations.

Figure 4.9 shows a histogram of the measured pulse heights with a FWHM of 1 % and a clearly asymmetric shape, reflecting the power drops. While the power stability of 1 % is not the limiting factor for the Raman Rabi experiments, the instability in the repetition rate they might induce would be critical [R20].

[9] Agilent DSO
[10] Thorlabs DET10A

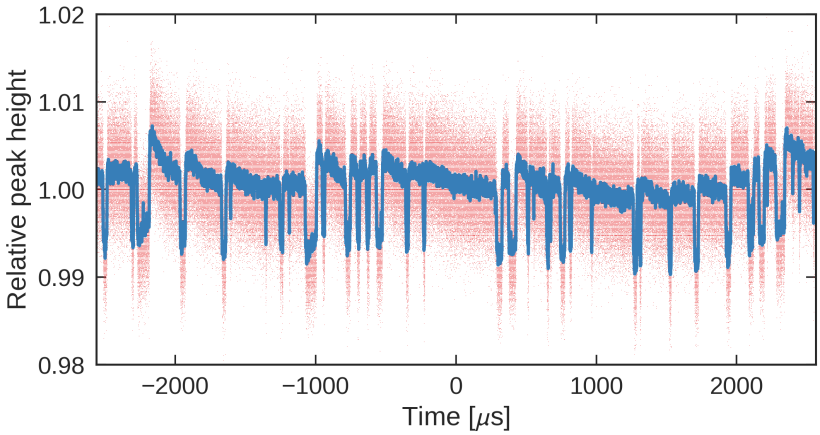

Figure 4.8: Relative pulse height of a total of about 380 000 individual Mira laser pulses (red), and 100 pulses moving average (1.3 µs). Drops in power of about 1 % happen on a timescale of about 100 µs.

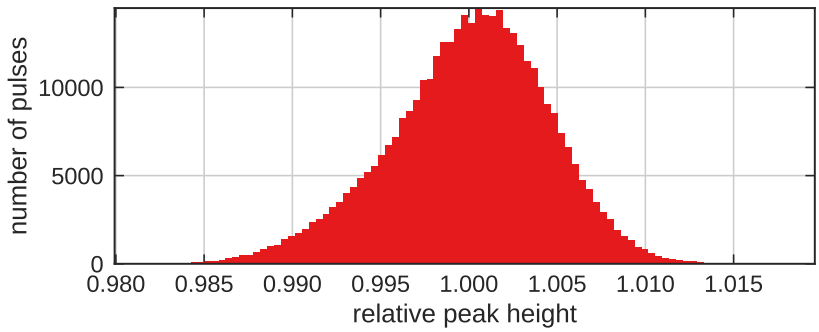

Figure 4.9: Distribution of the Mira laser pulse heights. The width of 1 % and the asymmetry reflect the random power drops due to pump power instabilities.

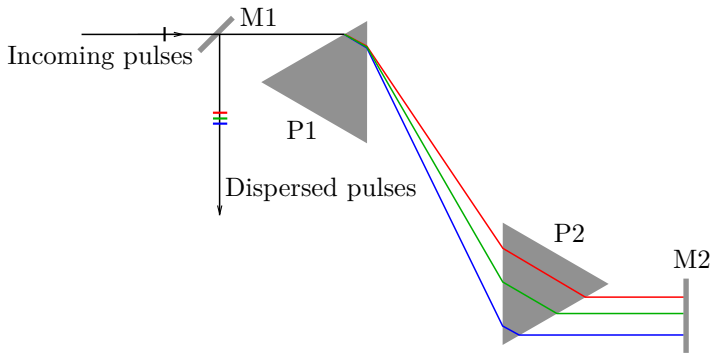

Figure 4.10: Sketch of a prism pulse compressor for group velocity dispersion compensation. The incoming broad bandwidth laser pulse is split by prism P1 into its wavelength components, collimated by prism P2 and sent back by the reflector M2. The effective optical path length for the red light is *longer* than for the blue light, due to the longer path in prism P2, introducing *negative* group velocity dispersion.

Power fluctuations in the laser cavity lead to a displacement of the cavity mode inside the cavity due to nonlinear effects, especially self-focusing in the Ti:sapph crystal. This changes the round trip time, and thereby the effective cavity length, resulting in repetition rate noise.

Despite the high bandwidth of the oscilloscope, the repetition rate stability cannot be extracted from this data with the required precision of $< 10^{-12}$. A comparison of the repetition rate stability with the Menlo system is presented in section 6.

4.3 Prism compressor

All frequency components of the frequency comb light directly in the laser have to be in phase to form the single laser pulse oscillating in the laser cavity. Outside the laser, optics such as lenses, mirrors and the window to the vacuum chamber introduce group delay dispersion, broadening the laser pulse due to different group velocities of the different wavelength components, and thereby altering the phase relation of the frequencies, as discussed in chapter 3.

Different approaches for the compensation of group velocity, and higher order dispersion, such as grating or fiber compressors, exist for specialized applications and very short pulses [B8]. For the Mira laser, with relatively long pulses of 60 fs, we use a simple double passed prism compressor for group velocity dispersion compensation [A83, A84, A85]. A top view sketch of such a prism compressor is shown in figure 4.10. The incoming laser pulse is split into its wavelength components by the first prism (P1), so that angular dispersion [A86] leads to different path length for the different colors in the second prism. The second prism P2, mounted under the exact same angle as P1, collimates the beam, and the reflector M2 sends the beam back along its incoming path.

The angle of both prisms is chosen to match Brewster's angle, to avoid power

losses due to reflections. Actually, the reflector M2 sends the beam back under a small vertical angle (into the drawing plane), so that the reflected beam can be separated from the incoming beam with mirror M1, leading to slightly different beam heights of the incoming and exiting beams. Compared to using a beam-splitter instead of mirror M1, there are no power losses or polarization issues in the described setup.

The wavelength components in the exiting beam are now displaced in time compared to the incoming beam. With correct alignment, the red light travels so much longer in prism P2 compared to the blue light, outweighing the longer travel in air between the prisms, and leading to negative dispersion in total. For an incoming beam already showing a linear frequency chirp, the setup allows to revert this chirp, resulting in bandwidth limited pulses. The amount of negative dispersion can be controlled via the distance between the two prisms. Note that, due to its geometry, the prism compressor only acts on the second order dispersion term in the Taylor expansion (3.17), explicitly acting as negative group velocity dispersion element.

4.4 Optical spectra

Before and during experiments on the ion, the spectra of the lasers are monitored with an optical spectrum analyzer. Figure 4.11a shows a spectrum of the Menlo laser's frequency doubled output (M-VIS). The original bandwidth limited spectrum of the seed laser is already strongly deformed by nonlinear processes in the fiber amplifier and SHG stage of M-VIS. Not visible in the intensity spectrum here is, that the spectral phase is also strongly affected by group velocity dispersion in the fiber components of M-VIS.

Figure 4.11b shows a typical spectrum of the Mira laser. The intensity is well described by a Gaussian with a FWHM of 18 nm or 8 THz, centered around 810 nm. When group velocity dispersion is well compensated with the prism compressor, we measure a close to bandwidth limited pulse length of 60 fs, as discussed in chapter 7.

A spectrum of the Menlo M-VIS light after sending it through the red photonic crystal fiber (PCF, see section 4.1.1), used to reference the 729 nm laser as described in chapter 9.2.6, was shown in a previous section in figure 4.2.

We use an OceanOptics model HR4000 with a wavelength range of 200 nm to 1100 nm for these measurements. The input to the optical spectrum analyzer (OSA) is connected to a robust multi-mode fiber, such that spectra can be easily obtained simply by pointing the other end of the fiber towards a diffusely reflective surface illuminated by the laser. To avoid distortion of the spectra due to coherent reflections from the surface (laser speckle), a paper is mounted on a rotating 12 V computer fan, acting as the reflective surface. OceanOptics provides a basic driver software I used to implement a simple python program, continuously acquiring spectra, automatically adjusting the exposure time, and streaming the data to a web interface, such that the spectra can be conveniently viewed on any network enabled device in the laboratory. This turned out to be very helpful for alignment of the Mira laser cavity. Additionally, the program stores the spectra in our central database, which allows us to verify the proper

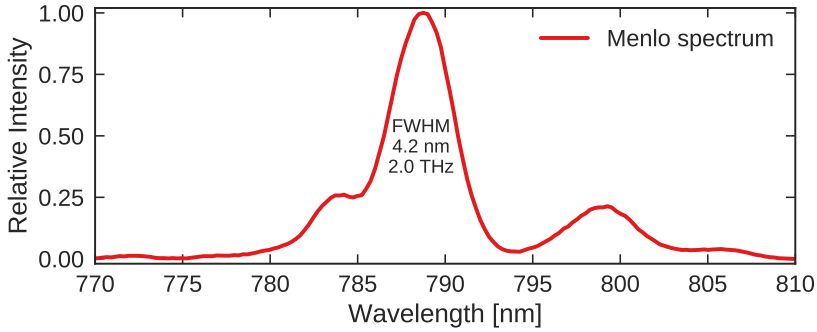

(a) Spectrum of the Menlo amplified and frequency doubled output (M-VIS).

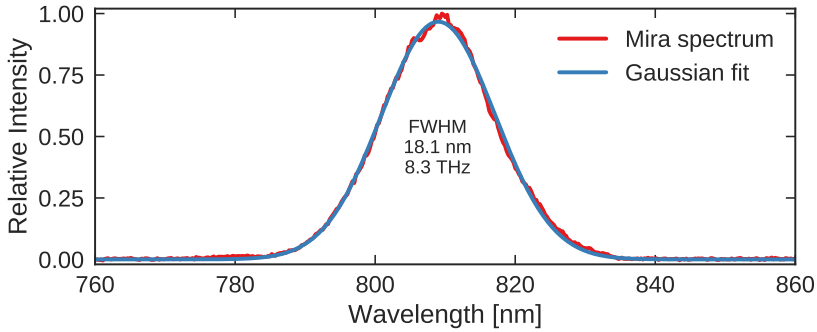

(b) Spectrum of the Mira laser.

Figure 4.11: Typical spectra of the Mira and Menlo laser. The Mira spectrum is well described by a Gaussian with a FWHM of 18 nm or 8 THz centered around 810 nm. The spectrum of the amplified Menlo laser is strongly affected by nonlinear effects in the SHG and amplifier stage, and its pulses have to be expected to be far from bandwidth limited in the time domain, heavily affected by GVD. Note the factor of two on the wavelength axis between figure a and b.

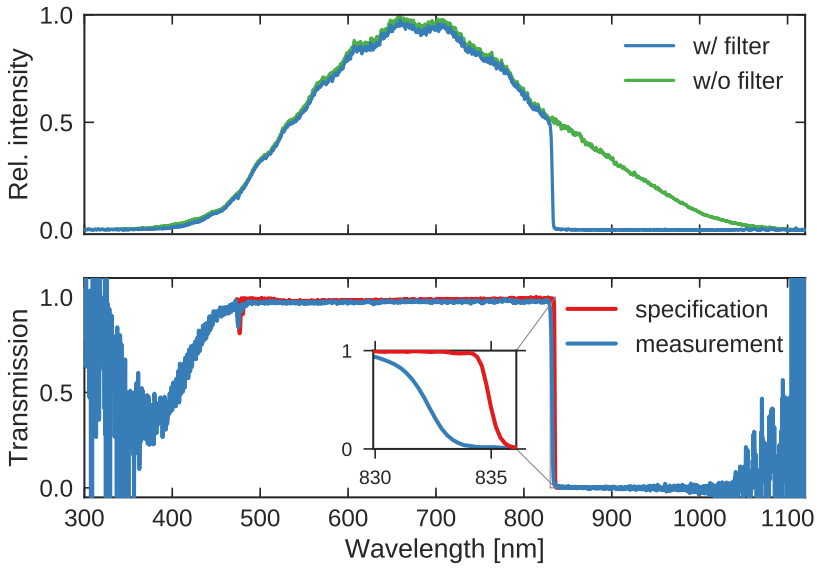

Figure 4.12: Spectrum (top) of a halogen light bulb measured with an optical spectrometer, with and without the wavelength low pass filter in place. The graph below shows the calculated transmission next to the specifications by the manufacturer.

operation of the laser during, and after Raman experiments.

4.4.1 Spectral low pass filter

To block resonant light unintentionally driving optical transitions, and off resonant light causing unwanted light shifts, we block frequency comb light above 835 nm using an interferometric wavelength low pass filter[11], effectively cutting the spectrum. Figure 4.12 (top) shows a spectrum of an incoherent light source, simply a halogen lamp, using an optical spectrometer. The filter is specified with an extinction ratio of better than 2×10^{-6} above 840.0 nm. Figure 4.12 (bottom) gives the transmission, i.e. the spectrum with filter divided by the spectrum without filter, calculated from the above measurement, together with the specifications by the manufacturer. A slight angle between the interference filter and the propagation direction of the frequency comb light during the measurement might cause the lower cut-off wavelength and less steep slope compared to the specifications.

A separate test was conducted with light specifically at 866 nm, since the spectrometer does not provide the necessary resolution in intensity. With a fiber coupled power meter[12], placing the filter in front of the fiber coupler, the extinction ratio at 866 nm was confirmed to be better than 10^{-6}. For the frequency comb light, we actually use a set of two identical filters, so that resonant

[11] Semrock FF01-842/SP-25
[12] Thorlabs S151C - Compact Fiber Photodiode Power Sensor

light can be ignored, and light shifts are completely dominated by light below the cut-off wavelength. Another identical filter was also placed in the 729 nm laser beam-path to block a hypothetical broad wavelength pedestal of the tapered amplifier (see chapter 9.2.6 on the 729 nm laser).

5 Frequency Standard

Optical spectroscopy is the art of precisely determining the frequency of a light field in resonance with a given transition of interest. Since measuring a frequency is basically counting the number of oscillations over a well defined time interval, the achievable resolution and accuracy of such a measurement is fundamentally limited by the resolution and accuracy of the clock being used as a reference. Generally, it is of course desirable to have a measurement device (clock) which is much better than the expected stability of the quantity being measured. For this work, however, we will see that the experimental resolution on the order of 10^{-11} is similar to the resolution of the available time reference, which makes a careful analysis indispensable.

5.1 Overview

The central device for time keeping in our laboratory is a commercial bench top rubidium oscillator[1], also referred to simply as "clock" in the following. A diagram illustrating the dependencies of the clock within the chain of frequency referencing and measuring is shown in figure 5.1. The clock provides a standard 10 MHz output which other devices can use as reference signal, and is itself referenced to the Global Positioning System (GPS).

For frequency comb Raman spectroscopy, the repetition rate of the comb is the critical quantity determining the resonance condition as discussed in chapter 2.1.6. The repetition rate is phase locked to a tunable reference, a homebuilt direct digital synthesizer[2] (DDS), referenced to the clock. By this chain of refer-

[1] Stanford Research FS725m rubidium frequency standard

[2] The DDS box is based on an Analog Devices AD9912 DDS chip, and was built by Frank Korfix Mikkelsen at the physics department's electronics workshop. Specifications: tuning range 10 MHz to 250 MHz, input resolution 1 µHz, output resolution is given by internal reference clock / 2^{48} = $\frac{66 \cdot 10\,\mathrm{MHz}}{2^{48}}$ = 2.34 µHz, amplitude −18 dBm to 15.5 dBm in 50 Ω (given by

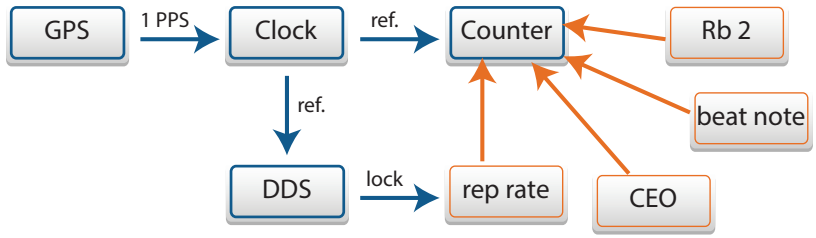

Figure 5.1: Diagram illustrating the chain of frequency referencing (blue), and measured quantities (orange). Note that, for instance, the repetition rate is effectively locked to the clock while being measured with a counter,itself referenced to the same clock. In such a measurement scenario, long term drifts are not measurable by design.

Table 5.1: Manufacturer specifications for the Stanford Research FS725m rubidium frequency standard without external 1PPS reference.

Quantity	Value
Accuracy	$\pm 5 \times 10^{-11}$
Settability	$< 5 \times 10^{-12}$
Aging (monthly)	$< 5 \times 10^{-11}$
Allan variance (1s)	$< 2 \times 10^{-11}$
Allan variance (10s)	$< 1 \times 10^{-11}$
Allan variance (100s)	$< 2 \times 10^{-12}$

ences, the stability and accuracy of the clock is finally transferred to the comb's repetition rate. Table 5.1 lists the most relevant specifications of the clock. While the short term stability ultimately gives the lower limit for the achievable spectroscopic linewidth or coherence time, discussed in chapter 12.2, the long term stability determines the achievable accuracy of the final spectroscopy result presented in chapter 13.

5.2 GPS disciplining

To overcome the limited long term accuracy of the bare clock, mostly due to aging and environmental effects, we phase lock the clock to a slow, but on long timescales more stable, time reference with a long integration time [O5]. This slow reference was set up in form of a GPS receiver during a bachelor project in the group [T5]. The Global Positioning System [P1, B9] relies on the precise measurement of signal transit times between several satellites and the receiver. For this purpose, every GPS satellite carries atomic oscillators, synchronized each orbit (about 12 hours) with the US Naval Observatory, whose time is in

variable gain amplifier AD8368).

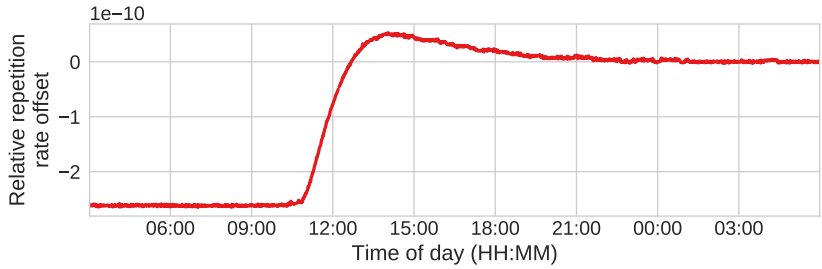

Figure 5.2: GPS disciplining. Shown is the relative frequency change of the Rb clock when it was locked for the first time to GPS in May 2016.

close agreement with Coordinated Universal Time (UTC). The GPS receiver[3] contains a simple oscillator, constantly synchronized to GPS time. The receiver's time is made available via a one pulse per second (1 PPS) output signal, fed to the rubidium clock, used in a digital phase lock loop with variable integration time to prevent the clock from drifting. This setup is then called a *GPS disciplined rubidium oscillator*.

To verify the proper operation of our GPS implementation, I used the frequency comb to monitor the clock. Figure 5.2 shows a measurement of the initial GPS lock of the clock in May 2016. While the frequency comb was optically locked to the JPX laser as described in chapter 4.1.4, the repetition rate was measured on the frequency counter referenced to the Rb clock. The actual repetition rate is not affected by the GPS disciplining[4], but the measured repetition rate changes due to the change of the time reference. The phase lock loop's natural time constant of 2.25 hours is clearly visible in the data. The clock's absolute frequency correction of 2.6×10^{-10} corresponds to at least 5 months of aging according to table 5.1, less than the clock's age of more than one year, and thus well within specifications.

The clock's frequency is controlled by changing the internal magnetic field affecting the rubidium hyperfine clock transition. Due to the digital nature of the clock's electronics, this frequency adjustment happens in discrete steps given by the "settability" of 5×10^{-12}. Figure 5.3 shows a measurement of the relative frequency of the clock together with the clock's frequency control parameter (SF) over the course of two and a half days. The frequency jumps as expected in steps of about 5×10^{-12}, and these jumps are clearly triggered by the frequency control parameter. The accuracy on the timescale of the integration time is thereby limited.

The natural time constant of the 1 PPS phase lock loop can be adjusted via a computer interface from 0.14 to 17.99 hours. Figure 5.4 shows a relative frequency measurement while this time constant was changed. The measurement started without locking the clock to GPS (undisciplined). When the lock is

[3] Septentrio Satellite Navigation model AsteRx2e HDC, time accuracy of the 1 PPS specified to 10 ns [X1]

[4] Actually, the repetition rate is marginally affected since the CEO frequency is still locked to the clock. This effect, however, is suppressed by a factor of $1/n$ where $n \approx 777435$ is the comb tooth number used for the optical lock.

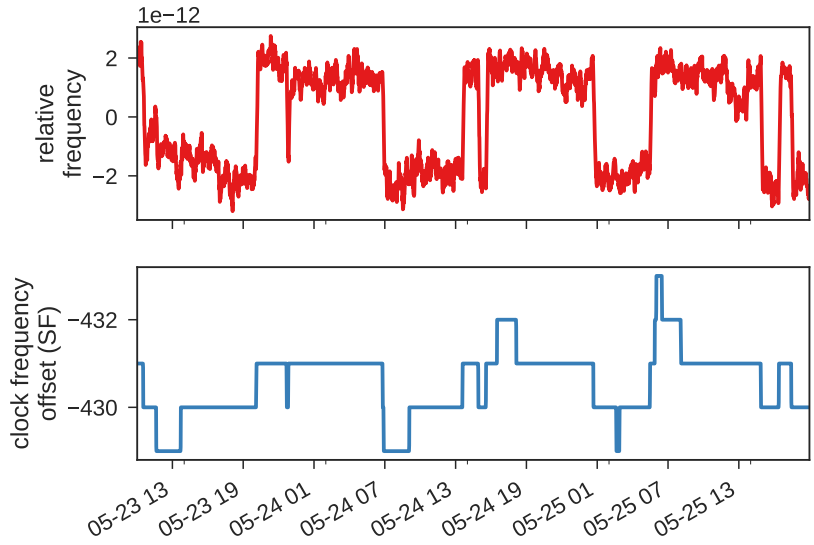

Figure 5.3: Rubidium clock frequency and frequency control parameter SF over time (format: MM-DD HH). The jumps in frequency are determined by the settability of the clock of 5×10^{-12}, and clearly triggered by the internal frequency adjustment parameter SF. The accuracy on the timescale of the integration time is thereby limited.

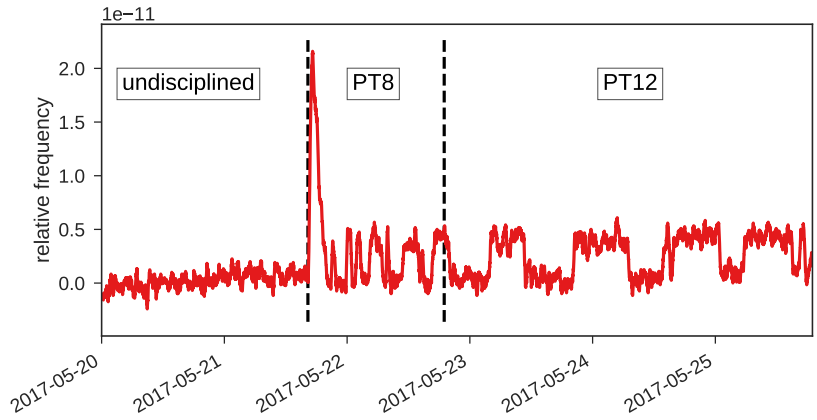

Figure 5.4: Rubidium clock frequency measurement while adjusting the time constant of the GPS lock. Control parameter PT8 = 2.25 hours, PT12 = 8.99 hours. The observed behavior is explained in the text.

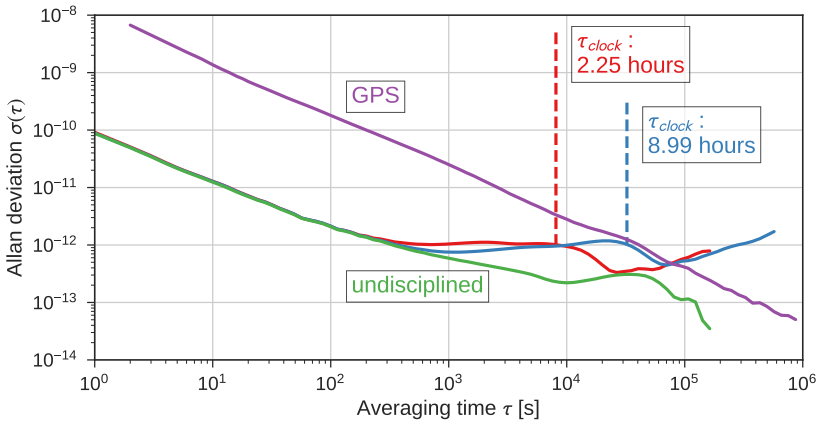

Figure 5.5: Allan deviation of the clock and GPS 1 PPS frequency stability.

engaged, the frequency changes dramatically, just to settle at almost the same frequency afterwards. This effect is expected, since the lock is an actual phase lock, and not only matching the frequencies, meaning that an accumulated phase offset between GPS and the Rb clock needs to be compensated by purposefully detuning the clock's frequency until both signals are again in phase. The middle section of figure 5.4 shows the clock locked with a 2.25 hours time constant (control parameter PT = 8), while the last section shows the behavior after changing the time constant to 8.99 hours (PT = 12). The frequency jumps given by the settability of the clock happen, as expected, less frequently for the longer integration time.

A separate, all electronic measurement, not involving the frequency comb, reflecting the stability of the clock's frequency output is visualized in terms of the phase Allan deviation [A87], eq. (6.1), in figure 5.5. The GPS data was acquired by the clock measuring the time-tag[5] of each 1 PPS pulse while the clock is referenced to GPS. The extrapolated value of about 10^{-8} for each 1 s measurement corresponds to the specified time accuracy of 10 ns of the GPS receiver [X1]. The three measurements of the undisciplined, and locked clock, are facilitated by measuring the frequency of a second Rb oscillator on the frequency counter referenced to the clock. Thereby, the measured stability for short times is actually given by this second clock, and slightly higher than the specified values for our frequency standard itself (compare table 5.1). For the disciplined clock, the frequency jumps triggered by the internal frequency adjustment (compare figure 5.4) cause a bump in the Allan deviation at the corresponding averaging time. The observed drift for averaging times larger than 10^5 s $\approx$ 1.2 days is caused by the drift of the second (undisciplined) Rb oscillator.

[5]Each 1 PPS signal is tagged by the Rb clock with its arrival time relative to the Rb clock's internal 1 PPS signal (measurement parameter TT). The resolution of this measurement is 1 ns (10^{-9}).

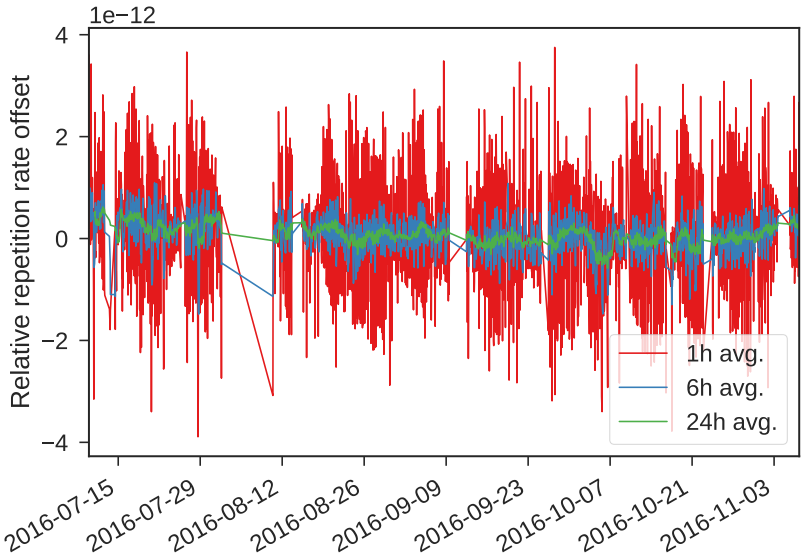

Figure 5.6: Long term frequency stability of JPX vs Rb clock, quantified via a beatnote measurement on the Menlo frequency comb.

5.3 Long term stability

The stability of a GPS disciplined oscillator for timescales long compared to the GPS satellites orbit time of 12 hours is theoretically perfect by definition, since the GPS satellites themselves are synchronized to the current definition of the SI second[6] [R2, A12]. However, technical issues such as cycle slips in the phase lock loop could possibly lead to inaccuracies.

With the JPX reference laser, we have a second, independent, and extremely stable frequency standard available (see chapter 4.1.4). Figure 5.6 shows the Menlo comb's repetition rate, measured by the frequency counter, while the comb is optically locked to the JPX. Assuming that the JPX is perfectly stable, the observed fluctuations are caused by the clock referencing the frequency counter, and reflect the clock's long term stability. On the other hand, if we assume the GPS lock to work properly, then the fluctuations are caused by instabilities in the JPX's laser frequency reflecting the JPX's long term stability. The JPX and the GPS disciplined Rb clock are fundamentally different devices, and it is fair to assume that no correlations between their frequency outputs exist. Thus, we can also see the stability of the measured repetition rate as an upper limit for both, the JPX and the clock at the same time. Over the observation period of about 4 months, the 24 hour averaged frequency fluctuations stay well within 10^{-12} which is smaller than our experimental spectroscopy resolution.

Another test of the clock accuracy is the $|S_{1/2}\rangle \rightarrow |D_{5/2}\rangle$ transition spectroscopy in $^{40}Ca^{+}$ using the 729 nm laser. The uncertainty of the measurement

[6] "The second is the duration of 9 192 631 770 periods of the radiation corresponding to the transition between the two hyperfine levels of the ground state of the caesium-133 atom."

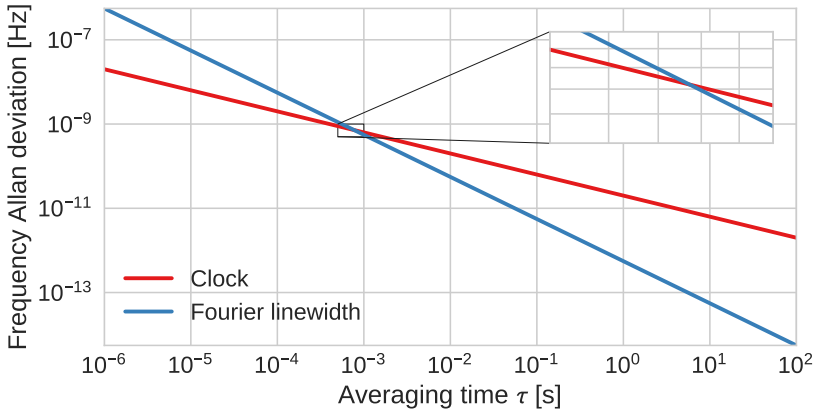

Figure 5.7: Frequency Allan deviation extrapolated from the specifications given in table 5.1 of the bare clock (red). In blue I plotted the Fourier limited linewidth of the D-finestructure transition at 1.8 THz as $\frac{1}{1.8 \times 10^{12} \cdot \tau}$. The crossing of the curves should give an estimate of the expected coherence time and Gaussian linewidth limit.

presented in chapter 11 is limited by the clock accuracy, as discussed here, and perfectly agrees with the most precise (2.4×10^{-15}) measurement of this transition [A88].

5.4 Short term stability

Assuming white noise, we can extrapolate the Allan deviation to shorter times based on the specified values given in table 5.1. This extrapolation is plotted in figure 5.7 together with the Fourier limited linewidth, simply given by

$$\delta_{\text{Fourier}} = \frac{1}{\tau}\,, \tag{5.1}$$

The two curves intersect at $\tau = 770\,\mu\text{s}$, and an Allan deviation of 7.2×10^{-10}. These values give a rough estimate on the maximum possible performance of the Menlo comb in the Raman experiments, since the clock stability directly translates into repetition rate stability in the RF locking scheme. The measured coherence time for Raman Rabi flopping with the Menlo comb is longer, 3.60(18) ms as discussed in chapter 12.2.3. The Gaussian linewidth is expected to be larger than

$$\delta_{\text{Fourier, D-fine}} = 7.2 \times 10^{-10} \cdot 1.8\,\text{THz} = 1.3\,\text{kHz}\,, \tag{5.2}$$

which needs to be compared to the measured Gaussian linewidth of 754(18) Hz, discussed in chapter 12.2.4. It seems that the stability of the clock is actually better than specified.

5.5 Notes on data acquisition

The Menlo frequency comb exposes a XML-RPC (remote procedure call) interface for data extraction and partial remote control. We use a simple python program to extract all available data once per second, including the frequency counter readings, and store them in a SQL database. In a similar fashion, the Rb clock provides a serial interface exposing about 50 parameters, including the time-tag (TT) of each 1 PPS signal, which are also logged once per second to the database. Constantly logging these data allows not only to analyze long term behavior, such as the JPX frequency stability in figure 5.6, but also offers the possibility to verify the correct operation after spectroscopy data was taken. Additionally, NIST provides a database with the measured deviation of the GPS satellite time on a daily basis [O6]. This deviation is typically smaller than 10^{-14} for an averaging time of one hour.

5.6 Conclusion

The examination of our GPS disciplined Rb clock clearly revealed its limitations. While the GPS disciplining has proven to eliminate drifts on the time scale of hours, determined by the integration constant, there is a fundamental short term accuracy limitation of 5×10^{-12} due to the digital settability of the clock. For very short times, the clock contributes to decoherence and gives a lower limit for the achievable spectroscopic linewidth. Nonetheless, the clock behaves as expected and is perfectly suitable for the conducted frequency comb measurements, with an accuracy on the same level as other systematic effects, discussed in chapter 8.

6
Repetition Rate Stability

In the Raman experiments, the repetition rate stability of the frequency comb defines the effective laser linewidth, since the Raman process depends only on the frequency difference of the driving light fields. This repetition rate linewidth turns out to be very different for the two different frequency combs. The Menlo comb is about one order of magnitude more stable than the Mira laser, clearly reflected in the achievable coherence times and spectroscopic resolution, as discussed in detail in chapter 12. I characterized the repetition rate stability using two different methods, addressing different timescales. The results will be given in terms of the phase noise Allan deviation, a common measure in metrology.

6.1 Allan deviation

For a series of phase measurements with constant sampling rate $1/\tau_0$, the overlapping Allan variance [A87, A89] is defined as

$$\sigma^2_{OADEV}(m\tau_0) = \frac{1}{2(m\tau_0)^2(N-2m)} \sum_{n=1}^{N-2m} (x_{n+2m} - 2x_{n+1m} + x_n)^2 \,, \qquad (6.1)$$

where $\sigma^2_x(m\tau_0)$ is the overlapping Allan variance for an averaging time of $\tau = m\,\tau_0$, and x_n is the time-series of N phase observations divided by the carrier frequency.

The Allan deviation characterizes a signal on different timescales, and allows to derive short term noise as well as drifts from the same dataset, which is not possible using traditional statistical quantities such as the standard deviation. The Allan deviation is usually presented in form of a $\sigma_{OADEV}(\tau)$ versus averaging time τ plot. For a constant signal with purely white noise, the Allan deviation is constant and identical with the standard deviation over the given measuring time.

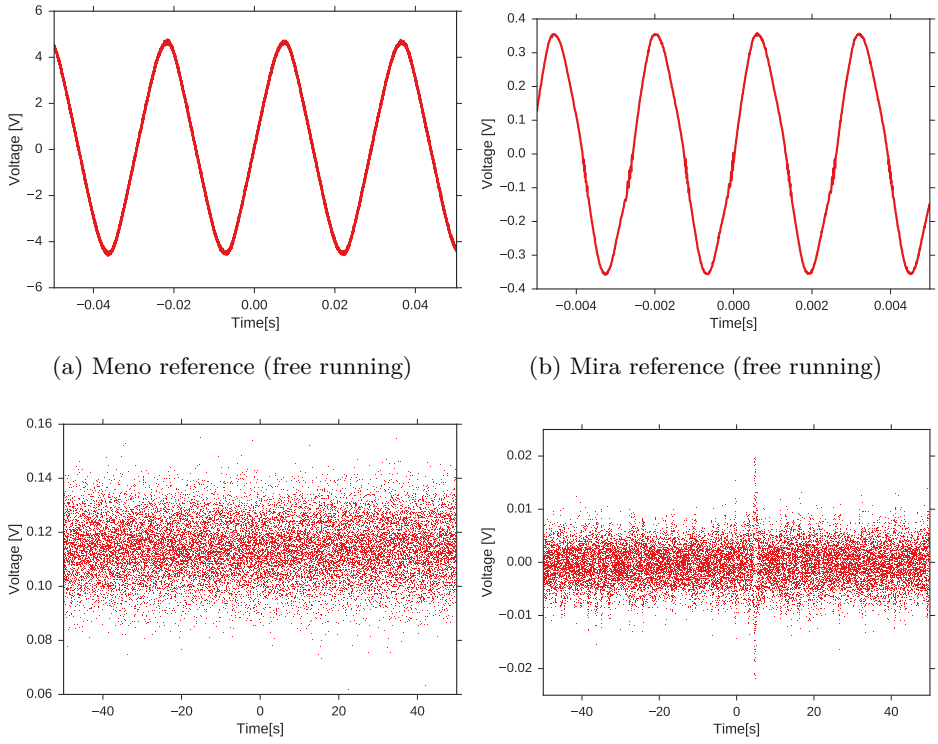

(a) Meno reference (free running)

(b) Mira reference (free running)

(c) Menlo phase noise (locked)

(d) Mira phase noise (locked)

Figure 6.1: Measured phase noise of the repetition rate phase lock loop for the Menlo system (left) and Mira laser (right).

6.2 Direct phase noise measurement

Experimentally, we measured the phase noise of the repetition rate by recording the error signal from the repetition rate RF phase lock loop, as described in section 4.2.2. Figure 6.1 shows the measured phase lock voltage noise of the Menlo (c) and Mira (d) laser, when the repetition rate is locked. To convert from voltage to phase, we calibrate the voltage scale using a measurement of the error signal when the phase lock loop is open as shown in figures (a,b). The error signal oscillates with the difference frequency of the free running repetition rate and the reference signal from the DDS. The peak to peak voltage of this oscillation then corresponds to a phase mismatch of π.

The calibrated phase noise is analyzed by calculating the overlapping Allan deviation, equation (6.1), and plotted in figure 6.3, discussed in section 6.5. Note that only the curves in the interval $50\,\mathrm{ps} \leq \tau \leq 50\,\mathrm{s}$ were obtained using the method described here This timescale is determined by the sampling rate of $1/50\,\mathrm{ps}$, and total acquisition time of $100\,\mathrm{s}$ of the oscilloscope[1] used for the measurement.

[1] Keysight DSO, 20 GHz sampling rate

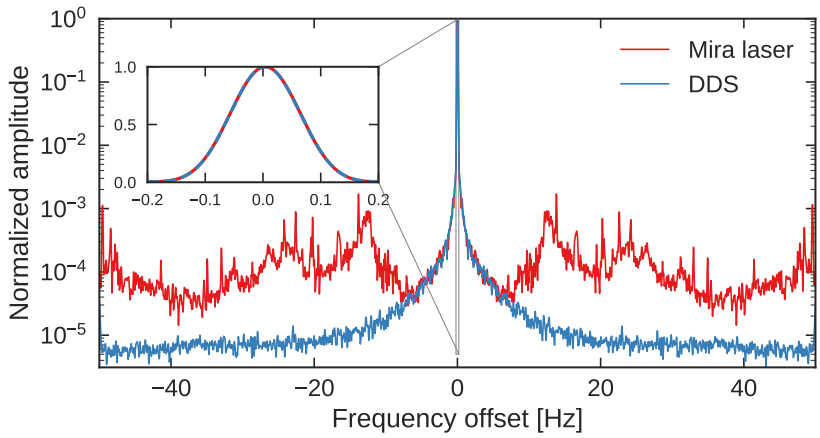

Figure 6.2: Repetition rate of the Mira laser (relative to 76 MHz) measured with a fast photo-diode on a spectrum analyzer, together with the DDS signal used in the phase lock loop. The measurement is bandwidth limited by the resolution of the spectrum analyzer of 0.1 Hz, apparent in the linear scale inset, where the amplitude data perfectly follows a Gaussian distribution with 0.14 Hz FWHM.

6.3 Frequency counter measurement

The second method to determine the stability of the repetition rate is by analyzing the readings of a frequency counter fed with the repetition rate signal from a fast photodiode monitoring the reprate directly. The Menlo frequency counter (see section 4.1.5) has a gate time of 1 s, limiting the lowest Allan deviation averaging time to this value. The measured frequency noise can easily be converted to phase noise, simply by calculating the cumulative sum of the measured frequencies. The result is plotted together with the direct phase noise analysis from the previous section in figure 6.3.

The benefit of the frequency counter is that we can monitor the frequency stability even when the system is not locked, which is naturally impossible for the direct noise analysis of the phase lock loop.

6.4 Simple spectrum analyzer measurement

A first attempt of measuring the repetition rate stability of the Mira laser was conducted by monitoring the repetition rate on a fast photo-diode[2] with a spectrum analyzer[3]. Figure 6.2 shows this measurement together with the corresponding DDS signal used to lock the repetition rate. The measurement is bandwidth limited by the measurement device, averaging out fluctuations faster than the acquisition time of 10 s, and thereby hiding the real dynamics of the repetition rate behavior over time.

[2]Thorlabs DET10A, 1 ns typical rise time with 50 Ω termination
[3]Tektronix RSA5103B, 0.1 Hz resolution bandwidth

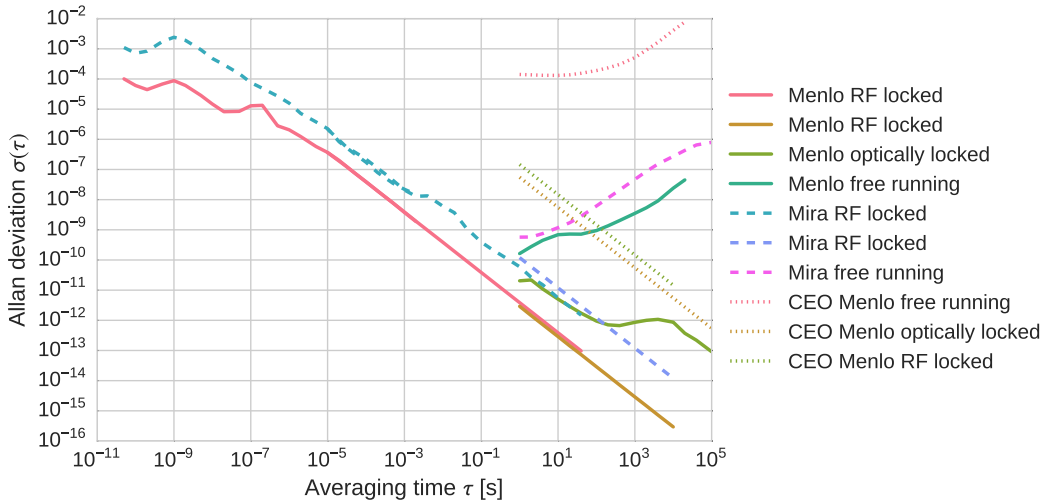

Figure 6.3: Allan deviation comparison of the Menlo and Mira laser systems for averaging times spanning 15 orders of magnitude, from 50 ps to more than one day. The repetition rate of the Menlo system is about one order of magnitude more stable than the Mira for the direct repetition rate RF lock. Besides, the optically locked Menlo's repetition rate is much less stable compared to the direct RF lock, as explained in the text. The repetition rate drift of the free running lasers as well as the CEO stability of the Menlo system is also plotted.

6.5 Interpretation

Figure 6.3 shows the Allan deviation curves obtained using the direct phase noise, and frequency counter measurements, as described above. In the overlapping time interval $1\,\mathrm{s} \leq \tau \leq 50\,\mathrm{s}$, both methods give almost the same result, with a slight offset most likely due to the limited accuracy of the calibration measurements for the direct phase noise measurements.

The repetition rate Allan deviation of both lasers follows over a wide averaging time range a τ^{-1} power law, characteristic for white noise. The noise level of the Mira laser is about one order of magnitude higher compared to the Menlo. This noise difference will turn out to be extremely important for the coherence time of Raman Rabi oscillations, and the achievable spectroscopic linewidth, as discussed in chapter 12.

For the Menlo laser, we can also compare the repetition rate stability when the laser is optically locked versus the direct repetition rate RF lock. Even though the absolute frequency of the comb tooth the frequency comb is optically locked to will be extremely stable, the repetition rate is clearly less stable for the optical lock. This is due to the fact that the noise of the carrier envelope offset frequency (CEO), which is orders of magnitudes higher than the repetition rate noise, is partly converted into repetition rate noise. When the CEO fluctuates during the optical lock, the system uses the much faster repetition rate lock to compensate, keeping the comb tooth which is optically locked stable, but introducing anti-correlated fluctuations on the repetition rate. All frequency comb Raman experiments were carried out with the RF lock for exactly this reason.

In order to measure an event in time, you must use a shorter one. But then, to measure the shortest event, you must use an even shorter one. And so on. So, now, how do you measure the shortest event ever created?

Rick Trebino

7 Pulse Characterization

The inventor of frequency resolved optical gating (FROG), the technique I use to characterize the Mira comb light, Rick Trebino, starts his book on the subject with the quote [B10]:

> "In order to measure an event in time, you must use a shorter one. But then, to measure the shortest event, you must use an even shorter one. And so on. So, now, how do you measure the shortest event ever created?"

This dilemma, of measuring an ultra-short event in time, without having a shorter event to ones disposal to measure it, is solved by autocorrelation techniques, especially in a very elegant way by frequency resolved optical gating (FROG) [A90, A91, B10, R21]. These measurement methods basically use the laser pulse of interest to measure itself. This self-referencing, in form of the interferometric autocorrelation, is briefly described in section 7.1, together with a measurement of the Mira laser pulses. A comprehensive discussion can be found in ref. [B8]. The simple optical autocorrelator, can only give a qualitative idea of the laser pulse being measured, whereas FROG, described in section 7.2, allows to extract the full electric field information from a single laser pulse, that is, not only the intensity profile vs. time but also the phase information vs. time.

7.1 Autocorrelation

Optical carrier frequencies, and even the envelope of a fs pulse, are too fast for direct electronic measurements. Thus, we need an optical signal $I_r(t)$, ideally faster than the signal $I_s(t)$ we want to measure. The cross correlation $CC(\tau)$ of the two signals is defined as

$$CC(\tau) = \int_{-\infty}^{+\infty} I_s(t)\, I_r(t-\tau)\, dt\,, \tag{7.1}$$

and for an infinity short reference signal $I_r(t) = \delta(t)$, we perfectly retrieve the optical (intensity) signal, since $CC(\tau) = I_s(\tau)$ in this case. Another way to look at this is through the Fourier transformed quantities

$$CC(\omega) = I_r(\omega)\, I_s^*(\omega)\,, \tag{7.2}$$

where the signal $I_s^*(\omega)$ is retrieved by measuring the cross correlation $CC(\omega)$ and dividing by the known reference $I_r(\omega)$. Again, we see that this will work best for short reference pulses, corresponding to broad reference spectra, since noise will otherwise dominate the measurement when $I_r(\omega)$ becomes small. For the ideal case of $I_r(t) = \delta(t)$, the reference spectrum $I_r(\omega)$ is simply a constant, thus infinity broad. However, even in this ideal case we do not gain any phase information.

Often, there is no well known reference signal available to measure the cross correlation. However, the signal $I_s(t)$ can be used as the reference itself, such that $I_s(t) = I_r(t) = I(t)$. The cross correlation (7.1) then becomes the autocorrelation

$$AC(\tau) = \int_{-\infty}^{+\infty} I(t)\, I(t-\tau)\, dt\,, \tag{7.3}$$

which is always a symmetric function, hence containing only limited information about the actual pulse shape, which might be asymmetric.

7.1.1 Interferometric autocorrelation

A simple Michelson interferometer can be used to measure the field autocorrelation, also called first order autocorrelation, when one arm of the interferometer has an adjustable length, thereby scanning the time delay τ between the pulsed traveling in the two arms. The field autocorrelation

$$AC^{(1)}(\tau) = \int_{-\infty}^{+\infty} E(t)\, E^*(t-\tau)\, dt\,, \tag{7.4}$$

can then be detected on a photo-detector at the output of the interferometer as illustrated in figure 7.1 (without the SGH crystal for the *field* AC). From the Wiener–Khinchin theorem, we know that the Fourier transform of the autocorrelation corresponds to the spectral intensity. In other words, the information gained through first order autocorrelation is equivalent to measuring the spectrum, but does not contain any information on the pulse shape.

If we instead add a second harmonic generation (SHG) crystal in front of the detector, and filter out the residual fundamental light, we get the second order interferometric autocorrelation (IAC)

$$AC^{(2)}(\tau) = A_0(\tau) + Re[A_1(\tau)\, e^{-i\omega_c\tau}] + Re[A_2(\tau)\, e^{-2i\omega_c\tau}]\,, \tag{7.5}$$

where we have written the field as a product of carrier frequency ω_c and pulse

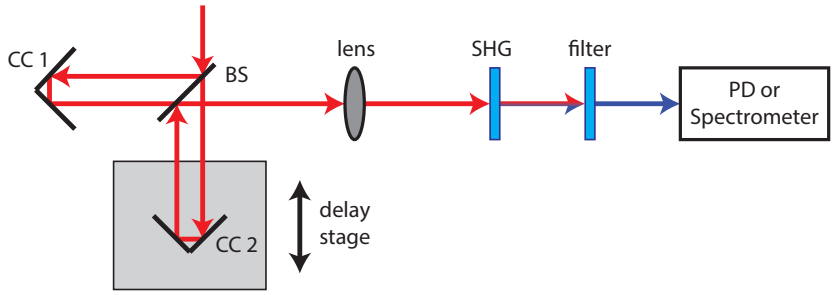

Figure 7.1: Scheme of an interferometric autocorrelator or SHG FROG. The light is sent through a Michelson interferometer, i.e. split by a beam splitter (BS) in two arms, and reflected back by two corner cube reflectors (CC). One CC is mounted on a delay stage to scan the length of this arm of the interferometer. After the light is combined again in the beam splitter, it is focused in a SHG crystal, and the fundamental light is blocked in a filter. The frequency doubled light is detected on a photo-detector (PD) for the autocorrelation. Simply by replacing the photo-detector with a spectrometer, the setup becomes a SHG FROG.

envelope $E(t)$ according to equation (3.4), and the three terms are given by

$$A_0(\tau) = \int_{-\infty}^{+\infty} \left[2\mathcal{E}^4(t) + 4\mathcal{E}^2(t-\tau)\,\mathcal{E}^2(t)\right] dt \tag{7.6}$$

$$A_1(\tau) = 4\int_{-\infty}^{+\infty} \mathcal{E}(t-\tau)\,\mathcal{E}(t)\left[\mathcal{E}^2(t-\tau) + \mathcal{E}^2(t)\right] e^{i[\phi(t-\tau)-\phi(t)]}\, dt \tag{7.7}$$

$$A_2(\tau) = 2\int_{-\infty}^{+\infty} \mathcal{E}^2(t-\tau)\,\mathcal{E}^2(t)\, e^{i[\phi(t-\tau)-\phi(t)]}\, dt\,. \tag{7.8}$$

From (7.5) we see that the second order autocorrelation signal $AC^{(2)}(\tau)$ will oscillate at different frequencies when varying the delay τ. The first term A_0 is the intensity autocorrelation with background, and is typically measured if the detector is too slow to detect the faster oscillating terms A_1 and A_2. However, it is only these terms A_1 and A_2, containing phase information.

For zero delay, we find

$$AC^{(2)}(\tau = 0) = 16\int_{-\infty}^{+\infty} \mathcal{E}^4(t)\, dt\,, \tag{7.9}$$

and for no overlap between the two pulses

$$\lim_{\tau\to\infty} AC^{(2)}(\tau) = 2\int_{-\infty}^{+\infty} \mathcal{E}^4(t)\, dt\,. \tag{7.10}$$

Thus, the peak to background ratio for the second order interferometric autocorrelation is $8:1$. If only A_0 is resolved, the signal to background ratio for the intensity autocorrelation with background is $3:1$.

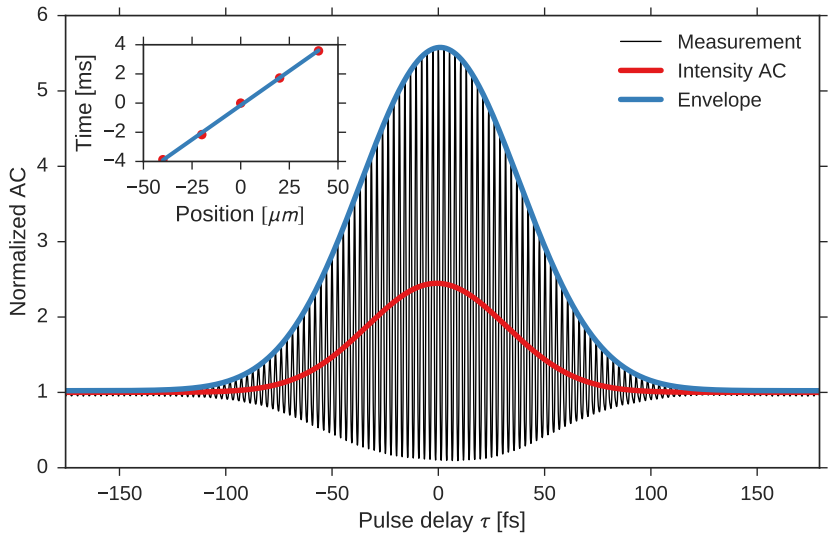

Figure 7.2: Interferometric autocorrelation measurement of Mira fs pulses. The autocorrelation trace is measured on an oscilloscope and the time axis is converted into position of the scanning mirror of the Michelson interferometer, using a calibration measurement (inset). The pulse delay is then obtained by dividing the position by the speed of light. The blue and red curve are Gaussian least squares fits to the envelope and raw data (black) respectively. The red curve can also be obtained by averaging over the fast oscillations and is equivalent to the intensity autocorrelation A_0, equation (7.6). The FWHM of the red and blue fit is identical, as expected, and is 77 fs, corresponding to a close to bandwidth-limited pulse length of $0.707 \cdot 77\,\text{fs} = 55\,\text{fs}$.

7.1.2 Mira IAC measurement

Figure 7.2 shows an interferometric SHG autocorrelation measurement of the Mira fs laser pulses, when group velocity dispersion (GVD) is well compensated, such that the pulses are close to bandwidth limited. The signal to background ratio is not the ideal ratio of 8 : 1, probably due to imperfect alignment. The autocorrelation trace is measured on an oscilloscope while the delay stage is periodically moved back and forth at about 10 Hz. The scope time axis is converted into position of the scanning mirror of the Michelson interferometer, using a calibration measurement shown as an inset in figure 7.2. The calibration is obtained by moving the position of the corner cube (CC 1) by a known amount, and observing the shift of the AC signal in time on the oscilloscope. The pulse delay is then obtained by dividing the position by the speed of light. A Gaussian least squares fit to the raw data is equivalent to averaging over the fast oscillations, and corresponds to the intensity autocorrelation A_0, equation (7.6). The FWHM is expected to be identical to the FWHM of the envelope, and is 77 fs which corresponds to a pulse length of

$$\tau_{\text{ICA}} = 0.707 \cdot 77\,\text{fs} = 55\,\text{fs}\,, \tag{7.11}$$

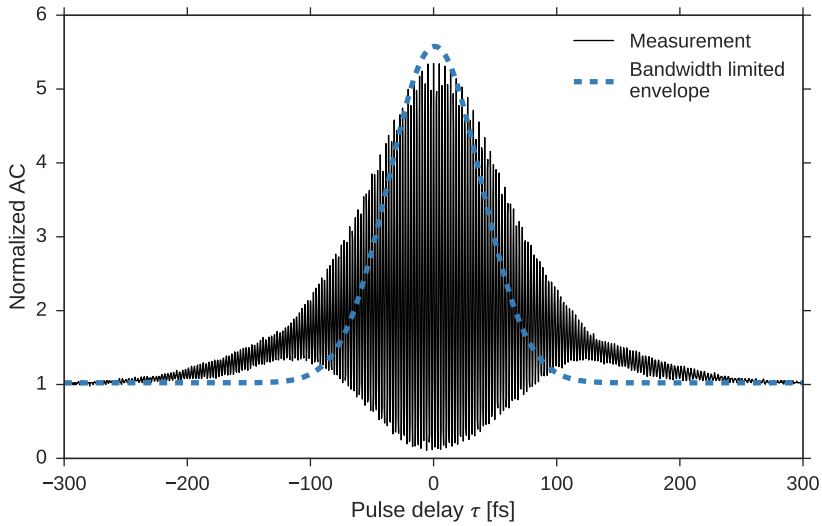

Figure 7.3: Interferometric autocorrelation measurement of Mira fs pulses without GVD compensation. Compare with figure 7.2, showing a bandwidth-limited pulse measurement.

where the factor 0.707 relates the FWHM of the AC signal to the underlying signal width, in case of a Gaussian envelope. This should be compared with the bandwidth limed pulse length obtained from the spectrum, shown in chapter 4.4, figure 4.11b, with a width of 8.3 THz for this autocorrelation measurement. For a Gaussian envelope, the time-bandwidth product gives a pulse length of

$$\tau_{\mathrm{BWL}} = 0.441/8.3\,\mathrm{THz} = 53\,\mathrm{fs}\,, \tag{7.12}$$

very close to the measured pulse length, indicating almost perfect GVD compensation. This is confirmed by the FROG measurements in the following section.

For comparison, figure 7.3 shows an interferometric autocorrelation measurement of Mira fs pulses when the external dispersion compensation is bypassed. The pulse is broadened and chirped, qualitatively observable from the very different shape of the trace. As discussed, the exact pulse shape and phase cannot be indistinguishably determined using autocorrelation, which is why I ultimately used frequency resolved optical gating (FROG) for pulse characterization, as described in the next section.

7.2 Frequency resolved optical gating

A sketch of a second harmonic generation FROG [A90, A91, B10, R21], is depicted in figure 7.1. An unknown laser pulse is split by a beam splitter into two paths of similar length. One arm of the interferometer is adjustable in length and the two pulses are focused in a SHG crystal. The resulting pulse with second harmonic wavelength is sent into a spectrometer, and the length of the adjustable

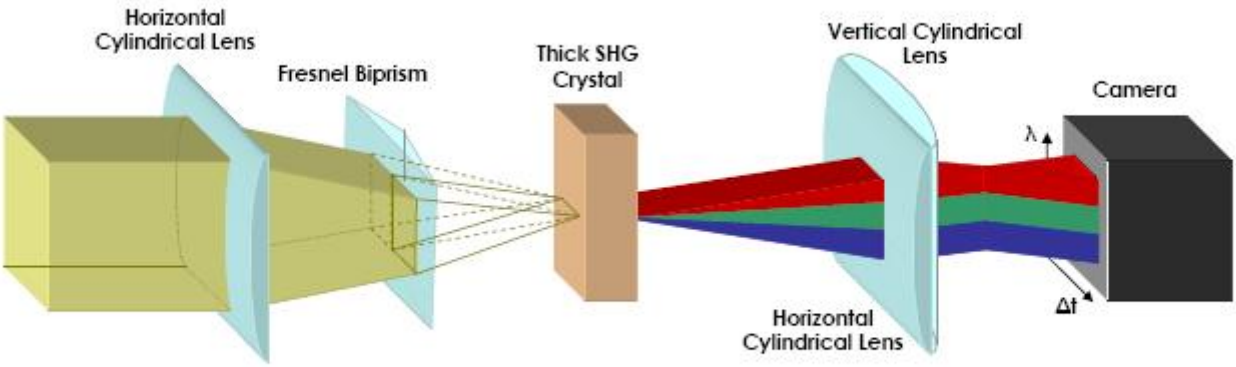

Figure 7.4: Scheme of a GRENOUILLE. Compared to the FROG, the beam splitter, delay stage, and beam recombination elements are replaced by a prism, and the thin SHG crystal and spectrometer are replaced by a thick SHG crystal plus a CCD camera. This setup is cheaper, more compact, highly insensitive to the beam alignment. Image by Patrick A. Berry, 2005 [X2]

delay stage is swept continuously. The setup is basically identical to an intensity autocorrelator, with the photo-detector replaced by the spectrometer.

The same information can be gained in an experimentally easier to implement, and more robust setup, the GRENOUILLE[1], sketched in figure 7.4 [A92, A93]. In the GRENOUILLE, the beam splitter, delay stage, and beam recombination elements of the FROG are replaced by a prism, and the thin SHG crystal and spectrometer are replaced by a thick SHG crystal plus a CCD camera. This setup is cheaper, more compact, and more importantly, highly insensitive to the beam alignment, which makes it easy and reliable to operate.

The gained information, as for the FROG, is usually displayed in a two dimensional contour plot, with time-delay on one axis, wavelength or frequency on the other axis, and the measured intensity encoded in color, as plotted in figure 7.5a.

This 2-d image is then iteratively compared with an image calculated (figure 7.5b) from a hypothetical laser pulse, resulting in the measured image. The algorithm to find the pulse resulting in the measured FROG trace is described in ref. [R21]. In short, the electric field of the pulse, i.e. intensity and phase as functions of time, must comply with two constraints. The first is the so called *data constraint*, that means the pulse must generate the measured FROG trace. The second constraint is the *mathematical form constraint*, that means the pulse must be compatible with the known second harmonic generation process. Start-

[1] Grenouille is the French word for frog, and stands for *Grating-eliminated no-nonsense observation of ultrafast incident laser light e-fields.*

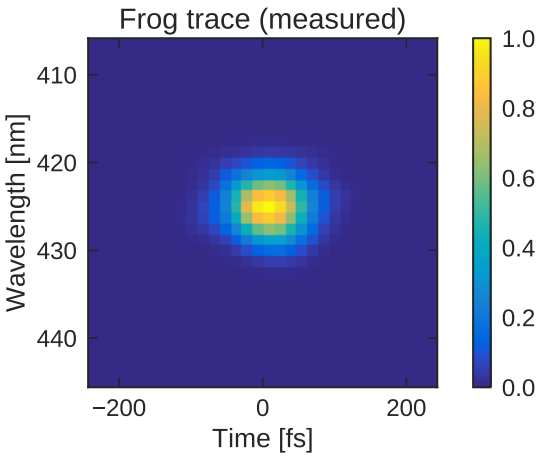

(a) Experimentally measured FROG trace.

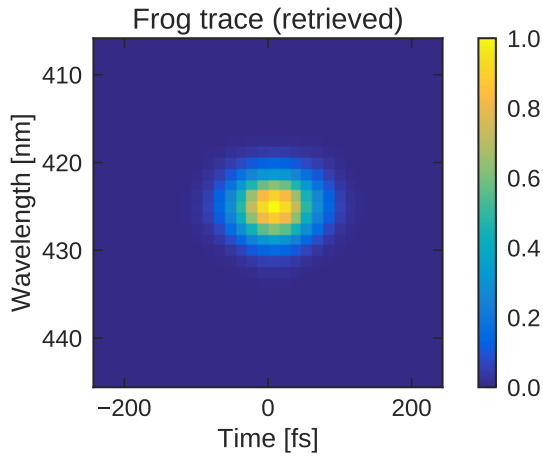

(b) Calculated trace as retrieved by the FROG algorithm.

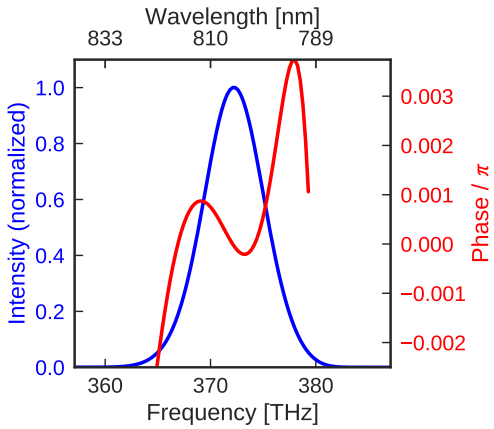

(c) Retrieved spectral intensity and phase.

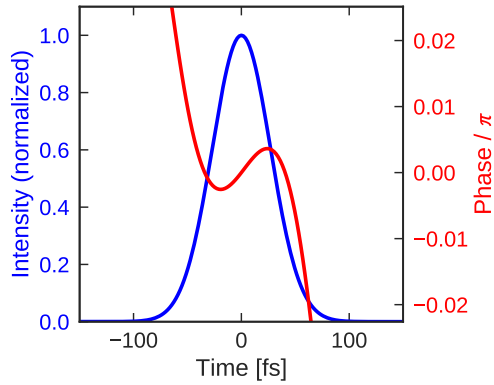

(d) Retrieved temporal intensity and phase.

Figure 7.5: Measured and retrieved FROG traces of the Mira pulses, together with the underlying spectral and temporal intensity and phase. The almost constant spectral phase demonstrates almost perfect GVD compensation.

ing from an initial pulse guess, the method of generalized projections is used, to find the pulse matching both constraints. The information contained in a FROG image is a two dimensional array, leading to a largely overdetermined set of equations. This makes FROG very robust, and allows to check for consistency using all the information in the image.

Figure 7.5c and 7.5d show the retrieved spectral and temporal intensity and phase for the Mira laser with GVD compensation. the pulses are close to bandwidth-limited, as can be seen from the almost constant phase $\phi \ll \pi$. The most significant residual contribution to the phase stems from higher order dispersion, not GVD. The retrieved spectral width is slightly narrower than what is measured with a dedicated spectrometer, as shown in chapter 4.4, and the temporal pulse length of 62.7 fs appears slightly longer than the 55 fs measured using interferometric autocorrelation in the previous section. However, the agreement within about 10 % is satisfying.

The GRENOUILLE we are using is a Swamp Optics model 8-20-USB, specified for pulse lengths between 20 fs and 200 fs. I tried to measure the Menlo comb using this device, but the SHG light is not enough to calculate the FROG trace. This suggests that the Menlo pulses are longer than 200 fs, which is expected from the fiber components with large GDD in the Menlo system, as described in chapter 4.1. For the same reason, we were unable to retrieve an autocorrelation measurement for the Menlo light.

Part III

Experiments with Ca^+: High Precision Spectroscopy and Isotope Shifts

I cannot define the real problem, therefore I suspect there's no real problem, but I'm not sure there's no real problem.

Richard Feynman

8 Systematic Shifts in Ion Traps

In this chapter, I will discuss systematic effects perturbing the high precision spectroscopy measurements presented in chapter 13. Systematic frequency shifts in ion traps have been extensively studied experimentally [A94, A95, R22] as well as theoretically [A96, A97]. The main interest often is to implement a frequency standard based on an optical transition in a single trapped ion. One candidate is the $^{40}Ca^{+}$ $|S_{1/2}\rangle \rightarrow |D_{5/2}\rangle$ "clock" transition at 411 THz [A88, A98, R23]. The goal in accuracy of such a clock is often stated to be 1×10^{-18}, implying that systematic shifts need to be controlled better than 1 mHz. For the D-finestructure transition in Ca^{+} at 1.8 THz, with our current experimental statistical uncertainties on the 10 Hz level, we reach a relative precision of about 5×10^{-12}. As we will see in the following sections, only the second order Zeeman shift is relevant on this level of precision, while many other effects contribute only to negligible shifts.

8.1 Zeeman shift

When an atom is exposed to an external magnetic field, its energy levels are perturbed by the Zeeman effect. For the calcium ion in our Paul trap, we are interested in the shift caused by the applied magnetic field of about 6.5 G, a weak field compared to the atom's internal magnetic field. In this case, the external magnetic field can be treated by perturbation theory with the zero order states being the ones found in the LS coupling approximation.

In the following, I will calculate the first order energy shift, the well known linear Zeeman shift $E^{(1)}$, and the second order Zeeman shift $E^{(2)}$, sometimes also referred to as the quadratic Zeeman shift. The perturbation Hamiltonian can be written as [B11]

$$H_M = B\frac{\mu_B}{\hbar}\left(L_z + g_s S_z\right) . \tag{8.1}$$

The zero order states are given by the quantum numbers $|n\,l\,j\,m_j\rangle$. These states are not eigenstates of H_M, so that we need a few steps to evaluate the matrix elements. For the following equations, I will start with the approximation for the spin g-factor $g_s = 2$.

8.1.1 Linear Zeeman shift

For the first order term, we evaluate

$$E^{(1)} = \langle n\,l\,j\,m_j|H_M|n\,l\,j\,m_j\rangle \ . \tag{8.2}$$

J_z can be expressed as $J_z = L_z + S_z$ (for $g_s = 2$), and we can rewrite H_M as

$$H_M = B\frac{\mu_B}{\hbar}\left(J_z + S_z\right) , \tag{8.3}$$

so that the first term in (8.2) is trivially evaluated to

$$E^{(1)} = B\mu_B m_j + B\mu_B \langle n\,l\,j\,m_j|S_z/\hbar|n\,l\,j\,m_j\rangle \ . \tag{8.4}$$

To calculate the expectation value of S_z, we need to express our states as linear combinations of eigenstates of m_s. We know that $s = 1/2$ and $j = l \pm 1/2$, with $m_j = m_l + m_s$. These linear combinations are then

$$\begin{aligned}
|j = l + 1/2, m_j\rangle = &+ \left(\frac{l + 1/2 + m_j}{2l+1}\right)^{1/2} |m_l = m_j - 1/2, m_s = +1/2\rangle \\
&+ \left(\frac{l + 1/2 - m_j}{2l+1}\right)^{1/2} |m_l = m_j + 1/2, m_s = -1/2\rangle \\
|j = l - 1/2, m_j\rangle = &- \left(\frac{l + 1/2 - m_j}{2l+1}\right)^{1/2} |m_l = m_j - 1/2, m_s = +1/2\rangle \\
&+ \left(\frac{l + 1/2 + m_j}{2l+1}\right)^{1/2} |m_l = m_j + 1/2, m_s = -1/2\rangle \ .
\end{aligned} \tag{8.5}$$

In this basis, it is now straight forward to evaluate (8.4) since

$$S_z\,|n\,l\,m_l\,m_s\rangle = \hbar m_s\,|n\,l\,m_l\,m_s\rangle \ , \tag{8.6}$$

and, after simplifying the result, we find

$$E^{(1)} = g_j B\mu_B m_j \, , \tag{8.7}$$

where g_j is the so-called Landé g-factor

$$g_j = \frac{2j+1}{2l+1} \, . \tag{8.8}$$

If we instead carry through the exact spin g-factor $g_s \neq 2$, the exact Landé g-factor becomes

$$g_j = \frac{2j + (g_s - 1)}{2l+1} = 1 \pm \frac{g_s - 1}{2l+1} \, , \tag{8.9}$$

for $j = l \pm 1/2$. We see that the linear Zeeman effect lifts the m_j degeneracy, and splits each finestructure level into $2j+1$ Zeeman sub-states each, separated by the Zeeman splitting

$$\Delta\nu_Z = g_j B\mu_B/h \, . \tag{8.10}$$

Table 8.1: Linear Zeeman shift for Calcium. Given are approximate Landé g-factors (8.8), Zeeman splittings (8.10) per Gauss, as well as Zeeman splittings for our typical magnetic field of 6.5 G.

State	g_j approx.	$\Delta\nu_Z$[MHz/G]	$\Delta\nu_Z$[MHz/6.5 G]
$S_{1/2}$	2	2.802	18.22
$P_{1/2}$	2/3	0.934	6.072
$P_{3/2}$	4/3	1.867	12.14
$D_{3/2}$	4/5	1.120	7.282
$D_{5/2}$	6/5	1.680	10.92

Approximate values for the Landé g-factor (8.8) and the Zeeman splitting per Gauss for the relevant states of the calcium ion are summarized in table 8.1. The spectroscopy on the $|S_{1/2}\rangle \rightarrow |D_{5/2}\rangle$ and $|D_{5/2}\rangle \rightarrow |D_{3/2}\rangle$ transitions, as presented in chapter 11 and 13, is Zeeman resolved.

8.1.2 Second order Zeeman shift

The second order Zeeman shift is calculated via second order perturbation theory as

$$E_\beta^{(2)} = \sum_{\beta\neq\gamma} \frac{\left|\langle\beta^0|H_M|\gamma^0\rangle\right|^2}{E_\beta^{(0)} - E_\gamma^{(0)}}\,, \tag{8.11}$$

where β, γ each represent one state $|n\,l\,j\,m_j\rangle$. We use the linear combinations (8.5) to evaluate this expression for the D-finestructure states $\beta = |n = 3, l = 2, j = l \pm 1/2, m_j\rangle$ and find

$$E_{D5/2}^{(2)} = \frac{\frac{1}{25}\left(5/2 - m_j\right)\left(5/2 + m_j\right)}{\Delta E_{DD}}(B\mu_B)^2\,, \tag{8.12}$$

and

$$E_{D3/2}^{(2)} = -E_{D5/2}^{(2)}\,. \tag{8.13}$$

This result only depends on m_j. States with the same m_j within the finestructure doublet mix and repel each other in energy, so that we get a positive shift of the D-finestructure transition. Note that the $|D_{5/2},\, m_j = \pm 5/2\rangle$ states do not experience a second order shift, since there is no state to couple to in the $D_{3/2}$ manifold. In the same sense, the $|S_{1/2}\rangle$ states do not experience a second order Zeeman shift, since the interaction Hamiltonian (8.3) only mixes states with the same j and m_j value.

The frequency shift of the $D_{5/2}$ levels can be written in a simplified form as

$$\begin{aligned} \Delta\nu_{Z2} &= \frac{6}{25}K \quad \text{for m } = \pm 1/2 \\ \Delta\nu_{Z2} &= \frac{4}{25}K \quad \text{for m } = \pm 3/2 \\ \Delta\nu_{Z2} &= 0 \qquad \text{for m } = \pm 5/2 \end{aligned} \tag{8.14}$$

with

$$K = \frac{\mu_B^2}{h^2\nu_{DD}}B^2\,, \tag{8.15}$$

where ν_{DD} is the D-finestructure splitting frequency. This expression was used by other authors to calculate the second order Zeeman shift in $^{88}Sr^+$ [A99, sec. E] [A94, sec. F]. For Ca^+ we calculate

$$\begin{aligned} \Delta\nu_{Z2} &= 258\,\mathrm{mHz\,G^{-2}} \quad \text{for m } = \pm 1/2 \\ \Delta\nu_{Z2} &= 172\,\mathrm{mHz\,G^{-2}} \quad \text{for m } = \pm 3/2 \end{aligned} \tag{8.16}$$

and for a typical magnetic field in our trap of $B = 6.5\,\mathrm{G}$:

$$\begin{aligned} \Delta\nu_{Z2} &= 10.9\,\mathrm{Hz} \quad \text{for m } = \pm 1/2 \\ \Delta\nu_{Z2} &= 7.28\,\mathrm{Hz} \quad \text{for m } = \pm 3/2\,. \end{aligned} \tag{8.17}$$

Note that these shifts have to be added to those of the $|D_{3/2}\rangle$ state for fine-structure transitions where both levels are shifted. For the $|D_{5/2}, m = \pm 1/2\rangle \rightarrow |D_{3/2}, m = \pm 1/2\rangle$ and $|D_{5/2}, m = \pm 3/2\rangle \rightarrow |D_{3/2}, m = \pm 3/2\rangle$ transitions, we get the total shifts of

$$\Delta\nu_{Z2}(D_{5/2}, m = \pm 1/2) - \Delta\nu_{eq}(D_{3/2}, m = \pm 1/2) = +21.833(31)\,\mathrm{Hz} \tag{8.18}$$

$$\Delta\nu_{Z2}(D_{5/2}, m = \pm 3/2) - \Delta\nu_{eq}(D_{3/2}, m = \pm 3/2) = +14.555(21)\,\mathrm{Hz}\,, \tag{8.19}$$

where the error is conservatively estimated based on a long term stability of the magnetic field of better than 10^{-3}.

8.2 Electric quadrupole shift

The electric quadrupole moment originates from a deviation of the charge distribution from spherical symmetry. The interaction of a given state's atomic electric quadrupole moment with an electric quadrupole field introduces a frequency shift $\Delta\nu_{eq}$ of typically a few Hertz in ion traps [A95]. More precisely, the shift of a magnetic sub-state $|D_j, m_j\rangle$ is given by

$$\hbar\Delta\nu_{eq} = \frac{1}{4}\frac{dE_z}{dz}\Theta\left(D, j\right)\frac{j(j+1) - 3m_j^2}{j(2j-1)}\left(3\cos^2\beta - 1\right), \tag{8.20}$$

where $\frac{dE_z}{dz}$ is the electric field gradient along the field's symmetry axis z, β is the angle between the quantization axis (magnetic field) and z, and $\Theta\left(D, j\right)$ is the quadrupole moment in terms of the reduced quadrupole matrix element [A95, A96]. For the S-D clock transition, the shift is solely due to the shift of the D level, since the S level is spherically symmetric and therefore does not experience this shift.

The Ca^+ quadrupole moment was experimentally measured to be $\Theta\left(3d, 5/2\right) = 1.83(1)\,ea_0^2$, where e is the elementary electric charge, and a_0 is the Bohr radius [A95]. Theoretical values are [A97]

$$\begin{aligned} \Theta\left(3d, 3/2\right) &= 1.289(11)\,ea_0^2 \\ \Theta\left(3d, 5/2\right) &= 1.849(17)\,ea_0^2 \end{aligned} \tag{8.21}$$

and other authors calculate less precise but similar values [A100, A101, A102].

The electric potential in the center of a quadrupole ion trap can be written as [A103]

$$\phi = (Q_{DC} + Q_{AC}\cos\Omega t)\left(x^2 + y^2 - 2z^2\right)$$

where Q_{DC} and Q_{AC} are the constant, and time varying field components, respectively, Ω is the RF frequency and z is the symmetry axis of the trap. The electric field gradient then becomes

$$\frac{dE_z}{dz} = \frac{d^2\phi}{dz^2} = Q_{DC}. \tag{8.22}$$

We can calculate Q_{DC} based on the trap frequency ω_z

$$Q_{DC} = \omega_z^2 \frac{m}{e}, \tag{8.23}$$

where e is the electron charge and m is the mass of the ion. For $^{40}Ca^+$ and the trap frequency $\omega_z = (2\pi)\,509.1\,\mathrm{kHz}$, I calculate

$$Q_{DC} = \frac{dE_z}{dz} = 4.24 \times 10^6\,\mathrm{V\,m^{-2}}, \tag{8.24}$$

which results in an electric quadrupole shift of

$$\begin{aligned}
\Delta\nu_{eq}(D_{3/2},\, m_j = \pm 1/2) &= -5.810\,\mathrm{Hz}\\
\Delta\nu_{eq}(D_{3/2},\, m_j = \pm 3/2) &= +5.810\,\mathrm{Hz}\\
\Delta\nu_{eq}(D_{5/2},\, m_j = \pm 1/2) &= -6.599\,\mathrm{Hz}\\
\Delta\nu_{eq}(D_{5/2},\, m_j = \pm 3/2) &= -1.650\,\mathrm{Hz}
\end{aligned}$$

and thus a total shift of the $|D_{5/2},\, m_j = \pm 1/2\rangle \rightarrow |D_{3/2},\, m_j = \pm 1/2\rangle$ and $|D_{5/2},\, m_j = \pm 3/2\rangle \rightarrow |D_{3/2},\, m_j = \pm 3/2\rangle$ transitions of

$$\begin{aligned}
\Delta\nu_{eq}(D_{5/2}, m_j = \pm 1/2) - \Delta\nu_{eq}(D_{3/2}, m_j = \pm 1/2) &= -0.789\,\mathrm{Hz}\\
\Delta\nu_{eq}(D_{5/2}, m_j = \pm 3/2) - \Delta\nu_{eq}(D_{3/2}, m_j = \pm 3/2) &= -7.460\,\mathrm{Hz}\,.
\end{aligned} \tag{8.25}$$

8.3 Black body radiation

Black body radiation (BBR) emitted by the environment of the ion in the trap causes additional shifts. The spectrum of BBR at room temperature is mostly far in the infrared, so that this field can be treated as almost constant in time for optical transitions. The time averaged BBR electric field E and magnetic field B squared can be approximated as [A104]

$$\langle E^2(t)\rangle = \left(831.9\,\mathrm{V\,m^{-1}}\right)^2 \left(\frac{T(K)}{300}\right)^4, \tag{8.26}$$

and

$$\langle B^2(t)\rangle = (2.8\,\mu\mathrm{T})^2 \left(\frac{T(K)}{300}\right)^4, \tag{8.27}$$

where $T(K)$ is the temperature in Kelvin. Shifts are then calculated based on the (DC) second order Stark, and second order Zeeman effect [A105, A106, A99, R24].

8.3.1 Electric field contribution

The electric field BBR shift can be expressed in terms of the static electric dipole polarizability α_0 and the electric field squared from (8.26) as

$$\Delta\nu_{BBR} \approx -\frac{1}{2}\langle E^2(t)\rangle\alpha_0\,. \tag{8.28}$$

Calculations predict the polarizabilities of the D_j states in $^{40}Ca^+$ to be [A105]

$$\begin{aligned}\alpha_0(D_{3/2}) &= 32.0(3)a_0^3\\ \alpha_0(D_{5/2}) &= 31.8(3)a_0^3\quad .\end{aligned} \tag{8.29}$$

At room temperature ($T = 300\,\mathrm{K}$), the shift of each D_j level is

$$\begin{aligned}\Delta\nu_{BBR}(D_{3/2}) &\approx -276(3)\,\mathrm{mHz}\\ \Delta\nu_{BBR}(D_{5/2}) &\approx -274(3)\,\mathrm{mHz}\quad ,\end{aligned} \tag{8.30}$$

and the differential shift

$$\Delta\nu_{BBR}(D_{5/2}) - \Delta\nu_{BBR}(D_{3/2}) = 2(4)\,\mathrm{mHz}\,, \tag{8.31}$$

vanishes within the uncertainty. Even if we consider that the trap electrodes might be warmer due to the RF power dissipation, we only get a factor of $\left(4/3\right)^4 \approx 3$ higher shift for a 400 K environment. Note that α_0 is usually given in cgs units and can be converted to SI units via

$$\alpha_0(SI) = \alpha_0(cgs)\cdot a_0^3\cdot 4\pi\epsilon_0\,, \tag{8.32}$$

where a_0 is the Bohr radius and ϵ_0 is the vacuum permittivity.

8.3.2 Magnetic field contribution

Evaluating equation (8.27) for a temperature of 400 K results in an averaged magnetic field squared of $2.5\times10^{-3}\,\mathrm{G}^2$. This results in a negligible, sub-mHz second order Zeeman shift (8.15) for our Ca^+ D-finestructure transitions.

8.4 Relativistic shifts

The relativistic Doppler shift is given by

$$\frac{\Delta\nu_D}{\nu} = \frac{1}{\gamma\left(1-\frac{v_{||}}{c}\right)} - 1\,, \tag{8.33}$$

where $\gamma = 1/\sqrt{1-v^2/c^2}$, and can be approximated for $v \ll c$ to

$$\frac{\Delta\nu_D}{\nu} \approx \frac{v_{||}}{c} - \frac{v^2}{2\,c^2} + \mathcal{O}\left(v^3\right)\,. \tag{8.34}$$

8.4.1 Linear Doppler shift

A linear motion of the ion along the trap axis with velocity $v_{||}$ could be caused by slow charging or electric potential changes in the trap [R22], and would lead to a linear Doppler shift of

$$\frac{\Delta\nu_{D1}}{\nu} = \frac{v_{||}}{c}\,. \tag{8.35}$$

A constant motion of $1\,\mu\mathrm{m\,s^{-1}}$, an very high upper limit, which would be easily observable on the CCD camera, would only lead to a negligible relative shift of 3.3×10^{-15}.

8.4.2 Second order Doppler shift

The second term in (8.33) is independent of the direction of the motion and reflects the relativistic time dilation the ion experiences in the moving reference frame. For the harmonic motion in the trap, the second order Doppler shift can be expressed in terms of the ion's temperature as [R25, eq. 29]

$$\frac{\Delta\nu_{D2}}{\nu} = -\frac{E_K}{mc^2} = -\frac{3}{2}k_B T\frac{1}{mc^2}\,, \tag{8.36}$$

which results in a negligible relative shift of $-3.5 \times 10^{-15}\,\mathrm{K^{-1}}$ for $^{40}\mathrm{Ca}^+$.

Excess micromotion could theoretically lead to high average ion velocities, causing significant second order Doppler shifts [A3, R25, A107]. However, micromotion can be well compensated for a single ion, as used in our experiments. Micromotion along the Doppler cooling laser direction is easily detected by observing fluorescence oscillations when the imaging system is gated at the trap RF frequency. Axial micromotion can be extremely well compensated by observing the relative strength of RF sidebands on the well resolved 729 nm transition [T3]. Both aforementioned methods are not directly sensitive to a hypothetical motion of the ion along the vertical direction, towards the imaging system and perpendicular to the 729 nm laser. However, all motional directions are coupled for larger motional amplitudes due to the nonharmonic trapping potential, leading to a motion along one of the directions we are sensitive to. In total, we evaluated all micromotion related second order Doppler shifts to smaller than 10^{-15} in our experiments. During this evaluation, we also bound the Stark shift, caused by the trapping potential for an ion displaced from the RF-null to be negligible in our setup.

8.4.3 Gravitational shift

The gravitational shift on the earth's surface for small height changes Δh is given by

$$\frac{\Delta\nu}{\nu} = \frac{g\Delta h}{c^2} = 1.1 \times 10^{-16}\,\mathrm{m^{-1}}\,, \tag{8.37}$$

where $g = 9.82\,\mathrm{m\,s^{-1}}$ is the local acceleration due to gravity. Experimentally, a shift due to a change in height of 1 m has been demonstrated to be measurable using two Al^+ clocks [R22].

In our laboratory, we use a GPS referenced clock, as described in chapter 5, thereby taking the location of the clock into account, and rendering this shift negligible for our measurements.

8.5 Frequency reference

One major source of systematic error is our GPS disciplined rubidium clock, used as frequency reference for all optical transition measurements. This frequency standard is analyzed in detail in chapter 5, and turns out to be the main limiting factor in total accuracy. However, this is a technical issue and not a fundamental limitation of the methods presented in this thesis.

8.6 Light shifts

Residual light on the ion during spectroscopy leads to light shifts due to off-resonant coupling to other states in the atom. While running experiments, we turn off the room lights and other light sources in the room, as well as the ion gauge in the vacuum chamber, which produces IR radiation due to its heated filament. Most important, however, is to block all other lasers while exposing the ion to the spectroscopy laser. In the following, I discuss how potential light shifts, of each laser used in the experiment, are avoided or quantified.

8.6.1 866 nm and 854 nm repumpers

For the repumpers at 866 nm and 854 nm, described in chapter 9.2.5, mechanical shutters[1] directly on the laser table perfectly block the beam to the trap fibers after initial Doppler and sideband cooling, thus not contributing to any light shifts.

8.6.2 397 nm Doppler cooling laser

The 397 nm Doppler cooling laser is shuttered via a double-passed AOM with an extinction ratio of below 6×10^{-6}. In the worst case scenario, the residual light leads to an Autler-Townes splitting [A108] on the order of the Rabi frequency of the $|S_{1/2}\rangle \rightarrow |P_{1/2}\rangle$ transition. Since we usually operate the Doppler cooling laser at the saturation intensity of the $|S_{1/2}\rangle \rightarrow |P_{1/2}\rangle$ transition, the Rabi frequency will be on the same order as the 22 MHz linewidth. With the AOM shut off, the residual shift of the $|S_{1/2}\rangle$ states will be well below the 1 kHz level, negligible for spectroscopy with the 729 nm laser, as discussed in chapter 11. For the frequency comb spectroscopy, light shifts are negligible due to the large detuning from any transition involving one of the D-finestructure states.

8.6.3 729 nm spectroscopy laser

During frequency comb spectroscopy, the 729 nm laser needs to be blocked after preparing the $|D_{5/2}\rangle$ state. The laser is shuttered by a double-passed AOM,

[1] Uniblitz LS2

with a measured extinction ratio of 1×10^{-6}, and the quadrupole nature of the $|S_{1/2}\rangle \rightarrow |D_{5/2}\rangle$ transition results in negligible, sub-Hertz light shifts for light leaking through the turned off AOM. Additionally, we use a wavelength low-pass filter, as characterized in chapter 4.4.1, to block any light above 835 nm, possibly emitted by the tapered amplifier of the 729 nm laser system, which could couple on one of the D-P dipole allowed transitions.

8.6.4 866 nm light shift laser

The most delicate issue is the 866 nm light shift laser. This laser is used *during* frequency comb spectroscopy, as explained in chapter 13, hence it cannot be blocked with a slow mechanical shutter as the two repump lasers. It can, however, be completely ignored for spectroscopy on the $|S_{1/2}\rangle \rightarrow |D_{5/2}\rangle$ transition, where the frequency comb is not involved, and the 866 nm light shift laser is turned off, or is mechanically blocked. When the laser is turned on, using two separate AOMs in succession, the differential light shift on the D-finestructure transition was measured to ≈ 1 kHz per μW of power before the trap chamber, for a detuning of 2 GHz to the 866 nm repump transition. The extinction ratio of the AOMs was measured to be below 3×10^{-6}, and the maximum power on the trap table is reduced using ND filters to below 100 μW, resulting in sub-Hertz residual light shifts.

To verify that this laser has no effect on the D-finestructure spectroscopy, we compare the D-finestructure frequency measured for two different experiments; One with the 866 nm light shift laser detuned by +1 GHz, and one with a detuning of −1 GHz. For these measurements, the 866 nm laser was set to ≈ 10 times the laser power used in the regular spectroscopy experiments, thereby multiplying the potential, unwanted shift of the D-finestructure measurements by a factor of 10. Residual light shifts would then be visible as a discrepancy in transition frequency of the two measurements. At one fixed frequency comb power, we measured the D-finestructure transition for both 866 nm laser detunings, and the result agrees within (14 ± 41) Hz. For the real spectroscopy measurements, this value has to be downscaled by a factor of 2 for twice the detuning (2 GHz normally), another factor 2 for $\pm$ detuning, and a factor of 10 for the power, resulting in an estimated residual light shift of $(14 \pm 41)\,\text{Hz}/40 = (0.3 \pm 1.0)$ Hz.

8.7 Conclusion

In conclusion, all discussed shifts, except for the second order Zeeman shift, contribute less than 1 Hz to the spectroscopy measurements. The second order Zeeman shift of +21.8 Hz on the frequency comb driven $|D_{5/2}, m = \pm 1/2\rangle \rightarrow |D_{3/2}, m = \pm 1/2\rangle$ transition will be subtracted from the experimentally determined D-finestructure frequency in chapter 13.5. The second order Zeeman shift of −7.3 Hz on the 729 nm $|S_{1/2}, m = \pm 1/2\rangle \rightarrow |D_{5/2}, m = \mp 3/2\rangle$ transition is negligible compared to the experimental uncertainty of 2 kHz, as discussed in chapter 11.

9 Experimental Setup

The presented experiments were conducted in the Ion Trap Group "Molecule Lab". This chapter gives an overview of the general setup, and highlights the parts specific to the described measurements. Section 9.1 discusses the trap setup, including the vacuum chamber with the laser beam geometry, the linear Paul trap, the atom oven and the imaging system. Special attention is given to the magnetic field configuration, and the compensation of stray fields. The following section 9.2, describes the lasers used in the experiment, apart from the frequency combs already discussed in chapter 4, highlighting the newly implemented absolute frequency referencing of the 729 nm shelving laser. Lastly, section 9.3 explains the experimental soft- and hardware control, emphasizing the new databased storage of experimental data and the level of automation reached during the last three years.

9.1 Trap table

The heart of the experiment, the linear Paul trap, is described in section 9.1.2, and is mounted in a vacuum chamber with good optical access for lasers. The chamber's geometry is detailed in section 9.1.1. Above the chamber an imaging system collects the ion's fluorescence through the top viewport for state detection, as described in section 9.1.4. Around the vacuum chamber, magnetic field coils provide a well defined quantization axis and Zeeman splitting which is discussed in section 9.1.5. No lasers are mounted directly on the trap table. Polarization optics and lenses shape the laser light, mostly arriving via optical fibers on the table. A general description of laser beam paths and their physical location is given in section 9.2.

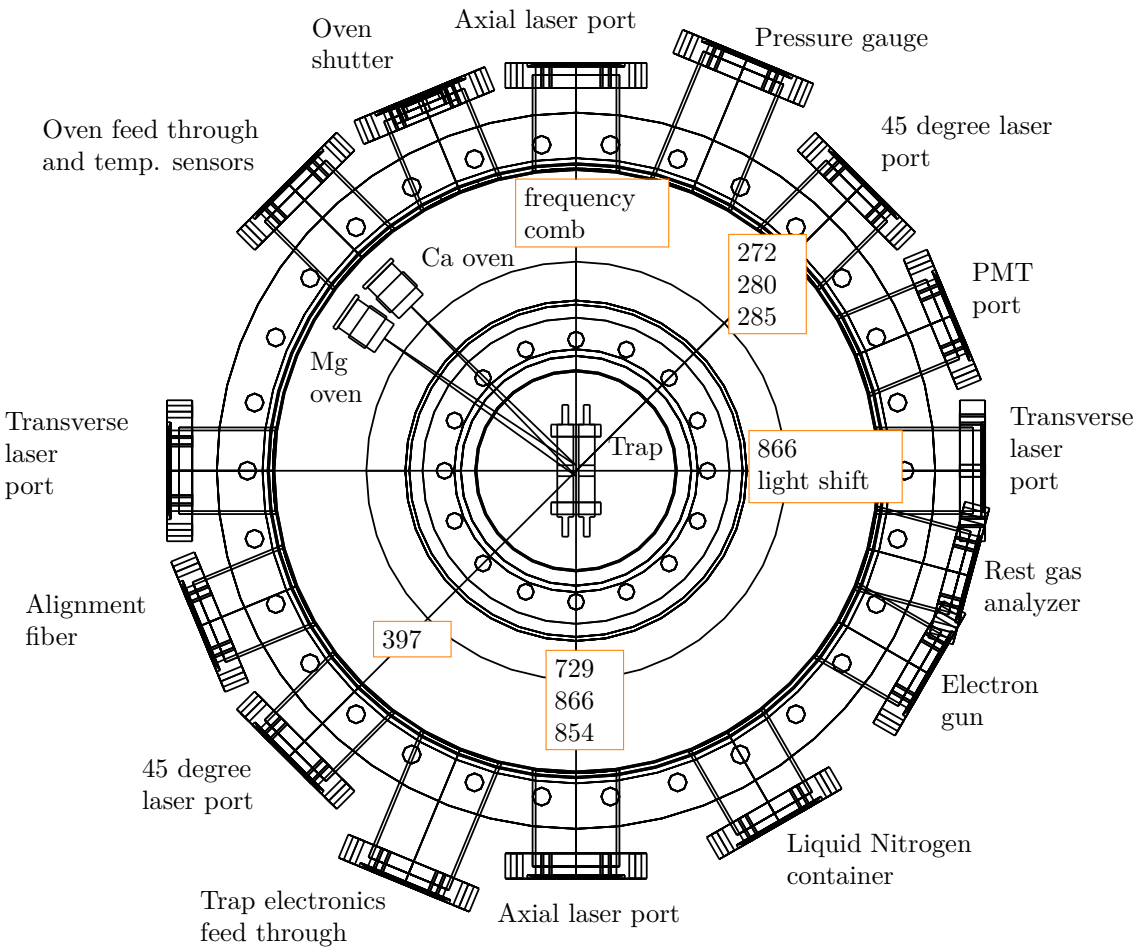

Figure 9.1: Top view of the vacuum chamber with labeled ports. The direction of the different lasers is also indicated. Graphic adapted from ref. [T6].

9.1.1 Vacuum chamber

The heart of the experiment is the vacuum chamber, housing the linear Paul trap, and granting optical access via different viewports. A schematic drawing is shown in figure 9.1. Horizontal optical access is possible via 7 viewports. The two axial ports are aligned with the trap axis, and are used for lasers interacting with the motion of the ion. This includes the 729 nm sideband cooling laser, as well as for future experiments with quantum logic spectroscopy on MgH^+ , also the frequency comb and quantum cascade laser. These future experiments are describe in chapter 15. At the moment, also the 866 nm and 854 nm repumpers are sent in via an axial port, which we might want to change in the future due of space constraints.

One of the two transverse ports is currently used by the 866 nm light shift laser, only relevant for experiments with Ca^+ involving the frequency comb.

The 45° port next to the pressure gauge[1] is used for the ionization lasers. This port is oriented 90° to the atom oven (see section 9.1.3), making the ionization process insensitive to first order Doppler broadening, and thereby enabling isotope selective loading, as explained in section 10.1.1. The second 45° laser port is used by the 397 nm Doppler cooling beam. This geometry results in a nonzero projection on all trap axes, allowing 3D Doppler cooling with a single beam. The last viewport is intended for a photomultiplier tube (PMT), not used in our current experiments. A lens is placed inside the chamber before this port to collect as many fluorescence photons as possible.

A piece of fiber on a 3D translation stage is mounted on one of the ports to help aligning new lasers. This alignment fiber simply acts as a small scattering target (125 µm diameter), which can be very precisely positioned in the known center of the trap. In this way, initial alignment of new laser beams, such as the frequency comb light[2], is simplified considerably.

The other ports are occupied by a rest gas analyzer, an electron gun, and a liquid nitrogen container, all not used in the experiments presented in this thesis. Under the table, an ion getter pump[3] is sufficient to maintain the pressure of typically 2×10^{-10} mbar in the chamber. A leak valve, which will be used to create MgH^+ , is also available. More details can be found in the thesis of Niels Kjærgaard, who designed the experiment around the year 2000 [T6, ch. 7].

9.1.2 Linear Paul trap

The linear Paul trap was designed by Niels Kjærgaard around the year 2000 [T6] (see details herein), and its geometric and typical operational parameters are listed in table 9.1. On an international scale, the trap is large, originally built to trap large Coulomb crystals with a large area where the potential can be assumed harmonic. However, the high precision measurements I conducted on single ions in this trap demonstrate its versatility.

The trap electrodes are constructed from gold-coated stainless steel rods, held in place by Macor mountings. Each rod is separated into three segments, with

[1] AML UHV Bayard-Alpert, measures typically 2×10^{-10} mbar

[2] about 1 mW of power is necessary to see the light on the CCD camera. Too high intensities might damage the fiber!

[3] Leybold IZ 270

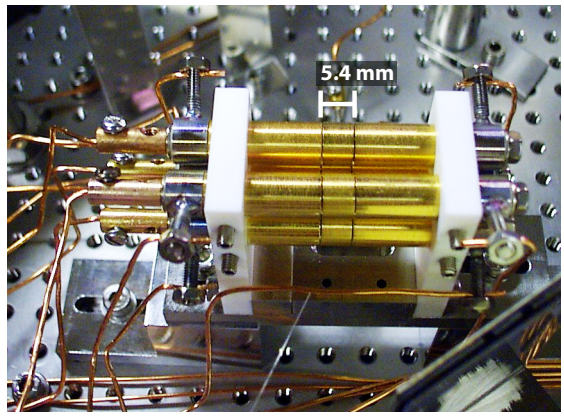

Figure 9.2: Photo of the linear Paul trap adapted from Niels Kjærgaard's thesis [T6].

Table 9.1: Geometrical and typical operational parameters of the linear Paul trap for $^{40}Ca^{+}$.

Quantity	Typical value
z_0	2.70 mm
r_0	3.50 mm
R	4.00 mm
z_e	20.00 mm
κ	0.248 mm
Ω_{RF}	$2\pi \cdot 4.682$ MHz

Quantity	Typical value
a	0.023
q	0.49
V_{end}	60 V
V_{RF}	1090 V
ω_{z}	$2\pi \cdot 509.1$ kHz
ω_{r}	$2\pi \cdot 730$ kHz

a center electrode of a length of 5.40 mm. The rods have a diameter of 8 mm, and opposite electrodes are separated by 7 mm. The resonance RC frequency is at 4.682 MHz.

The trap frequency along the trap axis can be determined via two methods. One is to pulse the Doppler cooling laser at roughly the trap frequency, thereby driving the harmonic motion of the ion. This pulsing is conveniently achieved by sending a continuous TTL square-wave to the RF switch feeding the AOM amplifier for the 397 nm laser. When we hit the resonance, the motional amplitude of the ion behaving as a driven oscillator increases to a point, where the fluorescence significantly drops due to the Doppler effect shifting the light out of resonance. This method allows to determine the trap frequency with about 100 Hz accuracy, simply by manually adjusting the pulse frequency of the Doppler cooling beam. In our trap, we find $\omega_{\mathrm{z}} = 2\pi \cdot 509.1$ kHz. A second method is driving motional sideband transitions with the 729 nm laser, with a similar accuracy as the previous method. For the radial direction, we find $\omega_{\mathrm{r}} = 2\pi \cdot 730$ kHz.

The trap electrodes are supplied by a homebuilt mixer, combining DC and RF potentials on all 12 electrodes. During the last three years, my colleague Karin Fisher developed and implemented a new programmable DC-supply, capable of

ramping the 12 DC potentials individually. Thereby, the trapping potential can be adiabatically lowered and raised during experimental sequences, which will be beneficial for future experiments with molecular ions, as detailed in Karin's thesis [T3].

9.1.3 Atom oven

The Ca^+ ions (and Mg^+ for future experiments) are produced via ionization of an effusive beam, emitted by a simple atom oven, containing a Ca sample with all naturally abundant isotopes. Typically, the Ca^+ oven[4] heating wires are supplied with a current of 5 A to heat the oven to 300 °C. Skimmers restrict the flow of neutral atoms to the center of the trap where they are isotope selectively ionized and trapped. The oven temperature is monitored by thermocouples, read out by a raspberry pi, which is continuously storing the measured temperature in our SQL database (see section 9.3.4).

9.1.4 Imaging system

The ion's fluorescence during Doppler cooling is collected on a CCD camera via an imaging system. Just above the vacuum chamber, a custom compound lens[5], mounted on a micrometer translation stage focuses the ion's fluorescence onto an image intensifier[6]. The image intensifier is gateable at sub-harmonics of the trap RF frequency to detect fluorescence modulation for micromotion compensation [R25]. A commercial photography objective[7] images the image intensifier onto a CCD camera[8]. The total magnification can be roughly calibrated using the known size of the alignment fiber, or more precisely via the distance of two ions with known trap frequency. For the measurements in this thesis, we use an imaging resolution of 0.677(3) camera pixels per µm [T3].

9.1.5 Magnetic field

State preparation on the $|S_{1/2}\rangle \rightarrow |D_{5/2}\rangle$ transition can be done using a fixed 729 nm polarization of 45° relative to the quantization axis, if the electronic levels are split by the Zeeman effect more than the total linewidth of the transition. Additionally, for sideband cooling, the Zeeman sub-states should be spaced much larger than the motional sideband frequency, to avoid overlaps between higher order sidebands of different Zeeman states. For high precision spectroscopy, a well defined and stable magnetic field is essential. Previously, our trap was equipped with only one magnetic field coil, placed on top of the imaging viewport, generating a mostly vertical magnetic field.

I improved the magnetic field setup in several ways. First of all, I replaced the old coil with a new, more sturdy one, tightly attached to the vacuum chamber, as can be seen in the photograph in figure 9.3. The coil is driven by a current

[4] Be aware of the much lower Mg^+ vapor pressure, never heat the Mg^+ oven with 5 A!

[5] About 7.5 cm distance to the ion, $f = 70$ mm, $NA = 0.28$, not transparent for Mg^+ fluorescence light!

[6] Proxitronic, BV 2581 BY-V 1N, gatable via custom electronic up to several MHz.

[7] Nikon AF Micro Nikkor 60mm f/2.8D

[8] PCO Sensicam QE, pixel size 6.45 µm × 6.45 µm

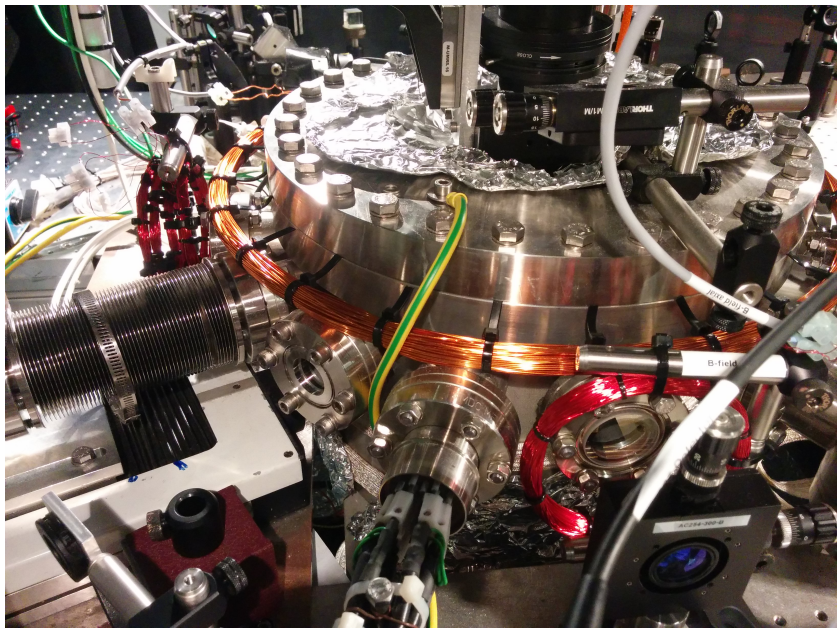

Figure 9.3: Photo of the vacuum chamber with magnetic field coils.

Table 9.2: Specifications of new magnetic field coils.

Parameter	DC quantization axis	DC compensation	AC compensation
Diameter	42 cm	10 cm	≈ 30 cm
Windings	100	400	≈ 100 mm
Distance to trap center	4.5 cm	23 cm	≈ 70 mm
max current	4 A (cable)	600 mA (coil below 40 °C)	was operated at 2 A
compensated	2.170 A (6.5 G)	454 mA (rad.) / 224 mA (ax.)	214 µA

stabilized Toellner `TOE 8852` power supply [O7], and generates a typical field of 6.5 G at the center of the trap, when supplied with 2.170 A. The wire between coil and power supply is designed to withstand approximately twice the current without becoming too hot[9]. According to table 8.1, a field of 6.5 G splits the $D_{5/2}$ states by 10.92 MHz, enough to separate the sidebands. A larger magnetic field would split the two $|S_{1/2}\rangle \rightarrow |P_{1/2}\rangle$ transitions with $\Delta m_j = 0$ for Doppler cooling more than the natural linewidth, rendering Doppler cooling with a single 397 nm laser inefficient to unfeasible.

Due to the earth's magnetic field, and stray fields in the lab, compensation coils are required to guarantee a geometrically strictly vertical quantization axis. Due to space constraints, these coils are rather small, and placed as close to the optical viewports as possible along the trap axis, and perpendicular to it, as can be seen in figure 9.3. These coils are supplied by a second, identical, 2-channel

[9]The temperature of the coils has to be monitored whenever it is increased above its current values!

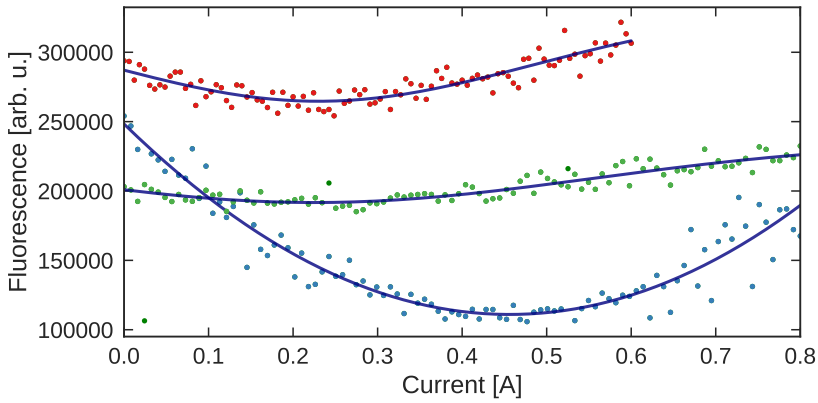

Figure 9.4: Magnetic field compensation. First, the axial compensation (red) current was scanned to find the minimum using a Gaussian fit. Then the radial compensation current (blue) was scanned to find the minimum. The process was iterated once more for the axial current (green). When the field is that well optimized, Doppler cooling does basically not work anymore and the crystal heats.

Toellner power supply.

The absolute magnetic field amplitude can easily be measured by probing two different $|S_{1/2}\rangle \rightarrow |D_{5/2}\rangle$ Zeeman transitions and using equation (8.10). The proper vertical alignment is a bit more difficult to adjust; We exploit the fact that the 866 nm laser cannot repump population on the $|D_{3/2}, m_j = \pm 3/2\rangle \rightarrow |P_{1/2}, m_j = \pm 1/2\rangle$ transition, if the laser is perfectly linearly polarized along the quantization axis. The $|D_{3/2}, m_j = \pm 3/2\rangle$ states become dark states, and do no longer fluoresce during Doppler cooling [A109].

To align the quantization axis vertically, we align and clean up the 866 nm laser polarization vertically using a Glan-Taylor polarizer with a specified extinction ratio of 100 000 : 1. Now, we scan the current in the compensation coil, and find a minimum in fluorescence of a trapped and Doppler cooled Coulomb crystal. Such a scan is plotted in figure 9.4. In an iterative process, finding the fluorescence minimum for the axial and radial compensation one after the other, the fluorescence minimum can be found with 10 mA precision. This corresponds to a magnetic field accuracy of 5 mG at a distance of 23 cm, corresponding to the center of the trap [A110, eq. 1 and 2].

Not all stray fields in the lab are static, and noise at 50 Hz, emitted by most devices and cables connected to the mains power, is still and issue. I compensate this noise along the quantization axis, by feeding a separate coil aligned on the quantization axis with a current directly derived from the mains. This current is provided by simple, homebuilt electronics, mixing the 3 phases from a 400 V socket, with variable gain after transforming each phase separately to 9 V. Thereby, the phase of the compensation current can be adjusted to the phase of the measured magnetic field noise.

The noise becomes visible during $|S_{1/2}\rangle \rightarrow |D_{5/2}\rangle$ spectroscopy, when the spectroscopy pulse is timed at different phases relative to the 50 Hz mains. Fig-

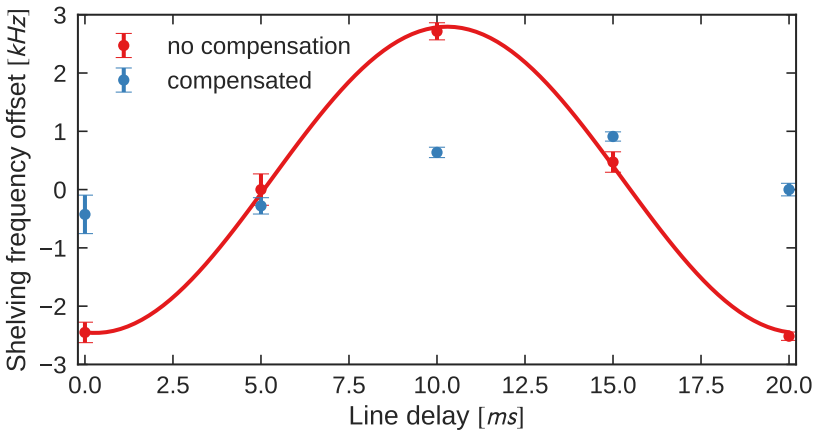

Figure 9.5: AC magnetic field compensation. The AC noise from the mains is compensated by applying a field with the same amplitude and apposite phase.

ure 9.5 shows such a spectroscopy measurement. The data plotted in red was taken without any compensation and nicely fits a 50 Hz sine wave, whereas the data in blue shows a measurement after compensation. From an initial shift on the $|S_{1/2}, m_j = -1/2\rangle \rightarrow |D_{5/2}, m_j = -5/2\rangle$ shelving transition of 5 kHz peak to peak, we compensate to less than 1 kHz. According to eq.(8.7), the shift on the shelving transition is $-2.8\,\mathrm{MHz\,G^{-1}}$, corresponding to $360\,\mu\mathrm{G/kHz}$ shift.

9.2 Laser systems

Here I describe the laser systems used in the experiments presented in this thesis, and focus on the aspects most relevant and unique for this work and point to previous theses in the Ion Trap Group when applicable.

9.2.1 Beam paths, fibers, and lab layout

No lasers are placed directly on the main experiment trap table. Instead, laser light is reaching this table via free space beam paths or optical fibers. The only laser hosted in the same laboratory as the trap is the Mira fs laser described in chapter 4.2, located on a separate optical table. This light is sent free space to the trap table, where the polarization is defined with a Glan-Taylor prism, and the laser power can be adjusted with a motorized filter ND wheel[10].

The other frequency comb, the Menlo system described in chapter 4.1, is located in a separate room across the corridor. The light from the Menlo laser is sent through the corridor in a metal tube, protecting it from air disturbances, to the Mira laser table in the Molecule Lab. In this way, parts of the beam path to the trap can be shared by the Mira and Menlo laser, especially the mechanical shutter, polarizer, and final focusing lenses.

[10] Thorlabs FW102C, 6 exchangeable filter positions, VISA compatible programming interface.

All UV lasers, i.e. 272 nm for Ca^+ ionization, 280 nm and 285 nm for Mg^+ Doppler cooling and ionization, respectively, are located on one optical table in the Main Laser Lab, next door to the Molecule Lab. Due to the lack of available optical fibers for these wavelength, we send these beams free-space via 10 cm diameter metal tubes to our trap.

The 729 nm and 397 nm lasers are also located on a separate table in the Main Laser Lab and are sent via optical fibers to the Molecule Lab. Similary, the 866 nm repump and light shift lasers, as well as the 854 nm repumper, are located on a separate table in the Main Laser Lab and sent via optical fibers. All fiber coupled lasers are also connected to the wavemeter via optical fibers.

9.2.2 Wavemeter

Most of the lasers in our lab are measured with a fiber-coupled HighFinesse wavemeter[11] with sub-MHz short terms relative accuracy and an absolute accuracy of several MHz.

The relative accuracy, i.e. the shot to shot measurement reproducibility, is smaller than the linewidth of our diode lasers (except the 729 nm laser, see section 9.2.6) and small compared to the natural linewidth of the addressed transitions in Ca^+ , which allows us to lock the lasers to the wavemeter reading. The HighFinesse wavemeter software calculates an error signal based on the wavemeter reading and the given target frequency, simulating a classical PID controller. The control signal is generated by a digital to analog converter, providing a voltage of maximal ± 10 V which can be used to feed back to the piezo actuator or current of the laser being locked.

To achieve high absolute accuracy, the wavemeter is referenced to a stabilized HeNe laser to which it recalibrates automatically once a minute. The absolute accuracy, i.e. the discrepancy between measured frequency and real light frequency, depends on the wavelength difference of measured frequency and calibration frequency. The HeNe line at 473.613 016 16 THz corresponds to ≈ 633 nm, well in the center of the most important wavelengths in Ca^+ . The measurement discrepancy at 397 nm and 866 nm is typically below 20 MHz, so that it can easily be corrected by adjusting the AOM frequencies of the corresponding laser systems.

HighFinesse provides a DLL[12] to interface to the wavemeter with external software. I implemented a data logger, storing the measured frequencies, powers etc. in a SQL database. This allows to check and verify proper operation of all lasers after measurements on the ion were taken, especially for unattended over night measurements. More details on data storage and analysis can be found in section 9.3.4.

9.2.3 Ionization

For photo-ionization of Ca^+ , we generate light at 272 nm[13] by frequency doubling the output of a fiber laser, operating at 1088 nm, to 544 nm and successive

[11] HighFinesse WS-Ultimate 2

[12] Microsoft Windows Dynamic-link library

[13] exact ionization frequencies for the different Ca^+ isotopes can be found in table A.3

frequency doubling to 272 nm in a second step. Both doubling stages are implemented as bow-tie cavities and are described in detail in ref. [A111, ch. 5.1][T7, ch. 3]. The green light at 544 nm is used to lock the fiber laser to the wavemeter while the 544 nm cavity is locked by a Pound-Drever-Hall lock [A112] and the 272 nm cavity by Hänsch-Couillaud lock [A113] to keep the cavities resonant with the corresponding fundamental light. The exact laser frequency can be controlled with MHz precision simply by dialing in the target frequency in the wavemeter locking interface. The 272 nm laser system allows isotope selective loading of Ca^+ as described in section 10.1.1.

9.2.4 Doppler cooling

The light for Doppler cooling Ca^+ at 397 nm is produced by a Toptica DL Pro diode laser system. The exact laser frequency is controlled by feeding back to the piezo using the wavemeter lock, and using feed forward on the current to prevent mode-hops. For the experiment, the light is shuttered, and shifted in frequency by an AOM in double pass configuration. The zero order light of the AOM is not dumped but instead is combined with the shifted light using a PBS, and coupled into the same fiber going to the trap table. The zero order light can be separately controlled by a Uniblitz LS2 mechanical shutter and is used for far red detuned Doppler cooling as explained in section 10.2.1.

9.2.5 Repumpers

For Doppler cooling in Ca^+ , the population from the $|D_{3/2}\rangle$ state needs to be transferred back in the 397 nm Doppler cooling cycle using a repump laser at 866 nm, and for sideband cooling, a repumper at 854 nm is needed to empty the $|D_{5/2}\rangle$ shelving level (see section 2.3.1).

Both lasers are homebuilt external cavity diode lasers, locked to the wavemeter, and shuttered and frequency shifted by AOMs. For spectroscopy, any residual light close to the measured Ca^+ transition frequency will cause unwanted light shifts, leading to systematic measurement errors, as discussed in chapter 8.6. Mechanical shutters[14] installed in the beam-paths of the repumpers allow to completely block the light during high precision measurements.

Figure 9.6 shows the population of the $D_{5/2}$ state after RAP state preparation for different wait times before state readout. The mechanical shutters are not used in this experiment, i.e. they are always open. The fit to an exponential decay gives a lifetime of the $|D_{5/2}\rangle$ state of

$$\tau_{D5/2} = 1.231(57)\,\mathrm{s}\,, \tag{9.1}$$

in agreement with the literature value of 1.168(7) s [A114]. This result shows that, even without the mechanical shutters, scattering due to light leeking through the shut off AOM is negligible. However, the mechanical shutters are an additional safety measure for spectroscopy.

[14] Uniblitz LS2 or LS6

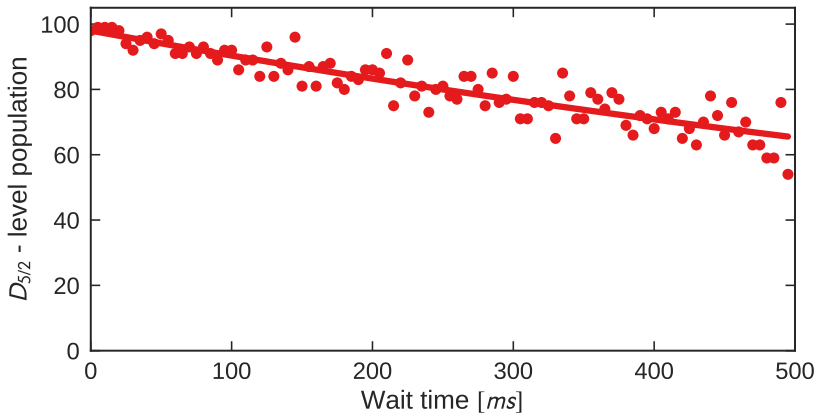

Figure 9.6: D decay thesis

9.2.6 Sideband cooling, state preparation, and $|S_{1/2} \rightarrow D_{5/2}\rangle$ spectroscopy

For sideband cooling, state preparation for the Raman experiments, and spectroscopy on the $|S_{1/2} \rightarrow D_{5/2}\rangle$ transition, a narrow and tunable light source at 729 nm is needed. We use a frequency stabilized and frequency narrowed Toptica TA Pro laser system.

An AOM in minus first order double pass configuration in the beampath to the trap is used to set the frequency and power of the light with µs precision, controlled by the PPG as described in section 9.3.2

The laser is locked to an ultra-stable high finesse cavity, described in detail in ref. [T4]. Based on direct spectroscopy on the $|S_{1/2} \rightarrow D_{5/2}\rangle$ transition in Ca^+ , and verified by a beatnote measurement with the Menlo frequency comb, the linewidth is estimated to be sub-kHz. The narrow linewidth is required for sideband cooling in order to resolve the ion's motional sidebands, and is obviously desirable for high precision spectroscopy. As described in chapter 11, the achieved linewidth of the laser is not the limiting factor for the spectroscopy. The cavity has a free spectral range of 600 MHz. The light going to the cavity is shifted with a tunable AOM by 600 MHz ± 300 MHz, allowing to tune the laser to an arbitrary frequency, independent of the cavity mode position in frequency space. This flexibility turned out extremely useful for the isotope shift measurements discussed in chapter 14.

The locking cavity is well isolated from the environment, but still shows a slow drift over time. For measurements on the ion over several hours, this drift needs to be continuously compensated. I implemented this drift compensation by continuously monitoring the laser frequency via a beatnote measurement with the Menlo frequency comb[15] and feeding back to the AOM shifting the light to the cavity. The logic is implemented in python and is also performing various checks such as making sure that the laser frequency reading on the wavemeter is

[15]The Menlo comb needs to be optically locked for this purpose to achieve the necessary absolute stability.

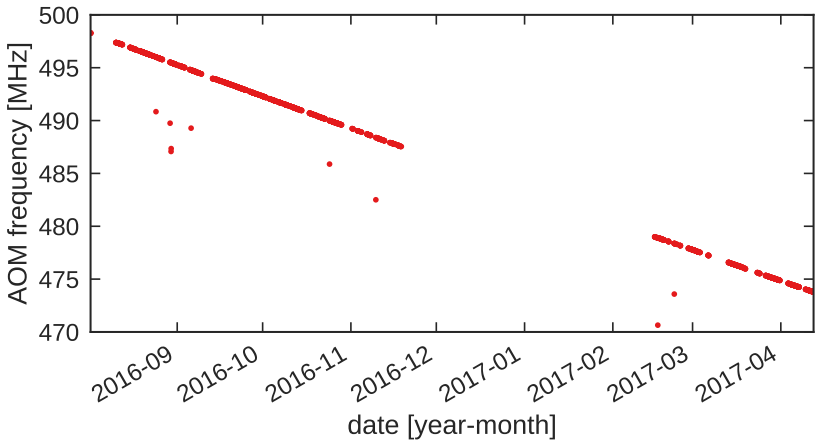

Figure 9.7: Long term 729 cavity drift in terms of the AOM frequency keeping the laser frequency stable. The average drift of the cavity is $-2.23\,\mathrm{Hz\,s^{-1}}$, or half this value for the double pass AOM frequency. Outliers are false measurements. The Menlo comb had to be sent in for repair at the end of 2016 which is why there is no data available for about 3 months.

within a reasonable range, or that the beatnote measurement shows high enough signal to noise for a reliable reading. If one of these checks fails, the software falls back to an average drift correction value of $-2.23\,\mathrm{Hz\,s^{-1}}$.[16] The AOM frequency is adjusted once every 30 s by $-2.23\,\mathrm{Hz\,s^{-1}}/2 \cdot 30\,\mathrm{s} = -33.5\,\mathrm{Hz}$, corresponding to an elongation of the cavity of

$$\frac{dL}{dt} = \frac{df}{dt}\frac{L}{c} = +1.86\,\mathrm{nm\,s^{-1}}\,. \tag{9.2}$$

This value corresponds to the average long term drift as plotted in figure 9.7. A zoom showing the drift over a few days together with the deviation from a linear model is shown in figure 9.8. The fluctuations on the order of a few kHz can be compensated via this feedback, keeping the laser stable within approximately 100 Hz.

A wavelength low pass filter, with a sharp cutoff at 835 nm is placed before the fiber-coupler to the trap table to block any light the laser might emit close to the $S_{1/2} \to D_{5/2}$ or $S_{1/2} \to D_{3/2}$ transitions, which would lead to unwanted light shifts in spectroscopy. The filter is the same model as is used for the frequency comb light, described in more detail in chapter 4.4.1.

9.2.7 Light shift laser

For the frequency comb Raman experiments, we use a laser close to the 866 nm transition to induce a light shift, essentially acting as a fast light switch, by shifting the transition in and out of resonance with the frequency comb light,

[16] $-2.23\,\mathrm{Hz\,s^{-1}} = -134\,\mathrm{Hz\,min^{-1}} = -8.0\,\mathrm{kHz\,h^{-1}} = -193\,\mathrm{kHz\,d^{-1}} = -5.8\,\mathrm{MHz\,m^{-1}} = -70.4\,\mathrm{MHz\,y^{-1}}$

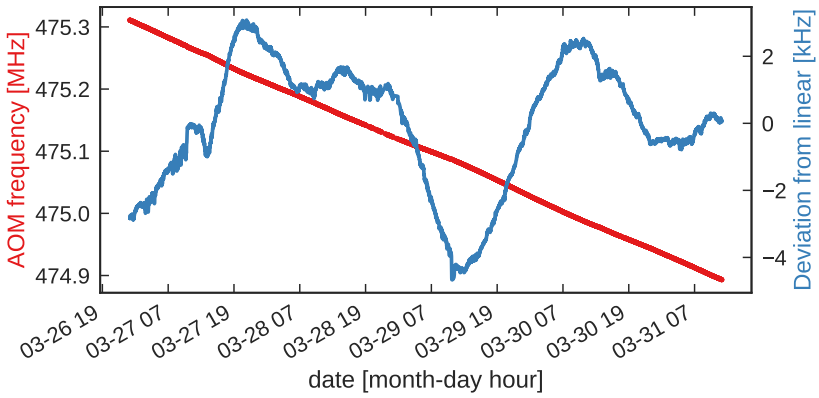

Figure 9.8: Short term 729 cavity drift. The deviation from a linear drift is within a few kHz and is corrected via the frequency comb beatnote measurement.

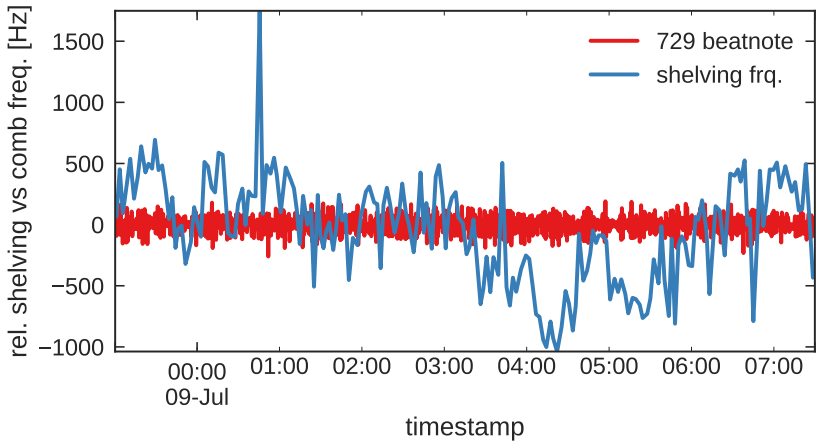

Figure 9.9: Spectroscopy on the $|S_{1/2}\rangle \rightarrow |D_{5/2}\rangle$ shelving transition with the 729 nm laser referenced to the Menlo frequency comb. The beatnote is kept within $\approx$ 200 Hz while the transition moves by about 2 kHz due to magnetic field fluctuations.

as described in chapter 12.1.2. The laser is a homebuilt 866 nm external cavity diode laser, similar in design as the repumpers described in section 9.2.5. It is locked to the wavemeter, typically with a detuning of 2.5 GHz. The laser occasionally mode-hops and changes frequency by about 5 GHz, such that the chosen detuning ensures off resonant light even in case of a mode-hop.

Since this laser is supposed to act as a fast switch, we cannot use any mechanical shutters to block residual light leaking through the AOM, as we do for the repumpers. Instead, we guarantee a good extinction ratio when switching the light, by using two separate AOMs in succession. The extinction ratio of the AOMs was measured to be below 3×10^{-6} with a Thorlabs fiber coupled power meter[17], and the residual light shift was tested as described in chapter 8.6.

Laser diodes typically show a broad pedestal of low intensity light over several nanometers in wavelength, even when operating single mode. Even light at low intensity, but very close to resonance, can lead to significant light shifts, which is why we use a reflective diffraction grating, about 1.7 m in front of the fiber-coupler, to extinguish this spectral pedestal.

9.2.8 Frequency comb

For the work presented in this thesis, two independent frequency combs were used. One is a repetition rate locked Coherent Mira Ti:Sapph fs laser system, described in detail in chapter 4.2. The second system is a MenloSystems fiber based frequency comb, described in detail in chapter 4.1. The frequency comb light is focused on the ion with a typical beam waist of 30 µm (radius), calculated from the measured laser power and measured frequency comb induced light shift on the 729 nm transition, as discussed in chapter 11.4. In this thesis, I sometimes refer to these laser systems just by "the Menlo comb" or "the Mira laser" or similar.

9.2.9 Mg^+ / MgH^+ lasers

For future experiments with MgH^+ we need light at 280 nm for Doppler cooling, and 285 nm for ionization of Mg. During my PhD project, I already worked on the existing laser systems to keep them operational. The Doppler cooling light is generated by frequency quadrupling the light from a fiber laser at 1120 nm in two separate SHG cavities. For ionization, we use a ring dye laser, pumped by and Argon ion laser, to generate light at 570 nm, which is subsequently frequency doubled in another SHG cavity. Both UV beams are combined with perpendicular polarization and sent free space to the Molecule Lab.

9.3 Experimental control

Experimental control is implemented in a modular way, mostly separating the logic layer from independent hardware modules. The data is stored in a SQL database, and can be retrieved remotely via any database enabled software. For

[17] Thorlabs S151C - Compact Fiber Photodiode Power Sensor

standard experiments, the data can be directly plotted in real-time via a custom python software.

9.3.1 Logic control and software

The central software for experimental control is qControl, a GUI[18] featured software initially implemented by Gregers Poulsen [T4] and subsequently extended by the following people working on the experiment.

qControl provides a basic programming interface to implement experimental sequences, i.e defining the timing of hardware events. Each sequence steps through one defined parameter, for instance the AOM frequency of the 729 nm laser for spectroscopy, or the pulse length of a laser for Rabi flopping. For each value of the parameter, the hardware such as AOM power or DDS frequencies is set up, and the programmable pulse generator (PPG) is programmed as explained in the following section. For each step of the parameter of choice, the experiment is repeated, typically 100 times, to gather sufficient statistics on a single ion experiment. Within the sequences, predefined blocks of code can be used for reoccurring tasks, such as Doppler cooling or state readout, which makes implementing new experiments straight forward.

On a daily basis, one interacts with qControl via its GUI, which presents all experimental control parameters in a modular interface. Several different experiments can be enqueued at the same time and are processed automatically.

Most of the hardware is interfaced via Ethernet on the lab network. When qControl starts, it establishes and keeps alive a connection to each hardware component, so that it is ready to use for experiments. We implemented most hardware interfaces in a python package, qDAQ[19], to have a semi-standardized way to access devices. In this way, one device can easily be replaced by another with similar functionality without major changes in the code.

9.3.2 Hardware control and timing

Hardware control can be categorized in time-critical and non time-critical events. For non time-critial communication, most hardware is interfaced via the lab network. For instance, before each experiment we set the DDS frequencies for various AOMs, the camera exposure time etc.

Time critical events are programmed in a programmable pulse generator (PPG) via qControl[20]. Our PPG is based on an open source design [O8, O9, S1, S2, T8, T9], and features 32 TTL channels as well as two fully programmable direct digital synthesizers (DDS). The TTL outputs are used to trigger previously programmed hardware with µs precision. The DDS is controlling the 729 nm laser experimental AOM and can produce amplitude as well as frequency shaped pulses, which is used for rapid adiabatic passage state preparation, as described in chapter 10.3.5.

For spectroscopy on the 729 nm $|S_{1/2}\rangle \rightarrow |D_{5/2}\rangle$ transition, the absolute accuracy of the DDS is important. I measured the DDS output at several different

[18] Graphical user interface

[19] quantum data acquisition

[20] Repeated connection problems between qControl and the PPG could be linked to a bad fiber switch connection in the past.

frequencies on the Menlo frequency counter (see chapter 4.1.5). For any frequency, the reading on the counter f_{real} was below the frequency set in the PPG f_{PPG}

$$f_{\mathrm{real}} = f_{\mathrm{PPG}} \cdot \left(1 - 8.0 \times 10^{-6}\right) . \tag{9.3}$$

For typical AOM frequencies on the order of 200 MHz, this corresponds to an error of 1.6 kHz, and a factor of two has to be taken into account for the double pass setup. The frequency offset was measured on several days and showed only negligible variations on the order of several Hz. The high precision $|S_{1/2}\rangle \rightarrow |D_{5/2}\rangle$ spectroscopy measurements presented in chapter 11 have been corrected for this discrepancy.

9.3.3 Automation

The presented experiments in this thesis rely on the proper operation of many pieces of hardware which are distributed over three separate rooms. Especially the number of lasers involved makes the experiments logistically challenging. We put a lot of effort into automating as many parts of the experiment as possible. This includes the real-time data analysis described in the following section, as well as a hardware status monitor, notifying the experimenter immediately of failed hardware. Here, I just want to describe two aspects of this automation in more detail.

The first is an automated ionization and loading sequence. Especially loading a single Ca^+ ion with low natural abundance, such as $^{46}Ca^+$ for the isotope measurements presented in chapter 14, can take up to several hours. I implemented a simple CCD image analysis algorithm, detecting the number of ions in the trap. This enables qControl to send a pulse of 272 nm light for ionization into the trap while trying to Doppler cool any ions produced in the process. If the software detects a single, or alternatively exactly 2 ions for future experiments, it stops the loading sequence. If more than the desired number of ions are detected, the trap is automatically dumped by resetting the endcap voltages, and the sequence starts over.

An even more valuable feature I implemented is the detection of erroneous measurements during an experiment. Due to collisions with background gas, the ion can be heated to a point where it is not visible on the CCD image anymore, making it appear dark when trying to read out its internal quantum state. These false data points make the analysis tedious, since these outliers need to be removed and holes in the data appear. Luckily, these heating events can be detected by statistically analyzing the sequence of (typically) $n = 100$ state readouts. We expect the dark / light state readout to be binomially distributed. Therefore, we can detect if there occurs a statistically unlikely long continuous sequence of s dark counts, while the rest of the sequence shows on average a probability smaller than 1 for the ion to be dark. If there was in total k out of n dark counts and a sequence of s dark counts in a row, we first estimate the underlying binomial probability for a dark count to be

$$p_{\mathrm{dark}} = \frac{k}{n} \tag{9.4}$$

and we discard and retake the data point if the probability of measuring s successive dark counts

$$p_s = p_{\text{dark}}^s \tag{9.5}$$

is smaller than 1 %. Using this definition, we do not discard sequences with 99 out of 100 dark counts. After the sequence finished its (typically) 100 cycles, the ion fluorescence is tested and the data point is retaken if the ion appears dark. This eliminates the problem of not being able to detect collision events in a row of 100 % dark counts, what is physically allowed.

Finally, the optimization and automation of the experiment allows us to take data fully automated over night since about one year ago, and all isotope shift measurements on the $|S_{1/2}\rangle \rightarrow |D_{5/2}\rangle$ transition were taken over night to minimize disturbances.

9.3.4 Data storage and access

Before I arrived at the Ion Trap group in Aarhus, qControl stored its configuration parameters and experimental results in local text files. Since then, we optimized and automatized many aspects of the experiment up to a level allowing us to take data unattended over night.

The large amount of data[21] required a more sophisticated way of storing and analyzing data in real-time, which is why I set up a mySQL database [O10] on a separate server to store the data in a structured and easily accessible way. For each experiment, the experiment's results as well as the current configuration, i.e. all experimental control parameters, are stored in the database.

The data can be accessed remotely via any database enabled software or programming language. For real-time plotting and simple real-time analysis such as standardized spectroscopy data or Rabi flopping, I wrote a python program, qDataPlot[22], which also allows to mark, comment and group measurements on the spot for later detailed analysis.

Most of the more involved data analysis for this thesis was done using python, in particular jupyter notebooks [O11, A115], pandas [A116, O12] and matplotlib [O13, A117].

Since the implementation of the database as a backbone for data storage, we also implemented many new data sources to continuously log to SQL. Examples are temperature loggers based on Raspberry Pi [O14] and DS18B20 temperature sensors [O15], wavemeter frequency reading and other parameters, Rb clock status and control parameters, all Menlo frequency comb parameters and beatnote measurements, and much more. All of this information stored in a common database environment allows to easily combine or correlate large amounts of data, or just to check for anomalies after data was taken over night.

[21] From June 2015 until August 2017, we recorded over 46 000 datasets.
[22] link

10 Experimental Procedures

This chapter explains the most important techniques used in the experiments presented in this thesis. The isotope selective loading of Ca^+ is discussed in section 10.1.1, followed by the implementation of Doppler cooling in section 10.2.1. Sideband cooling with the 729 nm laser, $|S_{1/2}\rangle$ Zeeman state initialization, and electron shelving is explained in section 10.2.2 to 10.3.2. Coherent manipulation on the $|S_{1/2}\rangle \rightarrow |D_{5/2}\rangle$ transition is presented in section 10.3.4.

10.1 Neutral Ca and the Ca^+ ion

10.1.1 Isotope selective loading of Ca

Each experiment in our trap obviously starts with loading the ion(s). All the results presented in this thesis were obtained by experimenting with single ions. Most of the time, we experiment with $^{40}Ca^+$ since it is the most abundant calcium isotope (see table A.3), but especially for the isotope shift measurements, presented in chapter 14, it is necessary to be able to load any specific isotope by choice. This isotope selective loading is facilitated by exciting the Ca atoms on the $4s^2\,{}^1S_0 \rightarrow 4s\,5p\,{}^1P_1$ transition with a 272 nm photon and subsequently ionizing the atom with a second 272 nm or 397 nm photon in a $1+1$ REMPI[1] process as depicted in figure 10.1 [A118, T6].

Typical loading rates when heating the Ca oven to 300 °C and turning on the ionization laser continuously are on the order of tens ions per second for

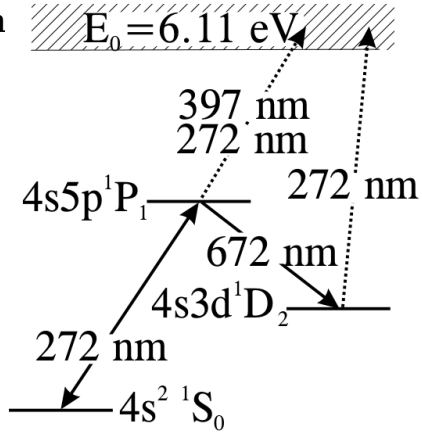

Figure 10.1: REMPI scheme for isotope selective ionization of Ca from ref. [A118].

[1] Resonance enhanced multi photon ionization

$^{40}Ca^+$. To load a single ion, we use a simple mechanical shutter to send a pulse of light of controlled length[2] on the ion and try to Doppler cool a possibly trapped ion afterwards. This initial cooling time depends on the alignment of the ionization and Doppler cooling beams relative to each other and relative to the trap center. An ion produced far from the trap center has a large amount of kinetic energy to be removed before it can scatter enough photons to be visible on the CCD image.

10.1.2 The Ca^+ ion

The electronic level structure of the $^{40}Ca^+$ ion is depicted in figure 10.2, and transition frequencies and decay rates are summarized in table 10.1.

Doppler cooling is performed on the $|S_{1/2}\rangle \rightarrow |P_{1/2}\rangle$ transition with a large scattering rate and repumping on the $|D_{5/2}\rangle \rightarrow |P_{3/2}\rangle$ transition as explained in section 10.2.1. Sideband cooling exploits the narrow linewidth of the $|S_{1/2}\rangle \rightarrow |D_{5/2}\rangle$ transition as discussed in section 10.2.2. Raman spectroscopy of the D-finestructure with the frequency comb uses the $|P_{3/2}\rangle$ state as virtual level for the two-photon process. The tabulated decay rates are used for the calculations of Raman Rabi frequencies and light shifts presented in chapter 12.

Table 10.1: Transitions between the lowest levels in $^{40}Ca^+$. Wavelengths are in vacuum $\lambda = c/\nu$.

Transition	Wavelength [nm]	Frequency [THz]	$\Gamma/2\pi$
$4\,^2S_{1/2} - 4\,^2P_{1/2}$	397	755.222 765 896(88) [j]	21.57(8) MHz [b]
$4\,^2S_{1/2} - 4\,^2P_{3/2}$	393	761.905 012 599(82) [i]	21.49(6) MHz [d]
$3\,^2D_{3/2} - 4\,^2P_{1/2}$	866	346.000 234 867(96) [k]	1.482(8) MHz [b]
$3\,^2D_{3/2} - 4\,^2P_{3/2}$	850	352.682 481 57(15) [m]	0.1520(10) MHz [d]
$3\,^2D_{5/2} - 4\,^2P_{3/2}$	854	350.862 882 55(15) [m]	1.350(6) MHz [d]
$4\,^2S_{1/2} - 3\,^2D_{5/2}$	729	411.042 129 776 393 2(10) [g,l] 411.042 129 776 824(2000) [o]	136.26(17) mHz [h]
$4\,^2S_{1/2} - 3\,^2D_{3/2}$	732	409.222 530 754 869(30) [p]	135.34(20) mHz [h]
$3\,^2D_{3/2} - 3\,^2D_{5/2}$	D-fine	1.819 599 021 504(37) [n] 1.819 599 021 524(32) [o]	

[a] Ref. Wolf et al. [A119]
[b] Ref. Hettrich et al. [A120]
[c] Ref. Wolf et al. [A121]
[d] Ref. Gerritsma et al. [A122]
[e] Ref. NIST [O16]
[g] Ref. Chwalla et al. [A88]
[h] Ref. Kreuter et al. [A123]
[i] Ref. Shi et al. [A50]
[j] Ref. Wan et al. [A48]
[k] Ref. Gebert et al. [A49]
[l] Ref. Hua et al. [A124]
[m] calculated from ref. [A50, A48, A49]
[n] Ref. Yamazaki et al. [A36]
[o] this work
[p] calculated from 729 nm ref. [A88] and this work's D-finestructure

[2] typically between 15 ms and 200 ms

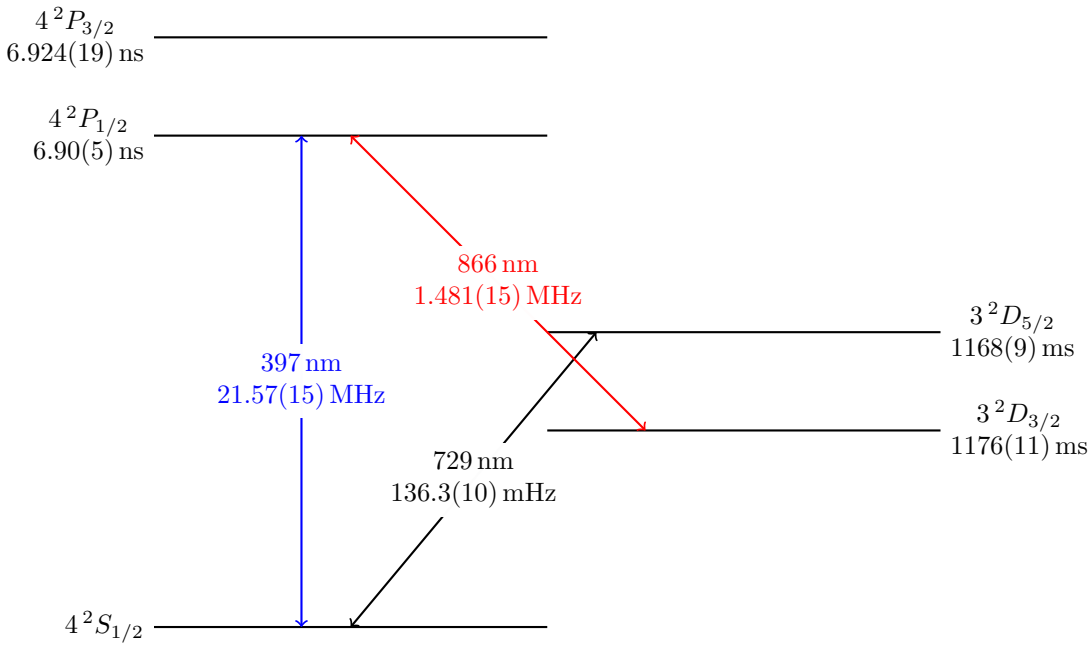

Figure 10.2: Level structure of $^{40}Ca^+$ [T10]. The given lifetimes, linewidths and transition wavelengths can be found with higher accuracy and references in table 10.1. Doppler cooling is carried out on the $S_{1/2} \rightarrow P_{1/2}$ transition with repumping on the $D_{3/2} \rightarrow P_{1/2}$ transition. Sideband cooling exploits the narrow linewidth of the $S_{1/2} \rightarrow D_{5/2}$ transition with a repumper on the $D_{5/2} \rightarrow P_{3/2}$ transition.

10.2 Laser cooling

10.2.1 Doppler cooling

The theory of Doppler cooling is discussed in chapter 2.3.1. In Ca^+ we cool on the $|S_{1/2}\rangle \rightarrow |P_{1/2}\rangle$ transition with a linewidth of 21.57(8) MHz using the 397 nm laser described in chapter 9.2.4. The polarization of the light is oriented vertically along the magnetic field quantization axis (π), allowing only $\Delta m_j = 0$ transitions. These transitions have a smaller relative frequency mismatch compared to the $\Delta m_j = \pm 1$ transitions when the m_j states are split by the Zeeman effect. The $|P_{1/2}\rangle$ level has a branching ratio of 0.935 65(7) [A125] to the $|S_{1/2}\rangle$ level, so that population from decay to the $|D_{3/2}\rangle$ state needs to be repumped in the cooling cycle using the 866 nm laser described in chapter 9.2.5. The 866 nm light needs to be horizontally polarized ($\sigma^{\pm}$), perpendicular to the quantization axis, in order to be able to depopulate the $|D_{3/2}, m_j = \pm 3/2\rangle$ states. Only a single Doppler cooling beam, oriented horizontally at 45° relative to the trap axis, is used, cooling the motion along all directions in space due to the coupling of the motional degrees of freedom by micromotion for "high" temperatures compared to the sideband-cooling regime. To efficiently cool the ion from initially

very high temperatures, after loading or a collision with background gas, we use the zero order beam from the 397 nm laser AOM, which is far red detuned, with high power.

10.2.2 Resolved sideband cooling

Resolved sideband cooling is explained theoretically in chapter 2.3.2. We use the 729 nm laser, described in chapter 9.2.6, to excite the ion on the $|S_{1/2},\, m_j = -1/2\rangle \rightarrow |D_{5/2},\, m_j = -5/2\rangle$ transition on a red sideband, and use the 854 nm laser, described in chapter 9.2.5, to bring the ion back to the $|S_{1/2}\rangle$ state via repumping on the $|D_{5/2}\rangle \rightarrow |P_{3/2}\rangle$ transition. In fact, we use a combination of first and second order red sideband transitions, together with state initialization pulses (see next section) in between. Sideband cooling to 99 % motional ground state population is typically achieved. The details of our implementation are described in ref. [T3].

10.3 State manipulation and detection

10.3.1 State initialization

After Doppler cooling, the ion is in the $|S_{1/2}\rangle$ level, with about equal probability[3] for both Zeeman sub-states $m_j = \pm 1/2$. To prepare the ion in the $|D_{5/2}\rangle$ state with high probability, usually using rapid adiabatic passage (RAP) as described in section 10.3.5, the ion needs to be prepared in a single well defined $|S_{1/2},\, m_j\rangle$ state first. This initial state preparation is implemented simply by pumping out the population of the other state using the 729 nm and 854 nm lasers. The efficiency of this process can strongly be enhanced by using a specific 729 nm transitions and exploiting dipole selection rules ($\Delta m_j = \pm 1$) on the unresolved 854 nm transition

$$|S_{1/2},\, m_j = -1/2\rangle \xrightarrow{729\,\mathrm{nm}} |D_{5/2},\, m_j = +3/2\rangle \xrightarrow{854\,\mathrm{nm}} |P_{3/2},\, m_j = +1/2,\, +3/2\rangle$$

to prepare the $|S_{1/2},\, m_j = +1/2\rangle$ state, and

$$|S_{1/2},\, m_j = +1/2\rangle \xrightarrow{729\,\mathrm{nm}} |D_{5/2},\, m_j = -3/2\rangle \xrightarrow{854\,\mathrm{nm}} |P_{3/2},\, m_j = -1/2,\, -3/2\rangle$$

to prepare the $|S_{1/2},\, m_j = -1/2\rangle$ state. Spontaneous decay back to the $|S_{1/2}\rangle$ state closes the circle, which is repeated typically 8 times in our experiment. The preparation fidelity is basically 100 %.

10.3.2 Electron shelving

The electron shelving technique [A126] provides a means of "storing" the atomic system in an excited state, which is perfectly stable on the timescale of a typical atomic physics experiment. For the Ca^+ ion, this state is one of the $3\,^2D$ levels with lifetimes of more than 1 s, which is long compared to any other experimental timescale such as Rabi frequencies or readout time. In this thesis, the expression

[3] Our sideband cooling scheme favors the $m_j = -1/2$ state over the $m_j = +1/2$ state.

"shelving" refers to preparing the ion in one of the $D_{5/2}$ Zeeman sub-states. Shelving the ion Zeeman selective in one of the $|D_{5/2}, m_j\rangle$ states is usually implemented via state initialization (section 10.3.1) followed by rapid adiabatic passage (section 10.3.5). Probing whether the electron is shelved or not is what we call "state readout", as described in section 10.3.3.

10.3.3 Internal state read out

At the end of each experimental sequence, we read out the internal state of the ion by probing whether the valence electron is shelved or not, specifically whether it is shelved in the $|D_{5/2}\rangle$ state. Experimentally, readout is implemented by turning on the Doppler cooling lasers (397 nm and 866 nm), and collection the fluorescence on the CCD camera. If the integrated fluorescence signal lies above a predefined threshold, the ion is considered "light". Since the Doppler cooling light couples the $|S_{1/2}\rangle$, $|P_{1/2}\rangle$, and $|D_{3/2}\rangle$ states, and since the $|P_{3/2}\rangle$ level has a lifetime short compared to the readout time of about 10 ms, the ion could not have been in the $|D_{5/2}\rangle$ state. On the other hand, if the ion does not fluoresce and is considered "dark", it must have been in the $|D_{5/2}\rangle$ state. The fidelity of this discrimination is basically 100 % if the fluorescence threshold has been adjusted correctly.

Readout times of 10 ms slightly reduce the experimental duty cycle. We currently consider using a photomultiplier tube (PMT) for state detection instead of the CCD in the future, which would allow much shorter readout times.

10.3.4 Coherent manipulation on the 729 nm transition

Coherent population transfer with the 729 nm laser on the $|S_{1/2}\rangle \rightarrow |D_{5/2}\rangle$ transition is shown in figure 10.3. With the correct pulse time, basically 100 % of the population can be transferred from the $|S_{1/2}\rangle$ state to a selected Zeeman state of the $|D_{5/2}\rangle$ manifold, using a *pi*-pulse as discussed in chapter 2.2. However, the fidelity of the $|D_{5/2}\rangle$ state preparation is easily affected by changing experimental parameters, laser intensity due to pointing or laser power instabilities, which is why we usually use rapid adiabatic passage (RAP) for state preparation, as explained in the following section.

10.3.5 Rapid adiabatic passage

An alternative technique for complete population transfer is *rapid adiabatic passage* (RAP)[4] [R26, A127, A128]. Instead of illuminating the system with resonant light for a given time, we sweep the laser frequency over the resonance. In figure 10.5 (top), we see how the energies of the "adiabatic states" show an avoided crossing, leading to ideally 100 % population transfer between the diabatic states (bottom) [R26]. The condition for adiabatic transfer is

$$\frac{1}{2}\left|\dot{\Omega}\Delta - \Omega\dot{\Delta}\right| \ll \left(\Omega^2 + \Delta^2\right)^{\frac{3}{2}} , \tag{10.1}$$

[4] sometimes also just called "adiabatic passage" or "adiabatic rapid passage" (ARP). "Rapid" refers to the fact that the sweep needs to be fast compared to the decay time of the 2-level system.

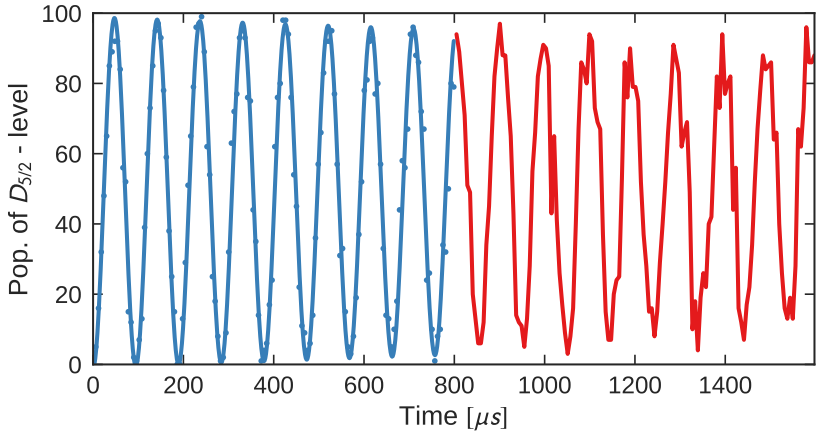

Figure 10.3: Rabi flopping on the $|S_{1/2}, m_j = -1/2\rangle \rightarrow |D_{5/2}, m_j = -5/2\rangle$ shelving transition with the 729 nm laser. The blue curve until 800 μs is a fit to the Bloch model. After the data up to 800 µs was taken, it seems the laser drifted slightly off transition. The red line is simply connecting the data points to visualize the oscillation more clearly.

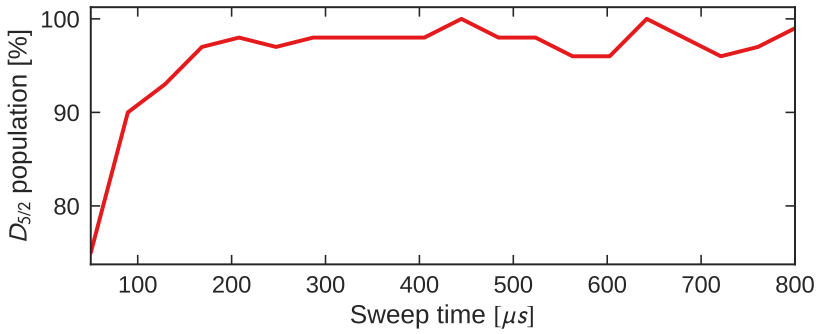

Figure 10.4: Rapid adiabatic passage (RAP) on the $|S_{1/2}\rangle \rightarrow |D_{5/2}\rangle$ transition for different sweep times for a fixed frequency sweep of ± 250 kHz ($\Delta = 500$ kHz). A stable plateau is reached at a sweep duration τ of around 400 μs, where about 98 % of the population is transferred.

which means that we need large Rabi frequency and detuning, and a smooth pulse shape [R26]. Experimentally, we use the PPG's DDS for intensity pulse shaping with a Blackman-window function [A129], and a linear frequency sweep, to drive the 729 nm laser AOM.

The Landau-Zener formula [R26, R27, A128, A130]

$$P_1 = 1 - p, \quad p = \exp\left[-\frac{\pi\Omega^2(t_0)}{2\left|\dot{\Delta}(t_0)\right|}\right], \tag{10.2}$$

where t_0 is the time of crossing the resonance, gives an estimate of the population transfer, and evaluates for typical experimental parameters in our experiment of

$$\Omega \approx 20\,\mathrm{kHz} \tag{10.3}$$

$$\dot{\Delta} = \frac{\Delta}{\tau} = \frac{500\,\mathrm{kHz}}{400\,\mu\mathrm{s}} \tag{10.4}$$

to

$$P \approx 96\,\%, \tag{10.5}$$

well in agreement with the observed population transfer of $\approx 98\,\%$ as shown in figure 10.4.

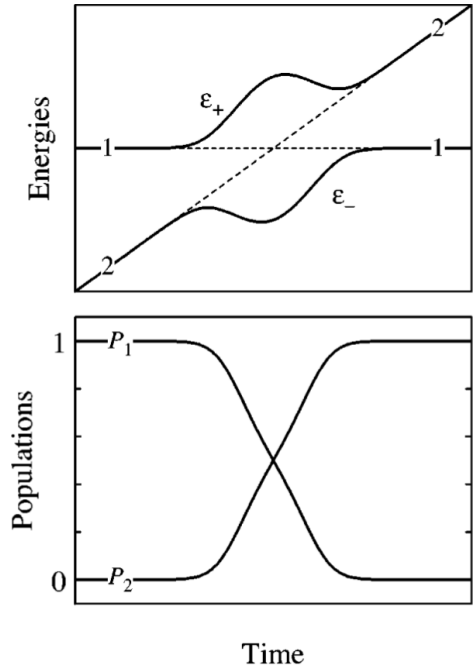

Figure 10.5: Sketch of Rapid adiabatic passage (RAP) from ref. [R26].

No amount of experimentation can ever prove me right; a single experiment can prove me wrong.

Albert Einstein

11

$|S_{1/2}\rangle \rightarrow |D_{5/2}\rangle$ Transition Spectroscopy

The $|D_{5/2}\rangle$ level in $^{40}Ca^{+}$ has a natural lifetime of 1174(10) ms [A123, A114, A124], resulting in a natural linewidth of the dipole forbidden $|S_{1/2}\rangle \rightarrow |D_{5/2}\rangle$ transition of 0.1356(12) Hz, thus making it ideal for high precision spectroscopy. The transition frequency has been determined with 1.0 Hz accuracy to 411 042 129 776 393.2(10) Hz by referencing the measurement to a portable Cs fountain clock in Innsbruck [A88], and was confirmed by a measurement in Wuhan, China [A124]. In Aarhus, we do not have access to a high accuracy atomic clock. Instead, we are limited by our GPS disciplined Rb standard to a relative accuracy of 5×10^{-12} as discussed in chapter 5. The clock accuracy is reflected in a limitation on the $|S_{1/2}\rangle \rightarrow |D_{5/2}\rangle$ transition accuracy of 2 kHz. However, other isotopes than $^{40}Ca^{+}$ have not been studied with high accuracy before, and our 2 kHz accuracy still allows us to measure the most precise spectroscopic isotope shifts in literature so far, as presented in chapter 14.

11.1 Experimental sequence

The experimental spectroscopy sequence is sketched in figure 11.1. After isotope selective loading of a single Ca^{+} ion (chapter 10.1.1), we Doppler- and sideband cool the ion to its motional ground state (chapter 10.2), and initialize the ion's internal state in one of the $|S_{1/2}, m_J = \pm 1/2\rangle$ levels (chapter 10.3.1). From a selected $|S_{1/2}, m_j\rangle$ state, the ion can be exited to any m_j state of the $|D_{5/2}\rangle$ manifold, due to the selection rule $\Delta m_J = \pm 1, \pm 2$ for linear polarized light with $\vec{k} \perp \vec{B}$, where $\vec{k}$ is the wave-vector, and $\vec{B}$ is the magnetic field quantization axis [T4, B.3]. Afterwards, the final state of the ion is detected via a fluorescence measurement on the $|S_{1/2}\rangle \rightarrow |P_{1/2}\rangle$ transition (section 10.3.3).

In the experiment, we scan the frequency of the 729 nm light in discrete steps using an AOM (section 9.2.6). For each AOM frequency, the experimental

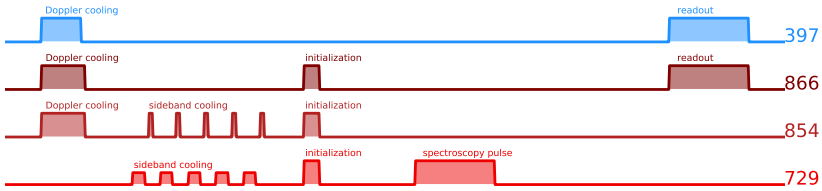

Figure 11.1: Experimental sequence for spectroscopy on the 729 nm transition. After cooling the ion to the motional ground state, and initializing the internal state to one selected m_j value of the $|S_{1/2}\rangle$ level, the ion is exposed to a *pi*-pulse on a Zeeman resolved $|S_{1/2}\rangle \rightarrow |D_{5/2}\rangle$ transition. Finally, the internal state is read on via fluorescence detection with the imaging system.

sequence as shown in figure 11.1 is repeated 10 to 100 times, and the number of shelving events is recorded for each AOM frequency.

11.2 Line broadening

Fast magnetic field fluctuations in our setup on the order of 10^{-4} lead to an incoherent broadening of the spectroscopic line. This broadening depends on the linear Zeeman shift (8.7) of the addressed transition. For our typical magnetic field of 6.5 G, we expect an incoherent linewidth for a specific $|S_{1/2}, m_j\rangle \rightarrow |D_{5/2}, m'_j\rangle$ transition of

$$\Delta\nu = 10^{-4}\,\frac{\mu_B\,B}{h}\,\left(g_{5/2}\,m'_j - g_{1/2}\,m_j\right)\,. \tag{11.1}$$

This results in a 2.5 kHz incoherent linewidth for the $|S_{1/2}, m_j = \mp 1/2\rangle \rightarrow |D_{5/2}, m'_j = \pm 3/2\rangle$ (reverse) initialization transitions, used for spectroscopy in the following.

The excitation is driven coherently by the 729 nm laser, as shown in the Rabi flopping traces in chapter 10.3.4, and the Rabi frequency can be chosen via the laser intensity. For Rabi frequencies large compared to the incoherent linewidth of 2.5 kHz, the line is well described by its theoretically expected sinc^2 shape. One such measurement is shown in figure 11.2.

11.3 High resolution spectroscopy

As mentioned already in the introduction, the $|S_{1/2}\rangle \rightarrow |D_{5/2}\rangle$ transition in $^{40}Ca^+$ has been measured with 1 Hz accuracy before. For this thesis, I am interested in the isotope shift on this transition, and a measurement on the $^{40}Ca^+$ ion is a valuable test, when comparing to the previous 1 Hz measurements.

From the discussion of the accuracy of our frequency reference in chapter 5, it is already clear that we will not reach a better relative accuracy than 5×10^{-12}, corresponding to 2 kHz for the $|S_{1/2}\rangle \rightarrow |D_{5/2}\rangle$ transition. This is more than 3

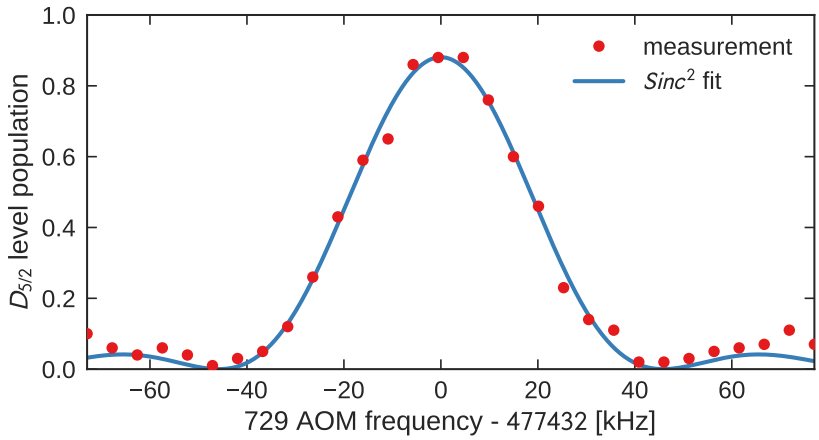

Figure 11.2: AOM frequency scan over the 729 nm transition resonance with high Rabi frequency Ω compared to the incoherent linewidth, resulting in a sinc^2 line-shape. In this measurement, the exposure time is chosen just below $t = \pi/\Omega$.

orders of magnitude lower accuracy than existing literature values for $^{40}Ca^+$, but will still lead, together with the D-finestructure measurements presented in the next section, to the most precise isotope shift measurements in literature, discussed in chapter 14.

Systematic shifts, discussed in chapter 8, being well below 1 kHz for the $|S_{1/2}\rangle \rightarrow |D_{5/2}\rangle$ transition do not need to be taken into account, unlike for the D-finestructure measurements. Also, the incoherent linewidth limit of 2.5 kHz is not an issue, since we can easily determine the center of such a line much better than the 2 kHz accuracy goal with a simple fit.

The only shift which needs to be taken into account is the purposefully imprinted linear Zeeman shift induced by the external quantization magnetic field. In a scheme similar to the D-finestructure spectroscopy described in chapter 13, we measure two Zeeman resolved $|S_{1/2}\rangle \rightarrow |D_{5/2}\rangle$ transitions, with opposite linear Zeeman shifts, at the same time, and take the average as the unshifted $|S_{1/2}\rangle \rightarrow |D_{5/2}\rangle$ value. The measurements are triggered at a fixed phase relative to the AC line, to make sure that the spectroscopy on the two transitions is taken at the same magnetic field amplitude (compare chapter 9.1.5). From this measurement we get the transition frequency in terms of the AOM frequencies $f_{\text{AOM, init}}$[1] and $f_{\text{AOM, rev. init}}$[2], the x-axis in figure 11.2, and not the absolute transition frequency.

To determine the absolute frequency, we measure the light directly from the 729 nm laser via a beatnote with the Menlo frequency comb (see chapter 4.1). The total frequency is then calculated as

$$f_{S-D} = (1 - 8.0 \times 10^{-6}) \cdot (f_{\text{AOM, init}} - f_{\text{AOM, rev. init}}) - 2\, f_{\text{CEO}} + q\, f_{\text{rep}} - f_{\text{beat}}\,, \tag{11.2}$$

[1]The "initialization" transition is $|S_{1/2}, m_j = +1/2\rangle \rightarrow |D_{5/2}, m_j = -3/2\rangle$

[2]The "reverse initialization" transition is $|S_{1/2}, m_j = -1/2\rangle \rightarrow |D_{5/2}, m_j = +3/2\rangle$

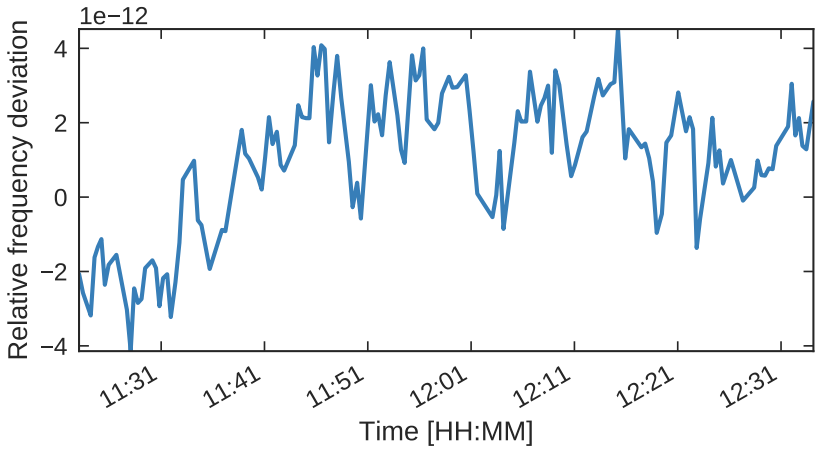

Figure 11.3: Relative frequency of the $^{40}Ca^{+}$ $|S_{1/2}\rangle \rightarrow |D_{5/2}\rangle$ transition, relative to the high precision measurement of Chwalla et al. [A88], determined via equation (11.2). A total of 77 transition measurements over the course of about one hour are shown.

where the comb tooth number $q = 1\,643\,856$ is determined from a rough measurement of the 729 nm laser frequency with our wavemeter, and the sign of the beatnote frequency f_{beat} can be determined by slightly changing the repetition rate. As mentioned in chapter 9.3.2, the PPG controlling the AOM is not referenced to our frequency standard, and we need to correct its frequency by a factor of $(1 - 8.0 \times 10^{-6})$.

Figure 11.3 shows the result calculated via equation (11.2) of 77 transition measurements on $^{40}Ca^{+}$ over the course of about one hour, relative to the $|S_{1/2}\rangle \rightarrow |D_{5/2}\rangle$ transition frequency determined by Chwalla et al. The measured deviation stays within the expected accuracy of the clock of 5×10^{-12}, and the absolute value in terms of the mean, and single measurement standard deviation, is

$$f^{40}_{S-D} = 411\,042\,129\,776\,824(769)\,\text{Hz}\,, \tag{11.3}$$

which is 431(769) Hz different from the value determined by Chwalla et al. [A88]. This measurement confirms the expected accuracy of 2 kHz, reachable with our current frequency standard. The better agreement with the real value is coincidental. In chapter 14, I present the results of identical measurements on all other naturally abundant even Ca^{+} isotopes.

11.4 Frequency comb induced light shift

The Raman Rabi frequency when driving the D-finestructure transition with the frequency comb is expected to be linear in intensity, a feature we exploit to extrapolate to zero intensity for the high precision Raman spectroscopy presented in section 13. Furthermore, we have the theory to calculate quantitatively the

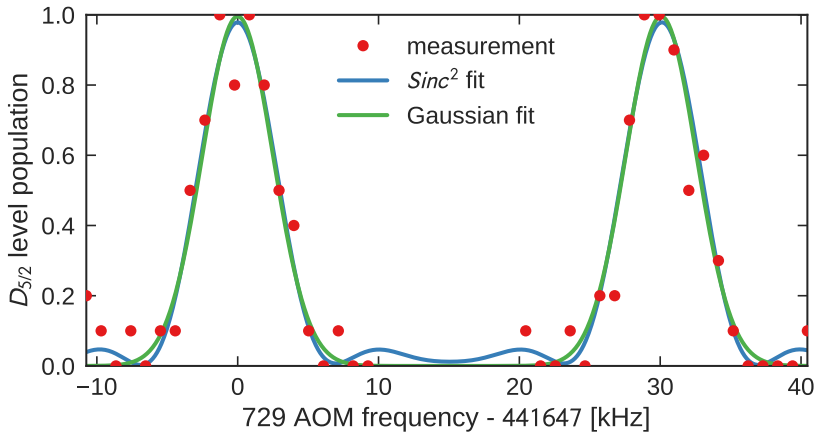

Figure 11.4: Frequency comb induced light shift measurement on the $|S_{1/2}\rangle \rightarrow |D_{5/2}\rangle$ transition. The light shift can be measured with a precision of about 200 Hz with only 10 experimental cycles per AOM frequency and 20 points per peak, corresponding to about 1 minute measurement time. A Gaussian fit is usually used for automated data analysis, since the linewidth is determined by magnetic field fluctuations for small Rabi frequencies.

expected Raman Rabi frequency, if not only the intensity, but also the spectrum and phase of the light is known, what I investigate in chapter 12.3.

In both cases, we need a handle on the exact light intensity at the position of the ion, without depending on unreliable estimates based on laser power and beam profile. In the Ca^+ ion, we have a convenient method to probe the frequency comb light intensity by measuring the light shift impressed on the 729 nm transition. The comb light around 800 nm shifts the $|D_{5/2}\rangle$ level to higher energies due to off-resonant coupling on the 854 nm $|D_{5/2}\rangle \rightarrow |P_{3/2}\rangle$ transition. This light shift can be calculated precisely as shown in chapter 12.3. And it can be measured with high accuracy by probing the $|S_{1/2}\rangle \rightarrow |D_{5/2}\rangle$ transition with the 729 nm laser, similar to the high resolution spectroscopy in section 11, while the frequency comb light is illuminating the ion at the same time. The comb will not drive Raman transitions between the D-finestructure states as long as the repetition rate is not in resonance, but it will only induce a light shift, proportional to the light intensity.

A measurement of the induced light shift is presented in figure 11.4. The left peak corresponds to plain spectroscopy on the $|S_{1/2}\rangle \rightarrow |D_{5/2}\rangle$ transition, without any frequency comb light. The right peak corresponds to the exact same experimental sequence, except that the ion is illuminated by the frequency comb during the 729 nm spectroscopy pulse, as sketched in figure 11.5. After Doppler and sideband cooling, the ion's state is initialized in one selected $|S_{1/2}\rangle$ state. During the following 729 nm spectroscopy pulse on the $|S_{1/2}\rangle \rightarrow |D_{5/2}\rangle$ transition, the frequency comb light is turned on simultaneously, before reading out the ion's final state. After one data point with a given 729 nm AOM frequency is taken, one data-point without any frequency comb light is taken at the

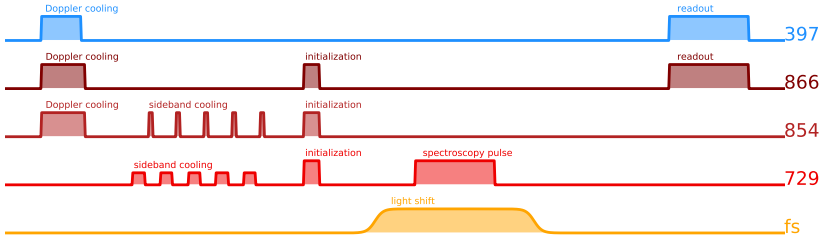

Figure 11.5: Experimental sequence of the frequency comb induced light shift on Ca^+ . The frequency comb light is illuminating the ion at the same time the $|S_{1/2}\rangle \rightarrow |D_{5/2}\rangle$ transition frequency is measured with the 729 nm laser, and compared to the unshifted transition frequency without the frequency comb light.

expected AOM frequency for the unshifted peak. All following data points are taken in the same way, alternating between comb light on and off. In this way, possible laser or magnetic field shifts do not systematically disturb the measurement. The Zeeman sub-states of the addressed $|S_{1/2}\rangle \rightarrow |D_{5/2}\rangle$ transition are chosen such, that the frequency comb induced light shift is the largest for the chosen polarization. The light shift can typically be determined with a precision of 200 Hz within about 1 minute measurement time.

Experimentally, we can adjust the comb light intensity at the ion using two methods. The first is simply to insert neutral density (ND) filters into the beampath. For automated measurements at different intensities, I implemented a computer controlled filter wheel[3] to change laser intensities between measurements. The second method is rotating the comb's polarization with a $\lambda/2$ waveplate versus the fixed direction of a Glan-Taylor polarizer, selecting the polarization for the experiment. For the Menlo comb, I implemented computer control of a motorized waveplate[4]. This method allows continuous intensity control, compared to the fixed steps determined by the selected ND filters in the first method.

[3]Thorlabs FW102C, 6 exchangeable filter positions, VISA compatible programming interface.

[4]Newport Model PR50PP, 4500 steps per rotation, controllable through XML-RPC interface exposed by the Menlo frequency comb software.

It doesn't matter how beautiful your theory is, it doesn't matter how smart you are. If it doesn't agree with experiment, it's wrong.

Richard Feynman

12 Frequency Comb Driven Raman Transitions

Coherent population transfer by frequency comb driven Raman transitions has been demonstrated, before by Hayes et al. for hyperfine transitions in $^{171}Yb^+$ [T1, A46]. The $|F = 1, m_F = 0\rangle \rightarrow |F = 0, m_F = 0\rangle$ hyperfine states of the $^2S_{1/2}$ level are split by 12.6428 GHz, so that transitions can be driven with a relatively long frequency comb pulse time of about 1 ps corresponding to a bandwidth limited spectral width of the comb of only about 400 GHz (0.85 nm width at 800 nm center wavelength).

In this chapter, I present the extension of this technique into the THz range, by directly driving Raman transitions between the D-finestructure levels in $^{40}Ca^+$, using a femtosecond frequency comb. I start with the experimental implementation in section 12.1, before showing coherent population transfer in section 12.2, where I also highlight the difference of the two frequency comb systems used for the experiments, the Mira and the Menlo comb, separately described in chapter 4. Following is a discussion on the impact of polarization in section 12.3, and the importance of group velocity dispersion, due to the high bandwidth of the comb light, in section 12.4.

12.1 Implementation

12.1.1 Experimental sequence

The experimental sequence is sketched in figure 12.1. As usual, we prepare the ion in a selected $|S_{1/2}\rangle$ state (see chapter 10.3.1) before transferring close to 100 % of the population into one selected Zeeman sub-state of the $D_{5/2}$ manifold using rapid adiabatic passage on the $|S_{1/2}\rangle \rightarrow |D_{5/2}\rangle$ transition as described in chapter 10.3.5.

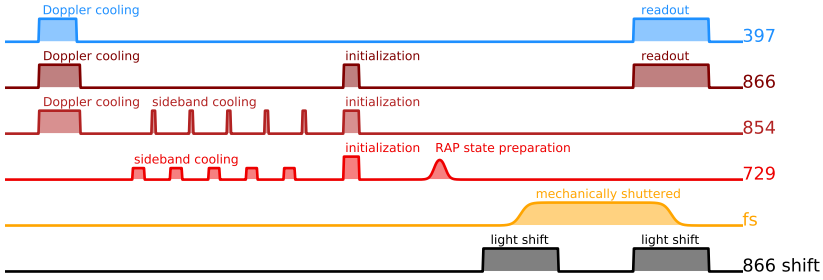

Figure 12.1: Experimental sequence of Raman Rabi flopping and Raman spectroscopy using the 866 nm laser light shift method (see text for details).

Now we want to apply a pulse of frequency comb light with well defined length on the ion to drive coherent Rabi oscillations. However, due to concerns about the impact of dispersion on the effective Raman Rabi frequency, we decided against using an AOM to shutter the frequency comb light. Instead, we apply controlled light shifts to shift the $|D_{5/2}\rangle \rightarrow |D_{3/2}\rangle$ transition in and out of resonance with μs precision. This method is explained in detail in the following section 12.1.2. After the well defined interaction time with the frequency comb light, the internal state of the ion is read out as described in chapter 10.3.3, that means we detect whether the ion is still in the $D_{5/2}$ level or not.

12.1.2 Light shift shutter method

Before the ion is exposed to resonant frequency comb light, we turn on light at 866 nm from a different laser (see chapter 9.2.7), as shown in figure 12.1, detuned from the $|D_{3/2}\rangle \rightarrow |P_{1/2}\rangle$ transition by typically about 2 GHz. This shifts the $|D_{5/2}\rangle \rightarrow |D_{3/2}\rangle$ transition out of resonance with the frequency comb light. The frequency comb light is turned on using a mechanical shutter[1] with a rise and fall time of about 2 ms. After the shutter is completely open, the light at 866 nm is turned off, and the transition is back in resonance with the frequency comb light. After a pre-programmed exposure time using the programmable pulse generator (see section 9.3.2), the transition is shifted out of resonance again by turning the 866 nm light back on, stopping the coherent population transfer. The frequency comb light is then turned off before the 866 nm light.

A plot showing frequency comb spectroscopy, as discussed later in section 13, on the $|D_{5/2}, m_j = +1/2\rangle \rightarrow |D_{3/2}, m_j = +1/2\rangle$ transition is shown in figure 12.2. The two plotted spectra were taken with the 866 nm laser on, or off respectively, with a total exposure time of the ion to the frequency comb light of ≈ 10 ms (mechanically shuttered). *Without* the light shift laser (blue), we measure the transition frequency as expected based on the addressed Zeeman sub-states and the measured magnetic field[2]. The contrast is about 50 %, as expected for an

[1] Uniblitz LS6, 20 Hz/150 Hz continuous/burst max. operational frequency, < 2 ms opening/closing time.

[2] The magnetic field can be calculated based on $|S_{1/2}\rangle \rightarrow |D_{5/2}\rangle$ spectroscopy with the

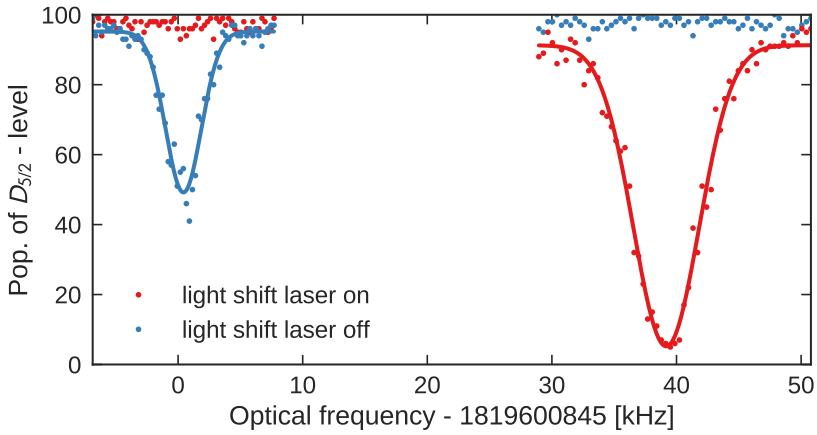

Figure 12.2: Menlo frequency comb spectroscopy on the $|D_{5/2}, m_j = +1/2\rangle \rightarrow |D_{3/2}, m_j = +1/2\rangle$ transition. Shown is a shifted and unshifted spectrum by the 866 nm light shift laser. The comb light is at the magic polarization (see section 12.3.2), and the 866 nm light shift laser is detuned by -2 GHz.

exposure time long compared to the decoherence time[3].

With the 866 nm light shift laser on (red), the transition is clearly shifted, leaving no transition probability at the original, unshifted, frequency. The peak is broadened, and shows higher contrast due to off resonant scattering on the 866 nm $|D_{3/2}\rangle \rightarrow |P_{1/2}\rangle$ transition, moving population during the $|D_{5/2}\rangle \rightarrow |D_{3/2}\rangle$ Rabi oscillations from the $|D_{5/2}\rangle$ states to the $|S_{1/2}\rangle$ states.

It is important to note that this scattering has no impact on the measurement real spectroscopy. When the light shift laser is used as a shutter, as depicted in the sequence in figure 12.1, and not for demonstration as in this section, no photons can be scattered during the first pulse of 866 nm light shift light, since the probability of the ion to be in the $|D_{3/2}\rangle$ state is zero. During the interaction time with the frequency comb, the 866 nm light is switched off. When the 866 nm light is switched on for the second time, the transition is shifted which terminates the interaction time with the frequency comb light. Scattering on the $|D_{3/2}\rangle \rightarrow |P_{1/2}\rangle$ transition has now no impact on the measurement result any longer, since the state of the ion is read out using resonant 866 nm light afterwards anyways for normal state readout, as explained in chapter 10.3.3, and the $|D_{5/2}\rangle$ state population is not affected by the 866 nm light shift laser.

12.2 Comparison of Menlo and Mira dynamics

In this section, I show coherent Raman Rabi flopping between the D-finestructure levels in Ca^+ using the Menlo, and separately the Mira frequency comb. The

729 nm laser, on two different Zeeman sub-states, as explained in chapter 9.1.5

[3] see chapter 2.2 for the model description, and section 12.2.3 for measured decoherence times.

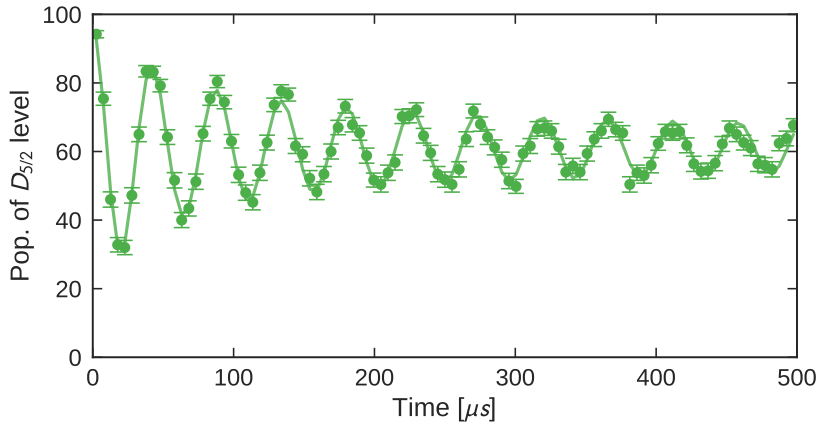

Figure 12.3: Raman Rabi flopping between the D-finestructure states in $^{40}Ca^{+}$ using the Mira laser. The fit to the laser linewidth model gives a Rabi frequency of $\Omega/2\pi = 21.55\,\text{kHz}$, and Gaussian laser linewidth of 40.64 kHz, consistent with the 59.4 kHz total spectroscopic linewidth shown in figure 12.4.

difference in their repetition rate stability becomes obvious by very different decoherence times.

12.2.1 Mira coherence and linewidth

As described in chapter 6, the stability of the repetition rate of the Mira laser is a major concern for our experiments. This repetition rate stability can be interpreted as the laser *linewidth* for the Raman process. If this linewidth is not small compared to the Rabi frequency broadening the transition, we cannot neglect it. The Mira laser's repetition rate lock turned out to provide a very small locking bandwidth, suggesting to model the Rabi flopping trace as a sum of Rabi flopping traces, where the detuning is randomly variating according to the laser's repetition rate jitter, as described in chapter 2.2.3.

Figure 12.3 shows Rabi flopping between the D-finestructure states in $^{40}Ca^{+}$ using the Mira laser. The solid line is a fit to the linewidth model equation (2.51), with a Gaussian line-shape function

$$g(\Delta) = \frac{1}{\sigma\sqrt{2\pi}} \exp\left(\frac{-\Delta^2}{2\,\sigma^2}\right), \tag{12.1}$$

with full width at half maximum (FWHM) of $2\sqrt{2\ln 2}\,\sigma$. We find the best fit parameters, Rabi frequency $\Omega/2\pi = 21.55\,\text{kHz}$ leading to a power broadened FWHM of $\sqrt{2\pi}\,21.55\,\text{kHz} = 30.48\,\text{kHz}$, and Gaussian linewidth (FWHM) of 40.64 kHz. The total line-shape of a spectroscopy scan is then expected to be a Voigt profile with a FWHM of approximately 59.3 kHz [R28]. Figure 12.4 shows spectroscopy under the same conditions as the Rabi flops in figure 12.3, revealing a total spectroscopic linewidth (FWHM) of 59.4 kHz, agreeing nicely with the model expectation. Another approach to estimate the direct incoherent laser

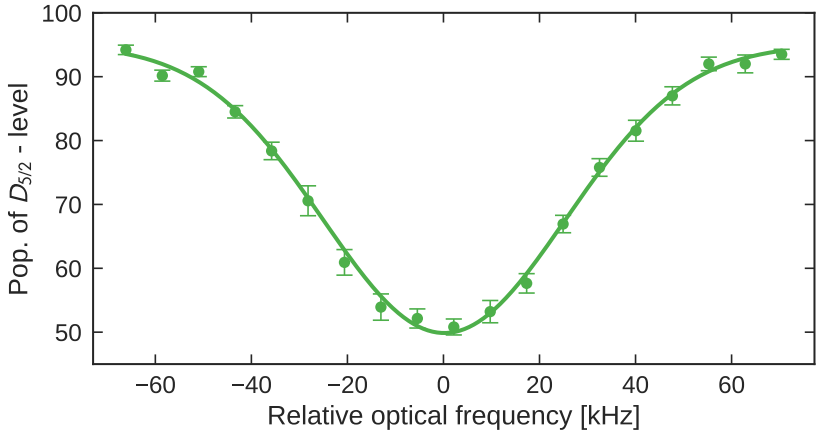

Figure 12.4: Frequency comb Raman spectroscopy with the Mira laser. The spectroscopic linewidth (FWHM) is 59.4 kHz, consistent with the Rabi frequency and incoherent laser linewidth determined from the the Raman Rabi flopping trace in figure 12.3, under the same experimental conditions.

linewidth is discussed in section 12.2.4, and the details of Raman spectroscopy, and high accuracy measurements with the Menlo laser, are described in section 13.

12.2.2 Mira test of Raman dynamics

Raman Rabi flopping on the $|D_{5/2}\rangle \rightarrow |D_{3/2}\rangle$ transition using the Mira laser shows incomplete population transfer, as shown in figure 12.3. In the previous section, I introduced a model accounting for the repetition rate linewidth of the Mira laser, which has proven to be much broader compared to the Menlo frequency comb, as discussed in chapter 6. To support this line of argumentation, that the repetition rate stability causes the reduced coherence time, I conducted a test measurement to exclude the possibility that the "missing" population in the Raman Rabi flopping traces could be lost in other states than the two addressed specific $|D_{5/2}, m_j\rangle$ and $|D_{3/2}, m'_j\rangle$ states.

The idea is to try to move the *residual* population, after an initial (incomplete) π-pulse already moved the majority of the population to the $|D_{3/2}\rangle$ state. The experimental sequence is identical to normal Raman Rabi flopping, as sketched in figure 12.1, except that after the first exposure to resonant frequency comb light, the ion is optionally exposed to a second and third pulse, each time using the light shift method described in section 12.1.2. In between exposures, the population in the $|D_{3/2}\rangle$ state is removed from the Rabi cycle, using the 866 nm repumper. A scope trace of this part of the sequence is plotted in figure 12.5, in the case of three consecutive exposures of the ion to the Mira comb light. The resulting Rabi flopping traces are shown in figure 12.6. The red data points correspond to the normal Rabi flopping sequence, with only a single exposure to resonant frequency comb light. Similar as was shown in figure 12.3, less than 70 % of the population is transferred out of the initial $|D_{5/2}\rangle$ state.

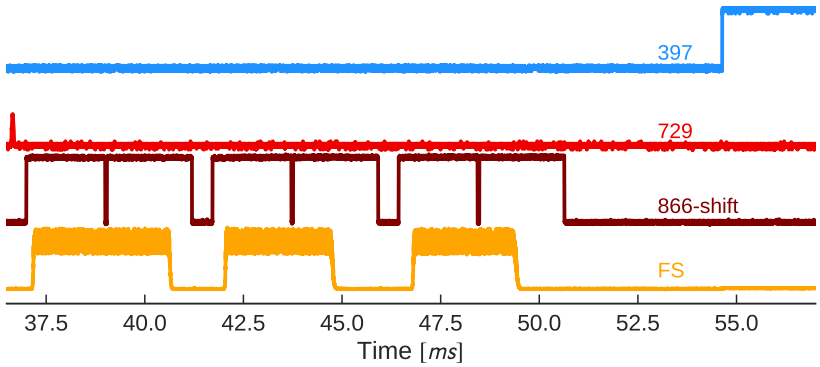

Figure 12.5: Experimental sequence used for the Mira population dynamics test, measured on photo detectors and an oscilloscope. The trace shows the relevant time between RAP state preparation with the 729 nm laser, and state read out with the 397 nm laser. In between, the ion is exposed to one to three pulses of resonant frequency comb (FS) light (3 exposures in the plotted trace), using the 866 nm light shift method as explained in section 12.1.1. The repumpers are also on during read out, and most importantly, the 866 nm repumper empties the $|D_{3/2}\rangle$ level in between frequency comb exposures, what is not shown in this trace.

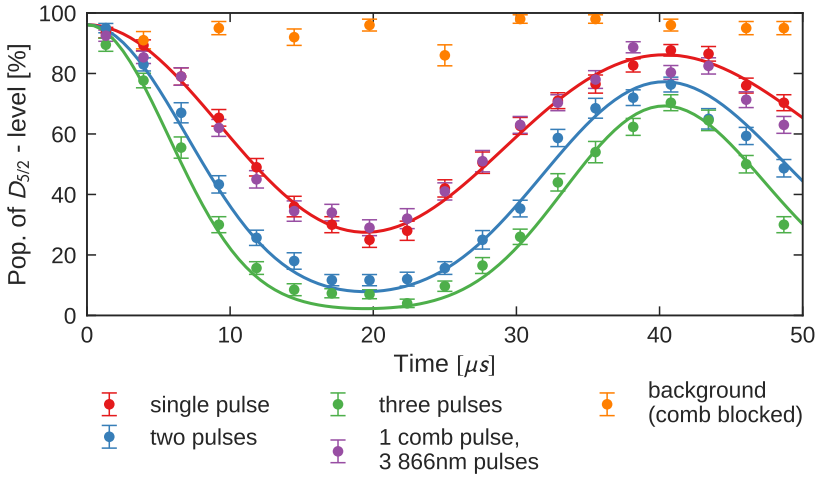

Figure 12.6: Testing the incomplete population transfer with the Mira laser. The population is initialized in the $|D_{5/2}, m_j = +3/2\rangle$ state using RAP with the 729 nm laser, and transferred to the $|D_{3/2}, m_j = -1/2\rangle$ state by the Mira frequency comb, using horizontally polarized light ($\sigma^+ + \sigma^-$).

The red line is a fit according to the model laser linewidth model (2.51),(12.1), described in section 12.2.1.

If we can treat the system as a true 2-level system, closed to the selected m_j states of the two D levels, we expect the population after the second pulse to be

$$P_2 = P_1^2 \,, \tag{12.2}$$

and after the third pulse

$$P_3 = P_2 \cdot P_1 = P_1^3 \,. \tag{12.3}$$

The blue and green data points in figure 12.3 represent the measured two and three pulse scenarios, while the corresponding solid lines are calculated from the fit to the red line, according to equations (12.2) and (12.3). These two calculated lines fit the data extremely well, supporting the assumption that we are indeed dealing with a 2-level system, i.e. without population loss in other than the addressed states, and that the linewidth model describes the data correctly.

As another check, the purple data was taken with a single exposure to the frequency comb light, but 3 exposures to the 866 nm light shift laser. The data shows that the light shift laser alone has no impact on the population, so that the dynamics is purely due to the frequency comb light, as expected. For completeness, a background trace (orange), with the Mira comb light mechanically blocked, is plotted as well, showing consistent RAP state preparation (see chapter 10.3.5), without loss of $|D_{5/2}\rangle$ population over time.

In conclusion, this test strongly supports the hypothesis, that the Mira laser repetition rate linewidth causes the incomplete population transfer, and that we are indeed dealing with a true 2-level system, addressing only the intended states.

12.2.3 Menlo Raman Rabi flopping

The repetition rate of the Menlo laser is much more stable than the Mira laser's, as discussed in depth in chapter 6. Thereby, the Menlo laser linewidth is not reducing the contrast in Raman Rabi flopping in the same way as the Mira laser, allowing close to 100 % population transfer with a π-pulse for achievable Rabi frequencies. One experiment showing Raman Rabi flopping with the Menlo laser is plotted in figure 12.7. The solid line shows a fit to the Bloch model, equation (2.47), and gives

$$\begin{aligned} \Omega/2\pi &= 4.121(3)\,\mathrm{kHz} \\ \tau &= 3.60(18)\,\mathrm{ms} \\ \text{contrast} &= 99.3(6)\,\% \,, \end{aligned} \tag{12.4}$$

where the contrast is defined as a simple scaling factor for the whole model. The Rabi frequency Ω can be considered large compared to the measured laser linewidth of 754(18) Hz, as shown in the next section, resulting in almost 100 % population transfer. The decoherence time τ is probably dominated by the stability of our frequency standard, referencing the comb's repetition rate, as discussed in chapter 5. Magnetic field fluctuations would impact the coherence of the $|D_{5/2}, m_j = +3/2\rangle \rightarrow |D_{3/2}, m_j = +3/2\rangle$ transition by a factor of $\approx$

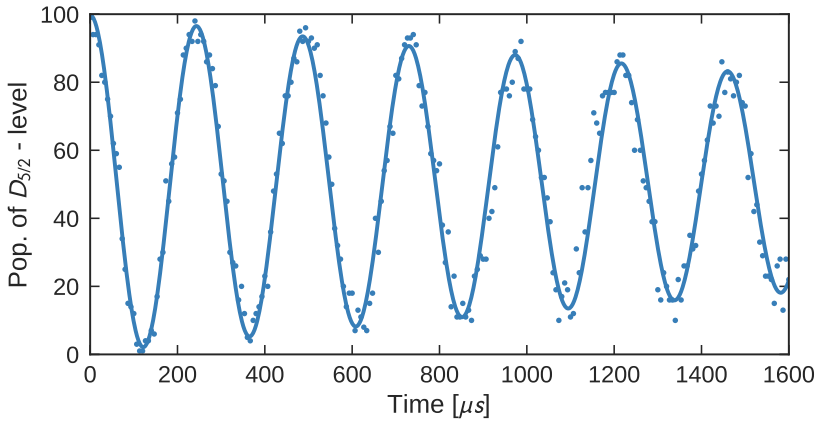

Figure 12.7: Raman Rabi flopping with the Menlo laser on the $|D_{5/2}, m_j = +3/2\rangle \rightarrow |D_{3/2}, m_j = +3/2\rangle$ transition, using vertically (π) polarized light.

3 less than for Rabi flopping on the $|S_{1/2}, m_j = -1/2\rangle \rightarrow |D_{5/2}, m_j = -5/2\rangle$ transition using the 729 nm laser, as shown in chapter 10.3.4, due to the different linear Zeeman shift.

12.2.4 Spectroscopy linewidth vs. Rabi frequency

The Rabi frequency Ω with which we drive the Raman transition can be directly observed in the Raman Rabi flopping experiments described in the previous sections. Ω depends linearly on the total laser intensity, or power for constant beam parameters, and the power broadened spectroscopic linewidth is proportional to Ω in the absence of any incoherent broadening. By extrapolating a series of spectroscopy measurements with different comb powers to zero power $\Omega = 0$, we can find the incoherent (laser) linewidth as the residual spectroscopic linewidth.

Figure 12.8 shows two Raman Rabi flopping on the $|D_{5/2}, m_j = -3/2\rangle \rightarrow |D_{3/2}, m_j = -3/2\rangle$ transition with the Menlo frequency comb for two different laser powers, the full output power (red), and half the power (blue), with otherwise unchanged experimental parameters. As expected, we observe about twice the Rabi frequency for twice the power. From the fits using the Bloch model, we find

$$\Omega_{\text{half}} = 0.809(3)\,(2\pi \cdot \text{kHz}) \tag{12.5}$$

$$\Omega_{\text{full}} = 1.527(3)\,(2\pi \cdot \text{kHz}) = 1.888(8)\;\Omega_{\text{half}}\,. \tag{12.6}$$

The power was experimentally adjusted by rotating the Menlo comb polarization against the horizontally aligned Glan-Taylor polarizer, as discussed in the end of chapter 11.4, and slight beam pointing instabilities or laser power drifts are likely candidates to cause the deviation from the exact factor of two. Additionally, the reduced contrast compared to the measurement shown in figure 12.7 suggests that the frequency comb was not perfectly on resonance.

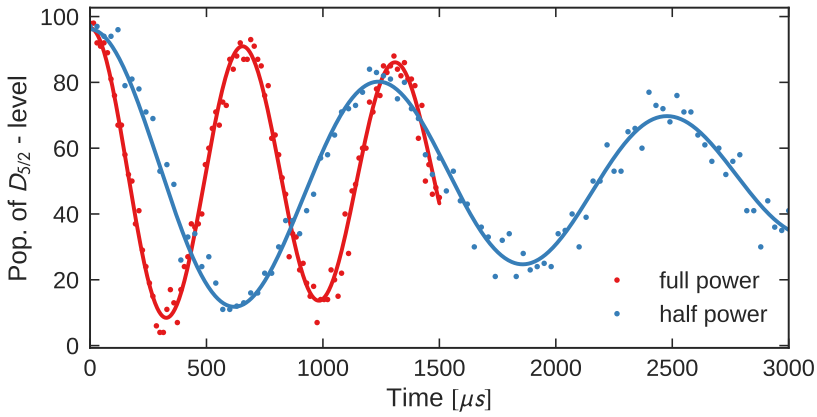

Figure 12.8: Raman Rabi flopping on the $|D_{5/2}, m_j = -3/2\rangle \rightarrow |D_{3/2}, m_j = -3/2\rangle$ transition, using π polarized light, for full Menlo laser power (red) and half the power (blue), for which we observe half the Rabi frequency, as expected.

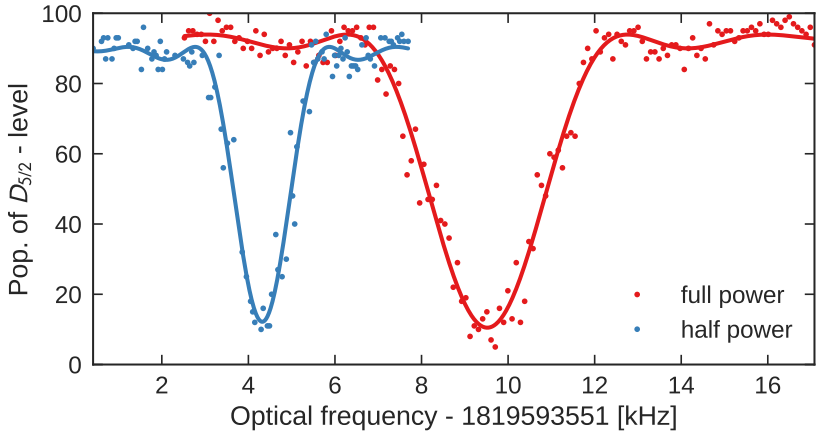

Figure 12.9: Menlo frequency comb spectroscopy on the $|D_{5/2}, m_j = -3/2\rangle \rightarrow |D_{3/2}, m_j = -3/2\rangle$ transition, using π polarized light, with the same experimental conditions as in the Raman Rabi flopping traces in figure 12.8. Light shift and the observed width of the transition are, as expected, about a factor of two larger for twice the power.

Between adjusting the laser power, we also took a spectroscopy trace on the same transition, plotted in figure 12.9. From a fit to a simple sinc^2 model, we

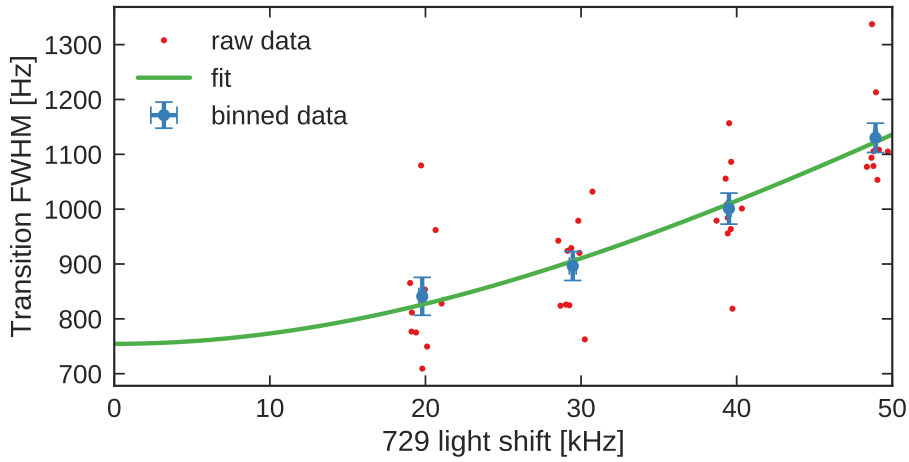

Figure 12.10: Spectroscopic linewidth using the *Menlo* laser for different laser intensities, measured by observing the 729 nm transition light shift.

extract the best fit parameters

$$\begin{aligned} \mathrm{FHWM}_{\mathrm{half}} &= 1.37(3)\,\mathrm{kHz} \\ \mathrm{center}_{\mathrm{half}} &= 4.32(2)\,\mathrm{kHz} \\ \mathrm{FHWM}_{\mathrm{full}} &= 2.87(4)\,\mathrm{kHz} \\ \mathrm{center}_{\mathrm{full}} &= 9.52(2)\,\mathrm{kHz}\,. \end{aligned} \tag{12.7}$$

The center is measured from the calculated, expected Zeeman shift, based on spectroscopy on two $|S_{1/2}\rangle \rightarrow |D_{5/2}\rangle$ transitions. Because the Rabi frequency is large compared to the incoherent laser linewidth, the spectroscopic linewidth scales linearly with the Rabi frequency. As expected, the frequency comb induced light shift is twice as high for twice the laser power, and on the order of 10 kHz, as calculated in section 12.3.2, for this transition.

Raman spectroscopy in Ca^+ close to the magic polarization[4] leads to small Rabi frequencies on the order of 1 kHz, such that the spectroscopic line-shape is influenced by incoherent broadening due to the frequency comb's repetition rate linewidth, as detailed in section 6.

Figure 12.10 shows the measured FWHM w_{tot} of a series of 40 spectroscopy measurements with 4 different *Menlo* comb intensities, determined by measuring the light shift f_{shift} on the 729 nm transition, as explained in chapter 11.4. The simple model

$$w_{\mathrm{tot}} = \sqrt{w_{\mathrm{laser}}^2 + (k \cdot f_{\mathrm{shift}})}\,, \tag{12.8}$$

where k is a scaling factor, relating Raman Rabi frequency and light shift, and w_{laser} is the incoherent laser linewidth we are trying to extract. The fit gives an estimate of

$$w_{\mathrm{Menlo}} = 754(18)\,\mathrm{Hz}\,. \tag{12.9}$$

[4]The magic polarization leads to zero differential light shift between the D-finestructure levels in Ca^+ , see chapter 12.3.2

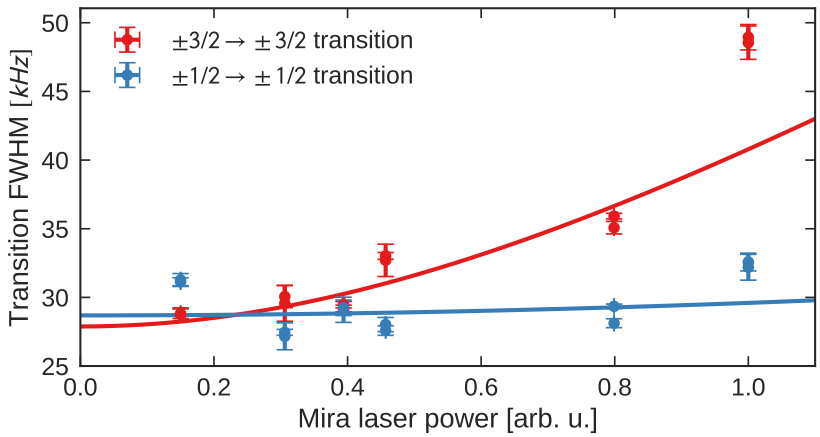

Figure 12.11: Spectroscopic linewidth of two $|D_{5/2}\rangle \rightarrow |D_{3/2}\rangle$ transitions with different m_j values, as indicated in the legend, using the *Mira* laser for different laser powers.

Note that this is *not* the linewidth of an individual comb tooth, but rather the residual, uncorrelated relative frequency fluctuation of two comb teeth which are spaced by the D-finestructure splitting of 1.8 THz. It is the relevant quantity for the Raman process though, and an estimate on the coherence time τ can be given by

$$\tau = \frac{2\sqrt{2\ln 2}}{w_{\text{Menlo}}} = 3.13(7)\,\text{ms}\,. \tag{12.10}$$

This value is close to the measured coherence time of about 3.60(18) ms in the Raman Rabi flopping experiments in section 12.2.3. The discrepancy might be explained by slightly different laser lock performances on the different days the data was taken.

A similar analysis for the *Mira* laser is presented in figure 12.11, for two transitions between different Zeeman sub-states. For the $|D_{5/2},\, m_j = \pm 1/2\rangle \rightarrow |D_{3/2},\, m_j = \pm 1/2\rangle$ transition, the Rabi frequency, even at maximum laser power, is too small to significantly power-broaden the transition. The $|D_{5/2},\, m_j = \pm 3/2\rangle \rightarrow |D_{3/2},\, m_j = \pm 3/2\rangle$ transition on the other hand is driven with about twice the Rabi frequency at the same laser power, according to the calculations presented in section 12.3.2, and shows significant power broadening. The extracted incoherent laser linewidths for the two transitions are

$$\begin{aligned} w_{\text{Mira}}\left(\pm 3/2\right) &= 27.9(9)\,\text{kHz} \\ w_{\text{Mira}}\left(\pm 1/2\right) &= 28.7(7)\,\text{kHz}\,, \end{aligned} \tag{12.11}$$

as expected independent of the specific transition in question. This linewidth is 38 times larger than for the Menlo laser, which is compatible with the electronically measured repetition rate stabilities discussed in chapter 6, and about 70 % of the laser linewidth extracted from the Rabi flopping traces presented in section 12.2.1. Again, this slight discrepancy arises probably due to differences in the daily performance of the Mira repetition rate lock stability.

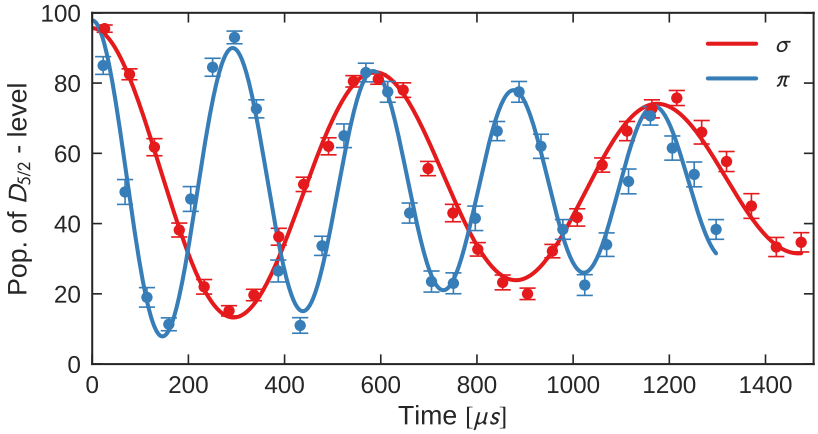

Figure 12.12: Rabi flopping between the $|D_{5/2}, m_j = -3/2\rangle$ and $|D_{3/2}, m_j = -3/2\rangle$ states ($\Delta m_j = 0$) with the Menlo frequency comb, using π (blue) and $\sigma^{\pm}$ (red) polarized light with the same intensity.

12.3 Polarization dependence

12.3.1 Measurement

The Raman Rabi frequency on the $|D_{5/2}\rangle \rightarrow |D_{3/2}\rangle$ transition depends on the addressed Zeeman sub-states and polarization of the frequency comb light. As explained in section 12.3.2, π and σ photons couple to different Zeeman sub-states of the $|P_{3/2}\rangle$ manifold, with different Clebsch–Gordan coefficients, in the Raman process. Figure 12.12 shows Rabi flopping between the $|D_{5/2}, m_j = -3/2\rangle$ and $|D_{3/2}, m_j = -3/2\rangle$ states using the Menlo frequency comb. As expected from the calculations in section 12.3.2, this $\Delta m_j = 0$ transition shows about twice the Rabi frequency driven with π polarized light compared to σ polarization. From the plotted fits to the Bloch model (chapter 2.2.1), we find

$$\Omega(\pi) = 1.705(5)\,\mathrm{kHz} \tag{12.12}$$
$$2\Omega(\pi) = 3.410(10)\,\mathrm{kHz} \tag{12.13}$$
$$\Omega(\sigma) = 3.426(7)\,\mathrm{kHz} \tag{12.14}$$

and within the uncertainty the same coherence time of

$$\frac{2}{\gamma_c}(\pi) = 1.78(12)\,\mathrm{ms} \tag{12.15}$$
$$\frac{2}{\gamma_c}(\sigma) = 1.60(15)\,\mathrm{ms}\,, \tag{12.16}$$

as expected.

The plot of the calculated Raman Rabi frequencies in figure 12.13, also shows a series of Rabi frequency measurements, extracted from individual Raman Rabi flopping traces with different polarization, using the Menlo comb. In our current setup, these measurements are actually quite tedious, since a change in

polarization is achieved by rotating the Glan-Taylor polarizer in front of the vacuum chamber. This rotation leads to a slight, but significant, misalignment of the comb beam on the ion. Thus, after each change of polarization, the beam needs to be realigned by maximizing the light shift induced on the 729 nm $|S_{1/2}\rangle \rightarrow |D_{5/2}\rangle$ transition, as described in chapter 11.4. This realignment also means that the intensity at the position of the ion will not be identical for each measurement plotted in figure 12.13, explaining the slight deviation from the theoretical prediction.

12.3.2 Calculated Raman Rabi frequency and light shifts

Knowing the spectrum of the frequency comb as shown in figure 4.11, and the structure of Ca^+, we can calculate the expected Raman Rabi frequencies and light shifts when driving the $|D_{5/2}\rangle \rightarrow |D_{3/2}\rangle$ transition.

Numerical calculations for typical[5] experimental conditions with the Menlo comb are plotted in figure 12.13 for the expected Raman Rabi frequency, and for the light shift induced by the frequency comb light itself. The light shift and Raman Rabi frequency are calculated as described in chapter 2.1.6, taking dipole coupling to all Zeeman resolved states in the Ca^+ ion into account. The dipole transition resonant Rabi frequencies (2.15) are calculated as explained in chapter 2.1.2, taking the measured spectrum, as shown in figure 4.11a, into account in form of a numerical integration over the wavelength weighted by the measured spectral density.

A "magic" polarization exists for some transitions, where the differential light shift vanishes, as indicated by the dashed horizontal line in the plot. The "magic" polarization for the $|D_{5/2}, m_j = 1/2\rangle \rightarrow |D_{3/2}, m_j = 1/2\rangle$ transition used for spectroscopy in chapter 13 is calculated to be around 78°. Note that the calculation is based on the measured decay rates in $^{40}Ca^+$, which have an uncertainty of up to 1 % on the absolute shifts of both D-finestructure levels. The magic polarization determined by spectroscopy is at 88(1)°, which seems reasonable since the slope of the light shift is not very steep for this transition. For the $|D_{5/2}, m_j = 3/2\rangle \rightarrow |D_{3/2}, m_j = 3/2\rangle$ transition, the calculated magic polarization is at 60°, and we measure 62(1)°, much closer due to the steeper slope.

[5] These curves are calculated based on the frequency comb induced light shift on the 729 nm transition, when the Menlo comb was working at its specified power. The output power of M-VIS degraded slowly by a factor of 2, until we fixed the alignment of the internal SHG crystal. Thus, some of the measurements shown in the previous sections were not taken at the nominal power, resulting in lower Rabi frequencies.

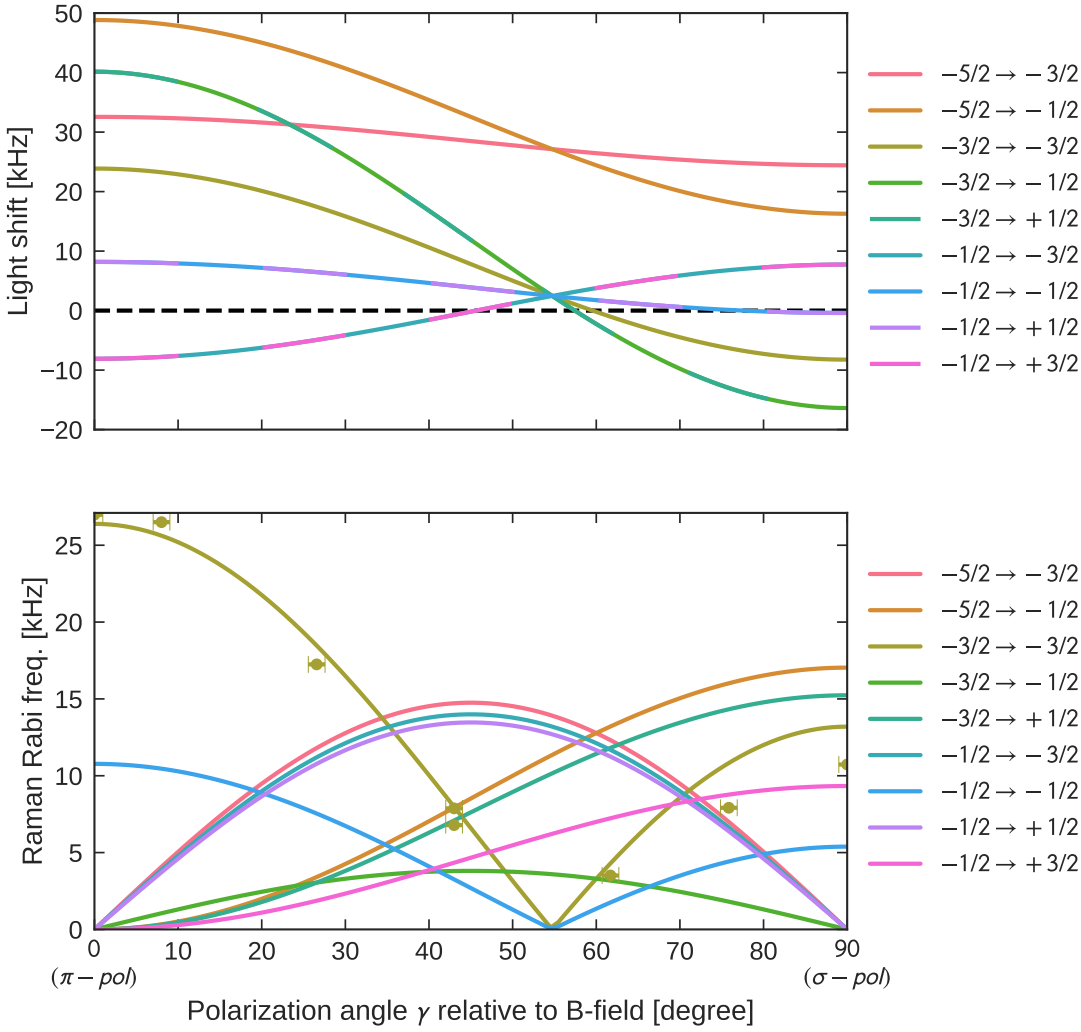

Figure 12.13: Numerical calculation of the Raman Rabi frequency and differential light shift for the $|D_{5/2}\rangle \rightarrow |D_{3/2}\rangle$ transition in Ca^+ using the Menlo frequency comb under typical experimental conditions, neglecting group velocity dispersion (GVD). The light shift induced by the frequency comb itself is not influenced by GVD, and for some transitions exists a "magic" polarization, where the differential light shift vanishes, as indicated by the dashed horizontal line, For the Raman Rabi frequency, GVD acts as a global scaling factor, independent of polarization. The experimentally achieved Rabi frequencies are almost one order of magnitude lower than calculated here, illustrating the big impact of GVD. The brown dots represent measured Rabi frequencies for the $|D_{5/2}, m_j = -3/2\rangle \rightarrow |D_{3/2}, m_j = -3/2\rangle$ transition, globally scaled to match the calculated curve.

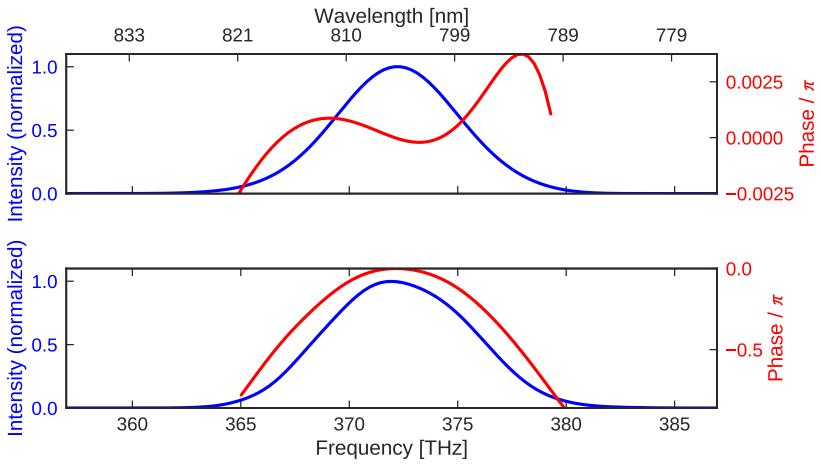

Figure 12.14: FROG measurement of the Mira spectrum. The GDD compensated intensity profile with almost constant spectral phase is shown (top), together with the uncompensated intensity and spectral phase (bottom). Note the very different vertical scales for the spectral phase in the two plots.

12.4 Raman Rabi frequency dependence on GDD

One main feature of the method of frequency comb driven Raman transitions is the dependence of the total Raman Rabi frequency on the spectral phase of the comb light, as discussed in chapter 3. If the spectral phase is not constant over the full spectrum of the comb light, destructive interference between all the Raman transitions, driven by different comb tooth pairs within the spectrum, reduces the total Raman Rabi frequency. The first approximation, neglecting higher order terms, only takes the group delay dispersion (GDD) into account, leading to a quadratic spectral phase over the spectrum. This effect is demonstrated in the following section experimentally using the *Mira* frequency comb.

12.4.1 Mira FROG Rabi comparison

To demonstrate the dependence of the total Raman Rabi frequency on the spectral phase, I took two Raman Rabi flopping measurements on $^{40}Ca^{+}$ between the D-finestructure states with the *Mira* frequency comb. The first measurement corresponds to measurements presented in section 12.2.1, where the external GDD is compensated with the prism compressor, as explained in chapter 4.3, leading to bandwidth limited fs pulses. A FROG measurement of these pulses, as discussed in chapter 7.2, is shown in figure 12.14 (top). The spectral phase is basically constant, deviating by less than 1 % of π over the whole spectrum. The residual phase modulation is due to higher order terms in the Taylor expansion (3.14), mostly reflecting third order dispersion, which cannot be compensated with the simple prism compressor.

In contrast to this measurement, figure 12.14 (bottom) shows a FROG measurement of the Mira fs pulses, when the prism compressor is completely by-

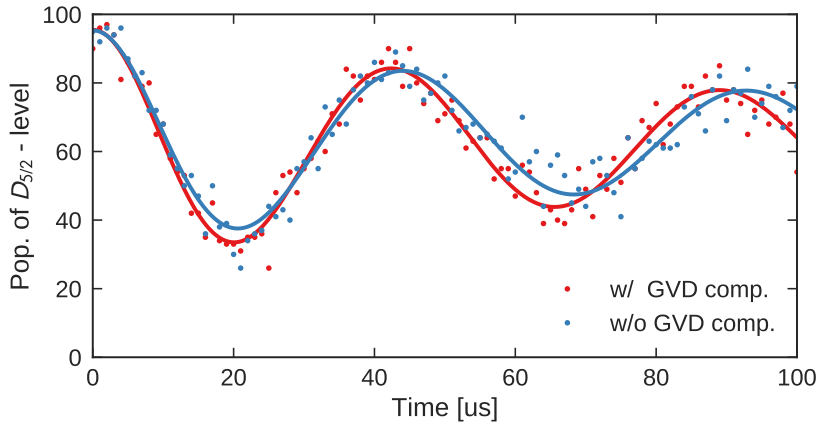

Figure 12.15: Raman Rabi flopping with the Mira comb. The red trace represents a measurement where GDD is compensated, as shown in the FROG measurement in figure 12.14 (top), and was taken with a total laser intensity characterized by the light shift measurement in figure 12.16 (also red). The blue curve is a measurement with the uncompensated spectrum in figure 12.14 (bottom), and the higher laser intensity (blue) in figure 12.16.

passed, so that the GDD from the optical elements in the beam-path is not compensated. The spectral phase is quadratic, as expected from second order dispersion (GVD) (3.17), and reaches a significant fraction of π over the spectral intensity profile. The measured spectral phase corresponds to a GDD of $2550\,\mathrm{fs}^2$, corresponding to a pulse broadening in time from bandwidth limited 63 fs to 129 fs. The GDD of $2550\,\mathrm{fs}^2$ corresponds to 57.2 mm of BK7 glass, or 16.3 mm of SF10, which roughly matches the estimated amount of glass of the lenses in the beam-path. For the same total frequency comb power, we would now expect a reduced Rabi frequency for the uncompensated spectrum, compared to the compensated.

Figure 12.15 shows two Raman Rabi flopping traces, taken with, and without GDD compensation, corresponding to the FROG measurements discussed above. The two traces show almost the *same* Rabi frequency of 21.1(1) kHz (compensated), and 20.3(1) kHz (uncompensated), with the GDD compensated Rabi frequency only slightly higher. However, the two traces were taken with *different* total frequency comb intensities. The different intensity in the two experiments comes from the fact, that laser power is lost due to reflections in the prism compressor for the GDD compensated measurement.

Figure 12.16 shows a measurement of the frequency comb intensity at the ion in terms of the 729 nm $|S_{1/2}\rangle \rightarrow |D_{5/2}\rangle$ transition light shift, as discussed in chapter 11.4. The total light shift of all comb teeth has to be summed up incoherently, as discussed in chapter 2.1.6, such that the spectral phase is irrelevant for this measurement. The light shift in the GDD compensated case is 61.5(2) kHz, and in the uncompensated case it is 75.5(3) kHz, corresponding to 23 % more power in the uncompensated case.

Figure 12.17 shows the calculated Raman Rabi frequency for the GDD com-

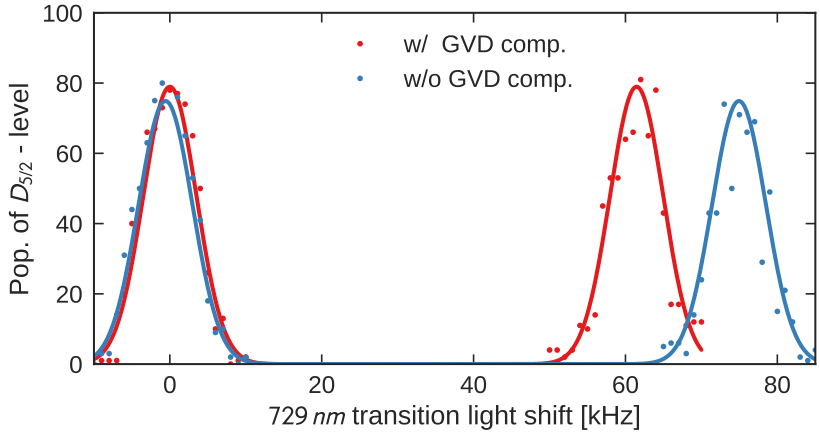

Figure 12.16: Intensity of the Mira comb in the experiments with (red) and without (blue) GVD compensation, via a 729 nm light shift measurement. The curves correspond to the Rabi flopping traces in figure 12.15 and the FROG measurements in figure 12.14.

pensated, lower power measurement in red, and the uncompensated measurement in blue. The Rabi frequency is *not* scaled to fit the measured Rabi frequency, but is only based on the measured light shift on the 729 nm transition (figure 12.16). Without GDD, the calculated Rabi frequencies for the measured intensities are 23 kHz, and 28 kHz, respectively, corresponding to the y-axis intercept in the plot. For the GDD compensated measurement, this calculated value matches well the measured value of 21.1(1) kHz. The vertical, dashed line in the plot at 2550 fs^2 intersects the uncompensated curve (blue) almost exactly at the measured Rabi frequency of 20.3(1) kHz. In conclusion, these measurements show that we understand, and are able to predict the dynamics of *frequency comb driven Raman transitions* based on the frequency comb spectrum and the addressed Atom.

12.4.2 GDD effect on the Raman Rabi frequency for different bandwidth

While the benefit of GDD compensation is outweighed by the loss of power in the prism compressor in our specific case, the measurement described in the previous section proves quantitatively the impact of the spectral phase on the total Raman Rabi frequency. In general, neglecting GDD, for instance by using high dispersive optics, or for frequency comb driven Raman transitions with an even broader spectrum, addressing transitions with higher transition frequency, can lead to almost total destructive interference.

Figure 12.18 illustrates this effect for the Ca^+ D-finestructure transition frequency of 1.8 THz by plotting the calculated Raman Rabi frequency against GDD, for frequency comb spectra of different bandwidth. Broad spectra compared to the transition frequency reach higher Rabi frequencies for perfectly

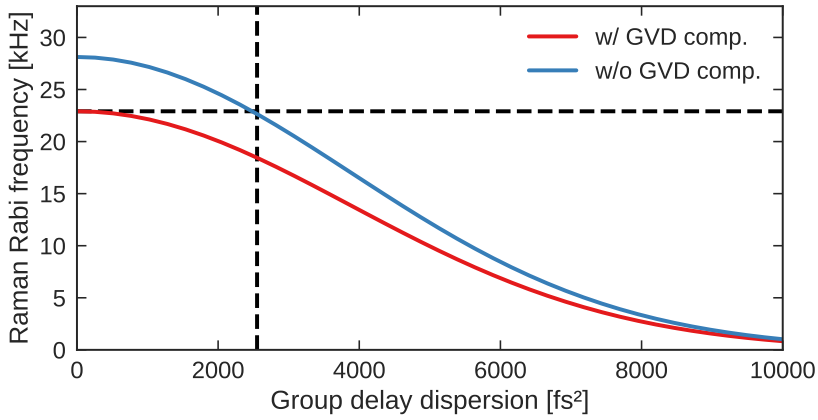

Figure 12.17: Calculated Mira Raman Rabi frequency as function of GDD, corresponding to the two measurements with (red) and without (blue) GDD compensation. The horizontal dashed line represents the measured Rabi frequency with GDD compensation. The vertical dashed line corresponds to GDD of 2550 fs^2, corresponding to the uncompensated spectrum from the FROG measurement in figure 12.14.

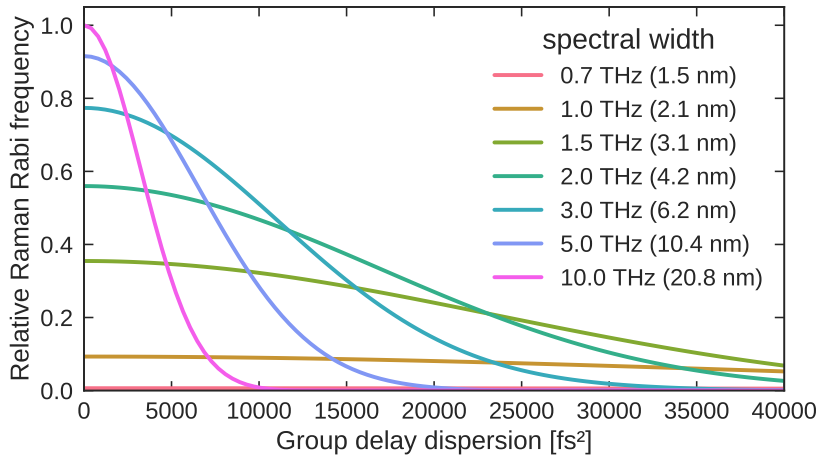

Figure 12.18: Calculated effect of group delay dispersion (GDD) on the Raman Rabi frequency Ω for Gaussian spectra of different width (FHWM) for our Ca^+ D-finestructure frequency of 1.8 THz. Broad spectra give higher Rabi frequency without GDD, but are more heavily affected by GDD.

compensated GDD, i.e. for a constant spectral phase. However, a broad spectrum is also stronger affected by the quadratic influence of GDD. The ideal laser for frequency comb driven Raman transitions has an infinitely broad spectrum with a constant spectral phase.

13

Menlo Comb Raman Spectroscopy

Spectroscopy on the Ca^+ D-finestructure is fundamentally limited only by the natural lifetimes of the D-states of more than 1 second each, resulting in sub-Hz transition linewidth. Experimentally, the observed line is much broader. On the one hand, power broadening is an effect controllable via the laser intensity. One the other hand, we are limited by decoherence due to magnetic field fluctuations and the repetition rate stability of the frequency comb, as discussed in chapter 6 and 12.2.4.

In figure 12.4, spectroscopy using the Mira laser was presented, where the precision with which we can determine the center of the line is limited to about 200 Hz by the laser linewidth of about 30 kHz[1].

For the Menlo laser, the laser linewidth of about 1 kHz allows to fit the center of the line with a statistical uncertainty of about 15 Hz for a measurement time of about 20 minutes, as shown earlier in figure 12.9. At this level of precision, the absolute accuracy of the measurement depends on external effects perturbing the atomic structure, and on the clock referencing the frequency measurement. In chapter 8, I analyze systematic shifts influencing the absolute accuracy of our spectroscopy measurements in detail, and the reference clock is thoroughly characterized in chapter 5.

In the following sections, I will present the experimental realization of high precision frequency comb Raman spectroscopy in $^{40}Ca^+$ using the Menlo laser, one of the main achievements of this thesis work. I describe how to experimentally average out the linear Zeeman shift in section 13.1, and how to pick the Zeeman sub-states least sensitive to perturbations in section 13.2. The experimental implementation is detailed in section 13.3, and the extrapolation of residual light shifts to zero is explained in section 13.4, before I finally present the experimental results combined with the calculated systematic shifts in sec-

[1] Typically, a factor of 100 between spectroscopic linewidth and uncertainty on the center of the line is easily achievable.

tion 13.5, to give the final value for the D-finestructure splitting in $^{40}Ca^{+}$.

13.1 Linear Zeeman shift elimination

The most significant effect shifting the atomic levels is the linear Zeeman shift, as discussed in chapter 8.1.1. Luckily, we can experimentally cancel this shift, by measuring not only a single Zeeman resolved D-finestructure transition, but a set of two transitions such that the total shift can be eliminated, as sketched in figure 13.1.

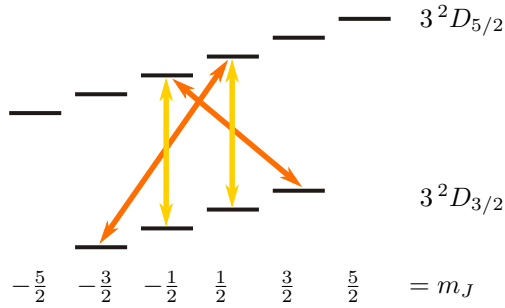

Figure 13.1: The linear Zeeman shift can be eliminated by averaging over two transitions with opposite shifts. An example of a transition pair with $\Delta m_j = 0$ (yellow), and $\Delta m_j = 2$ (orange) is shown in the drawing.

According to (8.7), the Zeeman shift of a transition

$$|D_{5/2},\, m_j\rangle \rightarrow |D_{3/2},\, m_j'\rangle \tag{13.1}$$

is

$$\Delta\nu = \frac{B\,\mu_B}{h}\left(g_{5/2}\,m_j - g_{3/2}\,m_j'\right) . \tag{13.2}$$

When we measure two Zeeman transitions, (1) and (2), and calculate the mean transition frequency

$$\frac{\Delta\nu^{(1)} + \Delta\nu^{(2)}}{2} = \frac{B\,\mu_B}{2\,h}\left(g_{5/2}\left(m_j^{(1)} + m_j^{(2)}\right) - g_{3/2}\left(m_j'^{(1)} + m_j'^{(2)}\right)\right) , \tag{13.3}$$

we can eliminate the shift by choosing

$$\begin{cases} m_j^{(1)} & = -m_j^{(2)} \\ m_j'^{(1)} & = -m_j'^{(2)} . \end{cases} \tag{13.4}$$

For instance, the two transitions

$$|D_{5/2},\, m_j^{(1)} = +1/2\rangle \rightarrow |D_{3/2},\, m_j'^{(1)} = +1/2\rangle \tag{13.5}$$

$$|D_{5/2},\, m_j^{(2)} = -1/2\rangle \rightarrow |D_{3/2},\, m_j'^{(2)} = -1/2\rangle \tag{13.6}$$

can be chosen.

13.2 Possible Zeeman transitions

In total, 18 distinct Zeeman resolved Raman transitions can be driven between the six m_j states of the $D_{5/2}$ manifold, and the four m_j states of the $D_{3/2}$ manifold in Ca^{+} . Due to the selection rule $\Delta m_j = 0, \pm 1, \pm 2$, depending on the polarization of the frequency comb light, 5 states of the $D_{5/2}$ manifold can be reached from each of the $|D_{3/2},\, m_j = \pm 1/2\rangle$ states, and 4 from each of the $|D_{3/2},\, m_j = \pm 3/2\rangle$ states, respectively.

Four pairs of transitions are degenerate in frequency, when the approximate Landé g-factors, given in table 8.1

$$g_{5/2} = 6/5 \tag{13.7}$$
$$g_{3/2} = 4/5 \tag{13.8}$$

are used for the calculation. These are the transition pairs $|D_{5/2},\, m_j\rangle \rightarrow |D_{3/2},\, m_j'\rangle$ with

$$m_j = -5/2 \rightarrow m_j' = -3/2 \qquad \Delta m = +1$$
$$m_j = -1/2 \rightarrow m_j' = +3/2 \qquad \Delta m = +2$$

and

$$m_j = -3/2 \rightarrow m_j' = -3/2 \qquad \Delta m = 0$$
$$m_j = +1/2 \rightarrow m_j' = +3/2 \qquad \Delta m = +1$$

and

$$m_j = -1/2 \rightarrow m_j' = -3/2 \qquad \Delta m = -1$$
$$m_j = +3/2 \rightarrow m_j' = +3/2 \qquad \Delta m = 0$$

and

$$m_j = +1/2 \rightarrow m_j' = -3/2 \qquad \Delta m = -2$$
$$m_j = +5/2 \rightarrow m_j' = +3/2 \qquad \Delta m = -1$$

These transition pairs are actually split by $3.2\,\mathrm{kHz\,G^{-1}}$, taking the correct electron spin factor $g_s \neq 2$ into account, which is, depending on the exact transition, about 2 to 3 orders of magnitude smaller than the total transition Zeeman shift.

The sub-kHz linewidth observed in spectroscopy using the Menlo laser, shown in section 12.2.4, allows to resolve this splitting, and using either pure σ polarized light with $\Delta m = \pm 2$, or pure π polarized light with $\Delta m = 0$, will only allow one of the transitions of each pair.

However, the two transitions

$$|D_{5/2},\, m_j^{(1)} = +1/2\rangle \rightarrow |D_{3/2},\, m_j'^{(1)} = +1/2\rangle \tag{13.9}$$
$$|D_{5/2},\, m_j^{(2)} = -1/2\rangle \rightarrow |D_{3/2},\, m_j'^{(2)} = -1/2\rangle \tag{13.10}$$

are the preferred ones for high precision spectroscopy. First of all, they are not part of the described near degenerate transitions, thereby avoiding possible asymmetries in the spectroscopic lines, which could arise from off-resonantly driving a second transition at the same time. Additionally, they show the minimum difference in transition frequency, making it easier to tune the frequency comb's repetition rate between the two transitions for the linear Zeeman shift elimination, discussed in section 13.1. And last but not least, these transitions have a "magic polarization", for which the second most important external shift, the light shift induced by the frequency comb itself, vanishes, as discussed in chapter 12.3.2.

13.3 Experimental implementation

The experimental sequence for each transition is implemented exactly as the Raman Rabi flopping experiments, described in chapter 12.1.1, except that it is the repetition rate of the frequency comb, and not the pulse time, which is varied between individual measurements.

As I will explain in the next section, we need to take data with different laser intensities to eliminate residual light shifts. This is done fully automated, either via the ND filter wheel, or via the motorized waveplate plus polarizer, as discussed in section 12.1.1.

For each chosen laser intensity, a previously calibrated pulse time, i.e. 866 nm light shift laser off time (remember figure 12.1), is used to achieve the maximum possible contrast via a π-pulse. The Menlo frequency comb's repetition rate, i.e. the Raman two photon detuning, is randomly scanned over the expected transition frequency, typically taking 100 repetitions at each detuning. The repetition rate is RF locked to the DDS, and can be controlled as described in chapter 4.1.3.

The two transitions for linear Zeeman shift elimination are probed interleaved, e.g. one data point (100 repetitions) is taken for each transition before switching to the other, by sweeping the repetition rate to the next transition. One data point takes typically about 10 s on average, and typically 30 points per transition are required to achieve about 15 Hz resolution on the fitted line center. After the frequency comb spectroscopy sequence, the comb light intensity at the ion is measured via the light shift imposed on the 729 nm $|S_{1/2}\rangle \rightarrow |D_{5/2}\rangle$ transition as described in chapter 11.4. The whole experiment, i.e. frequency comb spectroscopy of two Zeeman transitions followed by a 729 nm light shift measurement takes about 20 minutes.

Such an experiment is then repeated many times, typically in a fully automated, unattended, over night measurement series, for different laser intensities, as described in the following section.

13.4 Residual light shift extrapolation

As discussed in chapter 12.3, we will choose the "magic polarization" for spectroscopy, for which the differential light shift of the D-finestructure transition vanishes. In a real world experiment, we can set the polarization with respect to the magnetic field quantization axis only with a given accuracy. From experience, we know that we can adjust the absolute polarization with about 1° accuracy, and the relative polarization angle much better, about 5′, via an adjustable rotation mount[2] holding the Glan-Taylor polarizer.

The differential light shift can change by hundreds of Hz per degree, for typical laser intensities in our experiments, as discussed in chapter 12.3, which is larger than the absolute accuracy we aim for. Therefore, we eliminate the residual differential light shift due to imperfect polarization alignment, by measuring the D-finestructure at different laser intensities on the ion, precisely determined

[2] Thorlabs PRM1/M

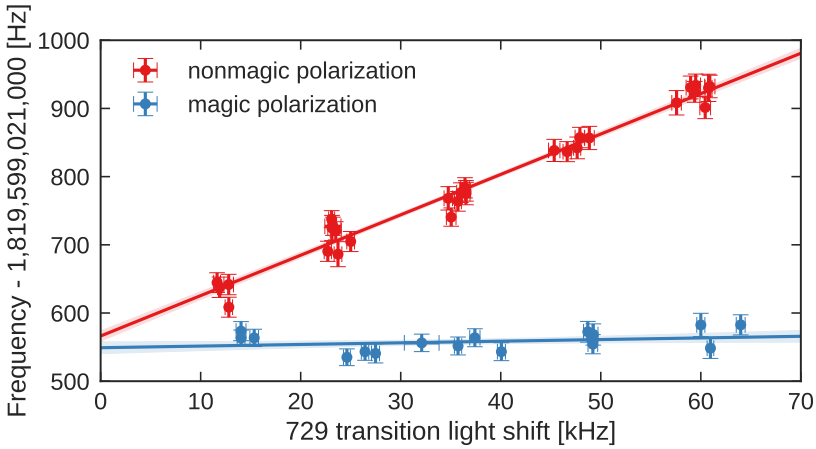

Figure 13.2: Frequency comb spectroscopy power extrapolation with the "magic" (88(1)°, blue) and non-magic (78(1)°, red) polarization on the $|D_{5/2}, m_j = \pm 1/2\rangle \rightarrow |D_{3/2}, m_j = \pm 1/2\rangle$ transition. The relative polarization difference is 9.8(1)°.

by a light shift measurement with the 729 nm laser, as described in section 11.4, and extrapolating to zero intensity.

Figure 13.2 illustrates the impact of choosing the magic polarization. The red line is a linear fit to a series of measurements of the $|D_{5/2}, m_j = \pm 1/2\rangle \rightarrow |D_{3/2}, m_j = \pm 1/2\rangle$ transition with non-magic, polarized light. The blue line represents a measurement series taken directly afterwards, just with the polarization adjusted to be "magic", leading to close to zero differential light shift for arbitrary frequency comb intensity. The small difference in polarization has a big impact on the slope of the extrapolation, and thereby on the error on the intercept.

For the final measurement of the D-finestructure frequency in $^{40}Ca^{+}$, three measurement series with the magic polarization were taken, as presented in figure 13.3. The different colored data points correspond to separate measurement series on different days, with slightly adjusted polarization, to become even more "magic". A linear model fitted to each data set, plotted as solid lines together with the $1\,\sigma$ confidence bounds as shaded areas around the line, yields

$$\begin{aligned} f_{\text{blue}} &= 1\,819\,599\,021\,567(17)\,\text{Hz} \\ f_{\text{red}} &= 1\,819\,599\,021\,532(9)\,\text{Hz} \\ f_{\text{green}} &= 1\,819\,599\,021\,549(9)\,\text{Hz} \end{aligned} \tag{13.11}$$

for the zero intensity intersect. Note that the measurements presented in this section have not yet been corrected for the systematic shifts discussed in chapter 8. The final result is analyzed in the following section.

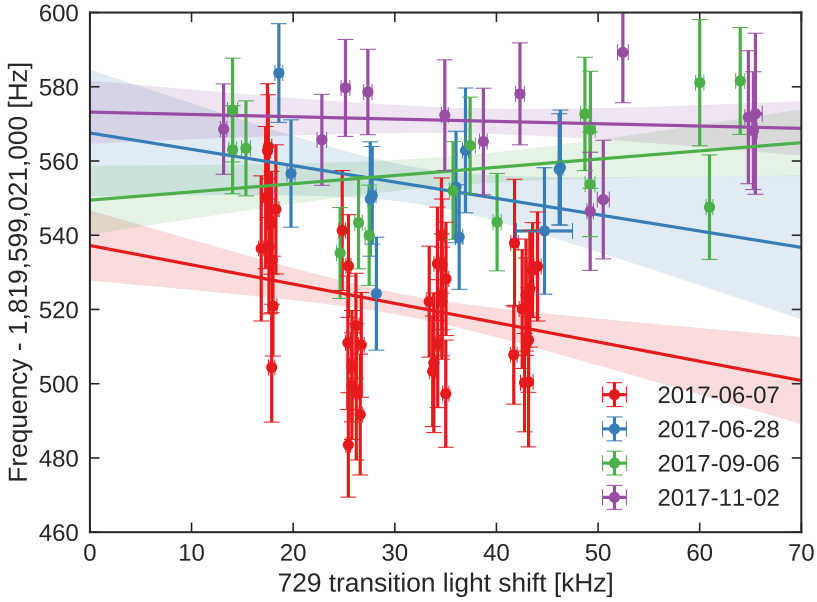

Figure 13.3: Frequency comb spectroscopy intensity extrapolation. 68 % confidence bounds as shaded regions around the fitted line. Data are not corrected for systematic shifts.

13.5 Absolute $^{40}Ca^{+}$ D-finestructure frequency evaluation

The final D-finestructure frequency is evaluated including all previously discussed aspects:

1. Spectroscopy on the non near-degenerate $|D_{5/2}, m_j = \pm 1/2\rangle \rightarrow |D_{3/2}, m'_j = \pm 1/2\rangle$ transitions.
2. Averaging over the $m_j = m'_j = +1/2$ and $m_j = m'_j = -1/2$ transition to eliminate the linear Zeeman shift.
3. Choosing the "magic polarization" to minimize the differential light shift, and interpolating to zero laser intensity to eliminate residual light shifts.
4. Correction for systematic shifts.

The final result for the D-finestructure transition frequency $f_{\text{D-fine}}$ is composed of the measurements presented in section 13.4, and the evaluation of systematic shifts in chapter 8. From the three independent measurements (13.11) presented in the previous section, I calculate the mean, weighted by the inverse statistical uncertainty of each measurement. This value is

$$f_{\text{D-fine, mean}} = 1\,819\,599\,021\,546\,\text{Hz}\,. \tag{13.12}$$

The uncertainty of a typical individual measurement, simply taking the statistical uncertainty of the intercept for the intensity interpolation, is

$$S_{\text{fit}} = 10\,\text{Hz}\,. \tag{13.13}$$

However, we are not a metrology institution, and the spread of the intercepts might indicate very small shifts we do not fully control yet. Therefore, we conservatively add a separate uncertainty of

$$S_{\text{sys}} = 30\,\text{Hz}\,, \tag{13.14}$$

accounting for these additional systematic effects.

From the evaluation of systematic shifts in chapter 8, we concluded that the only significant contribution is the second order Zeeman shift, contributing to a positive frequency shift of the D-finestructure transition of +21.833(31) Hz, such that this value needs to be subtracted from the measured number (13.12).

Finally, the corrected D-finestructure frequency in $^{40}Ca^{+}$ is

$^{40}Ca^{+}$ D-finestructure frequency

$$f_{\text{D-fine}} = 1\,819\,599\,021\,524\,\text{Hz} \pm 10\,\text{Hz} \pm 30\,\text{Hz} \tag{13.15}$$

As discussed above, the uncertainty of 10 Hz represents the statistical uncertainty of a single overnight measurement run, and the additional uncertainty of 30 Hz represents possible systematic effects between measurement runs. Based on the assumption that these two uncertainties represent uncorrelated, Gaussian variables, we can combine them to the total uncertainty of $\pm\sqrt{10^2 + 30^2}\,\text{Hz} = \pm 32\,\text{Hz}$.

The final value (13.15) is in agreement with a value by Yamazaki et al. published in 2008 [A36][3]. They measured a value of 1.819 599 021 504(37) Hz using direct Raman spectroscopy with two phase locked CW lasers. Their absolute accuracy was limited by their GPS referenced frequency standard, and unknown electric quadrupole shifts in their Paul trap due to patch potentials. While I reach a similar absolute accuracy as, the method of frequency comb driven Raman transitions is much easier to implement for the large transition frequency in the THz-range. Yamazaki et al. use two separate Raman lasers, which need to be phase locked, bridging the large frequency gap via an optical comb generator [A37]. Due to their preparation scheme, not resolving the Zeeman sub-states, but simply preparing the $|D_{3/2}\rangle$ state by turning off the 866 nm repumper before the 397 nm Doppler cooling beam, they only reach about 10 % contrast in their spectroscopy measurements. To eliminate light shifts, they use a similar laser intensity extrapolation as I do. However, their intensity scale relies simply on the laser power outside the vacuum chamber, and not on a real intensity measurement on the ion, as I implemented via the 729 nm transition light shift method, discussed in chapter 11.4.

Another comparison of the final D-finestructure frequency with previous measurements, however, does not hold. The 397 nm $|S_{1/2}\rangle \rightarrow |P_{1/2}\rangle$ transition, and the 866 nm $|D_{5/2}\rangle \rightarrow |P_{3/2}\rangle$ transition have been measured in the group of Piet

[3] Their trap is described in a separate publication [A131].

Schmidt at the PTB [A48, A49], and the 729 nm $|S_{1/2}\rangle \rightarrow |D_{5/2}\rangle$ transition has been precisely determined with 1 Hz resolution by Chwalla et al. [A88]. The transition frequencies f_i for the "closed" transition

$$|S_{1/2}\rangle \xrightarrow{397\,\mathrm{nm}} |P_{1/2}\rangle \xrightarrow{866\,\mathrm{nm}} |D_{3/2}\rangle \xrightarrow{\text{D-fine}} |D_{5/2}\rangle \xrightarrow{729\,\mathrm{nm}} |S_{1/2}\rangle \tag{13.16}$$

should obey

$$f_{\mathrm{closed}} = f_{397} - f_{866} + f_{\text{D-fine}} - f_{729} = 0\,. \tag{13.17}$$

However, we find

$$\begin{aligned} f_{\mathrm{closed}} = \;& + \; 755\,222\,765\,896(88)\,\mathrm{kHz} \\ & - \; 346\,000\,234\,867(96)\,\mathrm{kHz} \\ & + \; 1\,819\,599\,021\,524(32)\,\mathrm{Hz} \\ & - \; 411\,042\,129\,776\,393.2(10)\,\mathrm{Hz} \\ = \;& 274(130)\,\mathrm{kHz} \neq 0\,. \end{aligned} \tag{13.18}$$

This discrepancy is significant with about $2\,\sigma$ deviation from zero, and exists also for the isotope shift measurements presented in chapter 14. In the discussion there, it will become evident that the problem lies in the underestimated errors of measurements of the $|S_{1/2}\rangle \rightarrow |P_{1/2}\rangle$ and $|D_{5/2}\rangle \rightarrow |P_{3/2}\rangle$ transitions, and not the D-finestructure measurement presented here.

13.6 Conclusion

In this chapter, I presented the main experimental technique developed in this thesis work, frequency comb driven Raman transitions in the THz range.

Section 12.1 focused on the experimental implementation, especially the method of using a separate CW laser at 866 nm to shift the Raman transition into and out of resonance with the frequency comb light.

In section 12.2, I showed experimental results comparing the dynamics of the two different frequency comb systems used, the Mira and the Menlo system. While the Mira system offers high spectral bandwidth compared to the Menlo system, we experienced difficulties to stabilize the Mira's repetition rate to a level which allows high precision spectroscopy, reflected in the much broader laser linewidth. With the Menlo system, I achieved close to 100 % contrast for Rabi oscillations between the D-finestructure levels.

The impact of the polarization of the frequency comb light on the differential light shift and total Raman Rabi frequency on the $|D_{5/2}\rangle \rightarrow |D_{3/2}\rangle$ transition was demonstrated in section 12.3. For some specific Zeeman resolved transitions, there exists a "magic" polarization, where the differential light shift vanishes.

In section 12.4, the effect of group delay dispersion (GDD) was shown experimentally with the Mira laser, by measuring the Raman Rabi frequency for GDD compensated, bandwidth limited fs pulses versus the uncompensated scenario.

Finally, in section 13, I presented the direct measurement of the $^{40}Ca^{+}$ D-finestructure transition frequency, using frequency comb driven Raman transitions with the Menlo system. The high accuracy measurement yields a value of 1 819 599 021 524(32) Hz, in agreement with a previous measurement, and thereby highlighting the huge potential of the presented method.

Be precise. A lack of precision is dangerous when the margin of error is small.

Donald Rumsfeld

14

Spectroscopic Isotope Shifts

See appendix B for a revised analysis

The energy of a spectral line is a characteristic property of an element, that means a characteristic of the number of protons in the nucleus. However, precision spectroscopy reveals a slight dependence of the transition energy on the number of neutrons in the core, so that different isotopes of an element have slightly different transition energies between the same electronic levels. This effect is called the spectroscopic isotope shift [B6, R13] and can be divided into two leading contributions.

One obvious difference between isotopes is the different mass of the core. The electronic levels are simultaneous eigenfunctions of angular momentum and energy, where the angular momentum comes in fixed, quantized values, such that the energy must change with a change in mass. This effect is called the *normal mass shift* (NMS). Besides, for a multi-electron system, i.e. all elements heavier than hydrogen, the correlation between the electrons gives rise to the *specific mass shift* (SMS), and the total shift is simply called the *mass shift* (MS).

The second important effect originates from the difference in nuclear charge distribution when neutrons are added to the nucleus, and is called the *field shift* (FS). Even though the nucleus is small compared to the size of the atom, the electron's wave-function overlaps with the nuclear charge distribution, influencing the electronic energy levels. For S-orbitals, the only non-relativistic orbitals with non-zero probability density at the origin, the effect is obviously the largest. To lowest order, the charge distribution can be described by its second moment, the mean charge radius squared $\langle r_c^2 \rangle$, which is why the field shift is also sometimes called the *volume shift*.

Isotope shift measurements have the potential to discover new physics beyond the standard model, for instance in finding new bosons mediating new forces [A54, A53, A56]. While large-scale experiments such as the Large Hadron Collider probe the high end of the energy range, up to particle masses of some

TeV, atomic physics experiments benefit from unprecedented accuracy in the optical regime, sensitive to new bosons in the sub-MeV range. The impact of the isotope measurements presented here on this field is discussed in the end of this chapter.

In the following sections, I will first describe the basic theoretical tools needed to extract the relevant quantities such as mass and field shift constants, and the mean nuclear charge radii, from optical transition measurements in a series of isotopes. Afterwards, I will present, to the best of my knowledge, the most precise optical isotope shift measurements conducted so far, followed by a discussion about their impact.

14.1 Theoretical treatment

The isotope shift of a transition i is defined as the difference in transition frequency between isotope A and A' as

$$\delta\nu_i^{AA'} \equiv \nu_i^A - \nu_i^{A'} \,, \tag{14.1}$$

where ν_i^A and $\nu_i^{A'}$ are the transition frequencies of the two isotopes. The two leading contributions to the isotope shift are the mass shift (MS) and field shift (FS)

$$\delta\nu_i^{AA'} = \delta\nu_{i,\mathrm{MS}}^{AA'} + \delta\nu_{i,\mathrm{FS}}^{AA'} \,. \tag{14.2}$$

14.1.1 Mass shift

The mass shift can be partly calculated based on the simple assumption of a two body system, a single electron and the nucleus. This is the normal mass shift (NMS)

$$\delta\nu_{i,\mathrm{NMS}}^{AA'} = m_e\nu_i^A \frac{m_{A'} - m_A}{m_A\,(m_{A'} + m_e)} = K_{i,\mathrm{NMS}}\frac{1}{\mu} \,, \tag{14.3}$$

where m_e is the electron mass, m_A and $m_{A'}$ are the masses of the two isotopes, and the mass factor μ is given by

$$\mu = \frac{m_A(m_{A'} + m_e)}{m_{A'} - m_A} \approx \frac{m_A m_{A'}}{m_{A'} - m_A} \,. \tag{14.4}$$

The factor $K_{i,\mathrm{NMS}} = m_e\nu_i^A$ is called the normal mass shift constant. The normal mass shift is always positive for the heavier isotope, i.e. the heavier isotope has larger transition frequency. The NMS becomes less relevant for heavy elements since $\mu \propto m_A^2$. To account for the other electrons in a multi-electron system, we can add another constant, the specific mass shift constant $K_{i,\mathrm{SMS}}$, which is not straight forward to calculate since it depends on the correlation between all electrons [A132]. The specific mass shift (SMS) can be positive or negative, and can outweigh the NMS. In total, the mass shift can be written as

$$\mu\delta\nu_{i,\mathrm{MS}}^{A,A'} = \left(K_{i,\mathrm{NMS}} + K_{i,\mathrm{SMS}}\right) = K_i \,, \tag{14.5}$$

with the mass shift constant K_i.

14.1.2 Field shift

The field shift (FS) is proportional to the difference in the charge distribution $\lambda^{A,A'}$ of the nucleus

$$\delta\nu_{i,\mathrm{FS}}^{AA'} = F_i\,\lambda^{AA'}\,, \tag{14.6}$$

where F_i is the field shift constant, and $\lambda^{AA'}$ can be written as

$$\lambda^{AA'} = \delta\left\langle r_c^2\right\rangle^{AA'} + \frac{C_2}{C_1}\delta\left\langle r_c^4\right\rangle^{AA'} + \frac{C_3}{C_1}\delta\left\langle r_c^6\right\rangle^{AA'} + \dots\,. \tag{14.7}$$

If the electron wave-function can be considered constant over the nucleus, we can neglect higher order moments and get

$$\lambda^{AA'} \approx \delta\left\langle r_c^2\right\rangle^{AA'}\,. \tag{14.8}$$

The FS can be positive or negative, depending on whether the upper or lower state has a higher electronic charge density at the nucleus, and is usually on the same order of magnitude as the mass shift.

14.1.3 Splitting isotope shift

The so-called splitting isotope shift (SIS) is the difference of the fine-structure for different isotopes [A133]

$$\delta\nu_{\mathrm{SIS}}^{AA'} = \delta\nu_i^{AA'} - \delta\nu_j^{AA'}\,. \tag{14.9}$$

The SIS of the $D1$, $D2$ lines in ^{6,7}Li has been used to benchmark state of the art QED calculations [A51, A52].

14.1.4 Modified isotope shift

Adding the field and mass shift contributions, we can write eq. (14.2) as

$$\mu\delta\nu_i^{AA'} = K_i + F_i\,\mu\,\delta\left\langle r_c^2\right\rangle^{AA'} \tag{14.10}$$

where $\mu\delta\nu_i^{AA'}$ is called the modified isotope shift. Using equation (14.10) for a *single* transition, and taking values for the charge radii from other sources, we can directly extract the field and mass shift constants by plotting the modified isotope shift vs. the modified charge radius. This analysis is shown in section 14.3, and also allows to predict new best estimates for the charge radii.

14.1.5 The King plot

If the isotope shift has been measured for more than one transitions, we can write up equation (14.10) for a second transition j and eliminate the common charge radius by combining the two equations to

$$\mu\delta\nu_i^{AA'} = K_i - \frac{F_i}{F_j}K_j + \frac{F_i}{F_j}\,\mu\,\delta\nu_j^{AA'}. \tag{14.11}$$

Plotting the modified isotope shifts $\mu\delta\nu_{i,j}^{AA'}$ against each other, equation (14.11) suggests a linear dependence. A linear fit then allows to extract the ratio of the

field shift constants $\frac{F_i}{F_j}$, and the difference in mass shift constants from the slope and intercept, respectively. This plot is called the King plot [A55]. If we had measured more than two transitions, one could plot each modified isotope shift on a separate axis to obtain a multidimensional King plot [A47, A134]. This multidimensional King plot can be fitted using multidimensional least squares, giving more consistent results than fitting individual 2-d King plots.

14.2 Isotope shift measurements

We measured the absolute transition frequencies of the two transitions, $|S_{1/2}\rangle \rightarrow |D_{5/2}\rangle$ at 729 nm, and the D-finestructure $|D_{3/2}\rangle \rightarrow |D_{5/2}\rangle$ transition, for all stable, even isotopes in Ca^+, that means the isotopes with nucleon number 40, 42, 44, 46, 48. The isotope selective ionization scheme, explained in section 10.1.1, allows us to load and trap a single Ca^+ ion of any naturally abundant Calcium isotope[1]. The abundance of the Calcium isotopes is tabulated in table A.3. Interesting to mention is that $^{46}Ca^+$ is actually the least abundant naturally occurring isotope of all elements, with a relative abundance of 4×10^{-5}, and that calcium is the element with the largest number of stable isotopes. Additionally, calcium is particularly interesting for nuclear theory, since there are two "double magic" isotopes, $^{40}Ca^+$ and $^{48}Ca^+$, both having closed shells for the protons as well as for the neutrons in the nuclear shell model [A136]. The closed shells suggest that $^{40}Ca^+$ and $^{48}Ca^+$ have the same nuclear charge distributions, a fact we will exploit to separate mass shift and field shift in section 14.3.

14.2.1 D-finestructure

The measurements of the D-finestructure transition for the different isotopes were carried out using frequency comb driven Raman transitions, as described in this thesis, in the same way as the measurement of $^{40}Ca^+$ described in chapter 13. The intercepts, extracted from the linear fits shown in figure 14.1, relative to the $^{40}Ca^+$ value of 1.819 599 021 524 MHz, are in MHz

$$\begin{aligned} \delta\nu_D^{40,42} &= -3.519\,890(46) \\ \delta\nu_D^{40,44} &= -6.792\,451(45) \\ \delta\nu_D^{40,46} &= -9.901\,512(44) \\ \delta\nu_D^{40,48} &= -12.746\,597(45) \end{aligned} \tag{14.12}$$

The given uncertainties $S_{40,A'}$ are calculated based on the assumption that the individual isotope measurement is independent from the previous $^{40}Ca^+$ measurement to

$$S_{40,A'} = \sqrt{S_{40}^2 + S_{A'}^2}\,, \tag{14.13}$$

where $S_{40} = 32$ Hz is the error on the $^{40}Ca^+$ measurement presented in chapter 13.5, and the error of each isotope measurement is given by

$$S_{A'} = \sqrt{S_{\text{fit}}^2 + (30\,\text{Hz})^2}\,, \tag{14.14}$$

[1] However, $^{43}Ca^+$ has nuclear spin and thus hyperfinestructure [A135], which is why we cannot directly cool this isotope in our current setup.

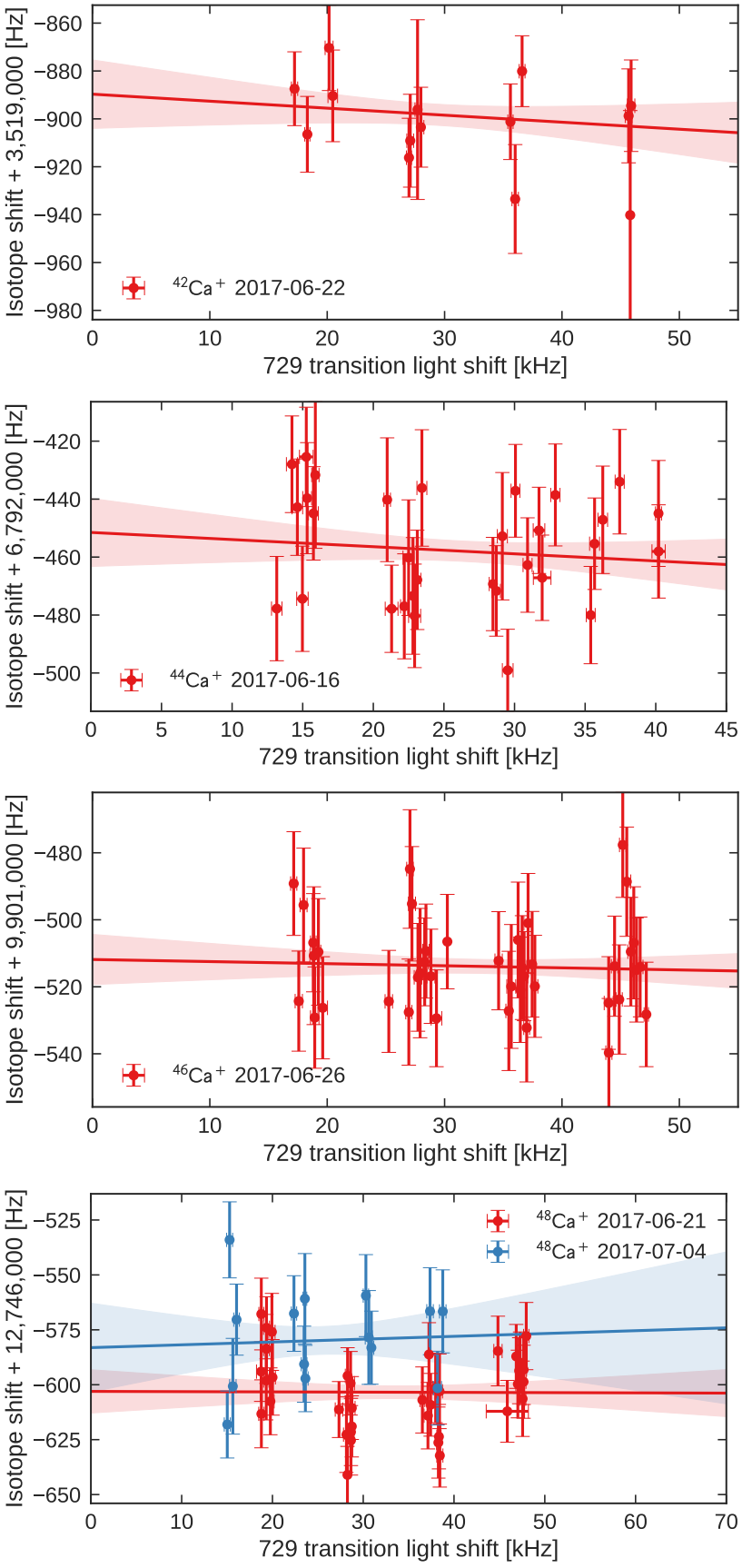

Figure 14.1: Isotope D-finestructure measurements

Table 14.1: Calcium isotope shifts relative to $^{40}Ca^+$ in MHz. The values for the 732 nm transition are calculated based on the measured 729 nm and D-finestructure transitions.

transition	[nm]	42	44	46	48
$4\,^2S_{1/2} - 4\,^2P_{1/2}$	397	+425.706(94) [b]	+849.534(74) [b]	+1287(3) [d]	+1705.389(60) [b]
$4\,^2S_{1/2} - 4\,^2P_{3/2}$	393	+425.932(71) [a]	+850.231(65) [a]	+1292(18) [d]	+1707.945(67) [a]
$4\,^2P_{1/2} - 4\,^2P_{3/2}$	P-fine	+0.226(118) [a]	+0.697(98) [a]		+2.556(90) [a]
$3\,^2D_{3/2} - 4\,^2P_{1/2}$	866	−2349.974(99) [b]	−4498.883(80) [b]		−8297.769(81) [b]
$3\,^2D_{3/2} - 4\,^2P_{3/2}$	850	−2352.2(21) [c]	−4498.7(30) [c]		−8297.7(58) [c]
$3\,^2D_{5/2} - 4\,^2P_{3/2}$	854	−2350.4(43) [c]	−4495.2(43) [c]		−8287.8(70) [c]
$4\,^2S_{1/2} - 3\,^2D_{3/2}$	732	+2775.393(2) [l]	+5347.680(2) [l]	+7778.302(2) [l]	+10 003.130(2) [l]
$4\,^2S_{1/2} - 3\,^2D_{5/2}$	729	+2771.873(2) [k]	+5340.888(2) [k]	+7768.401(2) [k]	+9990.383(2) [k]
$3\,^2D_{3/2} - 3\,^2D_{5/2}$	D-fine	−3.519 896(24) [k]	−6.792 470(22) [k]	−9.901 524(21) [k]	−12 746 611(27) [k]

[a] Ref. Shi et al. [A50]
[b] Ref. Gebert et al. [A49]
[c] Ref. Nörtershäuser et al. [A137]
[d] Ref. Mårtensson-Pendrill et al. [A138]
[k] This work
[l] This work, calculated

where S_{fit} is the statistical error of the fitted intercept. The uncertainty of 30 Hz is added in the same way as for $^{40}Ca^+$, discussed in chapter 13.5.

For $^{48}Ca^+$ two separate measurements were taken, one before measuring the other isotopes, and one two weeks later, after $^{42,44,46}Ca^+$ were measured. The two $^{48}Ca^+$ datasets give the same isotope shift within the statistical uncertainty S_{fit},

$$\begin{aligned} \delta\nu_D^{40,48}(1) &= -12.746\,603(32) \\ \delta\nu_D^{40,48}(2) &= -12.746\,583(36) \end{aligned} \tag{14.15}$$

and the $^{48}Ca^+$ value stated above is the weighted average of these two.

14.2.2 $|S_{1/2}\rangle \rightarrow |D_{5/2}\rangle$ transition

The $|S_{1/2}\rangle \rightarrow |D_{5/2}\rangle$ transition was measured using the 729 nm laser and determining the laser frequency by a beatnote measurement with the Menlo frequency comb, as described in chapter 11 for ^{40}Ca. The measured isotope shifts relative to $^{40}Ca^+$, together with the most recent literature values for other transitions[2], are summarized in table 14.1.

Note that the isotope shift of the D-finestructure transition is about three orders of magnitude smaller, and negative, compared to the $|S_{1/2}\rangle \rightarrow |D_{5/2}\rangle$ transition, and even though the absolute uncertainty of the D-finestructure measurement is much smaller compared to the 729 nm transition, the relative uncertainty is smaller for the latter one. In figure 14.2, the isotope shifts are plotted directly versus the isotope mass for illustration. In the next section, we will use linearized versions of these plots to extract the mass and field shifts from the data.

[2] Data on $^{43}Ca^+$ can be found in ref. [A135].

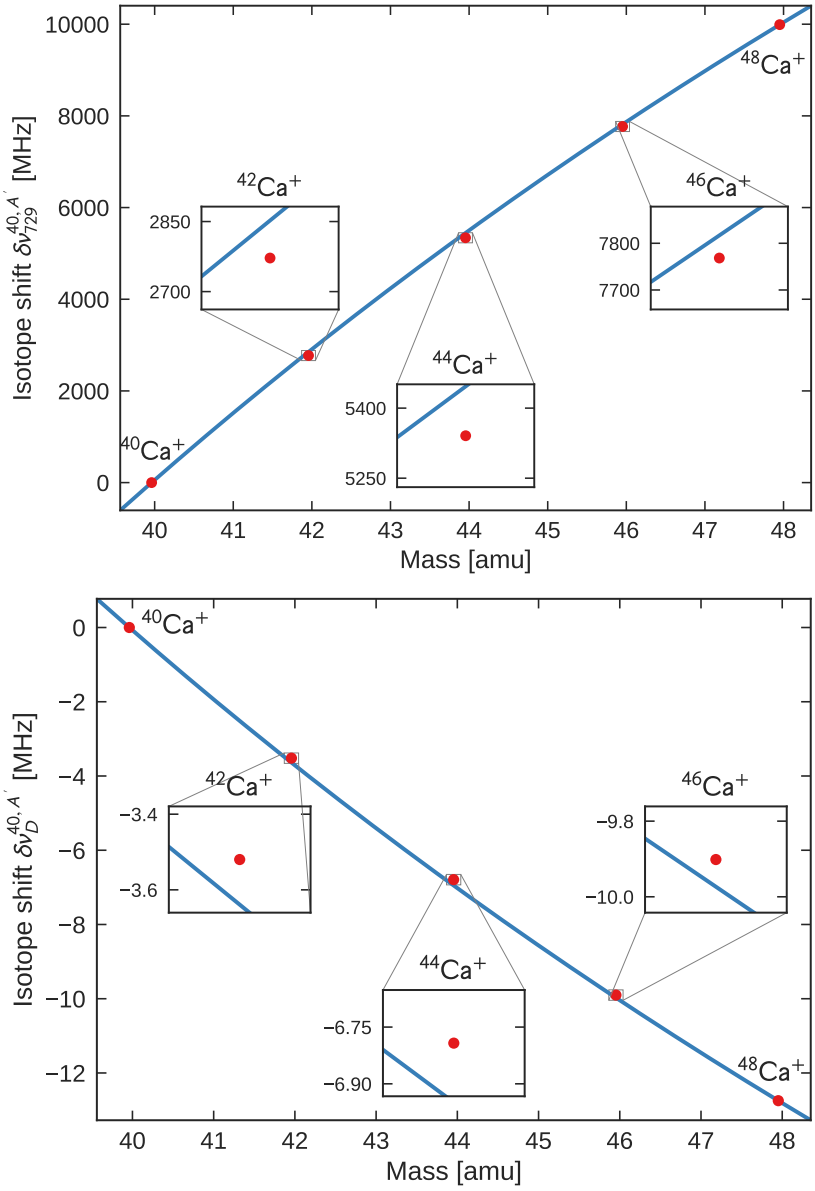

Figure 14.2: Isotope shift relative to $^{40}Ca^+$ of the 729 nm transition (top) and D-finestructure transition (bottom) vs. isotope mass. The red dots show the measured value (with error bars too small to be visible on this scale) and the blue line is plotted according to equation (14.10) and forced through $^{40,48}Ca^+$ based on the assumption that $\delta\left\langle r_c^2\right\rangle^{40,48} = 0$.

Table 14.2: Neutral calcium isotope masses from ref. [A139] and calculated mass factors $1/\mu$ according to the approximate expression in equation 14.4.

Ca isotope	mass [u]	mass factor μ [amu]
40	39.962 590 864(22)	inf
41	40.962 277 92(15)	1637.382 37(24)
42	41.958 617 83(16)	840.011 295(65)
43	42.958 766 44(24)	572.947 942(43)
44	43.955 481 6(3)	439.902 560(30)
45	44.956 186 4(4)	359.755 311(26)
46	45.953 689 0(24)	306.510 45(11)
47	46.954 542 4(24)	268.355 665(78)
48	47.952 522 77(13)	239.828 150 6(34)

14.3 Direct Separation of mass and field shift

Figure 14.3 shows linearized versions of the plots in figure 14.2 by plotting the isotope shift vs $1/\mu$, as explained in section 14.1.4. The calcium isotope masses are very precisely known, and tabulated in table 14.2 together with the mass factor μ. However, the derived uncertainty on the mass factor μ is up to 3.5×10^{-7} for $^{46}Ca^{+}$, similar to the relative error on the $|S_{1/2}\rangle \rightarrow |D_{5/2}\rangle$ transition isotope shift.

Assuming the same nuclear charge radius $\delta \left\langle r_c^2 \right\rangle^{40,48} = 0$, due to the fact that both isotopes are "magic" in terms of proton number as well as neutron number in the nuclear shell model, we directly get the mass shift constants K_i from the isotope shift $\delta\nu_i^{40,48}$ via

$$K_i = \mu\delta\nu_i^{40,48}\,. \tag{14.16}$$

We find

$$\begin{aligned} K_{\text{D-fine}} &= -3041.60(50)\,\text{MHz u} \\ K_{729} &= 2383.91(95)\,\text{GHz u}\,. \end{aligned} \tag{14.17}$$

Note that these values are not obtained by fitting all isotope measurements but are solely based on the $^{40,48}Ca^{+}$ isotope shift.

Furthermore, we can extract the field shift as the vertical distance between the measured isotope shift and the straight line representing the mass shift contribution in equation (14.10). The extracted field shifts are summarized in table 14.3.

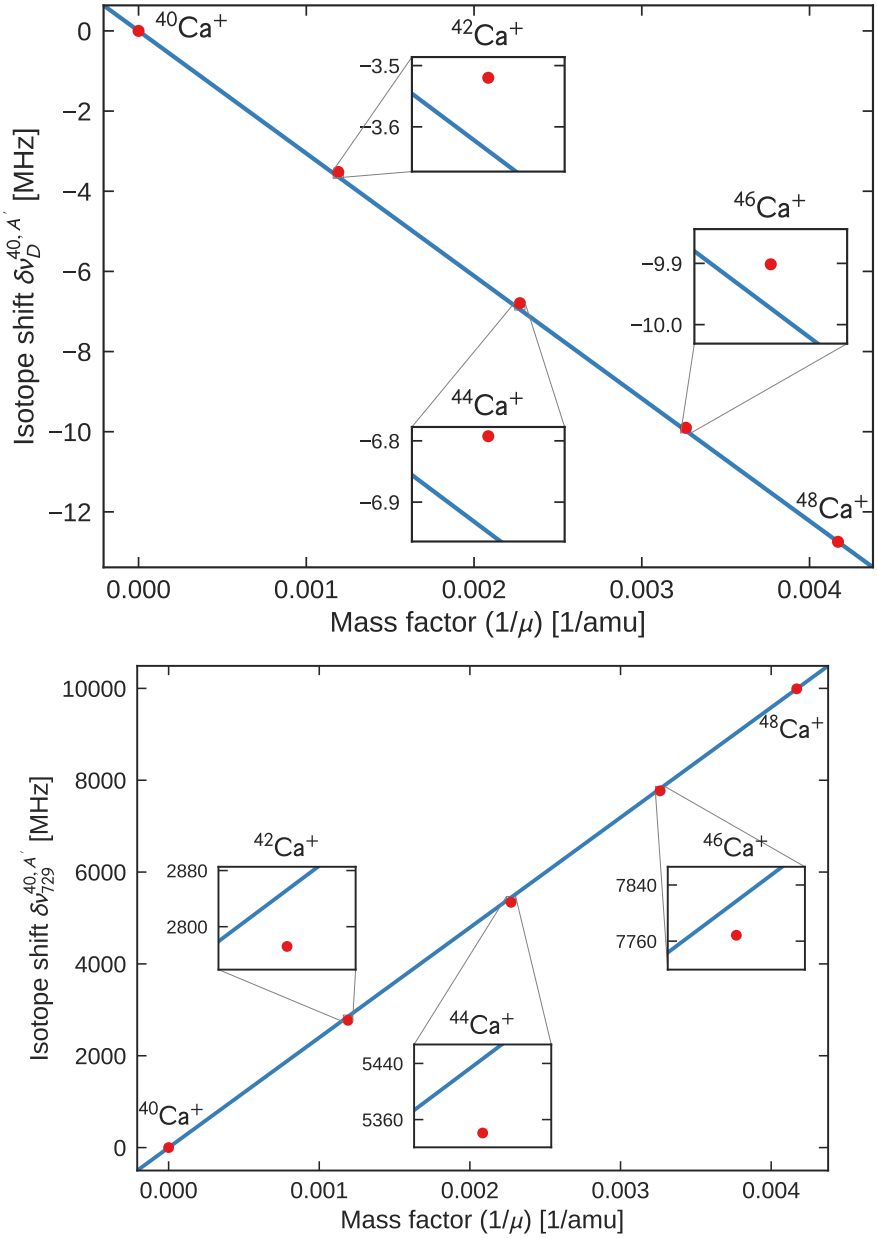

Figure 14.3: Isotope shift relative to $^{40}Ca^+$ of the 729 nm transition (top) and D-finestructure transition (bottom) vs. mass factor $1/\mu$. The red dots show the measured value (with error bars too small to be visible on this scale) and the blue line is plotted according to equation (14.10) and forced through $^{40,48}Ca^+$ based on the assumption that $\delta\left\langle r_c^2\right\rangle^{40,48} = 0$.

Table 14.3: Field shifts in MHz, extracted based on the assumption $\delta\left\langle r_c^2\right\rangle^{40,48} = 0$. Values for the 732 nm transition are calculated based on the other two transitions.

transition	[nm]	42	44	46
$4\,^2S_{1/2} - 3\,^2D_{3/2}$	732	−80.560(3)	−105.873(3)	−48.616(3)
$4\,^2S_{1/2} - 3\,^2D_{5/2}$	729	−80.440(3)	−105.716(3)	−48.543(3)
$3\,^2D_{3/2} - 3\,^2D_{5/2}$	D-fine	+0.119 338(65)	+0.156 799(64)	+0.072 023(62)

Another approach is to use equation (14.10) again, but now plotting the modified isotope shift $\mu\delta\nu_i$ versus the modified charge radius squared $\mu\delta\left\langle r_c^2\right\rangle^{40A'}$. This plot directly gives the mass shift constant K_i as intersect, and the field shift constant F_i as slope, in a linear regression model.

This analysis also allows to predict charge radii, by inter- or extrapolation of the linear fit, of isotopes which have not been (precisely) measured before, for instance for radioactive, short lived isotopes. However, this procedure can only improve already existing data and is limited by the accuracy of this data, i.e. previously measured charge radii. Charge radii can be precisely measured by muonic spectra and electronic scattering experiments, as well as optical isotope shift measurements [A140, A141], and table 14.5 lists the measurements by Palmer et al. [A47], which were used as seed values in the fits here.

Since the present relative error on the charge radii in literature is much larger than on our isotope shift measurements, we reverse the axes and use regular least squares fitting, ignoring the negligible uncertainty on the isotope shift measurements. The result of the fit is shown in figure 14.4. We get the slope $1/F_i$ and intercept $-K_i/F_i$ instead of F_i and K_i directly as explained above. The mass and field shift constants obtained from the fit are summarized in table 14.4. The values are close to the values given in section 14.3, which were only based on the $^{48}Ca^+$ isotope shift and the simple assumption of equal charge radii $\delta\left\langle r_c^2\right\rangle^{40,48} = 0$, which does not hold as we will see in the following.

From the fit, we can also extract new best estimates for the mean charge radii squared $\delta\left\langle r_c^2\right\rangle^{40\,A'}$, simply by evaluating the fitted curve at the measured modified isotope shift for each isotope. The results are summarized in table 14.5, together with the measurements by Palmer et al. [A47], used as seed values in the fit, and other recent values obtained by Shi et al. [A50]. Note that the result is limited by the relative accuracy of the seed values for $\delta\left\langle r_c^2\right\rangle^{40\,A'}$ and not by

Table 14.4: Mass and field shift constants extracted from plotting modified charge radius squared vs modified isotope shift in figure 14.4.

Parameter	729	D-fine
Field shift F	$-371(7)\,\mathrm{MHz\,fs^{-2}}$	$+550(10)\,\mathrm{kHz\,fs^{-2}}$
Mass shift K	$+2395(63)\,\mathrm{GHz\,u}$	$-3056(80)\,\mathrm{MHz\,u}$
Covariance	$-6.0\,\mathrm{fs^2\,GHz^{-1}\,u^{-1}}$	$+3.5\,\mathrm{fs^2\,MHz^{-1}\,u^{-1}}$

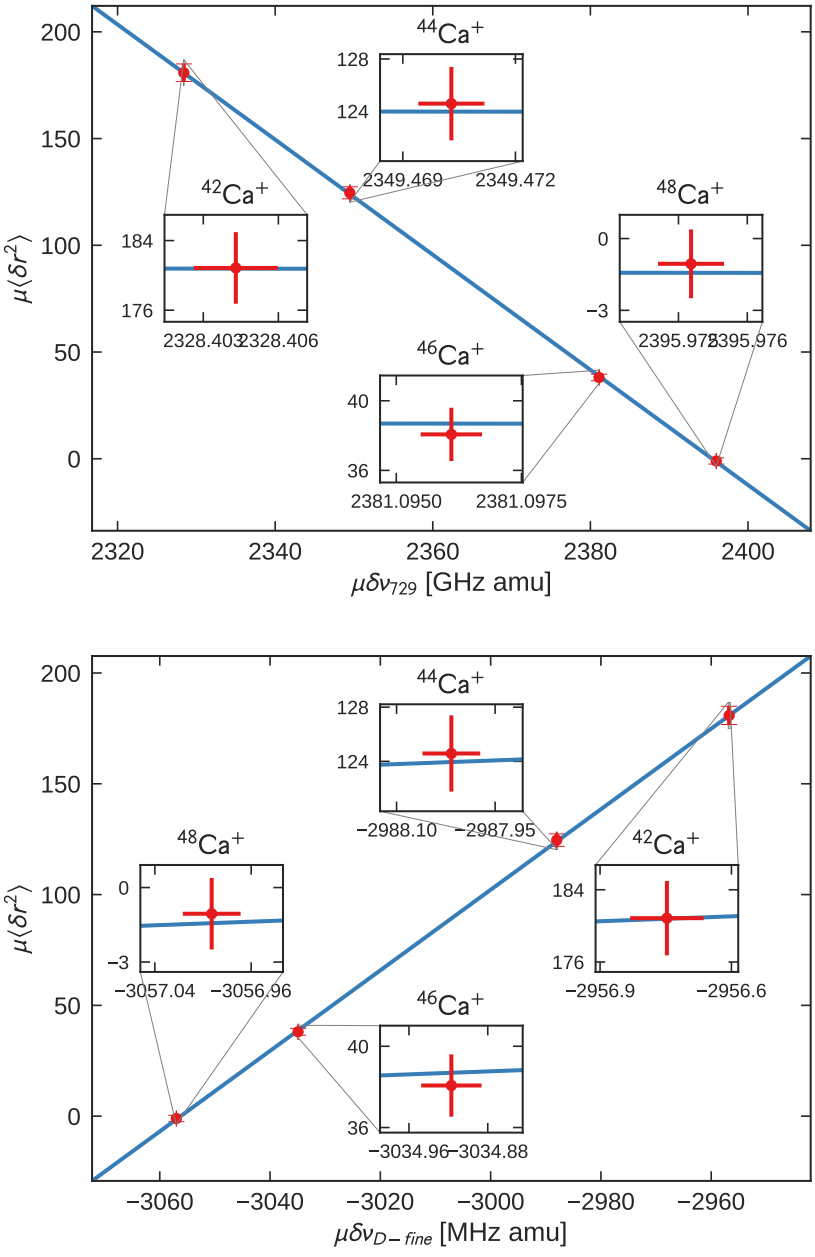

Figure 14.4: Modified charge radius vs. modified isotope shift

Table 14.5: Mean charge radii squared $\delta\left\langle r_c^2\right\rangle^{40\,A'}$ in fm^2 extracted from the linear fit shown in figure 14.4, together with literature values. The values from Palmer et al. were used as seed values in the fit.

isotope	this work	Palmer et al. [A47]	Shi et al. [A50]
40	+0		
41		+0.0032(25)	
42	+0.2152(34)	+0.2153(49)	+0.2160(49)
43		+0.1254(32)	
44	+0.2818(42)	+0.2832(64)	+0.2824(64)
45		+0.1188(59)	
46	+0.1262(31)	+0.1242(50)	
47		+0.005(13)	
48	−0.0060(50)	−0.0044(60)	−0.0045(59)

our isotope shift measurements. This is why only one column is given for the result in table 14.5; the prediction from the 729 nm transition data and from the D-finestructure transition data gives the exact same result with the same uncertainties. The obtained value of $-0.0060(50)\,\mathrm{fm}^2$ suggests that the there is a slight deviation in the nuclear charge radius between $^{40}Ca^+$ and $^{48}Ca^+$, even though both nuclei are double magic.

14.4 King plot

The King plot, according to equation (14.11), allows to eliminate the a priori unknown charge radii from the analysis, by directly plotting the modified isotope shifts of two different transitions against each other. This is shown in figure 14.5 for the 729 nm and D-finestructure transitions. The slope of a linear fit gives the ratio of the field shift constants, and from the intercept we can extract the difference of the mass shift constants. We find the slope

$$\frac{F_{\text{D-fine}}}{F_{729}} = -1.4833(4) \times 10^{-3}\,. \tag{14.18}$$

This is in agreement with the field shifts directly extracted and listed in table 14.4, from which we find

$$\frac{F_{\text{D-fine}}}{F_{729}} = -1.48(4) \times 10^{-3}\,, \tag{14.19}$$

but with 100 times better accuracy.

Within the uncertainty, the linear fit describes the data perfectly well. The linearity of the King plot is strongly supported by theory, and violations would indicate *new physics*, as discussed later in section 14.5.2.

The same data can also be visualized in a King plot of the 732 nm vs. 729 nm transition, where the isotope shifts for 732 nm, as given in table 14.1, were calculated as

$$\delta\nu_{732} = \delta\nu_{729} - \delta\nu_{\text{D-fine}}\,. \tag{14.20}$$

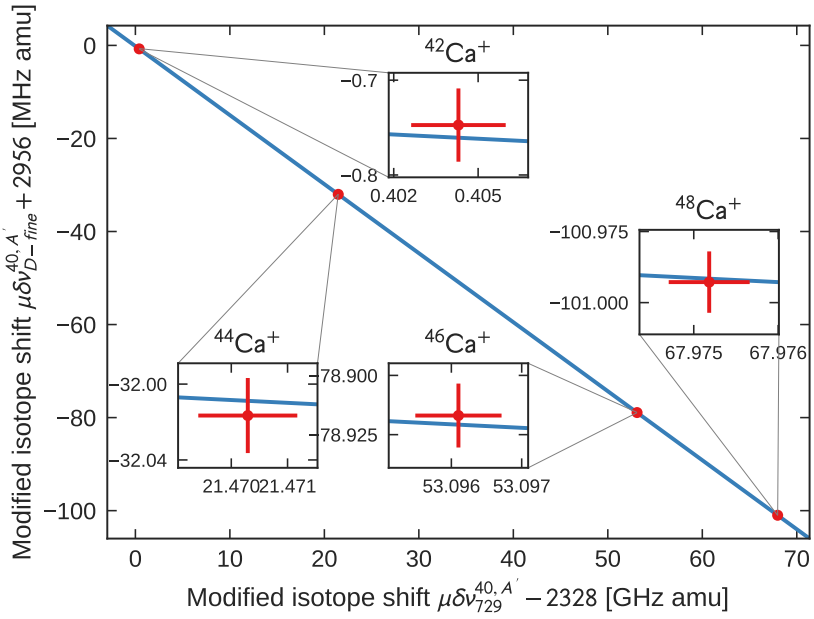

Figure 14.5: King plot D-finestructure vs. 729

This plot is shown in figure 14.6. Since $\delta\nu_{732}$ is dominated by the 729 nm shift, and the D-finestructure shift is only a small contribution, there is a strong correlation of the uncertainties in this plot. An error on the 729 nm measurements moves the data point along the diagonal of the plot, and does not contribute to a possible non-linearity in the King plot. The uncertainty of the D-finestructure measurements on the other hand directly translates into an error of the calculated 732 nm value, and is indicated by the horizontal error bars.

14.5 Comparison with previous measurements and impact on “new physics”

To the best of my knowledge, the measured spectroscopic isotope shifts are the most precise measurements in literature so far, not just for Ca^+ but for any given element.

The isotope shifts $\delta\nu^{40,A'}_{S-P}$ on the $|S_{1/2}\rangle \rightarrow |P_{1/2,3/2}\rangle$ transition measured by Shi et al. [A50] have an absolute accuracy of ≈ 100 kHz, corresponding to a relative accuracy for $\delta\nu^{40,48}_{S-P}$ of 6×10^{-5}. Our absolute accuracy of 45 Hz for the D-finestructure $|D_{5/2}\rangle \rightarrow |D_{3/2}\rangle$ transition is at least 2000 times more accurate. Actually, the measurements by Shi et al. show a discrepancy with our data, and also previous measurements by other authors, as I will discuss in the following section. In relative term, we reach an accuracy of 3.5×10^{-6} for $\delta\nu^{40,48}_{D}$. For the $|S_{1/2}\rangle \rightarrow |D_{5/2}\rangle$ transition with an accuracy of 2 kHz, we reach a relative accuracy of 2×10^{-7} for $\delta\nu^{40,48}_{D}$.

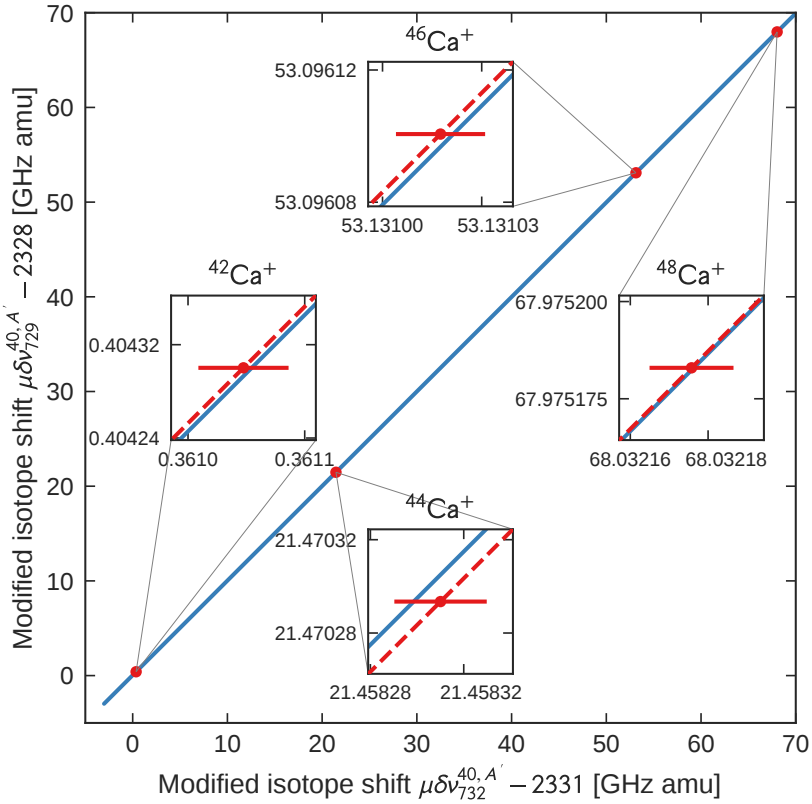

Figure 14.6: King plot of the 729 nm vs. 732 nm transition calculated as the sum of 729 nm and D-finestructure transition. The error originating from the measurement uncertainty of the 729 nm transition equally contributes to both axis, and is indicated by the dashed red line, exceeding the range of the insets. However, this error only moves the data points along the diagonal, with constant distance to the fitted line. The measurement uncertainty of the D-finestructure transition only contributes to the 732 nm value, and is indicated as horizontal error bars.

One very interesting aspect of these measurements is, that the high accuracy of optical isotope shift measurements has the potential to discover new physics beyond the standard model. For instance, a nucleus consisting of "strange matter", where some of the nuclei decayed into particles consisting of up, down and strange quarks [A142], would lead to a very different charge radius, reflected in the spectroscopic isotope shift. Another possibility is to detect new bosons, mitigating a new force between the nucleus and the electron. This new force would lead to a nonlinearity in the King plot, which I will discuss in section 14.5.2.

14.5.1 Comparison with previous measurements

As already discussed in chapter 13.5, the measurements of the P-finestructure in $^{40}Ca^+$ of Shi et al. [A50] do not agree with previous, much more precise measurements. The argument is, that the "closed" transition (compare chapter 13.5)

$$|S_{1/2}\rangle \xrightarrow{397\,\mathrm{nm}} |P_{1/2}\rangle \xrightarrow{866\,\mathrm{nm}} |D_{3/2}\rangle \xrightarrow{\text{D-fine}} |D_{5/2}\rangle \xrightarrow{729\,\mathrm{nm}} |S_{1/2}\rangle \tag{14.21}$$

should obey

$$f_{\text{closed}} = f_{397} - f_{866} + f_{\text{D-fine}} - f_{729} = 0\,, \tag{14.22}$$

where f_i are the measured frequencies of the corresponding transitions. For the $^{40}Ca^+$ isotope, this condition is violated with

$$f^{40}_{\text{closed}} = 274(130)\,\mathrm{kHz} \neq 0\,, \tag{14.23}$$

solely based on measurements by Shi et al. and other authors [A50, A88, A36, A49], not including any input from the data presented in this thesis.

For the isotope shifts, using the data from Shi et al. and the data presented in this thesis, we find for the isotope shifts, in the same way as eq. (14.22)

$$\begin{aligned}
\delta\nu^{40,42}_{\text{closed}} &= 288(136)\,\mathrm{kHz}\\
\delta\nu^{40,44}_{\text{closed}} &= 736(109)\,\mathrm{kHz}\\
\delta\nu^{40,46}_{\text{closed}} &= \text{(not measured by Shi et al.)}\\
\delta\nu^{40,48}_{\text{closed}} &= 28(101)\,\mathrm{kHz}\,.
\end{aligned}$$

Only for $^{48}Ca^+$, there is agreement within the uncertainty, and the value for $^{44}Ca^+$ disagrees by almost 7 standard deviations from $\delta\nu^{40,44}_{closed} = 0$. Together with the $^{40}Ca^+$ discrepancy, this is a strong indication that the uncertainties were underestimated by Shi et al. for their measurements. The transition frequencies for $^{40}Ca^+$ measured in this thesis work, agree very well within the uncertainties with previous measurements by other authors, as discussed in chapter 13.5 for the $|D_{5/2}\rangle \to |D_{3/2}\rangle$ transition, and in chapter 11 for the 729 nm $|S_{1/2}\rangle \to |D_{5/2}\rangle$ transition, both with much higher sensitivity compared to the measurements by Shi et al.

14.5.2 Non-linearity of the King plot and "new physics" beyond the standard model

Equation (14.10) leads to the strictly linear dependence for the King plot (14.11). Since this linear dependence is based on our current physical understanding, a

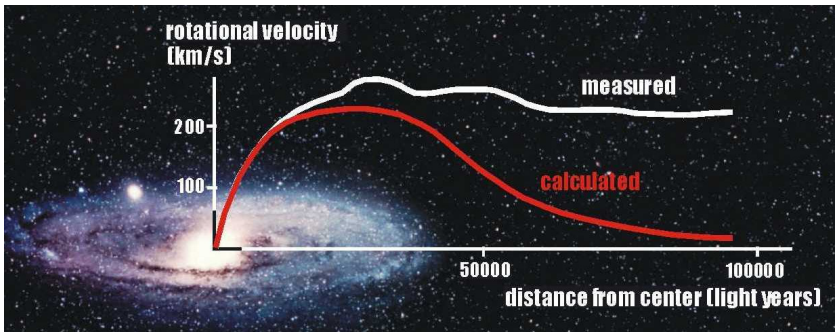

Figure 14.7: Illustration of rotational velocities of stars in a spiral galaxy [X3]. According to Kepler's law, the velocity of the stars should decrease with distance from the center (red curve). However, the measured velocities (white curve) deviate significantly from this prediction, revealing the presence of dark matter.

significant violation would indicate "new physics", that means physics beyond the standard model. That there is physics beyond the standard model is already clear from astrophysical observations proving the existence of dark matter [A143, A144, R14, A145]. The velocity of stars in spiral galaxies, such as the Andromeda galaxy shown in figure 14.7, requires the presence of "dark matter", interacting gravitationally with the "normal matter" described by the standard model, which was already suggested in 1933 by Zwicky [A146].

The King plot in its linear form discussed above contains only the leading orders for the field and mass shifts. Thus, I will discuss expected non-linearities of the King plot within the standard model. In section 14.5.2 I will then summarize theoretical suggestions, especially new particles beyond the standard model, mitigating a force which would lead to nonlinearities of the King plot. Finally, I will explain how our current Ca^+ spectroscopic isotope shift measurements can set bounds for this new force.

Expected King non-linearities within the standard model

Having a closer look at the origin of eq. 14.10 reveals non-linearities in the King plot even within the standard model. To claim a violation of the standard model, measured nonlinearities in any experimentally derived King plot need to be larger than theses expected nonlinearities. The following discussion is based on the calculations by Flambaum et al. [A56].

Relativistic corrections The simple linear dependence of the field shift (FS) on the nuclear charge radius

$$FS = F_i \delta \left\langle r_c^2 \right\rangle^{AA'} \tag{14.24}$$

stems form the non-relativistic Schrödinger equation. However, the field shift depends on the electron's probability density overlap with the nuclear charge distribution. For example, the electronic $p_{1/2}$-wave-function has zero probability

at the origin in the non-relativistic case, which is not true in the relativistic case solving the Dirac equation. In the relativistic case, eq. (14.24) becomes

$$FS = \tilde{F}_i \left\langle r^{2\gamma} \right\rangle^{AA'} , \tag{14.25}$$

where

$$\gamma = \left[\left(j + 1/2\right)^2 - Z^2\alpha^2 \right]^{1/2} , \tag{14.26}$$

where $j = l + s$ is the total of electronic orbital angular momentum and spin, Z is the proton number, and $\alpha \approx 1/137$ is the finestructure constant. From equation (14.26), we see that the relativistic effect for s-orbitals ($j = 1/2$) becomes more important for heavier elements, where $Z \approx 137$. In the non-relativistic limit, i.e. $Z \ll 137$, we find $\gamma = 1$ for s-waves, that means eq. (14.24) leading to the linear King plot.

The isotope shift can be written as

$$\delta\nu_i^{AA'} = K_i/\mu + F_i \left\langle r^{2\gamma_1} \right\rangle^{AA'} + G_i \left\langle r^{2\gamma_2} \right\rangle^{AA'} , \tag{14.27}$$

where γ_1 represents the s-wave contribution with $\gamma_1 \to 1$ in the non-relativistic case, and the third term represents a correction to the field shift caused by higher waves, for instance, $G_i \left\langle r^4 \right\rangle^{AA'}$ for $p_{3/2}$. The King plot will then only be linear for the special case where $F_i/G_i = F_k/G_k$ for the two transitions i, k.

Another important effect is the nuclear polarizabilitiy [A147, A148]. The electrons affect the nuclear charge distribution, which leads to nonlinearities in the King plot, via eq. 14.27.

King nonlinearity due to new particles

New particles, mediating a new force [A149] between the nucleus and the electron would be detectable via the King plot analysis. Adding a third term to the leading mass and field shift contributions, so that the isotope shift becomes [A53][3]

$$\delta\nu_i^{AA'} = K_i/\mu + F_i\,\delta \left\langle r_c^2 \right\rangle^{AA'} + \alpha_{NP} X_i \gamma_{A\,A'} , \tag{14.28}$$

leads to a non-linearity of the King plot [A56]. Here, α_{NP} is the new particle's coupling constant, X_i depends on the form of the new potential and on the specific electronic transition i, and $\gamma_{A\,A'}$ depends only on the nuclear properties. The potential of the interaction can be parameterized by a Yukawa type of potential

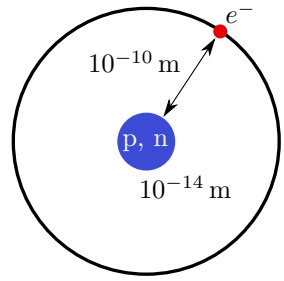

Figure 14.8: Typical length scales in an atom.

$$V_\phi(r) = -y_e\, y_n\, N\, \frac{e^{-r/L_R}}{r} \tag{14.29}$$

where N is the neutron number, y_e and y_n are the particle coupling strengths to the electrons and neutrons, respectively, and the characteristic length range

[3] Berengut et al. [A53] define μ as we define $1/\mu$.

of the force is given by

$$L_R = \frac{\hbar\, c}{e\, m_\phi[\mathrm{eV}]} = \frac{2.0 \times 10^{-7}\,\mathrm{m}}{m_\phi[\mathrm{eV}]}\,, \tag{14.30}$$

with $m_\phi[\mathrm{eV}]$ being the mass of the particle in electron volt. Since the rms charge distribution radius of the $^{40}Ca^+$ nucleus is $3.48\,\mathrm{fm} = 3.48 \times 10^{-15}\,\mathrm{m}$ [A136] the mass of the particle needs to be smaller than $\approx 57\,\mathrm{MeV}$ to reach outside the nucleus[4]. To effectively couple the nucleus with the outer electron, the characteristic length of the force needs to be at least on the order of the electron-nucleus distance, with a typical length scale of the Bohr radius

$$a_0 = 5.3 \times 10^{-11}\,\mathrm{m}\,, \tag{14.31}$$

so that the mass of the particle needs to be smaller than $\approx 3.7\,\mathrm{keV}$.

Figure 14.9 shows the bounds, calculated by Berengut et al.[A53], a spectroscopic isotope shift measurement can set on the mass and strength of such a new particle. My current calcium D-finestructure measurement lies in between the 100 kHz accuracy of Shi et al. and a hypothetical measurement of the D-finestructure isotope shift with 1 Hz accuracy. The black line was calculated based on the isotope shifts measured in this thesis by Elina Fuchs and Matthias Schlaffer, authors of the papers [A54], based on the methods in ref. [A53]. The calculated bound is **preliminary**, and reached me just before the thesis deadline. The mass dependence of the bound is still work in progress, which is why only the bound for an infinite ranging force, corresponding to a massless mediator particle is shown.

[4] A force between the neutrons and the electron would also be possible, in which case we would need to consider the size of the neutron distribution [A150] instead of the charge radius, which is on a similar scale.

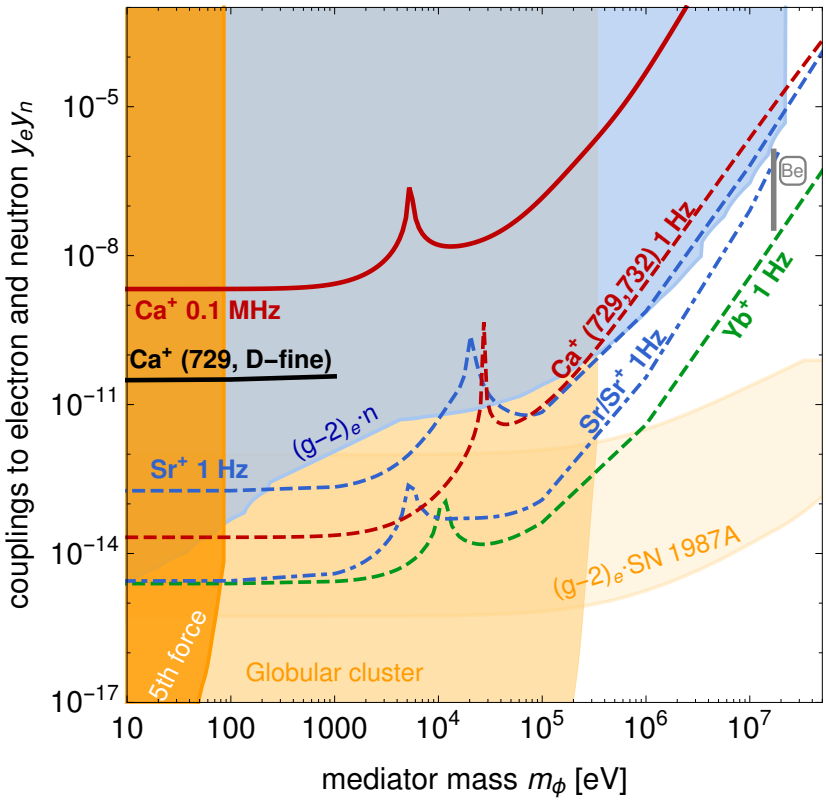

Figure 14.9: Isotope shifts and “new physics”. The plot shows an updated version of the plot in ref. [A53], with the bounds calculated based on the isotope shifts measured in this thesis by Elina Fuchs and Matthias Schlaffer, authors of the papers [A54], based on the methods in ref. [A53]. The calculated bound is **preliminary**.

Part IV

Outlook and Conclusion

15

Future Experiments with MgH^+

In the Ion Trap Group, we plan to apply the technique of *frequency comb driven Raman transitions* developed in this thesis work to perform rotational spectroscopy in MgH^+ [A40]. The potential energy curves of the lowest electronic levels of MgH^+ are illustrated in figure 15.1a, together with the lowest vibrational levels $\nu = 0\,, 1\,, 2$ and the frequency comb light. The idea is to drive Raman transitions with the frequency comb between rotational levels J of the vibrational ground state $\nu = 0$, sketched in figure 15.1b. The rotational con-

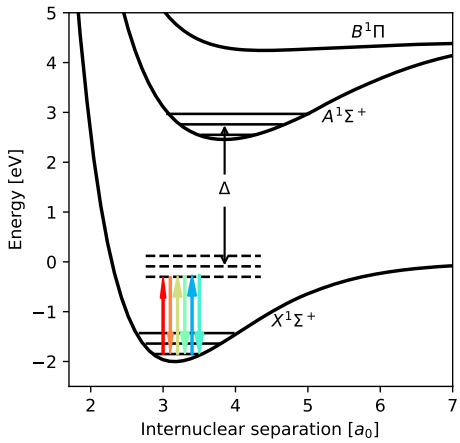

(a) Potential energy curves of MgH^+

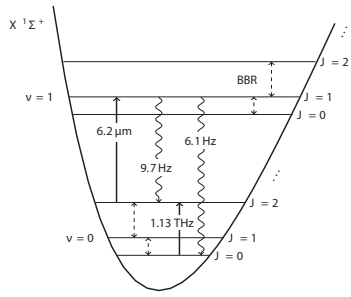

(b) Sketch of rovibrational levels and rotational cooling.

Figure 15.1: Potential energy curves of MgH^+ (left) and a sketch of the rovibrational levels of the electronic ground state (right, not to scale).

	$\nu = 0$	$\nu = 1$	$\nu = 2$	$\nu = 3$	$\nu = 4$	$\nu = 5$
E_{vib} [THz]	0	48.997	96.018	140.995	183.845	224.474
B_e [THz]	0.189	0.183	0.178	0.172	0.166	0.159

Table 15.1: Rotational constants B_e and vibrational energies E_{vib} for the lowest vibrational states of the electronic ground state $X\,^1\Sigma^+$ in $^{24}MgH^+$ [A151].

stants of MgH^+ are listed in table 15.1 and the energy splitting ΔE between rotational levels J'' and J' can be calculated to first order by

$$\Delta E = B_e \left(J''(J''+1) - J'(J'+1) \right) \tag{15.1}$$

where B_e is the rotational constant. This leads to rotational transition frequencies in the THz range, similar to the successfully driven D-finestructure transition in Ca^+ with a frequency of 1.8 THz. In particular, the $J = 0 \rightarrow J = 2$ transition has a frequency of 1.13 THz. Dipole selection rules require $\Delta J = \pm 1$ for transitions between the electronic Σ^+ levels, so that the selection rule for the Raman process becomes $\Delta J = \pm 2$. The auxiliary level for the Raman process is the first electronically excited level $A\,^1\Sigma^+$. The coupling happens via all dipole allowed rovibrationally states of this electronic level, indicated by multiple virtual levels as dashed lines in the figure.

The first electronically excited level lies 1067 THz above the ground state, so that the single photon detuning $\Delta \approx 700$ THz in MgH^+ is much larger compared to Ca^+ with $\Delta \approx 20$ THz for our Mira frequency comb with a carrier frequency of about 370 THz. The Raman Rabi frequency is inversely proportional to the single photon detuning, so that we expect a reduction by a factor of $\frac{700}{20} = 35$. At the current experimental status, *coherent* manipulation of MgH^+ is not possible due to short coherence times compared to the expected Rabi frequencies. The Menlo frequency comb intrinsically suffers from strong destructive interference of individual Raman Rabi frequencies of the comb spectrum by group delay dispersion (GDD) in the laser's fiber components, leading to small Rabi frequencies compared to the Mira Ti:sapph comb. However, one could think about using the (M-NIR) output of the Menlo and amplify the light in a GDD compensated fiber amplifier to high powers to achieve higher Rabi frequencies. The additional factor of ≈ 2 due to half the carrier frequency could be outweighed by higher total power.

The Mira comb on the other hand currently has a lower repetition rate stability compared to the Menlo comb, as discussed in depth in chapter 6, which leads to decoherence. We are working on improving the repetition rate stability by replacing the piezo actuator and mirror for the cavity length adjustment, which should lead to much better performance. A tighter focus on the ion, and possibly a stronger pump laser for the Mira comb could also push the Rabi frequency easily by a factor of 2.

Raman spectroscopy can be performed on any rotational transition with a transition frequency within the spectral bandwidth of about 8 THz of the Mira comb. The rotational levels are populated according to a thermal distribution at room temperature, as shown in figure 15.2, leading to small signal to noise

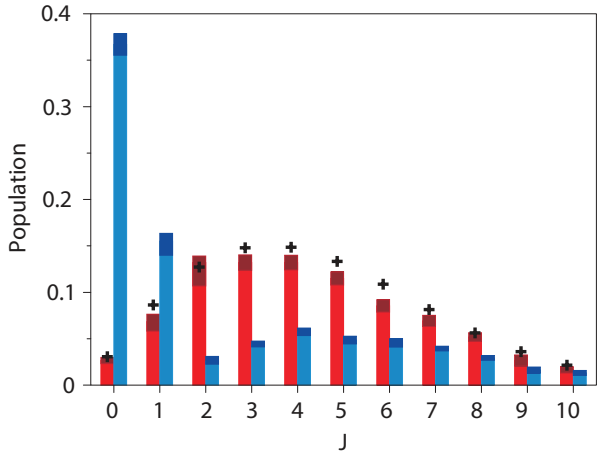

Figure 15.2: Measured rotational state distribution at room temperature (red) and after rotational cooling (blue) from ref. [A152].

when addressing only one selected rotational state [A152].

Rotational cooling can however dramatically increase the population in the rovibrational ground state $|\nu = 0,\, J = 0\rangle$ and first excited state. The idea of rotational cooling, previously implemented in our group [A152], is sketched in figure 15.1b. A laser at 6.2 µm is driving the $|\nu = 0,\, J = 2\rangle \rightarrow |\nu = 1,\, J = 1\rangle$ transition, thereby emptying the $|\nu = 0,\, J = 2\rangle$ state. From the $|\nu = 1,\, J = 1\rangle$ state, the dipole selection rule $\Delta J = \pm 1$ restricts spontaneous decay to the $|\nu = 0,\, J = 2\rangle$ state, from where it is immediately pumped back by the laser, and to the $|\nu = 0,\, J = 0\rangle$ state, effectively pumping the transition $|\nu = 0,\, J = 2\rangle \rightarrow |\nu = 0,\, J = 0\rangle$. However, blackbody radiation (BBR) couples neighboring rotational states, so that the population from the $|\nu = 0,\, J = 0\rangle$ state migrates to the $|\nu = 0,\, J = 1\rangle$ state and finally to the $|\nu = 0,\, J = 2\rangle$ state, from where it is pumped back to $|\nu = 0,\, J = 0\rangle$. Additionally, the BBR coupling of states with $J \geq 2$ moves population slowly towards the almost empty $|\nu = 0,\, J = 2\rangle$ state, including the population in the cooling cycle.

In our laboratory, I was working on the characterization of a quantum cascade laser (QCL) intended for these experiments, partly during assisting the lab work of two bachelor students on the project [T11, T12]. Together with a High-Finesse WS6-200 IR-III wavemeter with an operating wavelength range form approximately 2 µm to 11 µm, which we characterized to an absolute accuracy of ≈ 15 MHz via absorption spectroscopy in ammonia, the infrastructure for the experiments is almost ready.

Another complication arises due to the hyperfine structure in $^{24}MgH^+$, splitting the rotational levels for $J > 0$ into two hyperfine states with $F = J \pm 1/2$. Additionally, the hyperfine levels are split in a magnetic field B by the Zeeman effect into $2F+1$ sub-states $m_F = -F,\, -F+1 \ldots + F$. The energy levels $|J,\, F\rangle$ can be calculated via

$$E = E_J + \frac{C_I}{2}\left[F(F+1) - I(I+1) - J(J+1)\right], \tag{15.2}$$

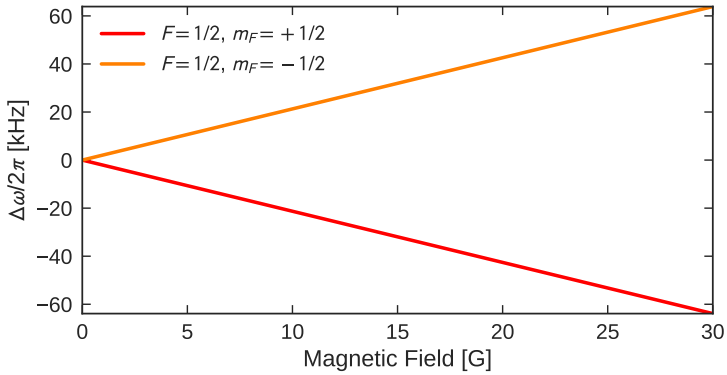

Figure 15.3: Zeeman splitting of the $|J = 0,\ F = 1/2\rangle$ Zeeman sub-states.

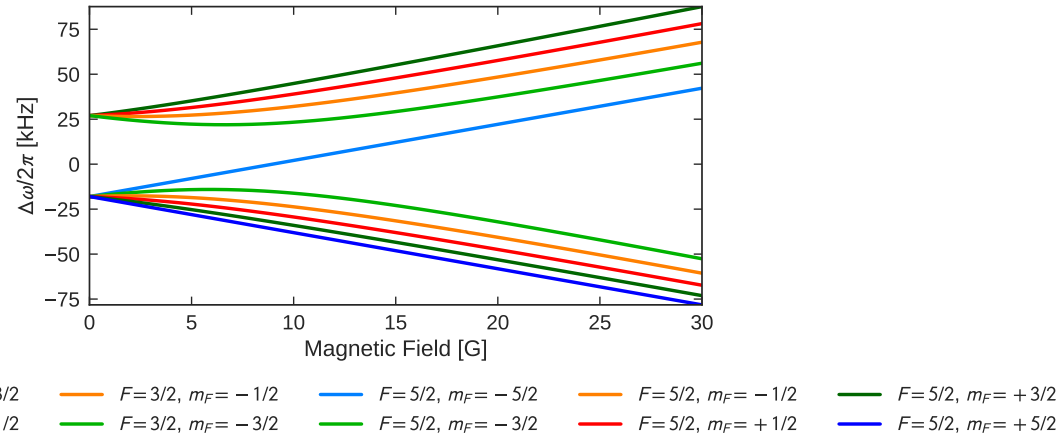

Figure 15.4: Zeeman splitting of the $|J = 2,\ F = 3/2\rangle$ and $|J = 2,\ F = 5/2\rangle$ Zeeman sub-states.

where $J = 1/2$ is the nuclear spin, and the hyperfine constant $C_I = -18(1)\,\mathrm{kHz}$ has been calculated by Frank Jensen from the Department of Chemistry at Aarhus University.

The Zeeman energy

$$\hat{H}_{\mathrm{Zeeman}} = -g_p\mu_N \hat{I}_p\cdot\hat{B} - g_{\mathrm{rot}}\mu_N \hat{J}\cdot\hat{B};\quad \mu_N = \frac{e\hbar}{2M_p},\quad g_p = 5.586,\quad g_{\mathrm{rot}} \approx -0.08\,, \tag{15.3}$$

has been calculated in the Ion Trap Group before [T3], and is plotted for the $J = 0$, $F = 1/2$ level in figure 15.3 and for $J = 2$, $F = 3/2,\ 5/2$ in figure 15.4. In total, there are 18 possible transitions between the $J = 0$ and $J = 2$ levels, and 10 particularly interesting transition frequencies are plotted in figure 15.5. One interesting pair of transitions is

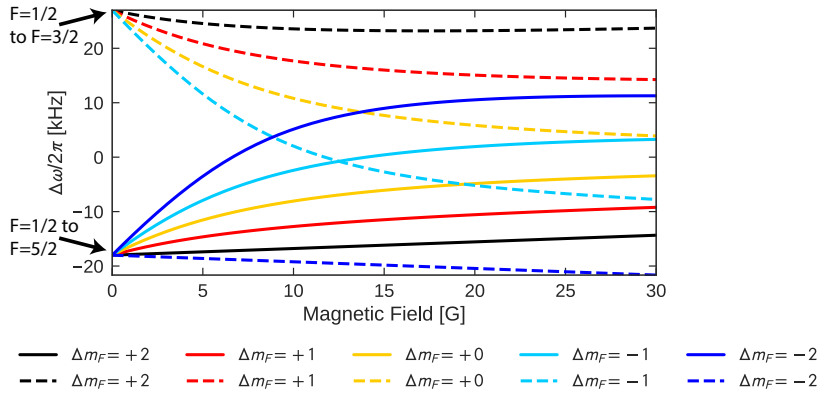

Figure 15.5: $|J = 0,\, F = 1/2\rangle$ and $|J = 2,\, F = 3/2,\, 5/2\rangle$ transition frequencies between selected m_F states. Solid lines correspond to the initial state $|J = 0,\, F = 1/2,\, m_F = +1/2\rangle$ and dashed lines to the initial state $|J = 0,\, F = 1/2,\, m_F = -1/2\rangle$.

$$|J = 0,\, F = 1/2,\, m_F = +1/2\rangle \rightarrow |J = 2,\, F = 5/2,\, m_F = 5/2\rangle \quad \text{(solid black line)}$$
$$|J = 0,\, F = 1/2,\, m_F = -1/2\rangle \rightarrow |J = 2,\, F = 5/2,\, m_F = -5/2\rangle \quad \text{(dashed blue line)}$$

because these transitions have the same, but opposite frequency f dependence on the magnetic field with a slope of

$$\frac{df}{dB} = \pm 122\,\text{Hz}\,. \tag{15.4}$$

By measuring both transitions, the difference frequency can be converted to magnetic field and could be used to determine the magnetic field. Turning around this argument, a measurement of the difference frequency in a known magnetic field can be used to determine the molecular constants.

Another interesting transition is the

$$|J = 0,\, F = 1/2,\, m_F = -1/2\rangle \rightarrow |J = 2,\, F = 3/2,\, m_F = +3/2\rangle \quad \text{(dashed black line)}$$

transition, which is insensitive to first order magnetic field fluctuations $\frac{df}{dB} = 0$ at a magnetic field around 17.5 G. Magnetic field fluctuations are often the experimental limiting factor on the coherence time. Long coherence times are beneficial for almost all applications, for instance quantum computing where these two rotational states can be used as qubit.

To detect the internal state of MgH^+ we plan to implement quantum logic spectroscopy (QLS) with a co-trapped $^{40}Ca^+$ ion, as described in chapter 2.4. QLS requires to drive sideband transitions on the spectroscopy ion, which means that we have to drive Raman sideband transitions with the frequency comb. Sideband transitions involve momentum transfer from the light field to the motion of the ions, which scales with the Lamb-Dicke parameter η, defined in eq. (2.25), and the Lamb-Dicke parameter itself is proportional to the wavevector k of the light. For a Raman transition, the effective k vector is given by

the difference of the two light fields driving the transition

$$\vec{k}_{\mathrm{Raman}} = \vec{k_1} - \vec{k_2} \tag{15.5}$$

so that co-propagating beams only lead to negligible momentum transfer. Therefore, we need to split the frequency comb light into two counter-propagating beams, which need to be overlapped at the ion position in space *and* time. The overlap in space is experimentally straight forward to achieve by observing carrier transitions in a single Ca^+ ion with each beam independently, similar to the experiments shown in this thesis. The overlap in time is more challenging, since the laser pulse length on the order of 50 fs corresponds to an extend of only 15 µm, which is the precision the two beam-lines need to be set up with the same total length.

One interesting aspect of this challenge, however, is the possibility to drive sideband transitions in one selected ion within a string of ions trapped together. The ion separation can be adjusted by the end-cap voltage of the trap, and ion separations on the order of several 10 µm are feasible. Addressing a single selected ion by slightly adjusting the beam path length with a single laser could be interesting for quantum computing.

The laser infrastructure for ionization and laser cooling of Mg^+ is already available in our laboratory, and was briefly described in chapter 9.2.9 and currently we are working on the implementation of quantum logic spectroscopy [T3].

16 Conclusion

This thesis presented the successful extension of the technique of *frequency comb driven Raman transitions* to the THz range, by driving Raman transitions between the D-finestructure states in a single Ca^+ ion confined in a linear Paul trap, and measuring the most precise spectroscopic isotope shifts reported in literature so far.

In Part I the theory of ion trapping, and the interaction of light fields with a trapped ion was explained, to set the frame for the experimental implementation.

Two different frequency comb systems were used in the experiments, a Mira Ti:sapph oscillator and a Menlo fiber based frequency comb. Part II introduced the Fourier relation between time and frequency domain, and explained the generation of the frequency comb spectrum by mode-locked, repetition rate stabilized, pulsed lasers. A thorough characterization of the two combs was presented, including pulse length measurements of the Mira laser using interferometric autocorrelation and frequency resolved optical gating (FROG). The Fourier limited pulse length of the Mira laser was determined to $\approx 55\,\mathrm{fs}$, consistent with the spectral bandwidth of 8.3 THz. The effect of group delay dispersion (GDD) in optical materials is quantitatively discussed and later verified in the experiments on Ca^+. Moreover, the repetition rate stability of the two frequency combs is quantitatively compared and can explain the different observed behavior of coherent Rabi oscillations between the D-finestructure levels in Ca^+. Besides, the stability of the frequency standard referencing the spectroscopy measurements is verified, and is found to limit the relative accuracy to 5×10^{-12}.

The main experiments are detailed in part III. A discussion of the experimental setup and implementation introduces the spectroscopic measurements of the $|S_{1/2}\rangle \rightarrow |D_{5/2}\rangle$ transition with the 729 nm laser, and the D-finestructure measurements with the Menlo frequency comb. Spectroscopy on the $|S_{1/2}\rangle \rightarrow |D_{5/2}\rangle$ transition with an absolute accuracy of 2 kHz was shown to be consistent with previous, extremely precise measurements by Chwalla et al. [A88], only limited

by the relative accuracy of the frequency standard referencing the measurement. The potential of *frequency comb driven Raman transitions* was demonstrated by performing high resolution spectroscopy of the D-finestructure splitting in $^{40}Ca^{+}$, determining its frequency to be 1 819 599 021 524(32) Hz. Systematics were investigated and the measured frequency was corrected from the quadratic Zeeman shift (21.8 Hz), which is the dominating frequency shift in our experimental setup. Additionally, spectroscopy on both transitions, the $|S_{1/2}\rangle \rightarrow |D_{5/2}\rangle$ transition and D-finestructure was performed on all naturally abundant even isotopes of Ca^{+} to determine the spectroscopic isotope shifts. Spectroscopic isotope shifts rely partly on the interaction of the electron with the nuclear charge distribution, and deviations from the predictions of the standard model can be used to test theories predicting new forces beyond the standard model. For this purpose, the isotope shifts were analyzed in a so-called King plot, and new preliminary bounds on the coupling strength of these hypothetical new forces were derived in collaboration with Elina Fuchs and Matthias Schlaffer from the Weizmann Institute of Science [A54, A53].

Finally, in part IV the application of the frequency comb technique on rotational spectroscopy in MgH^{+} as planned in the Ion Trap Group was discussed.

I expect *Frequency comb driven Raman transitions* in the THz range to be a driving force in future spectroscopic studies on molecular ions.

Part V

References and Appendix

References

Articles

[A1] Wolfgang Paul. "Electromagnetic Traps for Charged and Neutral Particles". In: *Reviews of Modern Physics* 62.3 (July 1, 1990), pp. 531–540. DOI: 10.1103/RevModPhys.62.531 (cit. on pp. 1, 7).

[A2] Hans G. Dehmelt. "Hans G. Dehmelt - Biographical". In: *Nobelprize.org. Nobel Media AB 2014.* (1989) (cit. on p. 1).

[A3] J. D. Prestage, G. J. Dick, and L. Maleki. "New Ion Trap for Frequency Standard Applications". In: *Journal of Applied Physics* 66.3 (Aug. 1, 1989), pp. 1013–1017. ISSN: 0021-8979, 1089-7550. DOI: 10.1063/1.343486 (cit. on pp. 1, 7, 77).

[A4] W. M. Itano, J. C. Bergquist, and D. J. Wineland. "Early Observations of Macroscopic Quantum Jumps in Single Atoms". In: *International Journal of Mass Spectrometry.* Special Issue: MS 1960 to Now 377 (Supplement C Feb. 1, 2015), pp. 403–409. ISSN: 1387-3806. DOI: 10.1016/j.ijms.2014.07.005 (cit. on p. 1).

[A5] E. Schrödinger. "ARE THERE QUANTUM JUMPS ?PART II*". In: *The British Journal for the Philosophy of Science* III.11 (Nov. 1, 1952), pp. 233–242. ISSN: 0007-0882. DOI: 10.1093/bjps/III.11.233 (cit. on p. 1).

[A6] W. Neuhauser et al. "Localized Visible Ba^+ Mono-Ion Oscillator". In: *Physical Review A* 22.3 (Sept. 1, 1980), pp. 1137–1140. DOI: 10.1103/PhysRevA.22.1137 (cit. on p. 1).

[A7] J. C. Bergquist et al. "Observation of Quantum Jumps in a Single Atom". In: *Physical Review Letters* 57.14 (Oct. 1986), pp. 1699–1702. ISSN: 0031-9007. DOI: 10.1103/physrevlett.57.1699 (cit. on p. 1).

[A8] Th. Sauter et al. "Observation of Quantum Jumps". In: *Physical Review Letters* 57.14 (Oct. 1986), pp. 1696–1698. ISSN: 0031-9007. DOI: 10.1103/physrevlett.57.1696 (cit. on p. 1).

[A9] Warren Nagourney, Jon Sandberg, and Hans Dehmelt. "Shelved Optical Electron Amplifier: Observation of Quantum Jumps". In: *Physical Review Letters* 56.26 (June 1986), pp. 2797–2799. ISSN: 0031-9007. DOI: 10.1103/physrevlett.56.2797 (cit. on p. 1).

[A10] D. Wineland and Hans Dehmelt. "Proposed $10^1 4\delta\nu\nu$ Laser Fluorescence Spectroscopy on the \ce{Tl+} Mono-Ion Oscillator III". In: *Bulletin of the American Physical Society.* 20.4 (1975), p. 637 (cit. on pp. 1, 22).

[A11] T. W. Hänsch and A. L. Schawlow. "Cooling of Gases by Laser Radiation". In: *Optics Communications* 13.1 (Jan. 1, 1975), pp. 68–69. ISSN: 0030-4018. DOI: 10.1016/0030-4018(75)90159-5 (cit. on pp. 1, 22).

[A12] H. Barrell. "Thirteenth General Conference of Weights and Measures". In: *Physics Bulletin* 20.2 (1969), p. 61. ISSN: 0031-9112. DOI: 10.1088/0031-9112/20/2/006 (cit. on pp. 2, 55).

[A13] L. Essen and J. V. L. Parry. "An Atomic Standard of Frequency and Time Interval: A Cæsium Resonator". In: *Nature* 176.4476 (Aug. 13, 1955), pp. 280–282. ISSN: 0028-0836. DOI: 10.1038/176280a0 (cit. on p. 2).

[A14] J. Guéna et al. "Improved Tests of Local Position Invariance Using ^{87}Rb and ^{133}Cs Fountains". In: *Physical Review Letters* 109.8 (Aug. 21, 2012), p. 080801. DOI: 10.1103/PhysRevLett.109.080801 (cit. on p. 2).

[A15] N. Huntemann et al. "Improved Limit on a Temporal Variation of ${m}_{p}/{m}_{e}$ from Comparisons of ${\mathrm{Yb}}{+}$ and Cs Atomic Clocks". In: *Physical Review Letters* 113.21 (Nov. 17, 2014), p. 210802. DOI: 10.1103/PhysRevLett.113.210802 (cit. on p. 2).

[A16] Patrick Gill. "When Should We Change the Definition of the Second?" In: *Phil. Trans. R. Soc. A* 369.1953 (Oct. 28, 2011), pp. 4109–4130. ISSN: 1364-503X, 1471-2962. DOI: 10.1098/rsta.2011.0237. pmid: 21930568 (cit. on p. 2).

[A17] S. A. Diddams et al. "An Optical Clock Based on a Single Trapped $^{199}Hg^{+}$ Ion". In: *Science* 293.5531 (Aug. 3, 2001), pp. 825–828. ISSN: 0036-8075, 1095-9203. DOI: 10.1126/science.1061171. pmid: 11452082 (cit. on p. 2).

[A18] N. Huntemann et al. "Single-Ion Atomic Clock with 3×10^{-18}Systematic Uncertainty". In: *Physical Review Letters* 116.6 (Feb. 8, 2016), p. 063001. DOI: 10.1103/PhysRevLett.116.063001 (cit. on p. 2).

[A19] N. Hinkley et al. "An Atomic Clock with 10–18 Instability". In: *Science* 341.6151 (Sept. 13, 2013), pp. 1215–1218. ISSN: 0036-8075, 1095-9203. DOI: 10.1126/science.1240420. pmid: 23970562 (cit. on p. 2).

[A20] C. W. Chou et al. "Frequency Comparison of Two High-Accuracy Al+ Optical Clocks". In: *Physical Review Letters* 104.7 (Feb. 17, 2010), p. 070802. DOI: 10.1103/PhysRevLett.104.070802 (cit. on p. 2).

[A21] T. Rosenband et al. "Frequency Ratio of Al^{+} and Hg^{+} Single-Ion Optical Clocks; Metrology at the 17th Decimal Place". In: *Science* 319.5871 (Mar. 28, 2008), pp. 1808–1812. ISSN: 0036-8075, 1095-9203. DOI: 10.1126/science.1154622. pmid: 18323415 (cit. on p. 2).

[A22] P. Giacomo. "News from the BIPM". In: *Metrologia* 20.1 (1984), p. 25. ISSN: 0026-1394. DOI: 10.1088/0026-1394/20/1/005 (cit. on p. 2).

[A23] Phil Schewe and B Stein. "Berkeley Symposium Celebrates Laser Pioneer". In: *Phys. News Update, http://www. aip. org/pnu/2005/749. html* (2005) (cit. on p. 2).

[A24] The ACME Collaboration et al. "Order of Magnitude Smaller Limit on the Electric Dipole Moment of the Electron". In: *Science* 343.6168 (Jan. 17, 2014), pp. 269–272. ISSN: 0036-8075, 1095-9203. DOI: 10.1126/science.1248213. pmid: 24356114 (cit. on p. 2).

[A25] E. J. Salumbides et al. "Bounds on Fifth Forces from Precision Measurements on Molecules". In: *Physical Review D* 87.11 (June 17, 2013), p. 112008. DOI: 10.1103/PhysRevD.87.112008 (cit. on p. 2).

[A26] S. Schiller, D. Bakalov, and V. I. Korobov. "Simplest Molecules as Candidates for Precise Optical Clocks". In: *Physical Review Letters* 113.2 (July 8, 2014), p. 023004. DOI: 10.1103/PhysRevLett.113.023004 (cit. on p. 2).

[A27] Max F. Riedel et al. "The European Quantum Technologies Flagship Programme". In: *Quantum Science and Technology* 2.3 (2017), p. 030501. ISSN: 2058-9565. DOI: 10.1088/2058-9565/aa6aca (cit. on p. 2).

[A28] Elizabeth Gibney. "Europe's Billion-Euro Quantum Project Takes Shape". In: *Nature News* 545.7652 (May 4, 2017), p. 16. DOI: 10.1038/545016a (cit. on p. 2).

[A29] Bjoern Lekitsch et al. "Blueprint for a Microwave Trapped Ion Quantum Computer". In: *Science Advances* 3.2 (Feb. 1, 2017), e1601540. ISSN: 2375-2548. DOI: 10.1126/sciadv.1601540 (cit. on p. 2).

[A30] David Deutsch. "Quantum Theory, the Church-Turing Principle and the Universal Quantum Computer". In: *Proc. Royal Society London Ser. A* (1985), pp. 96–117 (cit. on p. 2).

[A31] Richard P. Feynman. "Simulating Physics with Computers". In: *International Journal of Theoretical Physics* 21 (6-7 June 1, 1982), pp. 467–488. ISSN: 0020-7748, 1572-9575. DOI: 10.1007/BF02650179 (cit. on p. 2).

[A32] Paul Benioff. "The Computer as a Physical System: A Microscopic Quantum Mechanical Hamiltonian Model of Computers as Represented by Turing Machines". In: *Journal of Statistical Physics* 22 (May 1, 1980), pp. 563–591. ISSN: 0022-4715. DOI: 10.1007/BF01011339 (cit. on p. 2).

[A33] D. DeMille. "Quantum Computation with Trapped Polar Molecules". In: *Physical Review Letters* 88.6 (Jan. 24, 2002), p. 067901. DOI: 10.1103/PhysRevLett.88.067901 (cit. on p. 2).

[A34] P. O. Schmidt et al. "Spectroscopy Using Quantum Logic". In: *Science* 309.5735 (July 29, 2005), pp. 749–752. ISSN: 0036-8075, 1095-9203. DOI: 10.1126/science.1114375. pmid: 16051790 (cit. on pp. 2, 24, 25).

[A35] Jerome Faist et al. "Quantum Cascade Laser". In: *Science* 264.5158 (Apr. 22, 1994), pp. 553–556. ISSN: 0036-8075, 1095-9203. DOI: 10.1126/science.264.5158.553. pmid: 17732739 (cit. on p. 3).

[A36] Rekishu Yamazaki et al. "Stimulated Raman Spectroscopy and the Determination of the D-Fine-Structure Level Separation in $^{40}Ca^{+}$". In: *Physical Review A* 77.1 (Jan. 23, 2008), p. 012508. DOI: 10.1103/PhysRevA.77.012508 (cit. on pp. 3, 98, 135, 151, 201).

[A37] Rekishu Yamazaki et al. "Phase-Locked Laser System for a Metastable States Qubit in $^{40}Ca^{+}$". In: *Optics Letters* 32.15 (Aug. 1, 2007), pp. 2085–2087. ISSN: 1539-4794. DOI: 10.1364/OL.32.002085 (cit. on pp. 3, 135).

[A38] Theodor W. Hänsch and Nathalie Picqué. "Laser Spectroscopy and Frequency Combs". In: *Journal of Physics: Conference Series* 467.1 (2013), p. 012001. ISSN: 1742-6596. DOI: 10.1088/1742-6596/467/1/012001 (cit. on p. 3).

[A39] D Leibfried. "Quantum State Preparation and Control of Single Molecular Ions". In: *New Journal of Physics* 14.2 (Feb. 14, 2012), p. 023029. ISSN: 1367-2630. DOI: 10.1088/1367-2630/14/2/023029 (cit. on p. 3).

[A40] S. Ding and D. N. Matsukevich. "Quantum Logic for the Control and Manipulation of Molecular Ions Using a Frequency Comb". In: *New Journal of Physics* 14.2 (2012), p. 023028. ISSN: 1367-2630. DOI: 10.1088/1367-2630/14/2/023028 (cit. on pp. 3, 157).

[A41] Th. Udem et al. "Absolute Optical Frequency Measurement of the Cesium $D1$ Line with a Mode-Locked Laser". In: *Physical Review Letters* 82.18 (May 3, 1999), pp. 3568–3571. DOI: 10.1103/PhysRevLett.82.3568 (cit. on p. 3).

[A42] H. Schnatz et al. "First Phase-Coherent Frequency Measurement of Visible Radiation". In: *Physical Review Letters* 76.1 (Jan. 1, 1996), pp. 18–21. DOI: 10.1103/PhysRevLett.76.18 (cit. on p. 3).

[A43] Tobias Wilken et al. "A Spectrograph for Exoplanet Observations Calibrated at the Centimetre-per-Second Level". In: *Nature; London* 485.7400 (May 31, 2012), pp. 611–4. ISSN: 00280836 (cit. on p. 3).

[A44] A. Baltuska et al. "Attosecond Control of Electronic Processes by Intense Light Fields". In: *Nature* 421.6923 (Feb. 6, 2003), pp. 611–615. ISSN: 0028-0836. DOI: 10.1038/nature01414. pmid: 12571590 (cit. on p. 3).

[A45] Tobias Wilken et al. "A Frequency Comb and Precision Spectroscopy Experiment in Space". In: *CLEO: 2013 (2013), Paper AF2H.5*. CLEO: Applications and Technology. Optical Society of America, June 9, 2013, AF2H.5. DOI: 10.1364/CLEO_AT.2013.AF2H.5 (cit. on p. 3).

[A46] D. Hayes et al. "Entanglement of Atomic Qubits Using an Optical Frequency Comb". In: *Physical Review Letters* 104.14 (Apr. 5, 2010), p. 140501. DOI: 10.1103/PhysRevLett.104.140501 (cit. on pp. 3, 110).

[A47] C. W. P. Palmer et al. "Laser Spectroscopy of Calcium Isotopes". In: *Journal of Physics B: Atomic and Molecular Physics* 17.11 (1984), p. 2197. ISSN: 0022-3700. DOI: 10.1088/0022-3700/17/11/014 (cit. on pp. 4, 140, 146, 148, 195, 196, 198).

[A48] Yong Wan et al. "Precision Spectroscopy by Photon-Recoil Signal Amplification". In: *Nature Communications* 5 (Jan. 30, 2014), ncomms4096. ISSN: 2041-1723. DOI: 10.1038/ncomms4096 (cit. on pp. 4, 98, 136).

[A49] Florian Gebert et al. “Precision Isotope Shift Measurements in Calcium Ions Using Quantum Logic Detection Schemes”. In: *Physical Review Letters* 115.5 (July 29, 2015), p. 053003. DOI: 10.1103/PhysRevLett.115.053003 (cit. on pp. 4, 98, 136, 142, 151).

[A50] C. Shi et al. “Unexpectedly Large Difference of the Electron Density at the Nucleus in the $4p\,^2P_{1/2,\,3/2}$ Fine-Structure Doublet of Ca^+”. In: *Applied Physics B* 123.1 (Jan. 1, 2017), p. 2. ISSN: 0946-2171, 1432-0649. DOI: 10.1007/s00340-016-6572-z (cit. on pp. 4, 98, 142, 146, 148, 149, 151, 154, 198, 201).

[A51] M. Puchalski, D. Kędziera, and K. Pachucki. “D_1 and D_2 Lines in ^{6}Li and ^{7}Li Including QED Effects”. In: *Physical Review A* 87.3 (Mar. 7, 2013), p. 032503. DOI: 10.1103/PhysRevA.87.032503 (cit. on pp. 4, 139).

[A52] Wilfried Nörtershäuser et al. “Precision Test of Many-Body QED in the Be^+ $2p$ Fine Structure Doublet Using Short-Lived Isotopes”. In: *Physical Review Letters* 115.3 (July 13, 2015), p. 033002. DOI: 10.1103/PhysRevLett.115.033002 (cit. on pp. 4, 139).

[A53] Julian C. Berengut et al. “Probing New Light Force-Mediators by Isotope Shift Spectroscopy”. In: (Apr. 17, 2017). arXiv: 1704.05068 [hep-ph, physics:physics, physics:quant-ph] (cit. on pp. 4, 137, 153–155, 164).

[A54] Claudia Frugiuele et al. “Constraining New Physics Models with Isotope Shift Spectroscopy”. In: *Physical Review D* 96.1 (July 12, 2017), p. 015011. DOI: 10.1103/PhysRevD.96.015011 (cit. on pp. 4, 137, 154, 155, 164).

[A55] W. H. King. “Comments on the Article “Peculiarities of the Isotope Shift in the Samarium Spectrum””. In: *JOSA* 53.5 (May 1, 1963), pp. 638–639. DOI: 10.1364/JOSA.53.000638 (cit. on pp. 4, 140).

[A56] V. V. Flambaum, A. J. Geddes, and A. V. Viatkina. “Isotope Shift, Non-Linearity of King Plot and Search for Nuclear Island of Stability and New Particles”. In: (Sept. 2, 2017). arXiv: 1709.00600 [astro-ph, physics:hep-ph, physics:nucl-th, physics:physics] (cit. on pp. 4, 137, 152, 153).

[A57] Rudolf Grimm, Matthias Weidemüller, and Yurii B. Ovchinnikov. “Optical Dipole Traps for Neutral Atoms”. In: (Feb. 24, 1999). arXiv: physics/9902072 (cit. on p. 7).

[A58] S. J. M. Kuppens et al. “Loading an Optical Dipole Trap”. In: *Physical Review A* 62.1 (June 13, 2000), p. 013406. DOI: 10.1103/PhysRevA.62.013406 (cit. on p. 7).

[A59] F. M. Penning. “Die Glimmentladung Bei Niedrigem Druck Zwischen Koaxialen Zylindern in Einem Axialen Magnetfeld”. In: *Physica* 3.9 (Nov. 1, 1936), pp. 873–894. ISSN: 0031-8914. DOI: 10.1016/S0031-8914(36)80313-9 (cit. on p. 7).

[A60] Nobelprize.org. “”The Nobel Prize in Physics 1989””. In: (1989) (cit. on p. 7).

[A61] Wolfgang Paul. "Wolfgang Paul - Nobel Lecture: Electromagnetic Traps for Charged and Neutral Particles". In: (1989) (cit. on p. 7).

[A62] M. Drewsen and A. Brøner. "Harmonic Linear Paul Trap: Stability Diagram and Effective Potentials". In: *Physical Review A* 62.4 (Sept. 11, 2000), p. 045401. DOI: 10.1103/PhysRevA.62.045401 (cit. on p. 9).

[A63] G. Morigi and H. Walther. "Two-Species Coulomb Chains for Quantum Information". In: *The European Physical Journal D - Atomic, Molecular, Optical and Plasma Physics* 13.2 (Jan. 2001), pp. 261–269. ISSN: 1434-6060, 1434-6079. DOI: 10.1007/s100530170275 (cit. on p. 10).

[A64] D. F. V. James. "Quantum Dynamics of Cold Trapped Ions with Application to Quantum Computation". In: *Applied Physics B* 66.2 (Feb. 1, 1998), pp. 181–190. ISSN: 0946-2171, 1432-0649. DOI: 10.1007/s003400050373 (cit. on p. 13).

[A65] J. C. Bergquist, Wayne M. Itano, and D. J. Wineland. "Recoilless Optical Absorption and Doppler Sidebands of a Single Trapped Ion". In: *Physical Review A* 36.1 (July 1, 1987), pp. 428–430. DOI: 10.1103/PhysRevA.36.428 (cit. on p. 15).

[A66] Rui Han, Hui Khoon Ng, and Berthold-Georg Englert. "Raman Transitions without Adiabatic Elimination: A Simple and Accurate Treatment". In: *Journal of Modern Optics* 60.4 (Feb. 1, 2013), pp. 255–265. ISSN: 0950-0340. DOI: 10.1080/09500340.2013.770573 (cit. on pp. 16, 17).

[A67] F. Bloch. "Nuclear Induction". In: *Physical Review* 70 (7-8 Oct. 1, 1946), pp. 460–474. DOI: 10.1103/PhysRev.70.460 (cit. on p. 18).

[A68] Heung-Ryoul Noh and Wonho Jhe. "Analytic Solutions of the Optical Bloch Equations". In: *Optics Communications* 283.11 (June 1, 2010), pp. 2353–2355. ISSN: 0030-4018. DOI: 10.1016/j.optcom.2010.01.069 (cit. on p. 18).

[A69] W. Neuhauser et al. "Optical-Sideband Cooling of Visible Atom Cloud Confined in Parabolic Well". In: *Physical Review Letters* 41.4 (July 24, 1978), pp. 233–236. DOI: 10.1103/PhysRevLett.41.233 (cit. on p. 22).

[A70] D. J. Wineland, R. E. Drullinger, and F. L. Walls. "Radiation-Pressure Cooling of Bound Resonant Absorbers". In: *Physical Review Letters* 40.25 (June 19, 1978), pp. 1639–1642. DOI: 10.1103/PhysRevLett.40.1639 (cit. on p. 22).

[A71] Nobelprize.org. ""The Nobel Prize in Physics 1997"". In: (1997) (cit. on p. 22).

[A72] David S. Weiss et al. "Optical Molasses and Multilevel Atoms: Experiment". In: *Journal of the Optical Society of America B* 6.11 (Nov. 1, 1989), p. 2072. ISSN: 0740-3224, 1520-8540. DOI: 10.1364/JOSAB.6.002072 (cit. on p. 23).

[A73] Rockson Chang et al. "Three-Dimensional Laser Cooling at the Doppler Limit". In: *Physical Review A* 90.6 (Dec. 1, 2014). ISSN: 1050-2947, 1094-1622. DOI: 10.1103/PhysRevA.90.063407. arXiv: 1409.2519 (cit. on p. 23).

[A74] F. Diedrich et al. “Laser Cooling to the Zero-Point Energy of Motion”. In: *Physical Review Letters* 62.4 (Jan. 23, 1989), pp. 403–406. DOI: 10.1103/PhysRevLett.62.403 (cit. on p. 24).

[A75] C. Monroe et al. “Resolved-Sideband Raman Cooling of a Bound Atom to the 3D Zero-Point Energy”. In: *Physical Review Letters* 75.22 (Nov. 27, 1995), pp. 4011–4014. DOI: 10.1103/PhysRevLett.75.4011 (cit. on p. 24).

[A76] G. Poulsen, Y. Miroshnychenko, and M. Drewsen. “Efficient Ground-State Cooling of an Ion in a Large Room-Temperature Linear Paul Trap with a Sub-Hertz Heating Rate”. In: *Physical Review A* 86.5 (Nov. 26, 2012), p. 051402. DOI: 10.1103/PhysRevA.86.051402 (cit. on p. 24).

[A77] R. L. Fork et al. “Compression of Optical Pulses to Six Femtoseconds by Using Cubic Phase Compensation”. In: *Optics Letters* 12.7 (July 1, 1987), p. 483. ISSN: 0146-9592, 1539-4794. DOI: 10.1364/OL.12.000483 (cit. on p. 29).

[A78] Stéphane Schilt and Thomas Südmeyer. “Carrier-Envelope Offset Stabilized Ultrafast Diode-Pumped Solid-State Lasers”. In: *Applied Sciences* 5.4 (Oct. 14, 2015), pp. 787–816. DOI: 10.3390/app5040787 (cit. on p. 32).

[A79] David J. Jones et al. “Carrier-Envelope Phase Control of Femtosecond Mode-Locked Lasers and Direct Optical Frequency Synthesis”. In: *Science* 288.5466 (Apr. 28, 2000), pp. 635–639. ISSN: 0036-8075, 1095-9203. DOI: 10.1126/science.288.5466.635. pmid: 10784441 (cit. on p. 36).

[A80] Thomas Talvard et al. “Enhancement of the Performance of a Fiber-Based Frequency Comb by Referencing to an Acetylene-Stabilized Fiber Laser”. In: *Optics Express* 25.3 (Feb. 6, 2017), pp. 2259–2269. ISSN: 1094-4087. DOI: 10.1364/OE.25.002259 (cit. on pp. 37, 38).

[A81] Jan Hald et al. “Fiber Laser Optical Frequency Standard at 1.54 Mm”. In: *Optics Express* 19.3 (Jan. 31, 2011), pp. 2052–2063. ISSN: 1094-4087. DOI: 10.1364/OE.19.002052 (cit. on p. 38).

[A82] H. A. Haus, J. G. Fujimoto, and E. P. Ippen. “Analytic Theory of Additive Pulse and Kerr Lens Mode Locking”. In: *IEEE Journal of Quantum Electronics* 28.10 (Oct. 1992), pp. 2086–2096. ISSN: 0018-9197. DOI: 10.1109/3.159519 (cit. on p. 40).

[A83] W. Dietel, J. J. Fontaine, and J.-C. Diels. “Intracavity Pulse Compression with Glass: A New Method of Generating Pulses Shorter than 60 Fsec”. In: *Optics Letters* 8.1 (Jan. 1, 1983), pp. 4–6. ISSN: 1539-4794. DOI: 10.1364/OL.8.000004 (cit. on p. 45).

[A84] R. L. Fork, O. E. Martinez, and J. P. Gordon. “Negative Dispersion Using Pairs of Prisms”. In: *Optics Letters* 9.5 (May 1, 1984), pp. 150–152. ISSN: 1539-4794. DOI: 10.1364/OL.9.000150 (cit. on p. 45).

[A85] Zs. Bor and B. Rácz. “Group Velocity Dispersion in Prisms and Its Application to Pulse Compression and Travelling-Wave Excitation”. In: *Optics Communications* 54.3 (June 1, 1985), pp. 165–170. ISSN: 0030-4018. DOI: 10.1016/0030-4018(85)90284-6 (cit. on p. 45).

[A86] Selcuk Akturk et al. “Pulse-Front Tilt Caused by Spatial and Temporal Chirp”. In: *Optics Express* 12.19 (Sept. 20, 2004), pp. 4399–4410. ISSN: 1094-4087. DOI: 10.1364/OPEX.12.004399 (cit. on p. 45).

[A87] D. W. Allan. “Statistics of Atomic Frequency Standards”. In: *Proceedings of the IEEE* 54.2 (Feb. 1966), pp. 221–230. ISSN: 0018-9219. DOI: 10.1109/PROC.1966.4634 (cit. on pp. 54, 58).

[A88] M. Chwalla et al. “Absolute Frequency Measurement of the $^{40}Ca^{+}$ $4s\,^2S_{1/2}$–$3d\,^2D_{5/2}$ Clock Transition”. In: *Phys. Rev. Lett.* 102.2 (Jan. 13, 2009), p. 023002. DOI: 10.1103/PhysRevLett.102.023002 (cit. on pp. 56, 71, 98, 104, 107, 136, 151, 163, 201).

[A89] J. A. Barnes et al. “Characterization of Frequency Stability”. In: *IEEE Transactions on Instrumentation and Measurement* IM-20.2 (May 1971), pp. 105–120. ISSN: 0018-9456. DOI: 10.1109/TIM.1971.5570702 (cit. on p. 58).

[A90] Daniel J. Kane and Rick Trebino. “Single-Shot Measurement of the Intensity and Phase of an Arbitrary Ultrashort Pulse by Using Frequency-Resolved Optical Gating”. In: *Optics Letters* 18.10 (May 15, 1993), pp. 823–825. ISSN: 1539-4794. DOI: 10.1364/OL.18.000823 (cit. on pp. 62, 66).

[A91] Rick Trebino and Daniel J. Kane. “Using Phase Retrieval to Measure the Intensity and Phase of Ultrashort Pulses: Frequency-Resolved Optical Gating”. In: *JOSA A* 10.5 (May 1, 1993), pp. 1101–1111. ISSN: 1520-8532. DOI: 10.1364/JOSAA.10.001101 (cit. on pp. 62, 66).

[A92] Selcuk Akturk et al. “Measuring Pulse-Front Tilt in Ultrashort Pulses Using GRENOUILLE”. In: *Optics Express* 11.5 (Mar. 10, 2003), pp. 491–501. ISSN: 1094-4087. DOI: 10.1364/OE.11.000491 (cit. on p. 67).

[A93] Patrick O’Shea et al. “Highly Simplified Device for Ultrashort-Pulse Measurement”. In: *Optics Letters* 26.12 (June 15, 2001), pp. 932–934. ISSN: 1539-4794. DOI: 10.1364/OL.26.000932 (cit. on p. 67).

[A94] Pierre Dubé et al. “Evaluation of Systematic Shifts of the $^{88}Sr^{+}$ Single-Ion Optical Frequency Standard at the 10^{-17} Level”. In: *Physical Review A* 87.2 (Feb. 7, 2013), p. 023806. DOI: 10.1103/PhysRevA.87.023806 (cit. on pp. 71, 74).

[A95] C. F. Roos et al. “‘Designer Atoms’ for Quantum Metrology”. In: *Nature* 443.7109 (Sept. 21, 2006), pp. 316–319. ISSN: 0028-0836. DOI: 10.1038/nature05101 (cit. on pp. 71, 74).

[A96] Wayne M. Itano. “External-Field Shifts of the $^{199}Hg^{+}$ Optical Frequency Standard”. In: *Journal of Research of the National Institute of Standards and Technology* 105.6 (2000), pp. 829–837. ISSN: 1044-677X. DOI: 10.6028/jres.105.065. pmid: 27551639 (cit. on pp. 71, 74).

[A97] Dansha Jiang, Bindiya Arora, and M. S. Safronova. “Electric Quadrupole Moments of Metastable States of Ca^{+}, Sr^{+}, and Ba^{+}”. In: *Physical Review A* 78.2 (Aug. 20, 2008), p. 022514. DOI: 10.1103/PhysRevA.78.022514 (cit. on pp. 71, 74).

[A98] Y. Huang et al. "Hertz-Level Measurement of the $^{40}Ca^{+}$ $4s\,^2S_{1/2} - 3d\,^2D_{5/2}$ Clock Transition Frequency with Respect to the SI Second through the Global Positioning System". In: *Physical Review A* 85.3 (Mar. 23, 2012), p. 030503. DOI: 10.1103/PhysRevA.85.030503 (cit. on p. 71).

[A99] A. A. Madej et al. "Absolute Frequency of the $^{88}Sr^{+}$ $5s\,^2S_{1/2}\,4d\,^2D_{5/2}$ Reference Transition at 445 THz and Evaluation of Systematic Shifts". In: *Physical Review A* 70.1 (July 30, 2004), p. 012507. DOI: 10.1103/PhysRevA.70.012507 (cit. on pp. 74, 75).

[A100] J. Mitroy and J. Y. Zhang. "Long Range Interactions of the Mg+ and Ca+ Ions". In: *The European Physical Journal D* 46.3 (Mar. 1, 2008), pp. 415–424. ISSN: 1434-6060, 1434-6079. DOI: 10.1140/epjd/e2007-00320-5 (cit. on p. 74).

[A101] Chiranjib Sur et al. "Electric Quadrupole Moments of the D States of Alkaline-Earth-Metal Ions". In: *Physical Review Letters* 96.19 (May 18, 2006), p. 193001. DOI: 10.1103/PhysRevLett.96.193001 (cit. on p. 74).

[A102] Wayne M. Itano. "Quadrupole Moments and Hyperfine Constants of Metastable States of Ca^{+}, Sr^{+}, Ba^{+}, Yb^{+}, Hg^{+}, and Au". In: *Physical Review A* 73.2 (Feb. 17, 2006), p. 022510. DOI: 10.1103/PhysRevA.73.022510 (cit. on p. 74).

[A103] G. P. Barwood et al. "Measurement of the Electric Quadrupole Moment of the $4d\ ^2D_{5/2}$ Level in $^{88}Sr^{+}$". In: *Physical Review Letters* 93.13 (Sept. 22, 2004), p. 133001. DOI: 10.1103/PhysRevLett.93.133001 (cit. on p. 75).

[A104] Andreas Bauch and Roland Schröder. "Experimental Verification of the Shift of the Cesium Hyperfine Transition Frequency Due to Blackbody Radiation". In: *Physical Review Letters* 78.4 (Jan. 27, 1997), pp. 622–625. DOI: 10.1103/PhysRevLett.78.622 (cit. on p. 75).

[A105] M. S. Safronova and U. I. Safronova. "Blackbody Radiation Shift, Multipole Polarizabilities, Oscillator Strengths, Lifetimes, Hyperfine Constants, and Excitation Energies in Ca^{+}". In: *Physical Review A* 83.1 (Jan. 7, 2011), p. 012503. DOI: 10.1103/PhysRevA.83.012503 (cit. on pp. 75, 76).

[A106] Sergey G. Porsev and Andrei Derevianko. "Multipolar Theory of Blackbody Radiation Shift of Atomic Energy Levels and Its Implications for Optical Lattice Clocks". In: *Physical Review A* 74.2 (Aug. 30, 2006), p. 020502. DOI: 10.1103/PhysRevA.74.020502 (cit. on p. 75).

[A107] Karsten Pyka et al. "A High-Precision Segmented Paul Trap with Minimized Micromotion for an Optical Multiple-Ion Clock". In: *Applied Physics B* 114 (1-2 Jan. 1, 2014), pp. 231–241. ISSN: 0946-2171, 1432-0649. DOI: 10.1007/s00340-013-5580-5 (cit. on p. 77).

[A108] S. H. Autler and C. H. Townes. "Stark Effect in Rapidly Varying Fields". In: *Physical Review* 100.2 (Oct. 15, 1955), pp. 703–722. DOI: 10.1103/PhysRev.100.703 (cit. on p. 78).

[A109] D. J. Berkeland and M. G. Boshier. "Destabilization of Dark States and Optical Spectroscopy in Zeeman-Degenerate Atomic Systems". In: *Physical Review A* 65.3 (Mar. 2002), p. 033413 (cit. on p. 86).

[A110] T. Bergeman, Gidon Erez, and Harold J. Metcalf. "Magnetostatic Trapping Fields for Neutral Atoms". In: *Physical Review A* 35.4 (Feb. 1, 1987), pp. 1535–1546. DOI: 10.1103/PhysRevA.35.1535 (cit. on p. 86).

[A111] P. Herskind et al. "Loading of Large Ion Coulomb Crystals into a Linear Paul Trap Incorporating an Optical Cavity". In: *Applied Physics B: Lasers and Optics* 93 (2008), pp. 373–379. DOI: 10.1007/s00340-008-3199-8 (cit. on p. 89).

[A112] R. W. P. Drever et al. "Laser Phase and Frequency Stabilization Using an Optical Resonator". In: *Applied Physics B* 31.2 (June 1, 1983), pp. 97–105. ISSN: 0946-2171, 1432-0649. DOI: 10.1007/BF00702605 (cit. on p. 89).

[A113] T. W. Hansch and B. Couillaud. "Laser Frequency Stabilization by Polarization Spectroscopy of a Reflecting Reference Cavity". In: *Optics Communications* 35.3 (Dec. 1, 1980), pp. 441–444. ISSN: 0030-4018. DOI: 10.1016/0030-4018(80)90069-3 (cit. on p. 89).

[A114] P. A. Barton et al. "Measurement of the Lifetime of the $3d\,^2D_{5/2}$ State in $^{40}Ca^+$". In: *Physical Review A* 62.3 (Aug. 14, 2000), p. 032503. DOI: 10.1103/PhysRevA.62.032503 (cit. on pp. 89, 104).

[A115] Fernando Pérez and Brian E. Granger. "IPython: A System for Interactive Scientific Computing". In: *Computing in Science and Engineering* 9.3 (May 2007), pp. 21–29. ISSN: 1521-9615. DOI: 10.1109/MCSE.2007.53 (cit. on p. 96).

[A116] Wes McKinney. "Data Structures for Statistical Computing in Python". In: *Proceedings of the 9th Python in Science Conference*. Ed. by Stéfan van der Walt and Jarrod Millman. 2010, pp. 51–56 (cit. on p. 96).

[A117] J. D. Hunter. "Matplotlib: A 2D Graphics Environment". In: *Computing In Science & Engineering* 9.3 (2007), pp. 90–95. DOI: 10.1109/MCSE.2007.55 (cit. on p. 96).

[A118] N. Kjaergaard et al. "Isotope Selective Loading of an Ion Trap Using Resonance-Enhanced Two-Photon Ionization". In: *Applied Physics B* 71.2 (Aug. 2000), pp. 207–210. ISSN: 0946-2171, 1432-0649. DOI: 10.1007/s003400000296 (cit. on p. 97).

[A119] A. L. Wolf et al. "Frequency Metrology on the $4s\,^2S_{1/2} - 4p\,^2P_{1/2}$ Transition in the Calcium Ion for a Comparison with Quasar Data". In: *Physical Review A* 78.3 (Sept. 9, 2008). ISSN: 1050-2947, 1094-1622. DOI: 10.1103/PhysRevA.78.032511. arXiv: 0804.4130 (cit. on p. 98).

[A120] M. Hettrich et al. "Measurement of Dipole Matrix Elements with a Single Trapped Ion". In: *Physical Review Letters* 115.14 (Oct. 2, 2015), p. 143003. DOI: 10.1103/PhysRevLett.115.143003 (cit. on p. 98).

[A121] A. L. Wolf et al. "Direct Frequency Comb Spectroscopy of Trapped Ions". In: *Phys. Rev. Lett.* 102.22 (June 2009), p. 223901. DOI: 10.1103/PhysRevLett.102.223901 (cit. on p. 98).

[A122] R. Gerritsma et al. "Precision Measurement of the Branching Fractions of the $4p\,^2P_{3/2}$ Decay of Ca II". In: *The European Physical Journal D* 50.1 (2008), pp. 13–19. ISSN: 1434-6060. DOI: 10.1140/epjd/e2008-00196-9 (cit. on p. 98).

[A123] A. Kreuter et al. "Experimental and Theoretical Study of the $3d\,^2D$ Level Lifetimes of $^{40}Ca^+$". In: *Physical Review A* 71.3 (Mar. 11, 2005), p. 032504. DOI: 10.1103/PhysRevA.71.032504 (cit. on pp. 98, 104).

[A124] Guan Hua et al. "Precision Spectroscopy with a Single 40 Ca + Ion in a Paul Trap". In: *Chinese Physics B* 24.5 (2015), p. 054213. ISSN: 1674-1056. DOI: 10.1088/1674-1056/24/5/054213 (cit. on pp. 98, 104).

[A125] Michael Ramm et al. "Precision Measurement Method for Branching Fractions of Excited $P_{1/2}$ States Applied to $^{40}Ca^+$". In: *Physical Review Letters* 111.2 (July 9, 2013), p. 023004. DOI: 10.1103/PhysRevLett.111.023004 (cit. on p. 99).

[A126] D Wineland and Hans Dehmelt. "Proposed $10{14}\Delta\nu < \nu$ Laser Fluorescence Spectroscopy on $\text{Ti+$ Mono-Ion Oscillator III". In: *Bulletin of the American Physical Society*. Vol. 20. AMER INST PHYSICS CIRCULATION FULFILLMENT DIV, 500 SUNNYSIDE BLVD, WOODBURY, NY 11797-2999, 1975, pp. 637–637 (cit. on p. 100).

[A127] A. Turrin. "Pulse-Shape Dependence in Population Inversion with Frequency Chirping". In: *Optics Communications* 23.2 (Nov. 1, 1977), pp. 220–222. ISSN: 0030-4018. DOI: 10.1016/0030-4018(77)90311-X (cit. on p. 101).

[A128] Clarence Zener. "Non-Adiabatic Crossing of Energy Levels". In: *Proceedings of the Royal Society of London A: Mathematical, Physical and Engineering Sciences* 137.833 (Sept. 1, 1932), pp. 696–702. ISSN: 1364-5021, 1471-2946. DOI: 10.1098/rspa.1932.0165 (cit. on pp. 101, 103).

[A129] R. B. Blackman and J. W. Tukey. "The Measurement of Power Spectra from the Point of View of Communications Engineering — Part I". In: *Bell System Technical Journal* 37.1 (Jan. 1, 1958), pp. 185–282. ISSN: 1538-7305. DOI: 10.1002/j.1538-7305.1958.tb03874.x (cit. on p. 103).

[A130] Lev D Landau. "Zur Theorie Der Energieubertragung. II". In: *Phys. Z. Sowjetunion* 2.46 (1932), pp. 1–13 (cit. on p. 103).

[A131] H. Sawamura et al. "Observation of Motional Sidebands in Single 40Ca+ Ions with Improved Detection Efficiency". In: *Applied Physics B* 80.8 (June 1, 2005), pp. 1011–1014. ISSN: 0946-2171, 1432-0649. DOI: 10.1007/s00340-005-1856-8 (cit. on p. 135).

[A132] J. C. Berengut, V. A. Dzuba, and V. V. Flambaum. "Isotope-Shift Calculations for Atoms with One Valence Electron". In: *Physical Review A* 68.2 (Aug. 14, 2003), p. 022502. DOI: 10.1103/PhysRevA.68.022502 (cit. on p. 138).

[A133] E. Riis et al. “Lamb Shifts and Hyperfine Structure in $^6Li^+$ and $^7Li^+$: Theory and Experiment”. In: *Physical Review A* 49.1 (Jan. 1, 1994), pp. 207–220. DOI: 10.1103/PhysRevA.49.207 (cit. on p. 139).

[A134] Derek York. “Least-Squares Fitting of a Straight Line”. In: *Canadian Journal of Physics* 44.5 (May 1, 1966), pp. 1079–1086. ISSN: 0008-4204. DOI: 10.1139/p66-090 (cit. on p. 140).

[A135] J. Benhelm et al. “Measurement of the Hyperfine Structure of the $S_{12}-D_{52}$ Transition in $^{43}Ca^+$”. In: *Physical Review A* 75.3 (Mar. 15, 2007), p. 032506. DOI: 10.1103/PhysRevA.75.032506 (cit. on pp. 140, 142).

[A136] H. J. Emrich et al. “Radial Distribution of Nucleons in the Isotopes 48,40ca”. In: *Nuclear Physics A* 396 (Mar. 21, 1983), pp. 401–408. ISSN: 0375-9474. DOI: 10.1016/0375-9474(83)90034-9 (cit. on pp. 140, 154).

[A137] W. Nörtershäuser et al. “Isotope Shifts and Hyperfine Structure in the $3d^2D_J \rightarrow 4p^2P_J$ Transitions in Calcium II”. In: *The European Physical Journal D - Atomic, Molecular and Optical Physics* 2.1 (May 1, 1998), pp. 33–39. ISSN: 1434-6060, 1434-6079. DOI: 10.1007/s100530050107 (cit. on p. 142).

[A138] Ann-Marie Mårtensson-Pendrill et al. “Isotope Shifts and Nuclear-Charge Radii in Singly Ionized ${40\char21{}48}\mathrm{Ca}$”. In: *Physical Review A* 45.7 (Apr. 1, 1992), pp. 4675–4681. DOI: 10.1103/PhysRevA.45.4675 (cit. on p. 142).

[A139] M. Wang et al. “The Ame2012 Atomic Mass Evaluation”. In: *Chinese Physics C* 36.12 (2012), p. 1603. ISSN: 1674-1137. DOI: 10.1088/1674-1137/36/12/003 (cit. on pp. 144, 193).

[A140] Krassimira Marinova. “Nuclear Charge Radii Systematics”. In: *Journal of Physical and Chemical Reference Data* 44.3 (June 17, 2015), p. 031214. ISSN: 0047-2689. DOI: 10.1063/1.4921236 (cit. on p. 146).

[A141] I. Angeli and K. P. Marinova. “Table of Experimental Nuclear Ground State Charge Radii: An Update”. In: *Atomic Data and Nuclear Data Tables* 99.1 (Jan. 1, 2013), pp. 69–95. ISSN: 0092-640X. DOI: 10.1016/j.adt.2011.12.006 (cit. on p. 146).

[A142] Edward Witten. “Cosmic Separation of Phases”. In: *Physical Review D* 30.2 (July 15, 1984), pp. 272–285. DOI: 10.1103/PhysRevD.30.272 (cit. on p. 151).

[A143] Fermi-LAT Collaboration et al. “Dark Matter Constraints from Observations of 25 Milky Way Satellite Galaxies with the Fermi Large Area Telescope”. In: *Physical Review D* 89.4 (Feb. 11, 2014), p. 042001. DOI: 10.1103/PhysRevD.89.042001 (cit. on p. 152).

[A144] Douglas Clowe et al. “A Direct Empirical Proof of the Existence of Dark Matter”. In: *The Astrophysical Journal Letters* 648.2 (2006), p. L109. ISSN: 1538-4357. DOI: 10.1086/508162 (cit. on p. 152).

[A145] David N. Spergel and Paul J. Steinhardt. "Observational Evidence for Self-Interacting Cold Dark Matter". In: *Physical Review Letters* 84.17 (Apr. 24, 2000), pp. 3760–3763. DOI: 10.1103/PhysRevLett.84.3760 (cit. on p. 152).

[A146] F. Zwicky. "Die Rotverschiebung von Extragalaktischen Nebeln". In: *Helvetica Physica Acta* 6 (1933), pp. 110–127. ISSN: 0018-0238 (cit. on p. 152).

[A147] G. Breit, G. B. Arfken, and W. W. Clendenin. "Spectroscopic Isotope Shift and Nuclear Polarization". In: *Physical Review* 78.4 (May 15, 1950), pp. 390–406. DOI: 10.1103/PhysRev.78.390 (cit. on p. 153).

[A148] A. R. Bodmer. "Spectroscopic Isotope Shift and Nuclear Deformations". In: *Proceedings of the Physical Society. Section A* 67.7 (1954), p. 622. ISSN: 0370-1298. DOI: 10.1088/0370-1298/67/7/307 (cit. on p. 153).

[A149] Cédric Delaunay et al. "Probing The Atomic Higgs Force". In: (Jan. 19, 2016). arXiv: 1601.05087 [hep-ph, physics:physics, physics:quant-ph] (cit. on p. 153).

[A150] G. Hagen et al. "Neutron and Weak-Charge Distributions of the 48Ca Nucleus". In: *Nature Physics* 12.2 (Feb. 2016), pp. 186–190. ISSN: 1745-2473. DOI: 10.1038/nphys3529 (cit. on p. 154).

[A151] W. J. Balfour. "Rotational Analysis of the $A1\Sigma+ \rightarrow X1\Sigma+$ and $B1\Pi \rightarrow X1\Sigma+$ Systems of 24MgH+, 25MgH+, and 26MgH+". In: *Canadian Journal of Physics* 50.11 (June 1972), pp. 1082–1091. ISSN: 0008-4204, 1208-6045. DOI: 10.1139/p72-150 (cit. on p. 158).

[A152] Peter F. Staanum et al. "Rotational Laser Cooling of Vibrationally and Translationally Cold Molecular Ions". In: *Nature Physics* 6.4 (Apr. 2010), pp. 271–274. ISSN: 1745-2473. DOI: 10.1038/nphys1604 (cit. on p. 159).

[A153] Michael Berglund and Michael E. Wieser. "Isotopic Compositions of the Elements 2009 (IUPAC Technical Report)". In: *Pure and Applied Chemistry* 83.2 (2011), pp. 397–410. ISSN: 1365-3075. DOI: 10.1351/PAC-REP-10-06-02 (cit. on pp. 188, 189).

[A154] V. Batteiger et al. "Precision Spectroscopy of the $3s$-$3p$ Fine-Structure Doublet in Mg^+". In: *Physical Review A* 80.2 (Aug. 11, 2009), p. 022503. DOI: 10.1103/PhysRevA.80.022503 (cit. on p. 189).

[A155] G. Clos et al. "Decoherence-Assisted Spectroscopy of a Single Mg^+ Ion". In: *Physical Review Letters* 112.11 (Mar. 17, 2014), p. 113003. DOI: 10.1103/PhysRevLett.112.113003 (cit. on p. 189).

[A156] M. Herrmann et al. "Frequency Metrology on Single Trapped Ions in the Weak Binding Limit: The $3s_{1/2} - 3p_{3/2}$ Transition in $^{24}Mg^+$". In: *Physical Review Letters* 102.1 (Jan. 9, 2009), p. 013006. DOI: 10.1103/PhysRevLett.102.013006 (cit. on p. 189).

[A157] J. C. Pickering, A. P. Thorne, and J. K. Webb. "Precise Laboratory Wavelengths of the Mg I and Mg II Resonance Transitions at 2853, 2803 and 2796 Angstroms". In: *Monthly Notices of the Royal Astronomical Society* 300 (Oct. 1, 1998), pp. 131–134. ISSN: 0035-8711. DOI: 10.1046/j.1365-8711.1998.01874.x (cit. on p. 189).

[A158] W. Ansbacher, Y. Li, and E. H. Pinnington. "Precision Lifetime Measurement for the 3p Levels of Mg II Using Frequency-Doubled Laser Radiation to Excite a Fast Ion Beam". In: *Physics Letters A* 139 (3–4 July 31, 1989), pp. 165–169. ISSN: 0375-9601. DOI: 10.1016/0375-9601(89)90353-8 (cit. on p. 189).

[A159] A. Mortensen et al. "Isotope Shifts of the $4s^2 {}^1S_0 \rightarrow 4s5p {}^1P_1$ Transition and Hyperfine Splitting of the $4s5p {}^1P_1$ State in Calcium". In: *Physical Review A* 69.4 (Apr. 1, 2004), p. 042502. DOI: 10.1103/PhysRevA.69.042502 (cit. on p. 189).

[A160] A. Kramida et al. "NIST Atomic Spectra Database". In: (2018) (cit. on p. 193).

[A161] K. N. Huang et al. "NEUTRAL-ATOM ELECTRON BINDING ENERGIES FROM RELAXED-ORBITAL RELATIVISTIC HARTREE-FOCK-SLATER CALCULATIONS". In: 18th ser. (1976), p. 243 (cit. on p. 193).

[A162] Paul Boggs et al. "NISTIR 4834 User's Reference Guide for ODRPACK Version 2.01 Software for Weighted Orthogonal Distance Regression". In: (June 2018) (cit. on p. 195).

[A163] H. D. Wohlfahrt et al. "Nuclear Charge Distributions in $1f_{\frac{7}{2}}$-Shell Nuclei from Muonic x-Ray Measurements". In: *Physical Review C* 23.1 (Jan. 1, 1981), pp. 533–548. DOI: 10.1103/PhysRevC.23.533 (cit. on pp. 195, 196, 198).

[A164] H. D. Wohlfahrt et al. "Muonic Isotope Shifts in the Stable Ca Nuclei". In: *Physics Letters B* 73.2 (Feb. 13, 1978), pp. 131–134. ISSN: 0370-2693. DOI: 10.1016/0370-2693(78)90816-X (cit. on p. 198).

[A165] R. F. Garcia Ruiz et al. "Unexpectedly Large Charge Radii of Neutron-Rich Calcium Isotopes". In: *Nature Physics* 12.6 (June 2016), pp. 594–598. ISSN: 1745-2481. DOI: 10.1038/nphys3645 (cit. on p. 198).

Reviews

[R1] Jürgen Eschner et al. "Laser Cooling of Trapped Ions". In: *J. Opt. Soc. Am. B* 20.5 (May 2003), pp. 1003–1015. DOI: 10.1364/JOSAB.20.001003 (cit. on p. 1).

[R2] Michael A. Lombardi, Thomas P. Heavner, and Steven R. Jefferts. "NIST Primary Frequency Standards and the Realization of the SI Second". In: *NCSLI Measure* 2.4 (Dec. 1, 2007), pp. 74–89. ISSN: 1931-5775. DOI: 10.1080/19315775.2007.11721402 (cit. on pp. 2, 55).

[R3] Andrew D. Ludlow et al. "Optical Atomic Clocks". In: (July 13, 2014). arXiv: 1407.3493 [physics] (cit. on p. 2).

[R4] Stefan Willitsch. "Coulomb-Crystallised Molecular Ions in Traps: Methods, Applications, Prospects". In: *International Reviews in Physical Chemistry* 31.2 (Apr. 1, 2012), pp. 175–199. ISSN: 0144-235X. DOI: 10.1080/0144235X.2012.667221 (cit. on p. 2).

[R5] Paul Jansen, Hendrick L. Bethlem, and Wim Ubachs. "Perspective: Tipping the Scales: Search for Drifting Constants from Molecular Spectra". In: *The Journal of Chemical Physics* 140.1 (Jan. 7, 2014), p. 010901. ISSN: 0021-9606, 1089-7690. DOI: 10.1063/1.4853735 (cit. on p. 2).

[R6] T. D. Ladd et al. "Quantum Computers". In: *Nature* 464.7285 (Mar. 4, 2010), pp. 45–53. ISSN: 0028-0836. DOI: 10.1038/nature08812 (cit. on p. 2).

[R7] Rainer Blatt and David Wineland. "Entangled States of Trapped Atomic Ions". In: *Nature* 453.7198 (June 19, 2008), pp. 1008–1015. ISSN: 0028-0836. DOI: 10.1038/nature07125 (cit. on p. 2).

[R8] H. Häffner, C. F. Roos, and R. Blatt. "Quantum Computing with Trapped Ions". In: *Physics Reports* 469.4 (Dec. 1, 2008), pp. 155–203. ISSN: 0370-1573. DOI: 10.1016/j.physrep.2008.09.003 (cit. on p. 2).

[R9] Yu Yao, Anthony J. Hoffman, and Claire F. Gmachl. "Mid-Infrared Quantum Cascade Lasers". In: *Nature Photonics* 6.7 (July 2012), pp. 432–439. ISSN: 1749-4885. DOI: 10.1038/nphoton.2012.143 (cit. on p. 3).

[R10] R. A. Lewis. "A Review of Terahertz Sources". In: *Journal of Physics D: Applied Physics* 47.37 (2014), p. 374001. ISSN: 0022-3727. DOI: 10.1088/0022-3727/47/37/374001 (cit. on p. 3).

[R11] Th Udem, R. Holzwarth, and T. W. Hänsch. "Optical Frequency Metrology". In: *Nature* 416.6877 (Mar. 14, 2002), pp. 233–237. ISSN: 0028-0836. DOI: 10.1038/416233a (cit. on pp. 3, 36).

[R12] Theodor W. Hänsch. "Nobel Lecture: Passion for Precision". In: *Reviews of Modern Physics* 78.4 (Nov. 17, 2006), pp. 1297–1309. DOI: 10.1103/RevModPhys.78.1297 (cit. on p. 3).

[R13] G. Breit. "Theory of Isotope Shift". In: *Reviews of Modern Physics* 30.2 (Apr. 1, 1958), pp. 507–516. DOI: 10.1103/RevModPhys.30.507 (cit. on pp. 4, 137).

[R14] Gianfranco Bertone, Dan Hooper, and Joseph Silk. "Particle Dark Matter: Evidence, Candidates and Constraints". In: *Physics Reports* 405.5 (Jan. 1, 2005), pp. 279–390. ISSN: 0370-1573. DOI: 10.1016/j.physrep.2004.08.031 (cit. on pp. 4, 152).

[R15] Lowell S. Brown and Gerald Gabrielse. "Geonium Theory: Physics of a Single Electron or Ion in a Penning Trap". In: *Reviews of Modern Physics* 58.1 (Jan. 1, 1986), pp. 233–311. DOI: 10.1103/RevModPhys.58.233 (cit. on p. 7).

[R16] D. Leibfried et al. "Quantum Dynamics of Single Trapped Ions". In: *Reviews of Modern Physics* 75.1 (2003), p. 281 (cit. on p. 12).

[R17] John M. Dudley, Goëry Genty, and Stéphane Coen. "Supercontinuum Generation in Photonic Crystal Fiber". In: *Reviews of Modern Physics* 78.4 (Oct. 4, 2006), pp. 1135–1184. DOI: 10.1103/RevModPhys.78.1135 (cit. on p. 36).

[R18] Philip St J. Russell. "Photonic-Crystal Fibers". In: *Journal of Lightwave Technology* 24.12 (Dec. 1, 2006), pp. 4729–4749 (cit. on p. 36).

[R19] E. P. Ippen. "Principles of Passive Mode Locking". In: *Applied Physics B* 58.3 (Mar. 1, 1994), pp. 159–170. ISSN: 0946-2171, 1432-0649. DOI: 10.1007/BF01081309 (cit. on p. 40).

[R20] R. Paschotta et al. "Optical Phase Noise and Carrier-Envelope Offset Noise of Mode-Locked Lasers". In: *Applied Physics B* 82.2 (Dec. 3, 2005), pp. 265–273. ISSN: 0946-2171, 1432-0649. DOI: 10.1007/s00340-005-2041-9 (cit. on p. 43).

[R21] Rick Trebino et al. "Measuring Ultrashort Laser Pulses in the Time-Frequency Domain Using Frequency-Resolved Optical Gating". In: *Review of Scientific Instruments* 68.9 (Sept. 1, 1997), pp. 3277–3295. ISSN: 0034-6748. DOI: 10.1063/1.1148286 (cit. on pp. 62, 66, 67).

[R22] C. W. Chou et al. "Optical Clocks and Relativity". In: *Science* 329.5999 (Sept. 24, 2010), pp. 1630–1633. ISSN: 0036-8075, 1095-9203. DOI: 10.1126/science.1192720. pmid: 20929843 (cit. on pp. 71, 77).

[R23] Yao Huang et al. "Evaluation of the Systematic Shifts of a Single-$^{40}Ca^{+}$-Ion Frequency Standard". In: *Physical Review A* 84.5 (Nov. 21, 2011), p. 053841. DOI: 10.1103/PhysRevA.84.053841 (cit. on p. 71).

[R24] J. Mitroy, M. S. Safronova, and Charles W. Clark. "Theory and Applications of Atomic and Ionic Polarizabilities". In: *Journal of Physics B: Atomic, Molecular and Optical Physics* 43.20 (2010), p. 202001. ISSN: 0953-4075. DOI: 10.1088/0953-4075/43/20/202001 (cit. on p. 75).

[R25] D. J. Berkeland et al. "Minimization of Ion Micromotion in a Paul Trap". In: *Journal of Applied Physics* 83.10 (Apr. 28, 1998), pp. 5025–5033. ISSN: 0021-8979. DOI: 10.1063/1.367318 (cit. on pp. 77, 84).

[R26] Nikolay V Vitanov et al. "Laser-Induced Population Transfer by Adiabatic Passage Techniques". In: *Annual Review of Physical Chemistry* 52.1 (Oct. 1, 2001), pp. 763–809. ISSN: 0066-426X. DOI: 10.1146/annurev.physchem.52.1.763 (cit. on pp. 101, 103).

[R27] Curt Wittig. "The Landau–Zener Formula". In: *The Journal of Physical Chemistry B* 109.17 (May 1, 2005), pp. 8428–8430. ISSN: 1520-6106. DOI: 10.1021/jp040627u (cit. on p. 103).

[R28] J. J. Olivero and R. L. Longbothum. "Empirical Fits to the Voigt Line Width: A Brief Review". In: *Journal of Quantitative Spectroscopy and Radiative Transfer* 17.2 (Feb. 1977), pp. 233–236. ISSN: 0022-4073. DOI: 10.1016/0022-4073(77)90161-3 (cit. on p. 113).

Books

[B1] J. S. Bell. *Speakable and Unspeakable in Quantum Mechanics: Collected Papers on Quantum Philosophy*. Google-Books-ID: FGnnHxh2YtQC. Cambridge University Press, June 3, 2004. 292 pp. ISBN: 978-0-521-52338-7 (cit. on p. 1).

[B2] Max Jammer. *The Philosophy of Quantum Mechanics*. New York: Wiley, 1974 (cit. on p. 1).

[B3] Jérôme Faist. *Quantum Cascade Lasers*. OUP Oxford, Mar. 14, 2013. 322 pp. ISBN: 978-0-19-852824-1 (cit. on p. 3).

[B4] Yun-Shik Lee. *Principles of Terahertz Science and Technology*. Google-Books-ID: 4ZqkuUURxFcC. Springer Science & Business Media, Mar. 2, 2009. 348 pp. ISBN: 978-0-387-09540-0 (cit. on p. 3).

[B5] Jun Ye and Steven T. Cundiff. *Femtosecond Optical Frequency Comb: Principle, Operation and Applications*. Springer Science & Business Media, June 15, 2006. 373 pp. ISBN: 978-0-387-23791-6 (cit. on p. 3).

[B6] W. H. King. *Isotope Shifts in Atomic Spectra*. Google-Books-ID: eEgGCAAAQBAJ. Springer Science & Business Media, Nov. 11, 2013. 215 pp. ISBN: 978-1-4899-1786-7 (cit. on pp. 4, 137).

[B7] Jun Ye. *Femtosecond Optical Frequency Comb: Principle, Operation, and Applications*. Boston: Kluwer Academic Publishers, 2005. ISBN: 978-0-387-23790-9 (cit. on p. 27).

[B8] Jean-Claude Diels and Wolfgang Rudolph. *Ultrashort Laser Pulse Phenomena*. Burlington, MA, USA: Academic Press, 2006. ISBN: 978-0-08-046640-8 (cit. on pp. 45, 62).

[B9] Hofmann-Wellenhof, Bernhard, Lichtenegger, Herbert, Collins, James. *Global Positioning System - Theory and Practice*. Springer, 1994 (cit. on p. 51).

[B10] Rick Trebino. *Frequency-Resolved Optical Gating: The Measurement of Ultrashort Laser Pulses*. Google-Books-ID: 257aBwAAQBAJ. Springer Science & Business Media, Dec. 6, 2012. 428 pp. ISBN: 978-1-4615-1181-6 (cit. on pp. 62, 66).

[B11] G. K. Woodgate. *Elementary Atomic Structure*. Second Edition. Oxford, New York: Oxford University Press, Aug. 18, 1983. 238 pp. ISBN: 978-0-19-851156-4 (cit. on p. 71).

Theses

[T1] D. Hayes. "Remote and Local Entanglement of Ions with Photons and Phonons". University of Maryland, 2012 (cit. on pp. 3, 110).

[T2] C. Roos. "Controlling the Quantum State of Trapped Ions". 2000 (cit. on pp. 12, 13).

[T3] Karin Fisher. "Adiabatic Cooling for Rovibrational Spectroscopy of Molecular Ions". PhD Thesis. Aarhus University, July 2017 (cit. on pp. 15, 24, 77, 84, 100, 160, 162).

[T4] Gregers Poulsen. “Sideband Cooling of Atomic and Molecular Ions”. PhD thesis. Danish National Research Foundation Center for Quantum Optics - Quantop Department of Physics and Astronomy, Aarhus University, 2011 (cit. on pp. 24, 90, 94, 104).

[T5] Nicolai Friis Mortensen. “Disciplining a Rb Oscillator to GPS for Improved Accuracy in Absolute Optical Frequency Measurements”. Bachelor Thesis. Aarhus, Denmark: Aarhus University, June 2016 (cit. on p. 51).

[T6] Niels Kjærgaard. “Methods in Laser Cooling of Ions in Storage Rings and Traps”. PhD Thesis. Aarhus University, 2001 (cit. on pp. 81–83, 97).

[T7] Anders Kragh Hansen. “Cold Molecular Ions: Rotational State Preparation and Single Ion Reaction Experiments”. PhD Thesis. Aarhus University, Sept. 2012 (cit. on p. 89).

[T8] Philipp Shindler. “Frequeny Synthesis and Pulse Shaping for Quantum Information Proessing with Trapped Ions”. University of Innsbruk, Sept. 22, 2008 (cit. on p. 94).

[T9] Paul Tan The Pham. “A General-Purpose Pulse Sequencer for Quantum Computing”. Thesis. Massachusetts Institute of Technology, 2005 (cit. on p. 94).

[T10] Hans Harhoff Andersen. “Cooling and Manipulating Ions in Traps with Integrated Optical Cavities”. PhD Thesis. Aarhus, Denmark: Aarhus University, Aug. 2015 (cit. on p. 99).

[T11] William Lund Sommer. “Characterization of a Quantum Cascade Laser and Wavelength Meter for Molecular Spectroscopy”. Bachelor Thesis. Aarhus University, June 15, 2016 (cit. on p. 159).

[T12] Julie Harbo Arleth. “Characterization of a Quantum Cascade Laser and Wavelength Meter”. Bachelor Thesis. Aarhus University, Aug. 15, 2017. 32 pp. (cit. on p. 159).

Software

[S1] pschindler. *Vhdl-Ad9910: Vhdl Code for the Innsbruck Ad9910 Dds Board*. Jan. 7, 2015 (cit. on p. 94).

[S2] pschindler. *Sequencer2: Sequencer2 Python Compiler for the PBox Used in Innsbruck*. Feb. 7, 2015 (cit. on p. 94).

Patents

[P1] “Global Positioning System”. US5210540 A. Yutaka Masumoto. U.S. Classification 342/357.28, 701/468, 701/520; International Classification G01S19/50; Cooperative Classification G01C5/06, G01S19/42, G01S19/49, G01S19/32; European Classification G01S19/42. May 11, 1993 (cit. on p. 51).

Online resources

[O1] *The Nobel Prize in Physics 1989*. 1989. URL: http://www.nobelprize.org/nobel_prizes/physics/laureates/1989/ (visited on 11/18/2015) (cit. on p. 1).

[O2] *The Nobel Prize in Physics 2012*. 2012. URL: https://www.nobelprize.org/nobel_prizes/physics/laureates/2012/ (visited on 09/23/2017) (cit. on p. 1).

[O3] *The Nobel Prize in Physics 2005*. 2005. URL: https://www.nobelprize.org/nobel_prizes/physics/laureates/2005/ (visited on 09/23/2017) (cit. on p. 3).

[O4] Bureau international des poids et mesures. *BIPM - Recommended Values of Standard Frequencies*. URL: http://www.bipm.org/en/publications/mises-en-pratique/standard-frequencies.html (visited on 09/14/2017) (cit. on p. 37).

[O5] Michael A. Lombardi. *The Use of GPS Disciplined Oscillators as Primary Frequency Standards for Calibration and Metrology Laboratories*. 2008. URL: http://tf.nist.gov/general/pdf/2297.pdf (visited on 06/18/2016) (cit. on p. 51).

[O6] NIST. *GPS Data Archive*. Feb. 26–2015. URL: https://www.nist.gov/pml/time-and-frequency-division/services/gps-data-archive (visited on 04/09/2017) (cit. on p. 57).

[O7] *TOELLNER Electronic Instrumente GmbH - TOE 8850*. URL: http://www.toellner.de/html/pages/en-homepage-products-power-supplies-toe8850.htm (visited on 08/16/2017) (cit. on p. 85).

[O8] *Welcome to the PBox Documentation! — Python Documentation*. URL: http://pboxdoc.readthedocs.io/en/latest/ (visited on 08/16/2017) (cit. on p. 94).

[O9] *Pulse Programmer*. URL: https://sourceforge.net/projects/pulse-sequencer/ (visited on 08/16/2017) (cit. on p. 94).

[O10] Oracle Corporation. *MySQL*. URL: https://www.mysql.com/ (visited on 08/16/2017) (cit. on p. 96).

[O11] *Project Jupyter*. URL: http://www.jupyter.org (visited on 08/16/2017) (cit. on p. 96).

[O12] *Python Data Analysis Library — Pandas: Python Data Analysis Library*. URL: http://pandas.pydata.org/ (visited on 08/16/2017) (cit. on p. 96).

[O13] *Matplotlib: Python Plotting — Matplotlib 2.0.2 Documentation*. URL: https://matplotlib.org/ (visited on 08/16/2017) (cit. on p. 96).

[O14] *Raspberry Pi - Teach, Learn, and Make with Raspberry Pi*. URL: https://www.raspberrypi.org/ (visited on 08/16/2017) (cit. on p. 96).

[O15] *DS18B20 Programmable Resolution 1-Wire Digital Thermometer - Maxim*. URL: https://www.maximintegrated.com/en/products/analog/sensors-and-sensor-interface/DS18B20.html (visited on 08/16/2017) (cit. on p. 96).

[O16] Atomic Spectra Database NIST. *NIST Atomic Spectra Database*. URL: `http://www.nist.gov/pml/data/asd.cfm` (visited on 11/20/2015) (cit. on p. 98).

Other sources

[X1] Septentrio Satellite Navigation. *AsteRx2e Specifications*. Sept. 2011 (cit. on pp. 52, 54).

[X2] Patrick A. Berry. *File:GRENOUILLE Long.JPG*. In: *Wikipedia*. Page Version ID: 468453762. 2005 (cit. on p. 67).

[X3] *Public Domain, not the work of the author of this thesis* (cit. on p. 152).

A
Appendix

A.1 Group velocity dispersion in air

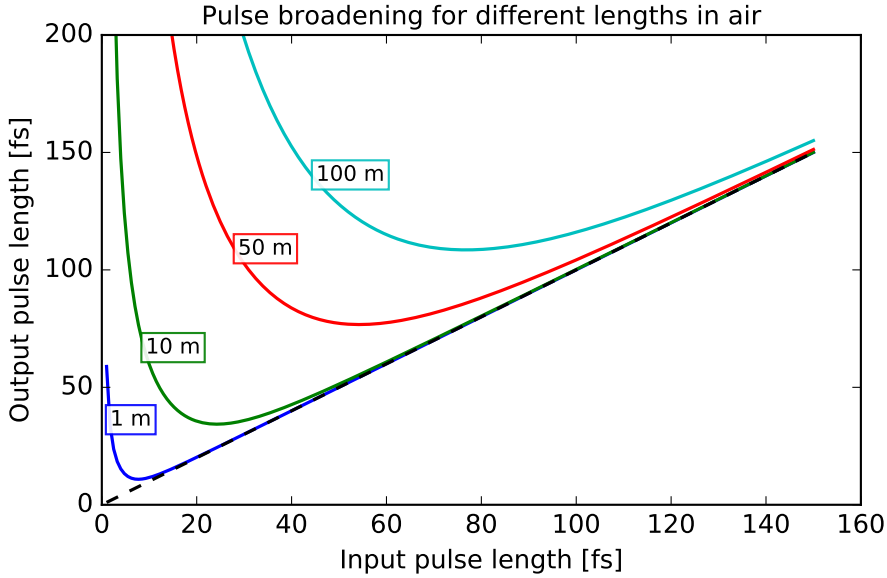

Figure A.1: Group delay dispersion in air.

A.2 Magnesium

	^{24}Mg	^{25}Mg	^{26}Mg
Abundance [%]	78.99(4) [a]	10.00(1) [a]	11.01(3) [a]
Nuclear Spin	0	5/2	0

Table A.1: Mg^+ isotope abundance and nuclear spin

[a] Ref. [A153]

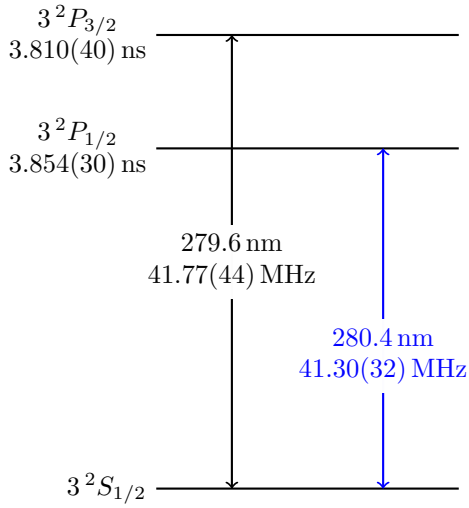

Figure A.2: Level structure of $^{24}Mg^+$. The given lifetimes and transition wavelengths can be found with higher precision and references in table A.2. Linewidths are calculated from the lifetimes.

Table A.2: Ground state transitions in Mg^+ isotopes. Wavelengths in vacuum are calculated from the given frequencies. Lifetimes are given for the upper level of each transition.

Transition	Wavelength [nm]	Frequency [THz]	Lifetime [ns]
$3\,^2S_{1/2} \rightarrow 3\,^2P_{1/2}$			
$^{24}Mg^+$	280.353	1069.338 342 56(16) [a, d]	3.854(30) [c,e]
$^{25}Mg^+$	280.353	1069.339 957(5) [b]	
$^{26}Mg^+$	280.352	1069.341 427 47(16) [a]	
$3\,^2S_{1/2} \rightarrow 3\,^2P_{3/2}$			
$^{24}Mg^+$	279.636	1072.082 934 33(16) [a, c, d]	3.810(40) [c, e]
$^{25}Mg^+$	279.635	1072.084 547(5) [b]	3.75(15) [e]
$^{26}Mg^+$	279.635	1072.086 021 89(16) [a]	3.81(10) [e]
$3\,^2S_{1/2} \rightarrow 2\,^2D_{5/2}$			
$^{25}Mg^+$	139.879	2143.223 903(7) [b]	
$3\,^2S_{1/2} \rightarrow 4\,^2P_{3/2}$			
$^{25}Mg^+$	123.992	2417.829 196(12) [b]	

[a] Ref. [A154]
[b] Ref. [A155]
[c] Ref. [A156]
[d] Ref. [A157]
[e] Ref. [A158]

Table A.3: Calcium isotope shifts for the ionization transition at 272 nm [A159] and natural abundance [A153]

A	shift [MHz]	abundance in %
40	0	96.941(156)
42	967(9)	0.647(23)
43	1455(9)	0.135(10)
44	1879(14)	2.086(110)
46	2746(16)	0.004(3)
48	3528(16)	0.187(21)

A.3 Laboratory layout plan

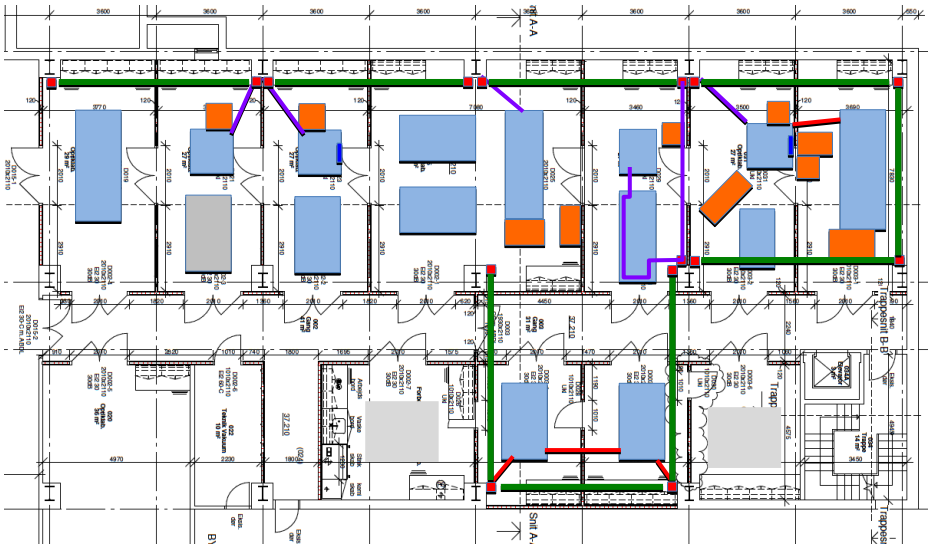

Figure A.3: Laboratory layout plan

B

Reevaluation of isotope shifts

B.1 Summary

This appendix is a summary of our improved isotope shift measurements and analysis after I handed in my thesis.

B.2 Isotope shift measurements

The measured isotope shifts for the D-fine structure transition $3\,^2D_{3/2} - 3\,^2D_{5/2}$, and the 729 nm transition $4\,^2S_{1/2} - 3\,^2D_{5/2}$ are listed in table B.1 together with the calculated shifts on the 732 nm transition. The isotope shift measurements are plotted in figure B.1 against the nuclear mass, see eq. (B.4).

Table B.1: Calcium$^+$ isotope shifts relative to $^{40}Ca^+$ in MHz. The values for the 732 nm transition are calculated based on the measured 729 nm and D-finestructure transitions.

transition	[nm]	42	44	46	48
$4\,^2S_{1/2} - 3\,^2D_{5/2}$	729	+2771.873(2)	+5340.888(2)	+7768.401(2)	+9990.383(2)
$3\,^2D_{3/2} - 3\,^2D_{5/2}$	D-fine	−3.519 896(24)	−6.792 470(22)	−9.901 524(21)	−12 746 611(27)
$4\,^2S_{1/2} - 3\,^2D_{3/2}$	732	+2775.393(2)	+5347.680(2)	+7778.302(2)	+10 003.130(2)

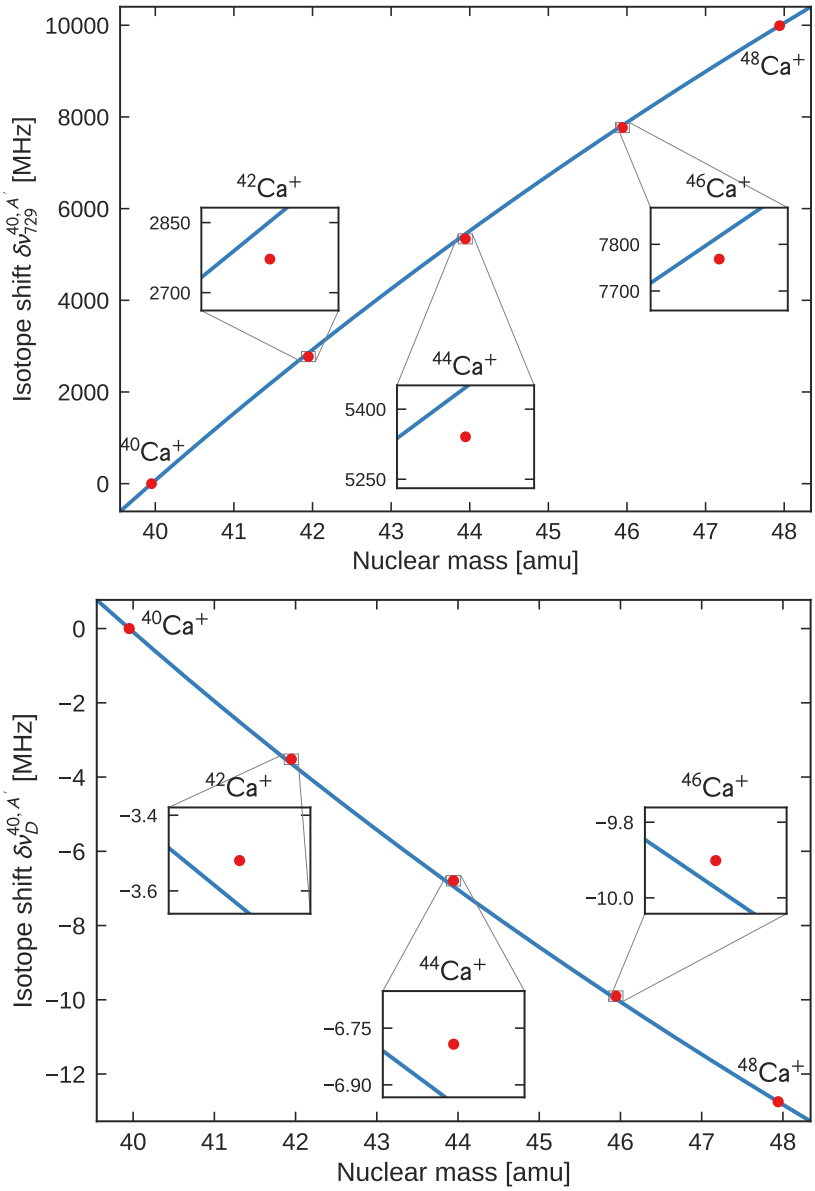

Figure B.1: Isotope shift relative to $^{40}Ca^+$ of the 729 nm transition (top) and D-finestructure transition (bottom) vs. nuclear mass. The red dots show the measured value (with error bars too small to be visible on this scale) and the blue line is plotted according to equation (B.6) and forced through $^{40,48}Ca^+$ based on the assumption that $\delta\left\langle r_c^2\right\rangle^{40,48} = 0$. The distance between the measurements and the line is due to the field shift.

B.3 Analysis

B.3.1 Definitions

The isotope shift of a transition i is defined as the difference in transition frequency between isotope A and A' as

$$\delta\nu_i^{AA'} \equiv \nu_i^A - \nu_i^{A'} , \tag{B.1}$$

where ν_i^A and $\nu_i^{A'}$ are the transition frequencies of the two isotopes. In our case, we reference all numbers to the $^{40}Ca^+$ isotope, thus $A = 40$.

The two leading contributions to the isotope shift are the mass shift (MS) and field shift (FS)

$$\delta\nu_i^{AA'} = \delta\nu_{i,\mathrm{MS}}^{AA'} + \delta\nu_{i,\mathrm{FS}}^{AA'} = K_i \frac{1}{\mu} + F_i \, \delta \left\langle r_c^2 \right\rangle^{AA'} . \tag{B.2}$$

where K_i and F_i are the mass and field shift constants, respectively, $\delta \left\langle r_c^2 \right\rangle^{AA'}$ is the difference of the nuclear charge radius squared, and the mass factor μ is given by

$$\mu = \mu^{AA'} = \frac{m_A(m_{A'} + m_e)}{m_{A'} - m_A} \tag{B.3}$$

where m_e is the electron mass, and m_A and $m_{A'}$ are the masses of the *nuclei* of the two isotopes. The nuclear mass can be calculated from the precisely known masses of the neutral atomic calcium isotopes [A139], and the binding energy as

$$m_A = m_{A,\,\text{neutral atom}} - 20\, m_e - m_{\text{binding energy}} , \tag{B.4}$$

where m_e is the electron mass, and

$$m_{\text{binding energy}} = \sum_{n=0}^{19} E_{\text{ionize}}(^{40}\mathrm{Ca}^{n+})/c^2 = 1.9871(5) \times 10^{-5}\,\mathrm{u} \approx 4\,\%\, m_e \tag{B.5}$$

is the additional mass of the neutral species due to the binding energy of the electrons, taken from the NIST database [A160] and agrees with theoretical calculations found in ref. [A161]. Here, we assume that the ionization energy is independent of the specific isotope. The correction due to the binding energy is only of the order of 5×10^{-7}, and the precision of the best isotope mass measurement is 6×10^{-10} for $^{40}Ca^+$. Therefore, we do not introduce an error if the isotope shift of the ionization energies is smaller than 10^{-3}. The resulting nuclear masses together with the corresponding mass factors μ are listed in table B.2.

The isotope shift in equation (B.2) can be rewritten as

$$\mu\delta\nu_i^{AA'} = K_i + F_i\, \mu\, \delta \left\langle r_c^2 \right\rangle^{AA'} \tag{B.6}$$

where $\mu\delta\nu_i^{AA'}$ is called the modified isotope shift.

Table B.2: Calcium isotope nuclear masses and (nuclear) mass factors calculated from equation (B.3).

Ca isotope	mass [u]	mass factor μ [u]
40	39.951 599 394(23)	inf
41	40.951 286 45(15)	1636.603 47(25)
42	41.947 626 36(16)	839.616 25(7)
43	42.947 774 97(24)	572.681 46(5)
44	43.944 490 13(30)	439.700 13(4)
45	44.945 194 93(40)	359.591 47(3)
46	45.942 697 53(240)	306.372 24(14)
47	46.943 550 93(240)	268.235 82(11)
48	47.941 531 30(13)	239.722 039(5)

B.3.2 Mass and field shift based on $\delta \left\langle r_c^2 \right\rangle^{40,48} = 0$

Using the assumption $\delta \left\langle r_c^2 \right\rangle^{40,48} = 0$, we can extract the mass shift constant K_i directly from equation B.6 by plugging in the isotope shift $\delta\nu_i^{40,48}$. We find

$$\begin{aligned} K_{\text{D-fine}} &= -3055.6432(65)\,\text{MHz u} \\ K_{729} &= 2394.915\,09(48)\,\text{GHz u}\,. \end{aligned} \tag{B.7}$$

Using these mass shift constants, we can calculate the individual field shifts $\delta\nu_{i,\text{FS}}^{AA'}$ as the difference between isotope shift measurement and the mass shift prediction as

$$\delta\nu_{i,\text{FS}}^{AA'} = \delta\nu_i^{AA'} - K_i/\mu^{AA'}\,. \tag{B.8}$$

Table B.3 lists the calculated field shifts, taking the error on the isotope shift and of the fit into account.

Table B.3: Field shifts in MHz, extracted based on the isotope shift measurements and the assumption $\delta \left\langle r_c^2 \right\rangle^{40,48} = 0$.

transition	[nm]	42	44	46	48
$4\,^2S_{1/2} - 3\,^2D_{5/2}$	729	−80.5199(21)	−105.8129(23)	−48.6098(25)	0
$3\,^2D_{3/2} - 3\,^2D_{5/2}$	D-fine	+0.119 437(25)	+0.156 910(26)	+0.072 106(30)	0

B.3.3 Isotope shifts as function of difference in charge radius

A different approach, not assuming $\delta \left\langle r_c^2 \right\rangle^{40,48} = 0$, is to plot the modified isotope shift $\mu\delta\nu_i^{AA'}$ from equation (B.6) versus the modified charge radius squared $\mu\delta \left\langle r_c^2 \right\rangle^{40A'}$. However, this approach requires literature values for the charge radii. A linear fit directly gives the mass shift constant K_i as intersect, and the field shift constant F_i as slope, in a linear regression model. Table B.4 gives the fitted mass and field shift constants together with the mass shift constants calculated before (see eq. (B.7)). The errors are scaled standard errors, that means forcing $\chi^2 = 1$, as usual.[1]

The fit can be done for each transition separately together with the charge radius, or in a three dimensional fit (3d King plot) with both transitions at the same time. In any case, I take the error on all variables x, y (,z) into account using Weighted Orthogonal Distance Regression (scipy.ODR) [A162]. For the fits, I use the charge radii reported by Palmer et al. [A47], or, alternatively, the original values reported by Wohlfahrt et al., tbl. IV [A163]. These charge radii are listed in table B.5, together with new estimates based on these fits, as described in the following section.

[1] This makes the fitted errors independent of a global scaling of all weights on the input data.

Table B.4: Extracted mass shift constants K_i and field shift constants F_i. The first row represents the direct measurement of $\delta\nu_i^{40,48}$ using the assumption $\delta\left\langle r_c^2\right\rangle^{40,48} = 0$. The following rows are the results from the two- and three-dimensional Weighted Orthogonal Distance Regression with charge radii taken from the results of Palmer et al. [A47] (top) and Wohlfahrt et al. [A163] (bottom).

source	$K_{\text{D-fine}}$ [MHz u]	$F_{\text{D-fine}}$ [MHz fm^{-2}]	$cov(K,F)_{\text{D-fine}}$ [u fm^{-2}]	K_{729} [GHz u]	F_{729} [MHz fm^{-2}]	$cov(K,F)_{729}$ [u fm^{-2}]
$\delta\left\langle r_c^2\right\rangle^{40,48} = 0$ and eq. (B.7)	−3055.6432(65)	+2394.915 09(48)				
2d (Palmer et al. [A47])	−3054.85(25)	+0.551(4)	-5.979×10^{8}	+2394.38(17)	−371(3)	-2.658×10^{14}
3d (Palmer et al. [A47])	−3054.9(10)	+0.551(15)		+2394.4(6)	−371(10)	
2d (Wohlfahrt et al. [A163])	−3057.4(11)	+0.568(17)	-1.138×10^{10}	+2396.1(7)	−383(11)	-5.190×10^{15}
3d (Wohlfahrt et al. [A163])	−3057.4(21)	+0.568(32)		+2396.1(14)	−383(21)	

B.3.4 Deduced charge radii

The charge radii can be calculated from eq. (B.2) as

$$\delta \left\langle r_c^2 \right\rangle^{AA'} = \delta\nu_i^{AA'}/F_i - K_i/(\mu\, F_i)\,, \tag{B.9}$$

using the fitted mass and field shift constants together with the isotope shift measurement.

The error on $\delta \left\langle r_c^2 \right\rangle^{AA'}$ is calculated as

$$S_\delta \left\langle r_c^2 \right\rangle^{AA'} = \sqrt{\sum_n \left(\frac{\partial\delta \left\langle r_c^2 \right\rangle^{AA'}}{\partial x_n} S_n \right)^2 - 2\frac{\partial\delta \left\langle r_c^2 \right\rangle^{AA'}}{\partial K_i} \frac{\partial\delta \left\langle r_c^2 \right\rangle^{AA'}}{\partial F_i} cov(F_i, K_i)} \tag{B.10}$$

where the derivatives are given by

$$\frac{\partial\delta \left\langle r_c^2 \right\rangle^{AA'}}{\partial\nu} = 1/F_i \tag{B.11}$$

$$\frac{\partial\delta \left\langle r_c^2 \right\rangle^{AA'}}{\partial\mu} = K_i/\mu^2 F_i \tag{B.12}$$

$$\frac{\partial\delta \left\langle r_c^2 \right\rangle^{AA'}}{\partial K_i} = -1/\mu F_i \tag{B.13}$$

$$\frac{\partial\delta \left\langle r_c^2 \right\rangle^{AA'}}{\partial F_i} = -\nu/F_i^2 + K/\mu F_i^2 \tag{B.14}$$

and $cov(F_i, K_i)$ is the covariance between field and mass shift constants from the linear fit, listed in table B.4.

The deduced charge radii are listed in table B.5 together with the seed values for the fits and other literature values for comparison. Note that we get *exactly* the same results and error for each of the two 2d fits, independent of which transition we use. This is due to the fact that we are limited by the accuracy of literature values for the charge radii.

Table B.5: Differences in mean charge radii squared $\delta \left\langle r_c^2 \right\rangle^{40\,A'}$ in fm^2. The columns represent: 0: Isotope number. 1: Our 2d fit seeded with the values fitted by Palmer (column 3). 2: Our 2d fit seeded with the values measured by Wohlfahrt tbl. IV (column 6). 3: Fitted values by Palmer. 4: Supposedly Wohlfahrt's data, as given by Palmer, which is not what I calculate (see next columns). 5-7: calculated from Wohlfahrt [A163, A164] using eq. (B.15). 8-9: Values from Shi et al. [A50] and Ruiz et al. [A165], which use Palmer's data to seed their fits (which I think is incorrect...).

isotope	this work P. seed	this work W. IV seed	Palmer et al. [A47]	W. by P. [A47]	W. tbl. VII [A163]	W. tbl. IV [A163]	W. 1978 [A164]	Shi et al. [A50]	Ruiz et al. [A165]
40	+0	+0							+0
41			+0.0032(25)						
42	+0.2152(13)	+0.2140(53)	+0.2153(49)	+0.210(7)	+0.210(42)	+0.211(8)	+0.2104	+0.2160(49)	
43			+0.1254(32)	+0.117(25)		+0.117(8)	+0.1158		+0.114(4)[8]
44	+0.2818(16)	+0.2834(67)	+0.2832(64)	+0.290(9)	+0.287(42)	+0.281(8)	+0.2807	+0.2824(64)	+0.288(2)[6]
45			+0.1188(59)						+0.125(3)[8]
46	+0.1263(12)	+0.1370(49)	+0.1242(50)	+0.147(45)		+0.147(8)	+0.1473		+0.125(2)[8]
47			+0.005(13)						+0.002(3)[9]
48	−0.0060(19)	+0.0128(78)	−0.0044(60)	−0.005(6)	−0.007(42)	+0.007(8)	+0.0063	−0.0045(59)	+0.001(3)[10]

Wohlfahrt et al. [A163] measured the absolute charge radii $((\left\langle r_c^2 \right\rangle^{A'})^{1/2}$ in units of fm. We need to convert to

$$\delta \left\langle r_c^2 \right\rangle^{40\,A'} = ((\left\langle r_c^2 \right\rangle^{A'})^{1/2})^2 - ((\left\langle r_c^2 \right\rangle^{A=40})^{1/2})^2 \tag{B.15}$$

and the error is calculated as

$$\begin{aligned} S\left(\delta \left\langle r_c^2 \right\rangle^{40\,A'}\right) &= \sqrt{\left[2 \cdot (\langle r_c^2 \rangle^{A'})^{1/2} \cdot S\left((\langle r_c^2 \rangle^{A'})^{1/2}\right)\right]^2 + \left[2 \cdot (\langle r_c^2 \rangle^{A})^{1/2} \cdot S\left((\langle r_c^2 \rangle^{A})^{1/2}\right)\right]^2} \\ &\approx 4 \cdot (\left\langle r_c^2 \right\rangle^{A=40})^{1/2} \cdot S\left((\left\langle r_c^2 \right\rangle^{A=40})^{1/2}\right) \end{aligned} \tag{B.16}$$

B.3.5 King plot

To be again independent of literature values for the charge radii, we can calculate the King plot from the two transition measurements using equation (B.6) twice to get

$$\begin{aligned}\mu\delta\nu_i^{AA'} &= K_i - \tfrac{F_i}{F_j}K_j + \tfrac{F_i}{F_j}\,\mu\,\delta\nu_j^{AA'} \\ &= c + m\cdot\left(\mu\,\delta\nu_j^{AA'}\right)\,.\end{aligned} \tag{B.17}$$

This equation was fitted to our D-fine and 729 data ($\mu\delta\nu_i^{AA'}$ from tables B.1 and B.2) using 2 different methods. One is ordinary least squares, taking only the error on the D-fine transition into account, since it is the dominant error compared to the 729 measurement. The other method is to use Weighted Orthogonal Distance Regression, taking the error on both measurements into account. The ODR analysis was also done with reversed axes for comparison. The results are listed in table B.6 and all fitting procedures are in agreement. A King plot is shown in figure B.2.

Table B.6: King plot analysis of the D-fine and 729 transition according to equation B.17. The slope gives the ratio of the field shift constants $\frac{F_i}{F_j}$. For the Weighted ODR, I took errors in both transitions into account and made two separate fits with reversed axes, and calculated the inverse slope for comparison. The two fits agree. Also for comparison, I fitted the D-fine vs 729 using ordinary least squares, and neglecting the error on the D fine structure, since it is orders of magnitudes smaller than the error on the 729 measurement. For the least squares fit, I also subtracted the modified isotope shift for $\delta\nu_{i,j}^{40,42}$ from each axis before fitting, in order to make the fitting work numerically. This fit agrees as well with the previous.

Axis direction (eq. B.17)	$m = \frac{F_i}{F_j}$	$c = K_i - \frac{F_i}{F_j}K_j$ [Hz u]	$\frac{1}{m} = \frac{F_j}{F_i}$
i = D-fine, j = 729			
ordinary least sq.	$-1.483\,05(21)\times10^{-3}$	N/A	$-674.288(10)$
ORD	$-1.483\,05(20)\times10^{-3}$	$+496.1(5)\times10^{6}$	$-674.29(9)$
i = 729, j = D-fine			
ODR	$-674.29(9)$	$+334.53(27)\times10^{9}$	$-1.483\,05(20)\times10^{-3}$

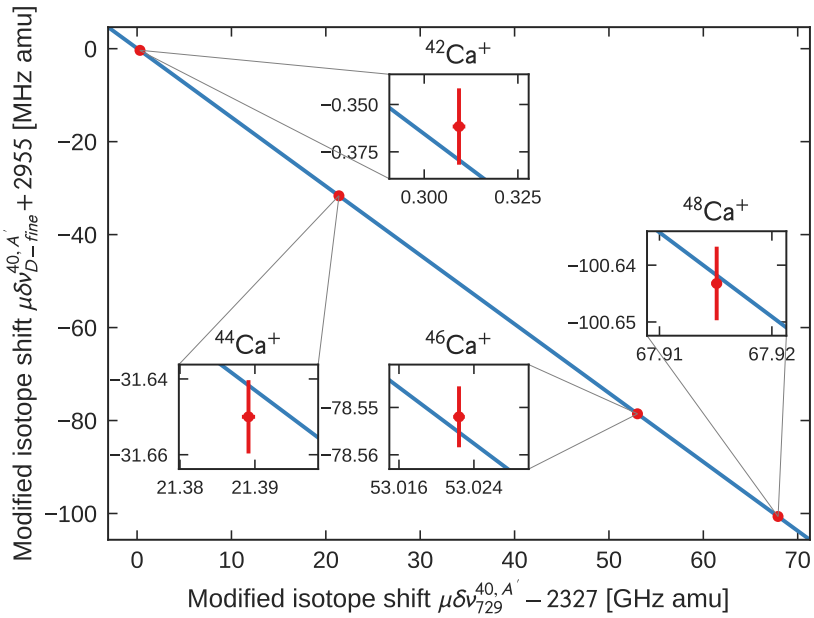

Figure B.2: King plot of the D-fine and 729 transition, with the line drawn according to the ordinary least squares fit given in table B.6.

B.4 Discrepancy with data by other authors

Table B.7: Measurement discrepancies for Ca^+ transitions. The sum should be zero. The measurements come from the cited references, except for the first row, which is independent of our measurements and takes instead the D-fine value from Yamazaki et al. [A36] and the 729 value from Chwalla et al. [A88]. All numbers in units of MHz. The significant error stems from the measurements by Shi et al. [A50].

isotope	729 [this work]	D-fine [this work]	397 [A50]	866 [A50]	$\sum$
40 (absolute)	−411 042 129.776 393 2(10)	+1 819 599.021 504(37)	+755 222 765.896(88)	−346 000 234.867(96)	+0.274(130)
40 (absolute)	−411 042 129.777(2)	+1 819 599.021 534(8)	+755 222 765.896(88)	−346 000 234.867(96)	+0.274(130)
42 (shift)	+2771.873(2)	−3.519 896(24)	+425.706(94)	−2349.974(99)	+0.288(136)
44 (shift)	+5340.888(2)	−6.792 470(22)	+849.534(74)	−4498.883(80)	+0.736(109)
46 (shift)	+7768.401(2)	−9.901 524(21)			
48 (shift)	+9990.383(2)	−12.746 611(27)	+1705.389(60)	−8297.769(81)	+0.028(101)